



**THE PUZZLING PROBLEMS OF THE LOCAL
GROUP DWARF SPHEROIDALS; THE FIGHT
FOR SURVIVAL IN THE EARLY UNIVERSE**

Claire Rachel Cashmore

Submitted for the degree of Doctor of Philosophy

September 2018

Theoretical Astrophysics Group
Department of Physics and Astronomy
University of Leicester

Abstract

The puzzling problems of the Local Group dwarf spheroidals; the fight for survival in the early Universe.

Claire Rachel Cashmore

The dwarf spheroidal galaxies (dSphs) of our Local Group pose challenges to our theories of galaxy formation and evolution in a Λ CDM Universe. Despite the wealth of information available from these systems provided by their close proximity, little is understood about their individual histories. The faintest dSphs host a single, ancient stellar population, the formation of stars in these galaxies ceased billions of years ago and they are devoid of gas. As these systems are so small, they are susceptible to gas loss, however this cannot be a simple process due to the diverse range of properties they exhibit, despite residing in haloes of the same mass.

In this thesis I address two processes resulting in gas removal at early times and attempt to further our understanding of these systems by isolating each process. I use hydrodynamical simulations to explore the impact of each process to assess their significance and to identify the dominant influences on their evolution. Firstly I simulate the effect of SNe feedback on dSph progenitors undergoing an initial burst of star formation at high redshift ($z \sim 10$) and the conditions under which they retain gas. In order to host an extended burst of star formation the number of supernovae must be lower than that expected if we assume star formation proceeds in a similar fashion to that in larger galaxies. The impact of an AGN outflow originating from the Milky Way on the surrounding dwarf galaxies is also simulated, which easily strips gas from these systems, leaving behind a halo with an ancient stellar population. The difficulty of retaining gas in the early Universe could be alleviated if they accreted gas during the period of extended star formation. I investigate these three processes in the context of isolated dwarfs.

The following chapters from this thesis have been published or are currently under preparation for future publication in the journal *The Monthly Notices of the Royal Astronomical Society*:

Too small to succeed: The difficulty of sustaining star formation in low mass haloes, **Cashmore C.R.**, Wilkinson M. I., Power C., Bourne M.A., 2017, MNRAS, 468, 451.

Do AGN outflows trigger or suppress star formation in dSphs?, **Cashmore C. R.**, Wilkinson M. I., Power C. Bourne M.A., 2017, *in prep.*

Cold mode gas accretion in dSph progenitors, **Cashmore C. R.**, Wilkinson M. I., Power C. *in prep.*

Acknowledgements

There are many people I would like to thank without whom the completion of this thesis would not have been possible. First of all I would like to thank my supervisor Mark Wilkinson for his continuous encouragement and support, his guidance was invaluable and I really appreciate all the time and effort he has put into being my supervisor. I would also like to thank my collaborators Chris Power and Martin Bourne for their support, advice and many insightful discussions. I am very thankful to all the staff in the theoretical astrophysics group; Andrew, Walter, Richard, Sergei, Graham and Chris for all of their regular input and advice, which has helped me to gain skills and confidence when discussing my work in an academic environment. Thanks must also go to Lisa for all the effort and time she puts into organising everything, especially when travelling to conferences. Thank you to all the people I have had the pleasure of sharing an office with over the years, Martin, Tom, Charlie, Hossam, Hastyar, Pete, Gillian, Lillian, Mark, Christian, Hasanuddin, Amery, Rob, Stuart, Stephen, and although somewhat brief, Elen, Jack, Anagha and Miriam, for a friendly, supportive work environment and many interesting discussions. Thank you to Martin especially for his invaluable support and guidance in relation to hydrodynamical simulations and always patiently answering my endless questions.

The work presented in this thesis would have not been possible without the use of both the ALICE high performance computing facility and the DiRAC Complexity system, operated by the University of Leicester IT Services, which forms part of the STFC DiRAC HPC Facility (www.dirac.ac.uk). This equipment is funded by BIS National E-Infrastructure capital grant ST/K000373/1 and STFC DiRAC Operations grant ST/K0003259/1. DiRAC is part of the National E-Infrastructure. When I first began I had much to learn about using these machines and I am grateful to the IT team for their support. Gary Gilchrist provided a large amount of general support, Jon Wakelin for support and providing valuable HPC courses, and Chris Rudge and Liam Gretton for answering my questions when I have experienced problems.

I would also like to thank those who supported me before the start of my journey at Leicester. Firstly to Dean McLaughlin for giving me the opportunity to gain my first research experience in theoretical astrophysics (and the institute of physics for funding it). Thanks also must go to Joana Oliveira and Rob Jeffries for all their support with my applications and non academic issues, as well as all of the other members of staff in the astrophysics department at the University of Keele who all added to my experience in one way or another.

I would also like to thank my close family, Wendy, Kevin and Rachel who have been by my side throughout all my years of study. Last but not least, I would like to thank David, whose patience, understanding and endless support has been an essential part of this accomplishment.

Contents

1	Introduction	7
1.1	Dwarf Galaxies	7
1.1.1	Types of dwarf galaxy	8
1.1.2	The surprising diversity of the local group dSphs	8
1.1.3	The local group dwarfs and the problems they present for Λ CDM	11
1.2	Mechanisms for gas removal	16
1.2.1	Photoionization	16
1.2.2	Stellar Feedback	18
1.2.3	Environmental effects: the influence of the Milky Way	20
1.3	This thesis	26
2	Hydrodynamical simulations	27
2.1	Astrophysical simulations	27
2.2	The Nbody Technique	28
2.3	SPH	31
2.3.1	Fluid Equations	32
2.3.2	The smoothing kernel	34
2.3.3	Dissipation	34
2.4	Radiative cooling	37
2.5	Star formation	40
2.6	Stellar feedback	41
3	Too small to succeed: The difficulty of sustaining star formation in low mass haloes	43
3.1	Introduction	43
3.2	Description of simulations	46
3.2.1	Initial conditions	47
3.2.2	Cooling and Feedback	51
3.3	Results	53
3.3.1	Spherical gas distributions	53
3.3.2	Flattened gas distributions	58
3.3.3	Metallicity	71
3.4	Discussion	72

3.5	Conclusions	77
4	Do AGN outflows trigger or suppress star formation in dSph progenitors?	79
4.1	Introduction	79
4.2	Models	81
4.3	Simulations	84
4.3.1	Initial Conditions	84
4.3.2	Simulation Code	86
4.4	Results	87
4.4.1	Outflow velocities of 250kms^{-1}	90
4.4.2	Outflow velocities of 500kms^{-1}	95
4.4.3	Outflow velocities of 1000kms^{-1}	100
4.5	Discussion	110
4.6	Conclusion	114
5	Cold mode accretion in dSph progenitors	116
5.1	Introduction	116
5.2	Simulations	118
5.2.1	Initial conditions	119
5.2.2	Smooth Inflow	120
5.2.3	Clumpy Inflow	121
5.3	Results	123
5.3.1	Clumpy Inflows	123
5.4	Discussion	129
5.5	Conclusion	132
6	Conclusions	133
6.1	Final comments	134
A	Convergence test	135
B	Stability test	139
C	Feedback implementations	141

List of Figures

2.1	The cooling function for primordial gas.	38
2.2	The cooling function as a function of metallicity.	39
3.1	The evolution of the density and mass profiles for a spherical gas distribution.	54
3.2	Evolution of the halo density profiles for a spherical gas distribution.	57
3.3	Evolution of the density and mass profiles with varying numbers of SNe for gas distributed in a disk.	60
3.4	Density and temperature maps for gas distributed in a disk.	61
3.5	Evolution of the angular momentum for gas distributed in a disk.	62
3.6	Maps of the initial and final gas temperature for the fiducial spherical run.	63
3.7	Evolution of the gas density and enclosed mass for gas distributed in a disk varying several model parameters.	64
3.8	Evolution of the gas density and enclosed mass when increasing the number of SNe for more concentrated disk models.	67
3.9	Fraction of gas with $v > v_{\text{esc}}$ for runs with gas distributed in a disk.	70
3.10	Dark matter halo evolution for runs with gas distributed in a disk.	71
3.11	Evolution of the gas density with varying metallicity.	72
4.1	Comparison of the restoring force and the gas pressure in the disk to the ram pressure of the AGN outflow when the dwarf is 100kpc away from the host galaxy.	88
4.2	Comparison of the restoring force in the disk and the gas pressure to the ram pressure of the AGN outflow when the dwarf is 50kpc away from the host galaxy.	89
4.3	Evolution of the gas density profiles, enclosed mass profiles and stellar surface density profiles with radius for disks with $r_s = 300\text{pc}$ and an outflow velocity of 250kms^{-1}	91
4.4	Evolution of the gas density profiles, enclosed mass profiles and stellar surface density profiles with radius for disks with $r_s = 400\text{pc}$ and an outflow velocity of 250kms^{-1}	93
4.5	The number of stars formed over time for simulations with an outflow velocity of 250kms^{-1} compared to the isolated case.	94

4.6	Evolution of the gas density profiles and enclosed mass profiles with radius for disks with $r_s = 300\text{pc}$ and an outflow velocity of 500kms^{-1}	96
4.7	Evolution of the stellar surface density profiles, enclosed stellar mass profiles, halo density profiles and halo enclosed mass profiles radius for disks with $r_s = 300\text{pc}$ and an outflow velocity of 500kms^{-1} at a distance of 100kpc from the host galaxy.	98
4.8	Evolution of the gas density profiles and enclosed mass profiles with radius for disks with $r_s = 400\text{pc}$ and an outflow velocity of 500kms^{-1}	99
4.9	Evolution of the gas density profiles, enclosed mass profiles and stellar surface density profiles with radius for disks with $r_s = 300\text{pc}$ and an outflow velocity of 1000kms^{-1}	101
4.10	Evolution of the gas density profiles, enclosed mass profiles and stellar surface density profiles with radius for disks with $r_s = 400\text{pc}$ and an outflow velocity of 1000kms^{-1}	103
4.11	Snapshots showing the evolution of the gas density, temperature and pressure for a disk with $r_s = 300\text{pc}$ at a distance of 100kpc from the host galaxy, orientated edge on to an outflow with velocity 500kms^{-1}	105
4.12	Snapshots showing the evolution of the gas density, temperature and pressure for a disk with $r_s = 300\text{pc}$ at a distance of 100kpc from the host galaxy, orientated edge on to an outflow with velocity 1000kms^{-1}	106
5.1	Evolution of the density profile as a function of radius for the gas in runs 1-4.	122
5.2	Evolution of the enclosed mass profiles as function of radius for the gas in runs 1-4.	124
5.3	Evolution of the density profiles as a function of radius for runs with and without SNe FB.	126
5.4	Snapshots showing the evolution of the gas density, temperature and pressure for run 2.	128
5.5	Snapshots showing the evolution of the density, temperature and pressure for run 4.	129
A.1	Evolution of the gas density and enclosed mass for simulated dSphs with an initially spherical gas distribution.	136
A.2	Evolution of the gas density and enclosed mass for simulated dSphs with gas initially distributed in a disk.	137
B.1	Evolution of the gas and halo density profiles for gas in a spherical distribution with no feedback.	140
B.2	Evolution of the gas and halo density profiles for gas distributed in a disk with no feedback.	140
C.1	Evolution of the radius of a SN-driven shell.	142
C.2	Evolution of the radial velocity of the SN-driven shell.	143
C.3	Evolution of the total momentum of the gas surrounding the SN.	144

List of Tables

3.1	Summary of the simulations presented in chapter 3.	47
4.1	List of rms velocities (in kms^{-1}) for the simulations with a disk scale radius $r_s = 300\text{pc}$	107
4.2	List of rms velocities (in kms^{-1}) for the simulations with a disk scale radius $r_s = 400\text{pc}$	109
5.1	Summary of the simulations presented in chapter 4.	121
5.2	The number of stars formed for the simulations presented in this chapter. .	127

List of Abbreviations

AGN	Active galactic nuclei
dSph	Dwarf spheroidal
dIrr	Dwarf irregular
DMO	Dark matter only
IMF	Initial mass function
IGM	Intergalactic medium
ISM	Interstellar medium
LMC	Large Magellanic Cloud
LG	Local Group
MSP	Missing satellite problem
MW	Milky Way
SMC	Small Magellanic Cloud
SFH	Star formation history
SFR	Star formation rate
SN	Supernova
SNe	Supernovae
SMBH	Supermassive black hole
SPH	Smoothed particle hydrodynamics
TBTF	Too big to fail
UF	Ultra faint
ΛCDM	Λ cold dark matter

Chapter 1

Introduction

1.1 Dwarf Galaxies

Dwarf galaxies dominate the total galaxy population by number (Marzke and da Costa, 1997) and would have been even more numerous at earlier times (Ellis, 1997). As the first bound objects in the universe, and the smallest substructures we can see today, understanding the evolution of dwarf galaxies is essential in order to understand the formation and evolution of the larger galaxies resulting from the merging of these 'building blocks' over time (Kauffmann and White, 1993). They are dark matter dominated (Strigari *et al.*, 2008; Wolf *et al.*, 2010), making them important tools for studying the nature of dark matter and testing long-standing theories on galaxy formation.

The Local Group (LG) consists of two large galaxies; our Galaxy, the Milky Way (MW), Andromeda and numerous smaller satellites which orbit these galaxies. The brighter satellites, the Large and Small Magellanic Clouds (LMC and SMC respectively,) were first identified with the naked eye in 954 A.D. by Al Sufi, due to their close proximity and large stellar masses. The fainter dwarf spheroidals (dSphs) were discovered gradually as they were more difficult to detect: Sculptor in 1937 (Shapley, 1938) and Draco and Ursa Minor around 1955 (Wilson, 1955). Prior to 2006, there were around 11 known satellites around the Milky Way (including 9 dSphs), presently there are around 56 as recent surveys have revealed a large population of low luminosity dwarfs.

1.1.1 Types of dwarf galaxy

The local group dwarf galaxies can be split into three categories: (i) Dwarf spheroidals are dominated by old or intermediate age stellar populations, spheroidal in morphology, lie close to the host galaxy and are devoid of gas; (ii) Dwarf irregulars (dIrrs) also host younger stellar populations, have an irregular morphology, lie further away from the host galaxy and contain significant amounts of gas; and (iii) Transition types which have properties common to both dSphs and dIrrs, they contain gas but at a much lower level than that of dIrrs, and they do not host ongoing star formation. These transition types would more closely resemble dSphs than dIrrs if their gas was removed.

It is the dSphs that are the most puzzling as they contain no gas at all. There are several processes which are capable of removing a significant mass of gas from dSphs which lie close to the Milky Way, (discussed in detail in section 1.2). However, it is debatable whether these processes would strip the galaxy of gas completely, even when combined, as the gas residing in the centre of the galaxy is the densest and most difficult to remove. The ultra faint dwarf galaxies (UF) are even fainter than the dwarf spheroidals, and resemble them in both morphology and their ancient stellar populations.

1.1.2 The surprising diversity of the local group dSphs

The local group dSphs have a very diverse range of properties with stellar masses in the range 10^3 - $10^7 M_{\odot}$, luminosities in the range 7×10^3 - $2 \times 10^7 L_{\odot}$, and mean metallicities $[\text{Fe}/\text{H}]$ in the range -2.72 to -1 dex (McConnachie, 2012). The properties of the known dwarfs which are satellites of the Milky Way are summarised in table 1.1. This diversity makes it difficult to create a simple model which fits the formation and evolution of all of the dwarf galaxies in the Local Group. All the known dSphs lie within ~ 300 kpc of the Milky Way (with a couple of exceptions such as Cetus and Tucana) enabling their brightest stars to be studied with ground based telescopes, allowing accurate measurements of kinematics, star formation histories and stellar populations. The star formation histories (SFHs) of a large number of local group dwarfs have been measured using the colour magnitude diagram synthesis method (Tolstoy *et al.*, 2009). Kinematics and metallicities for large numbers of individual stars have been obtained in dSphs by various methods (Tolstoy *et al.*, 2006; Simon and Geha, 2007; Martin *et al.*, 2007; Walker *et al.*, 2009d,b). It is difficult to compare dwarf galaxies with ongoing star formation with those that are not currently undergoing star formation as the methods used to measure their properties differ. The dSphs contain

no gas, so their internal kinematics can only be determined from stellar velocity dispersions, whereas dIrrs internal kinematics can be easily determined from the gas, and because of their larger distances, measuring the stellar velocity dispersion is much more difficult.

The dSphs of the local group also have very different fractions and ages in their distinct stellar populations, star formations histories (SFHs), metallicities and level of chemical enrichment (Tolstoy *et al.*, 2009; Weisz *et al.*, 2014a). No two dwarf galaxies are alike. They all contain stars that are more than 10Gyr old and they all have intermediate populations around 1-10Gyr old regardless of their morphology. Younger populations tend to be more centrally concentrated. Many also show spatial variations in age and metallicity. Fornax and Sagittarius are the brightest ($2 \times 10^6 L_{\odot}$) and most massive ($M_{*}=2 \times 10^7 M_{\odot}$) dSphs and the only ones known to contain globular clusters (Hodge, 1961; Sarajedini and Layden, 1995). They both have strong metallicity and age gradients, with populations of young, metal-rich stars residing in their centres. The observed mean metallicities are higher than those of other dSphs, $[Fe/H] \sim -0.8$ and -1 for Fornax and Sagittarius respectively, showing evidence of more metal enrichment from the extended periods of star formation, starting from > 10 Gyr ago and lasting until ~ 2 Gyr ago (possibly even more recently for Fornax (de Boer *et al.*, 2012a)). Sculptor and Leo I are both around ten times smaller than Fornax and Sagittarius, and have quite different properties. Sculptor shows evidence for continuous star formation from 14Gyr - 7Gyr ago with a steady increase in star formation rate (SFR) (de Boer *et al.*, 2012b). Like Fornax there is a gradient in age and metallicity, with the youngest stars concentrated at the centre, and metallicity increasing smoothly with age. However Leo I has two distinct bursts of star formation at ~ 3 and 12 Gyr ago, and $\sim 90\%$ of stars are young - between 7 and 1 Gyr old (Gallart *et al.*, 1999). There are no gradients in age or metallicity, and there is negligible evidence for external influences (Koch *et al.*, 2007a), so it seems a relatively undisturbed dSph.

Carina is possibly the most interesting dSph, with three distinct bursts of star formation, the stellar population is dominated by the second generation and the star formation rate in between these bursts is effectively zero (Hurley-Keller *et al.*, 1998; de Boer *et al.*, 2014). Despite three separate populations, there has been relatively little chemical enrichment with an average metallicity $[Fe/H]= -1.7$ (Koch *et al.*, 2006). Each distinct burst continued for a period of around 1Gyr. The distinct bursts and lack of enrichment suggests that SN feedback could have been responsible for this pattern, as gas was ejected along with a large fraction of metals after each burst.

In Draco 90% of the stars are > 10 Gyr old, and some low level star formation continued

until ~ 2 Gyr ago, although there is no metallicity gradient observed (Aparicio *et al.*, 2001). Ursa Minor is similar to Draco with $[\text{Fe}/\text{H}] = -1.9$, no detected metallicity gradient, and having 90% of its stars with ages > 13 Gyr. It has been suggested that it possibly hosts a pure old stellar population (Carrera *et al.*, 2002), although there was low level star formation up to 2Gyr ago. Sextans also appears to host only one old stellar population with no observed stars younger than 12Gyr (Olszewski and Aaronson, 1985), although the average metallicity of Sextans is $[\text{Fe}/\text{H}] = -1.5$ (Da Costa *et al.*, 1991), so it has retained more metals than Carina, even with only one burst of star formation.

The range in properties of the dSphs is surprising, as they are estimated to be embedded in roughly the same mass dark matter haloes, having a total mass of $\sim 10^7 M_\odot$ in the central 300pc, regardless of their luminosity (Mateo, 1998; Mateo *et al.*, 1993; Strigari *et al.*, 2008; Walker *et al.*, 2009a). This trend does not extend to the ultra faints however, whose mass is found to decrease with their luminosity, suggesting that they are hosted by less massive haloes than the dSphs (Simon and Geha, 2007; Martin *et al.*, 2007). With the number of ultra faint dwarfs increasing, extending the luminosity to lower and lower values as the detection limits of surveys improve, this suggests that if a minimum halo mass for galaxies exists current observations don't appear to have yet found it.

All dSphs contain stars, therefore at early times they must have contained significant amounts of gas and could have resembled dIrrs. At some point gas was lost, star formation ended and through a combination of processes the dwarfs evolved into dSphs. The differences in ages of stellar populations suggests that this happened at different times for different galaxies. Dwarf spheroidals do have a common property with dwarf irregulars - an exponential light distribution (Kormendy, 1985), which raised the suggestion that dSphs may originate from dIrrs by a loss of gas through any/all of the mechanisms described in section 1.2. However, Grebel *et al.* (2003) find there are fundamental differences between the dSphs and dIrrs. The metallicity of dIrrs is too low for their luminosity compared to the dSphs. This suggests that the dSphs, most of which have been quiescent for several billion years, experienced more efficient chemical enrichment at earlier times compared to the dIrrs which host ongoing star formation presently. Therefore it is highly unlikely that dIrrs (in which star formation and enrichment proceeds slowly over time) are dSph progenitors which have retained their gas as the early evolution of these systems are different.

A link between the close proximity of the dSphs to the MW and the mechanisms caused by the presence of the MW has been pointed out (van den Bergh, 1994), but there are exceptions to this trend which are not explained. The Magellanic Clouds are dIrrs that

are close to the MW, and Tucana and Cetus are dSphs which lie at distances of ~ 775 to 880pc respectively (Whiting *et al.*, 1999; Castellani *et al.*, 1996). From the diversity of their properties, the evolution of the local group dwarfs is likely to be extremely complex as these systems are influenced by multiple internal and external processes which depend on many different variables, so a model which describes all of their properties will be very challenging to create.

1.1.3 The local group dwarfs and the problems they present for Λ CDM

The current cosmological model of dark energy and cold dark matter (Λ CDM), which describes the formation and growth of structure in the Universe has survived rigorous testing through both observational and theoretical means. The current model provides excellent agreement with observations of the cosmic microwave background radiation (CMB)(see, e.g. Planck Collaboration *et al.*, 2016a; Hinshaw *et al.*, 2013), the lyman-alpha forest (Hernquist *et al.*, 1996), and supernovae (Riess *et al.*, 1998), as well as with simulations of large scale structure (Davis *et al.*, 1985). The properties of galaxies produced in simulations of a Λ CDM universe are in generally good agreement with those observed (see, e.g. Schaye *et al.*, 2015; Ludlow *et al.*, 2017). Although Λ CDM has been successful in reproducing large scale structure in the Universe in simulations, there are some discrepancies regarding the formation and growth of structure on the scales of dwarf galaxies.

- The 'Missing Satellite Problem' (MSP).

Cosmological simulations predict the number of satellites around the Milky Way to be an order of magnitude larger than those which we have observed (Klypin *et al.*, 1999; Moore *et al.*, 1999). Simulations following the growth of dark matter substructures predict ~ 300 satellites inside a 1.5Mpc radius around a MW sized halo, while the number observed, although continually increasing, is an order of magnitude smaller (presently around 55 - see table 1). Over the last decade surveys such as the Sloan Digital Sky Survey (SDSS; York *et al.*, 2000) and the dark energy survey(DES; Dark Energy Survey Collaboration *et al.*, 2016) have revealed a large population of ultra faint dwarf galaxies in different areas of the sky.

The MSP was identified in 1999 when there were around 11 known dwarfs around the Milky Way and this number was being compared to the number of subhaloes found in dark matter only simulations, which by construction neglected baryonic

processes. The number of known satellites of the Milky way has increased at least five-fold over the last decade. It is therefore a possibility that the problem is not that the satellites aren't actually present around our Galaxy, but simply that they haven't yet been observed by surveys carried out to date due to their extremely low surface brightnesses, especially if they lie at large distances (Koposov and Belokurov, 2008; Tollerud *et al.*, 2008; Bullock *et al.*, 2010). There are also other issues related to observation bias such as the fact that not all areas of the sky have been targeted, dwarfs which lie close to the plane of the Galaxy are difficult to observe, and fainter dwarfs at large radii won't be found as easily as the ones at smaller radii. When considering the number and locations of dwarfs observed along with the incompleteness of SDSS, Tollerud *et al.* (2008) estimate that this is consistent with there being 300-500 satellites brighter than Bootes II ($M_v = -2.7$), and a total count of up to 2000, depending on assumptions. However, Hargis *et al.* (2014) found lower numbers when correcting for the known population of SDSS dwarfs, predicting 37 – 114 regular dwarfs with $L > 10^3 L_\odot$ and 131 – 782 'hyperfaint' dwarfs with $L < 10^3 L_\odot$ within 300kpc over the entire sky. DES should be able to recover the full population of satellites with $L > 10^3 L_\odot$, along with increasing the number of hyperfaint dwarfs within 300kpc. Indeed, the DES has revealed many new dwarf galaxies, exceeding the number discovered in SDSS in just two years (see, e.g. Bechtol *et al.*, 2015; Drlica-Wagner *et al.*, 2015; Kim and Jerjen, 2015). Other surveys have also increased the numbers: for example Pan-STARRS 3 π (Laevens *et al.*, 2015b,a) and ATLAS (Torrealba *et al.*, 2016b,a). Future surveys that will have the ability to go deeper are expected to detect very faint satellites out to much larger distances from the MW, observing the complete luminosity function out to the virial radius. Without a doubt, surveys such as SDSS and DES have extended the dwarf galaxy regime to extremely low luminosities and sizes, alleviating the MSP and greatly adding to the number of satellites. Recent advances in simulations have shown that the inclusion of baryonic physics (rather than dark matter only runs) can suppress star formation which can lead to a significant number of low mass haloes at extremely low luminosities, making them almost unobservable. It is possible these galaxies exist but have not yet been observed. There is a limit to the smallest halo mass set by the free streaming length of DM particles (see, e.g. Bond *et al.*, 1980; Bond and Efstathiou, 1984; Schneider *et al.*, 2013), if there is a limit to the smallest size of a galaxy (DM and gas) then the observations haven't found it yet. Simulations which model baryonic physics have

shown that the inclusion of processes such as stellar feedback and reionization also make the problem less severe (discussed further below). It is not yet clear whether the galaxies yet to be found in future surveys will be consistent with the predictions made by Λ CDM, but the problem is certainly less severe than when first posed.

Free streaming length of DM set the smallest halo mass

- 'Too Big To Fail' (TBTf)

Although the MSP has a potential solution in that future surveys could detect many more low luminosity dwarfs, the number of satellites is not the only issue. Some of the largest satellites produced in dark matter only (DMO) cosmological simulations are also missing. These satellites are too massive, with central densities too high to be compatible with the satellites we presently observe. The ultra faint satellites recently discovered are much too small to account for this. These missing massive satellites are large enough to retain gas throughout the period of reionization and early starbursts, hence they are dubbed 'too big to fail'.

Observations of the brightest dSphs reveal central densities and circular velocities which are lower than those of the most massive satellites (that could host dSphs) produced in Λ CDM simulations (Boylan-Kolchin *et al.*, 2011, 2012). Λ CDM correctly predicts the abundance of satellites the size of the Magellanic clouds (Busha *et al.*, 2011) and dwarfs with circular velocities greater than 80kms^{-1} (Trujillo-Gomez *et al.*, 2011), the disagreements arise with satellites with $30\text{kms}^{-1} < V_{\text{circ}} < 80\text{kms}^{-1}$, which are present in simulations containing only dark matter (predicted number is 5-40 with $V_{\text{circ}} > 25\text{kms}^{-1}$) but are not observed (see figure 2). These satellites should exist in theory and be observable as their progenitors would have been some of the most massive at early times, forming stars and avoiding suppression of star formation from reionization due to their size. Abundance matching methods attempt to link the dwarfs in cosmological simulations with those we observe by placing the most the most luminous dwarfs in the most massive subhaloes in simulations, however their properties don't match. Several authors have suggested that the inclusion of baryonic physics can also alleviate this issue, as baryonic processes can lower the central masses of bright satellite galaxies (see, e.g. Zolotov *et al.*, 2012; Brooks and Zolotov, 2014, discussed in more detail below).

- 'Cusp-core' problem

A third discrepancy is that the rotation curves of gas rich dwarf galaxies and the

central kinematics of dSphs show evidence of a cored dark matter density profile rather than a cuspy profile as predicted. Dark matter haloes are predicted to have a universal density profile with a cuspy inner slope ($\alpha \sim 1$) as seen in simulations (Navarro *et al.*, 1996b, 1997), whereas observations of gas-rich dwarf (low surface brightness) galaxies show evidence of constant density cores ($\alpha \sim 0$) (see, e.g. de Blok *et al.*, 2001; de Blok and Bosma, 2002; Kuzio de Naray *et al.*, 2006; Oh *et al.*, 2008; Hague and Wilkinson, 2013). Constraining the dark matter profile for the dSphs is more problematic, as in the absence of gas, stars are the only kinematic tracers of the gravitational potential, making estimations difficult due to the small number of stars and low luminosities. The literature contains claims of both cores (Battaglia *et al.*, 2008a; Oh *et al.*, 2011; Walker and Peñarrubia, 2011; Agnello and Evans, 2012; Amorisco and Evans, 2012) and cusps (Strigari *et al.*, 2010, 2014; Richardson and Fairbairn, 2014), as well as suggestions that there is no clear evidence for either from the current available data (Breddels and Helmi, 2013, 2014; Jardel and Gebhardt, 2013).

It has been shown the DM density profiles of dwarfs could have been transformed from cusps to cores by SN feedback causing repeated fluctuations of the gravitational potential (Governato *et al.*, 2010, 2012; Pontzen and Governato, 2012). However, Garrison-Kimmel *et al.* (2013) also investigated the central density profiles, and even in the extreme cases they could not produce cored density profiles. It is likely there is a range of profiles for the dwarfs in the local group, possibly due to the influence of baryons (see section 1.2).

These three problems arise when comparing Milky Way type haloes in cosmological dark matter only simulations (where the particles only interact through gravity) to observations of the present day satellite population. Baryons certainly have an influence on the formation and evolution of all galaxies and their significant contribution is neglected in these comparisons. Since they have been identified several authors have claimed to have made progress towards solving these issues by improving cosmological simulations to explore the influence of baryons on the final satellite population. The number of luminous satellites is expected to be reduced by the presence of a photoionizing background (Babul and Rees, 1992; Thoul and Weinberg, 1996; Bullock *et al.*, 2000) as the heating of the gas in low mass haloes could suppress accretion of gas and subsequent star formation. In this picture, the satellites we observe are those that accreted enough gas before reionization.

It has been suggested that the central density of the haloes of bright satellite galaxies

could be lowered by repeated gas outflows driven by supernova feedback causing repeated fluctuations in the gravitational potential (Mashchenko *et al.*, 2008; Governato *et al.*, 2012; Pontzen and Governato, 2012; Di Cintio *et al.*, 2014; Chan *et al.*, 2015). This is only the case for satellites massive enough to produce enough stars to allow for a sufficient amount of energy to be deposited into the concentrated, central regions, generally galaxies with stellar masses greater than $M_* \sim 10^5 M_\odot$. Lower mass satellites which are unable to maintain bursty SFHs would not produce enough energy to form a core. Garrison-Kimmel *et al.* (2013) found that for this process to reduce the central densities of larger satellites enough to bring them into agreement with observations of the dSphs (effectively solving the TBTF problem) required $>40\,000$ SNe worth of energy which couples to the dark matter with 100% efficiency which is unrealistic. A similar figure is found by Peñarrubia *et al.* (2012). These are still isolated studies of individual dwarfs, which neglect the baryonic effects from the host halo which also has an influence of the evolution.

The ability of cosmological simulations to model baryonic processes is improving due to increased resolution and more accurate stellar physics. Several recent studies have shown that the presence of baryons does reduce the central densities of satellites compared to dark matter only simulations (Zolotov *et al.*, 2012; Brooks and Zolotov, 2014; Sawala *et al.*, 2016a) and bring them into agreement with observations. Generally they find that heating from the UV background works to suppress star formation in ultra faint progenitors, and the combined effects of stellar feedback and tidal stripping work to suppress star formation in larger haloes, and reduce their central densities. These studies can only investigate satellites down to their resolution limits, which is around $M_* \sim 10^5 - 10^6 M_\odot$, so although they produce populations of subhaloes compatible with observations, both by number and kinematics, this is only reliably tested down to $M_* \sim 10^6 M_\odot$ and the agreement with the ultra faint dwarfs, and the processes which determine their formation and evolution are still unclear. The formation of cusps is also still unclear from these simulations. Most of the simulated satellites do not have a cored dark matter profile, however this may be due to resolution issues. Even if a core is formed earlier on (the peak of star formation in low mass haloes), the growth of the subhaloes via hierarchical merging with an unperturbed halo would re-form the cusp (Dehnen, 2005). This is found in Oñorbe *et al.* (2015) who find that only dwarfs that form cores through stellar feedback at late times ($z < 2$) maintain their core to the present day. A dwarf which has almost exclusively early star formation (all stars formed by $z = 3$) may have hosted a core temporarily, but it gets erased by subsequent accretion and mergers, suggesting that the formation of dark matter cores is a continuous

rather than instantaneous process and is linked to late time star formation.

The task of modelling all baryonic effects and influences on the evolution of the satellites is incredibly difficult due to the large dynamic range of scales which must be simulated. It is clear the presence of baryons influences the central densities of satellites, but will the simulations eventually be able to reconcile theory with observations? That is still unclear. It still is not clear whether the reason for these problems is a lack of understanding of baryonic effects upon dark matter haloes, or whether it is something more fundamental.

Real galaxies are the products of their unique formation histories and complex baryonic processes will reshape the dark matter profiles in different ways dependant upon their evolution, resulting in non-universal DM profiles at present day redshifts. Whether or not all the discrepancies with Λ CDM on small scales are resolved with simulations of high enough resolution to capture every baryonic process in detail is still unclear, but it is clear the dwarfs have complex evolutionary histories.

1.2 Mechanisms for gas removal

All dSphs are devoid of gas (Greveich and Putman, 2009), even Fornax which has the most recent star formation (Coleman and de Jong, 2008; de Boer *et al.*, 2012a). There are several ways of removing gas from dwarf galaxies as their shallow potential wells mean these systems are easily influenced by both internal and external effects.

1.2.1 Photoionization

Photoionization by the ultra-violet background (UVB) during reionization in the early universe has been suggested as a mechanism to inhibit the accretion of gas in low mass haloes. Reionization began between $z \sim 10 - 15$ and was complete by $z \sim 6$ (see, e.g. Planck Collaboration *et al.*, 2016b) and could have acted to heat low density gas before it was accreted into the potential wells of dark matter haloes at high redshift. This heating would ionize neutral hydrogen, which dominates the cooling of primordial gas, preventing the gas from cooling and settling into low mass haloes, and hence acting to suppress star formation or prevent it altogether (Thoul and Weinberg, 1996; Bullock *et al.*, 2000; Sawala *et al.*, 2015a). If a low mass halo had not formed any stars before reionization, these simulations predict that the heating of the gas to a temperature higher than that of the halo virial temperature could prevent the formation of a luminous satellite in that halo, leaving to a population of dark haloes, devoid of gas and stars.

There is still a debate around whether these galaxies survive reionization in the early universe. It has been suggested that there is a characteristic mass scale below which low mass haloes lose a significant fractions of their gas and remain dark, due to the gas temperature at the virial radius ($\sim 6.5 \times 10^9 M_\odot$; see, Hoeft *et al.*, 2006, 2008; Okamoto *et al.*, 2008b). Models predict that photoionization will have no effect on galaxies with a circular velocity $V_{\text{circ}} > 60 \text{ km s}^{-1}$ (Benson *et al.*, 2002), however satellites with $v_{\text{circ}} < 60 \text{ km s}^{-1}$ are observed, so this cannot be a simple process which eliminates all galaxies below a certain mass. The faintest dSphs like Ursa Minor and Draco show evidence for continuous star formation during and after the period of reionization. If reionization was a significant event that influenced all low-mass structure, we would expect to see some imprint of this on the star formation histories of the local group dSphs. However there is no uniform signature in the observed dwarfs (Grebel and Gallagher, 2004; Weisz *et al.*, 2014b) to suggest a widespread event in all haloes below a certain mass: the star formation histories of the local group dSphs are very different. This suggests that reionization was not the dominant mechanism for the suppression of star formation, although it could have reduced the star formation rate.

When modelling the epoch of reionization in cosmological simulations it is generally assumed that the effect is homogeneous and instantaneous. In reality the process of reionizing the intergalactic medium (IGM) would have been a gradual process with local variations in the UVB, and the amount of heating each dwarf was subjected to would be dependant on the local environment. It is thus unlikely that heating from the UVB would have had the same effect on all subhaloes; infact it could have been one of the influences that produces the diverse range of properties we observe in present day dwarfs.

Self-shielding has been shown to have a significant effect when reionization is modelled with a radiative transfer code (Susa and Umemura, 2004), rather than being modelled using similar assumptions to those described above. Baryons that have collapsed into high density peaks before the onset of reionization are able to self-shield from the heating resulting in them being able to continue to cool and form stars. It is the star formation that occurs in haloes before the begining of reionization that is important for determining the final stellar fraction, at least in the case of the fant dSphs which host predominantly old stellar populations, (Ricotti and Gnedin, 2005). Self-shielding is quite a significant effect, yet it is neglected in many cosmological simulations. In these large scale simulations however, the collapse and cooling of baryons in the lowest mass haloes would not be modelled accurately due to resolution limits.

Sawala *et al.* (2010) confirm the importance of the ability of a halo to self-shield against the UVB. Star formation before reionization is important, as those subhaloes that form stars earlier and experience stellar feedback are more vulnerable to gas loss by heating via the UVB, as this results in a larger fraction of low density gas which is more easily removed, preventing the dwarf from self-shielding. The evolution of the faintest satellites *before* reionization is important, and until these systems are well resolved in simulations it is unclear how significant the effect of reionization is on the continuation of star formation in a cosmological context.

1.2.2 Stellar Feedback

Feedback from massive stars interacting with the interstellar medium (ISM) has a big influence on the evolution of the host galaxy. Large scale outflows have been observed in high (Pettini *et al.*, 2001) and low (Heckman *et al.*, 1990, 2000) redshift galaxies with velocities of hundreds of kms^{-1} . Evidence for these outflows can also be found in the high abundance of metals in the IGM (Cowie *et al.*, 1995) and the low abundance of metals contained in dSphs compared to that expected to be synthesised in SNe (Kirby *et al.*, 2011a). Feedback should be even more influential on dwarf galaxies due to their much lower masses and shallower gravitational potential wells (Larson, 1974; Dekel and Silk, 1986). If winds from stellar feedback are able to inject the gas with enough energy, it could be blown out of the galaxy completely, transporting the newly synthesised metals with it, resulting in significant gas loss which could prevent further star formation. If the gas is not able to escape the galaxy completely, feedback is still essential to the evolution of these systems because of the scale of the outflows and the effect they have on the ISM, on star formation, and on the transport of metals through the system.

Supernovae (SNe) feedback offers an explanation for the observed low surface brightnesses and low metal abundances of dSphs. Considering their low mass, it is questionable whether dwarf galaxies would actually survive several supernovae explosions after an initial episode of star formation due to their low escape velocities, based on simple energy arguments. However observations give evidence for complex star formation histories in several distinct dwarf galaxies. Escape speeds from typical galaxies are hundreds of kms^{-1} , whereas from dwarfs it is tens of kms^{-1} . The escape speed for a $10^9 M_\odot$ halo with a radius of 1kpc is 93kms^{-1} . The energy needed to eject $5 \times 10^6 M_\odot$ of gas at this speed is $\sim 40 \times 10^{53}$ erg, equivalent to ~ 400 SNe. Therefore after an episode of star formation, a significant proportion of the gas should have been injected with enough energy to eventually escape

the galaxy.

There are several observations of outflows from star forming dwarf galaxies. Martin (1996) observed a galactic-scale superbubble expanding at $30\text{-}60\text{kms}^{-1}$ with an estimated age of $15\text{-}27\text{Myr}$ and a scale of $\sim 900\text{pc}$. The galaxy, I Zw 18 (not in the local group) is thought to be experiencing an initial burst of star formation, still forming stars from primordial gas. Marlowe *et al.* (1995) observed seven dwarf galaxies with recent or ongoing star formation and found kpc scale filaments and/or superbubbles, comparable to the optical size of the galaxies with expansion speeds of around $\pm 50\text{kms}^{-1}$. SN should therefore have a substantial impact on the ISM of dwarf galaxies. However there are still examples (e.g. Fornax) that show a rich, continuous SFH and central concentration of young, metal rich stars, so metals and gas are not blown away in all cases.

The influence of stellar feedback on dwarf galaxies has been investigated by several authors in both isolated (Read and Gilmore, 2005; Revaz *et al.*, 2009; Sawala *et al.*, 2010; Governato *et al.*, 2010, 2012; Read *et al.*, 2016a) and cosmological conditions (Mashchenko *et al.*, 2008; Revaz and Jablonka, 2012; Shen *et al.*, 2013) with mixed results. Sawala *et al.* (2010) produce dwarfs similar to the Local Group dSphs, but fail to reproduce Fornax and the ultra faints. They find two different age distributions in the resulting dwarfs, a single burst of star formation lasting around 1Gyr , or an initial burst followed by a tail extended over several Gyr. The inclusion of the effects of a UV background also suggest that the observed variation in SFHs in the Local Group cannot be solely caused by small-scale variations in the UV background, leaving SN feedback as a key influence on the evolution of dwarfs at early times. Revaz and Jablonka (2012) successfully reproduce a variety of SFHs and levels of chemical enrichment in dwarfs, however all of the resulting dwarfs contain substantial amounts of gas at $z=0$.

The general consensus is that stellar feedback does have a significant influence on the baryon fraction of the host galaxy, in dwarfs which are more massive than that expected for a dSph progenitor. Larger dwarfs are able to form a large number of stars in a 'bursty' fashion, enabling energy injection over a continuous period (Governato *et al.*, 2010, 2012; Garrison-Kimmel *et al.*, 2013). These simulations suggest that a continuous, bursty SFH has a greater impact on the morphology of dwarf galaxies as it causes fluctuations in the gravitational potential over time.

The results of the simulations for possible dSph progenitors are inconclusive given the range of initial conditions and methods for simulating SNe feedback used. As resolution limits the size of galaxies that can be investigated in cosmological simulations, the smallest

galaxies at high redshift are often simulated in isolation requiring many assumptions about the initial conditions. For example, some authors used cored density profiles for the dark matter component initially, whereas it is generally expected that cores would form over time as a result of baryonic processes. This means the initial gravitational potential is lower than that for a cusped profile, allowing the SNe to have a greater impact on the host galaxy.

1.2.3 Environmental effects: the influence of the Milky Way

The majority of satellites within 300kpc of the Milky Way contain no gas component (see, e.g. Grcevich and Putman, 2009). The dependence of gas deficiency on galactocentric radius to a massive luminous host is thought to be evidence of the host galaxies' influence through tidal and/or ram pressure stripping (Bellazzini *et al.*, 1996).

Tidal stripping

If the orbit of a satellite brings it close enough to the host galaxy the gravitational pull from the host can exceed the gravitational pull from the satellite, resulting in the removal of material from the outer regions, known as tidal stripping. The 'tidal radius' outside of which gas, stars and dark matter are removed depends upon the gravitational potential of both the host galaxy and the satellite, the orbital radius of the satellite, and the orbital shapes of the gas/stars/dark matter within the satellite (Read *et al.*, 2006c). Gas and stars stripped from satellites produce 'tidal streams' which are visible in the Milky Way halo. The Magellanic stream, identified in radio observations in the 1970s (Wannier *et al.*, 1972; Mathewson *et al.*, 1974), is a giant stream of neutral gas trailing the large and small Magellanic clouds. The stream consists of two gas filaments which extend over 140 degrees. Information about the age and metallicity of this stream from observations have concluded that the majority of the gas in one filament originates from the Small Magellanic Cloud and would have been stripped around 2Gyr ago, while the other filament was likely stripped from the Large Magellanic Cloud more recently (Fox *et al.*, 2013; Richter *et al.*, 2013). It is unclear whether this stream is produced by tidal stripping alone as there are no stars present; it is likely a combination of tidal and ram pressure stripping (discussed below). The Sagittarius stream is a prominent stream of stars that have been stripped from the Sagittarius dSph and spans a full 360 degrees, tracing its orbit around the Milky Way disk. It was first identified by (Lynden-Bell and Lynden-Bell, 1995) and confirmed and analysed

by (Newberg *et al.*, 2002; Majewski *et al.*, 2003). There are two branches of the stream that correspond to material being stripped at different epochs (Belokurov *et al.*, 2006b).

The effects of tidal stripping have been explored in simulations, revealing that the total masses of satellites that fell into the halo could have been larger than the total masses of the presently observed dSphs, resulting in the low masses and velocities we observe presently (Read *et al.*, 2006b). Cosmological N-body simulations (dark matter and stars) have shown that gas rich disks can be transformed into dwarfs with properties that match those of the present day dSphs and are in agreement with the current trends (see, e.g. Kravtsov *et al.*, 2004; Kazantzidis *et al.*, 2011)

Ram pressure stripping

Ram pressure stripping occurs when a satellite passes through the hot intracluster medium (ICM) of a galaxy cluster as first pointed out by Gunn and Gott (1972). The same process happens on smaller scales with dwarf galaxies falling into the gaseous halo of their host galaxies, being stripped by the hot gas that resides there. Gas can be removed from the satellites when the incident gas pressure due to the relative velocities of the satellite and the halo gas becomes stronger than the gravitational force of the satellites, resulting in it being removed. The pressure can be estimated as: $P_{ram} \sim \rho_{halo} v_{sat}^2$, where ρ is the density of the gaseous halo which the satellites is moving through and v is the relative speed of the satellite with respect to the halo. This should be an effective mechanism for dwarf galaxies due to their low masses and shallow gravitational potential wells. Note that ram pressure stripping can remove gas from the satellite at all radii (if the conditions are met), whereas tidal stripping can only remove gas outside of the tidal radius.

The stripping of dwarfs as they move through the gaseous halo has been explored in hydrodynamical simulations. Simulations performed by Mayer *et al.* (2006a, 2007) transformed gas-rich disks into gas-poor dSph type galaxies via a combination of ram pressure and tidal stripping and assuming an early infall. The presence of a UVB increases the gas loss through these processes by keeping it hot and extended and a Draco type dwarf had been stripped of the entire gas content after around three pericentre passages. The dwarf galaxies resulting from these simulations had comparable properties to those of Ursa Minor and Draco. Analytical calculations by Nichols and Bland-Hawthorn (2011) suggest that unassisted stripping, that is modelling stripping without modelling star formation and stellar feedback, fails to account for the gas depletion of the dwarfs within ~ 250 kpc by an order of magnitude. Early star formation is required to heat the gas allowing it to be

easily removed by the host galaxy.

For those dwarfs with orbits bringing them close to the MW and those that are close enough to interact frequently with the MW, ram pressure stripping should easily remove some gas at least from the edges of the dwarf where it is most loosely bound. However removing the gas from the centre of the galaxy would be much more difficult. Dwarfs with close orbits could experience several passages through the halo through their lifetimes, enabling more gas to be stripped.

Summary

It is evident from observations of gas and stellar streams trailing dwarfs through the halo, along with the simulations carried out to explore these processes, that several passages close to the disk of the Milky Way can have a profound effect on the satellites whose orbits bring them close enough. It is very unlikely these processes alone account for the complete loss of gas in dSphs as they do not provide an explanation for the dSphs at radii greater than 500kpc, Cetus and Tucana, if more than one pericentre passage is required to remove the gas. The gas fraction of dwarf galaxies is dependant on the environment, Geha *et al.* (2006) survey dwarfs containing gas in a wide range of environments and find that the average gas fraction (ratio of gas mass to total baryonic mass) for stellar masses in the range $10^8 - 10^9 M_\odot$ is $f_{\text{gas}} < 0.6$. Dwarf galaxies with $f_{\text{gas}} < 0.4$ (which make up 15 percent of the sample) are found exclusively within 500kpc of a luminous host. The majority of the dwarfs are presently forming stars, some of the gas fractions are as high as $f_{\text{gas}} = 95$ percent, which is significantly higher than that for gas rich galaxies at higher luminosities. This suggests that dwarfs are inefficient at turning their gas into stars.

When searching for quenched dwarfs in isolation Geha *et al.* (2012) find they are rare, as the fraction of quenched galaxies decreases rapidly with increasing distance from a luminous host. No quenched galaxies with a stellar mass in the range $10^7 - 10^9 M_\odot$ are found in the field (masses below $10^7 M_\odot$ could not be tested due to observational limitations); all galaxies in this mass range are star forming. Most quenched galaxies in their sample in this mass range are within two virial radii of a massive host, and 97 percent of all the the quenched dwarfs in their sample are within four virial radii. In this study, Cetus and Tucana are not classed as isolated galaxies as they are within 3-4 virial radii of the Milky Way, so it's possible they are still influenced by the host galaxy.

The scarcity of gas-free dwarfs in the field, isolated from the haloes of more luminous galaxies suggests that although internal processes such as stellar feedback can reduce the

gas fraction of dwarf galaxies, external processes are required to remove all the gas. These studies however, focus on larger dwarfs, (the most massive dSphs have stellar masses close to their lower limit), so it's possible smaller dwarfs are found quenched in the field but their luminosities are low and they are challenging to observe. From the available data is it not clear whether a galaxy comparable in size to the dSphs or the ultra faint dwarfs would become quenched in isolation.

Several models claim to be able to transform dSphs into dIrrs through mechanisms both with and without the external influence from the Milky Way, leaving the solution still unclear. Most of these models are focussing and reporting on a specific mechanisms which neglects other significant processes. There are limitations to including every process in detail in cosmological simulations, as resolving the faintest dwarfs in these large scale simulations is problematic, so even if all relevant processes were included, they may not be modelled accurately for the smallest objects.

The evidence points to low luminosity dwarf galaxies being extremely complicated systems influenced by multiple internal and external processes by varying amounts to give us the diverse range of properties that are presently observed. Any model that attempts to explain the depletion of gas in the local group dwarfs must be take all of these processes into account in order to see the bigger picture. It is also interesting that these processes act on similar timescales, the internal dynamics, orbits of the dwarfs around their host, and the timescales required for star formation are all in competition with each other. It is the most dominant effects which will leave their mark on the evolution of the dwarfs, as different mechanisms will have a different significance to different dwarfs, depending on other properties such as their initial environment, their initial mass, the time they fell into the halo of the Milky Way, the radius of their orbits and how many close passages they had to the Milky disk. A model which describes the properties and evolution of these objects will be very challenging to create.

Table 1.1: Summary of properties of the local group dSphs and UFs. The columns represent: (1) name of the dwarf, (2) type of dwarf, (3) heliocentric distance in kpc, (4) absolute magnitude, (5) half light radius in pc, (6) velocity dispersion in kms^{-1} , (7) metallicity.

Dwarf (1)	Type (2)	Year (3)	D_{\odot} (4)	M_v (5)	r_h (6)	σ (7)	[Fe/H] (8)
Fornax	dSph	1938 ₁	147 ₂	-13.4 ₃	668 ₃	11.7 ₄	-0.99 ₅
Sagittarius	dSph	1994 ₆	26 ₇	-13.27 ₈	2587*	11.4 ₉	-0.4 ₁₀

Continued on next page

Table 1.1 –continued from previous page

Dwarf (1)	Type (2)	Year (3)	D_{\odot} (4)	M_v (5)	r_h (6)	σ (7)	[Fe/H] (8)
Carina	dSph	1977 ₁₁	100 ₁₂	-9.1 ₃	241 ₃	6.6 ₄	-1.59 ₁₃
Draco	dSph	1954 ₁₄	76 ₁₅	-8.75 ₁₆	221 ₁₆	9.1 ₁₇	-1.93 ₅
Ursa Minor	dSph	1955 ₁₈	76 ₁₉	-8.4 ₃	280 ₃	9.5 ₂₀	-2.13 ₅
Sculptor	dSph	1938 ₁	86 ₂₁	-11.1 ₃	260 ₃	9.2 ₄	-1.68 ₅
Leo I	dSph	1950 ₂₂	254 ₂₃	-12.0 ₃	246 ₃	9.2 ₂₄	-1.43 ₅
Leo II	dSph	1950 ₂₂	233 ₂₅	-9.8 ₃	151 ₃	6.6 ₂₆	-1.62 ₅
Sextans	dSph	1990 ₂₇	86 ₂₇	-9.3 ₃	682 ₃	7.9 ₄	-1.93 ₅
Cetus	dSph	1999 ₂₈	780 ₂₉	-11.3 ₃₀	600 ₃₀	17 ₃₁	-1.9 ₃₁
Tucana	dSph	1990 ₃₂	890 ₂₉	-9.55 ₃₃	270 ₃₃	15.8 ₃₄	-1.82 ₃₃
Coma Berenices	dSph	2006 ₃₅	44 ₃₅	-4.1 ₁₆	77 ₁₆	4.6 ₃₆	-2.60 ₅
Canes Venatici	dSph	2006 ₃₇	220 ₃₇	-8.6 ₁₆	564 ₁₆	7.6 ₃₆	-1.98 ₅
Canes Venatici II	dSph	2006 ₃₅	160 ₃₈	-4.9 ₁₆	74 ₁₆	4.6 ₃₆	-2.21 ₅
Hercules	dSph	2006 ₃₅	132 ₃₉	-6.6 ₁₆	330 ₁₆	3.7 ₄₀	-2.41 ₅
Leo IV	dSph	2006 ₃₅	154 ₄₁	-5.8 ₄₂	206 ₄₂	3.3 ₃₆	-2.54 ₅
Leo V	dSph	2007 ₄₄	178 ₄₄	-5.2 ₄₂	133 ₄₂	2.4 ₄₃	-2.0 ₄₂
Ursa Major I	dSph	2005 ₄₅	97 ₄₆	-5.5 ₁₆	318 ₁₆	11.9 ₄₇	-2.18 ₅
Ursa Major II	dSph	2006 ₄₈	30 ₄₈	-4.2 ₁₆	140 ₁₆	7.4 ₄₇	-2.47 ₅
Bootes I	dSph	2006 ₄₉	66 ₅₀	-6.3 ₁₆	242 ₁₆	2.4 ₅₁	-2.5 ₅₂
Bootes II	UF	2007 ₅₃	42 ₁₆	-2.7 ₁₆	51 ₁₆	10.5 ₅₄	-1.79 ₅₄
Bootes III	UF	2009 ₅₅	46 ₅₅	-5.8 ₅₆	...	14.0 ₅₇	-2.1 ₅₇
Segue I	UF	2006 ₃₅	23 ₃₅	-1.5 ₁₆	29 ₂₀	3.7 ₅₈	-2.5 ₅₈
Segue II	UF	2009 ₅₉	35 ₅₉	-2.5 ₅₉	34 ₅₉	3.4 ₅₉	-2.0 ₅₉
Pisces II	UF	2010 ₆₀	182 ₆₀	-5.0 ₆₀	60 ₆₀	...	-1.9 ₆₀
Wilman I	UF	2005 ₆₁	38 ₁₆	-2.7 ₁₆	25 ₁₆	4.3 ₄₇	-1.5 ₄₇
Reticulum II	UF	2015 ₆₂	30 ₆₃	-2.7 ₆₃	32 ₆₃	3.6 ₆₄	-2.58 ₆₄
Reticulum III	UF	2015 ₆₅	92 ₆₅	-3.3 ₆₅	64 ₆₅
Eridanus II	UF	2015 ₆₂	330 ₆₂	-7.1 ₆₆	277 ₆₆	6.9 ₆₇	-2.38 ₆₇
Eridanus III	UF	2015 ₆₂	77.6 ₆₈	-2.4 ₆₂	11 ₆₂	...	-2.01 ₆₈
Tucana II	UF	2015 ₆₂	57 ₆₉	-3.8 ₆₉	165 ₆₉	8.6 ₆₉	-2.23 ₆₉
Tucana III	UF	2015 ₆₅	25 ₆₅	-2.4 ₆₅	44 ₆₅	0.1 ₇₀	-2.42 ₇₀
Tucana IV	UF	2015 ₆₅	48 ₆₅	-3.5 ₆₅	127 ₆₅

Continued on next page

Table 1.1 –continued from previous page

Dwarf (1)	Type (2)	Year (3)	D_{\odot} (4)	M_v (5)	r_h (6)	σ (7)	[Fe/H] (8)
Tucana V	UF	2015 ₆₅	55 ₆₅	-1.6 ₆₅	17 ₆₅
Cetus II	UF	2015 ₆₅	30 ₆₅	0.0 ₆₅	17 ₆₅
Horologium I	UF	2015 ₆₂	79 ₇₁	-3.4 ₇₁	30 ₇₁	4.9 ₇₁	-2.76 ₇₁
Horologium II	UF	2015 ₇₂	78 ₇₂	-2.6 ₇₂	47 ₇₂	...	-2.1 ₇₂
Grus I	UF	2015 ₆₃	120 ₆₉	-3.4 ₆₉	62 ₆₉	<9.8 ₆₉	-1.42 ₆₉
Grus II	UF	2015 ₆₅	53 ₆₅	-3.9 ₆₅	93 ₆₅
Columba I	UF	2015 ₆₅	182 ₆₅	-4.5 ₆₅	103 ₆₅
Indus II	UF	2015 ₆₅	214 ₆₅	-4.3 ₆₅	181 ₆₅
Pictoris I	UF	2015 ₆₂	126 ₆₂	-3.7 ₆₂	43 ₆₂
Pegasus III	UF	2015 ₇₃	215 ₇₄	-3.4 ₇₄	53 ₇₄	5.4 ₇₄	-2.0 ₇₄
Draco II	UF	2015 ₇₅	20 ₇₅	-2.9 ₇₅	19 ₇₅	2.9 ₇₆	-2.2 ₇₅
Sagittarius II	UF	2015 ₇₅	67 ₇₅	-5.2 ₇₅	38 ₇₅	...	-2.2 ₇₅
Triangulum II	UF	2015 ₇₇	30 ₇₇	-1.8 ₇₇	34 ₇₇	3.4 ₇₈	-2.2 ₇₈
Hydra II	UF	2015 ₇₉	134 ₇₉	-4.8 ₇₉	68 ₇₉	<4.5 ₈₀	-2.02 ₈₀
Pictoris II	UF	2016 ₈₀	45 ₈₀	-3.2 ₈₀	46 ₈₀	...	-1.8 ₈₀
Crater II	UF	2016 ₈₂	117.5 ₈₂	-8.2 ₈₂	1066 ₈₂	...	-1.7 ₈₂
Aquarius II	UF	2016 ₈₃	108 ₈₃	-4.36 ₈₃	159 ₈₃	5.4 ₈₃	-2.3 ₈₃
Virgo I	UF	2016 ₈₄	87 ₈₄	-0.8 ₈₄	38 ₈₄

References for table 1.1: (1) Shapley (1938); (2) Pietrzyński *et al.* (2009); (3) Irwin and Hatzidimitriou (1995); (4) Walker *et al.* (2009b); (5) Kirby *et al.* (2011c); (6) Ibata *et al.* (1994); (7) Monaco *et al.* (2004); (8) Majewski *et al.* (2003); (9) Ibata *et al.* (1997); (10) Chou *et al.* (2007); (11) Cannon *et al.* (1977); (12) Karachentsev *et al.* (2004); (13) Norris *et al.* (2017); (14) Wilson (1955); (15) Bonanos *et al.* (2004); (16) Martin *et al.* (2008); (17) Walker *et al.* (2007); (18) Wilson (1955); (19) Carrera *et al.* (2002); (20) Walker *et al.* (2009a); (21) Pietrzyński *et al.* (2008); (22) Harrington and Wilson (1950); (23) Bellazzini *et al.* (2004); (24) Mateo *et al.* (2008); (25) Bellazzini *et al.* (2005); (26) Koch *et al.* (2007b); (27) Irwin *et al.* (1990); (28) Whiting *et al.* (1999); (29) Bernard *et al.* (2009); (30) McConnachie and Irwin (2006); (31) Lewis *et al.* (2007); (32) Lavery (1990); (33) Saviane *et al.* (1996); (34) Fraternali *et al.* (2009); (35) Belokurov *et al.*

(2007); (36) Simon and Geha (2007); (37) Zucker *et al.* (2006b); (38) Greco *et al.* (2008); (39) Coleman *et al.* (2007); (40) Adén *et al.* (2009); (41) Moretti *et al.* (2009); (42) de Jong *et al.* (2010); (43) Walker *et al.* (2009c); (44) Belokurov *et al.* (2008); (45) Willman *et al.* (2005b); (46) Okamoto *et al.* (2008a); (47) Martin *et al.* (2007); (48) Zucker *et al.* (2006a); (49) Belokurov *et al.* (2006a); (50) Dall’Ora *et al.* (2006); (51) Koposov *et al.* (2011); (52) Muñoz *et al.* (2006); (53) Walsh *et al.* (2007); (54) Koch *et al.* (2009); (55) Grillmair (2009); (56) Correnti *et al.* (2009); (57) Carlin *et al.* (2009); (58) Simon *et al.* (2011); (59) Belokurov *et al.* (2009); (60) Belokurov *et al.* (2010); (61) Willman *et al.* (2005a); (62) Bechtol *et al.* (2015); (63) Koposov *et al.* (2015b); (64) Walker *et al.* (2015); (65) Drlica-Wagner *et al.* (2015), (66) Crnojević *et al.* (2016); (67) Li *et al.* (2017); (68) Luque *et al.* (2017); (69) Walker *et al.* (2016); (70), Simon *et al.* (2017); (71) Koposov *et al.* (2015c); (72) Kim and Jerjen (2015); (73) Kim *et al.* (2015); (74) Kim *et al.* (2016); (75) Laevens *et al.* (2015b); (76) Martin *et al.* (2016); (77), Laevens *et al.* (2015a); (78) Kirby *et al.* (2017); (79) Martin *et al.* (2015); (80) Kirby *et al.* (2015); (81) Drlica-Wagner *et al.* (2016); (82) Torrealba *et al.* (2016b); (83) Torrealba *et al.* (2016a); (84) Homma *et al.* (2016).

1.3 This thesis

The aim of this thesis is to explore gas removal in dSph progenitors through high resolution simulations. In chapter 2.1 the methods for simulating baryonic and collisionless components are described. Chapter 3 explores the impact of supernova feedback on isolated dSph progenitors, where individual SNe explosions are resolved. Chapter 4 explores an additional external influence from the host galaxy in which the dwarf is in orbit around - the impact of a fast outflow resulting from active galactic nuclei (AGN). Chapter 5 explores the effect of gas accretion onto a dwarf and its ability to retain gas during an initial burst of star formation, and finally the conclusions are summarised in chapter 6.

Chapter 2

Hydrodynamical simulations

2.1 Astrophysical simulations

Numerical simulations of three dimensional self-gravitating fluids are an essential tool in order to further our understanding of the formation and growth of structure in the universe. Detailed observations can tell us many things about the galaxies we presently see, however viewing them as a snapshot in time limits how much we can discover about their evolution at early times. Theoretical models are required to reveal their evolutionary paths and the circumstances of their formation.

To follow the evolution of each component of the universe (baryons, dark matter and dark energy) from cosmological initial conditions through billions of years to the present day, enabling us to compare with observations of the present day galaxy population requires a large computational effort. Nbody simulations modelling only gravity marked the beginning of a long line of work aiming to describe the complex physical processes that shape the universe through the results of simulations. The rapid growth of computer performance over the last couple of decades has resulted in larger simulation volumes being possible and has driven the implementation of more sophisticated algorithms enabling baryons to be modelled alongside Nbody particles. The largest cosmological simulations to date, the Millennium-XXL simulations (Angulo *et al.*, 2012) use 303 billion particles in a box of 4.1Gpc. Although simulations of this size are currently unfeasible for runs including hydrodynamics due to the large increase in computing time required for the calculation of baryonic processes (star formation, cooling etc), the size is continually increasing. The Illustris simulations (Vogelsberger *et al.*, 2014b,a; Genel *et al.*, 2014) includes hydrodynamical modelling and is 106Mpc on a side.

Semi-analytical models have made significant progress in our understanding of galaxies, reproducing several observables such as the galaxy mass luminosity function, the Tully-Fisher relation and the galaxy morphology-density relation (see, e.g. Kauffmann *et al.*, 1993; Cole *et al.*, 1994; Somerville and Primack, 1999; Cole *et al.*, 2000; Springel *et al.*, 2001b; Somerville *et al.*, 2008; Guo and White, 2009; Guo *et al.*, 2011). However as they do not explicitly model the hydrodynamics, instead using phenomenological models, approximating various physical processes with analytical models they are limited by not explicitly modelling the fluid.

Although cosmological hydrodynamical simulations are much more computationally challenging due to the inclusion of baryonic physics at such large dynamical ranges, they generally reproduce a wide range of galactic properties at redshift zero. This includes the galaxy luminosity function, the cosmic star formation rate density, the impact of galaxy environment on red fractions of galaxies and galaxy morphology and colours. The limitations of these simulations are their inability to resolve the smallest structures, where discrepancies still lie (see 1.1.3). Resolution issues are somewhat alleviated when simulations of single galaxies are performed, but as the scale gets smaller, better approximations are needed for the subgrid physics describing processes like star formation and cooling.

Modelling galaxy formation requires the modelling of non-linear physics and a wide variety of complex physical processes and progress is continually being made in the field as computing power advances. On small scales however, this is not yet possible, and so it is beneficial to isolate some issues to further understand the complex physical processes that shape their evolution.

In this thesis I use a modified version of Gadget 2: **GA**laxies with **D**ark matter and **G**as **intE**rac**T** (Springel *et al.*, 2001a; Springel, 2005) which uses the Nbody technique along with smoothed particle hydrodynamics (SPH) to model hydrodynamics in isolated dwarf galaxies, below the scope of cosmological simulations. This chapter describes the code and the modifications made to model further baryonic processes than those mentioned in the code papers.

2.2 The Nbody Technique

Nbody simulations are the numerical solutions of the equations of motion for a system of N particles which interact through gravity. They are used across a wide range of systems, from small star clusters to galactic and cosmological scales. It is computationally challenging

to compute the gravitational forces of a system containing a large number of particles accurately and efficiently, making it difficult to model large scale structure formation like galaxies and clusters.

Realistic systems contain many more particles than it is feasible to include for a computer simulation. The collisionless Nbody approach models these systems using fewer particles, treating the underlying gravitational potential as a smooth distribution, allowing the gravitational potential to be solved using the mass density ρ , from Poisson's equation:

$$\nabla^2\Phi = 4\pi G\rho \quad (2.1)$$

The exact solution to the gravitational force acting on a single particle taking into account the contribution due to N other particles is:

$$\mathbf{F}_i = \sum_{j \neq i}^N Gm_j \frac{\mathbf{r}_i - \mathbf{r}_j}{|\mathbf{r}_i - \mathbf{r}_j|^3} \quad (2.2)$$

This is the direct summation approach, used in the first Nbody simulations modelling very few particles by Peebles (1970); Press and Schechter (1974); White (1976, 1978). This method is the most accurate but it comes with a large increase in computational cost. The calculation requires a loop over $N-1$ particles for each particle in the simulation, resulting in the time taken to calculate the gravitational force scaling with N^2 . While this is still useful today for simulations with small N , like stellar clusters and planetary systems, it is not feasible for galactic scale simulations. To overcome this issue, algorithms have been designed to use approximations of the gravitational force allowing for a more efficient computation.

Tree algorithms were first introduced by Appel (1985) and are Eulerian subdivisions of space. Distant particles are arranged into a hierarchy of groups and the gravitational field at a given point is computed by summing over the multipole expansions of these groups. It is assumed that close encounters are not important ('collisionless') and force contributions from very distant particles do not need to be computed at very high accuracy. The time taken to compute the gravitational force for these methods scales as $N \log N$, making it much more feasible for large numbers of particles. This is the method used in the work for this thesis and so the discussion is focused on this.

Gadget-2 models the dark matter and stellar components as self-gravitating, collisionless fluids. The collisionless Boltzmann equation describes the evolution of a collisionless system and is used in conjunction with the Poisson equation (2.1) to evolve the motion

of the particles over time. The hierarchical multipole expansion method is used to compute the gravitational forces of particles, specifically, the Barnes-Hut tree algorithm (BH, Barnes and Hut, 1986). A root node which encompasses the whole mass distribution is divided into eight smaller cubes of half a side length each, these are the 'nodes' of the tree. These nodes are then recursively subdivided until the 'leaves' of the tree are reached, which contain a single particle. The total gravitational force for each particle is then calculated by 'walking' the tree, and obtaining the force contributions from each node. The decision as to whether or not the multipole expansion should be continued along the branch is made by defining the opening criterion. This assumes the absolute size of the true total force is already known before the tree walk, in this case the total acceleration of the previous timestep is used as an approximation. Then the requirement is that the estimated error of an acceptable multipole approximation is some small fraction of this total force. Monopole expansion of a node of mass M and size l and a distance between the current particle to the centre-of-mass of the node r is considered if:

$$\frac{GM}{R^2} \left(\frac{l}{r}\right)^2 \leq \alpha |\mathbf{a}|, \quad (2.3)$$

where α is a tolerance parameter (to make the result some fraction of the total force) and $|\mathbf{a}|$ is the size of the total acceleration in the last timestep (Springel, 2005). If this requirement is not met the cell is divided further and the process is repeated. When this condition is true, no further cells are opened and the calculated contribution of the cell to the total gravitational force is obtained.

As particles approach each other and the distance between them decreases equation 2.2 diverges and this leads to arbitrarily large velocities. Close encounters between Nbody particles do not represent close encounters between the physical particles being modelled, and as the Nbody particles are much larger than those they represent (often by several orders of magnitude in simulations on galactic scales), it leads to unphysical properties from close encounters and the formation of artificial binaries. A softening is introduced to the gravitational force on small scales, enabling the particle to represent a smooth mass distribution rather than a point mass in order to avoid artificial properties. This is achieved by describing the force of a particle as a smoothed distribution. The potential at a distance \mathbf{r} due to a group of particles each of mass m_i and position \mathbf{x}_i can be calculated from

$$\Phi(\mathbf{r}) = -G \sum_k m_k g(|\mathbf{x}_k - \mathbf{r}|), \quad (2.4)$$

where $g(r)$ is the spline softened force law, which at large distances reverts back to the Newtonian form $g(r)=1/r$.

$$g(r) = -\frac{1}{h}W_2\left(\frac{r}{h}\right). \quad (2.5)$$

Where r is less than a defined gravitational softening length, h , the Nbody particle is replaced by a mass distribution, $\rho(\mathbf{r}) = mW(\mathbf{r}; h)$ where $W(r, h)$ is the normalized cubic spline kernel (Monaghan and Lattanzio, 1985):

$$W(r, h) = \frac{8}{\pi h^3} \begin{cases} 1 - 6\left(\frac{r}{h}\right)^2 + 6\left(\frac{r}{h}\right)^3, & 0 \leq \frac{r}{h} \leq \frac{1}{2} \\ 2\left(1 - \frac{r}{h}\right)^3, & \frac{1}{2} < \frac{r}{h} \leq 1 \\ 0, & \frac{r}{h} > 1. \end{cases} \quad (2.6)$$

Here, W_2 is by calculated by substituting the density distribution $\rho(\mathbf{r}) = mW(\mathbf{r}; h)$ into equation 2.1. The inclusion of a softening length is also computationally convenient, as it prevents the timesteps from becoming infinitesimally small due to close encounters and artificial binaries. For more information on the choice of softening length used I direct the reader to Power *et al.* (2003).

The tree algorithm represents an approximation of the true gravitational force, however the error can be controlled by modifying the opening angle for tree nodes where higher accuracy can be obtained by walking the tree to lower levels.

2.3 Smoothed Particle Hydrodynamics

Smoothed particle hydrodynamics is a common method of simulating fluids, originally introduced by Lucy (1977) and Gingold and Monaghan (1977). It is a mesh-free Lagrangian method, allowing the particles to move with the flow, rather than having a spatially fixed grid, allowing for a large dynamical range. The density of the fluid is determined by smoothing the density of the particles over a characteristic length scale - the smoothing length - with a kernel function. The density is calculated as a weighted sum over its neighbours, and the estimate for a given particle is given by:

$$\rho_i = \sum_{j=1}^N m_j W(|\mathbf{r}_{ij}|, h_i), \quad (2.7)$$

where $\mathbf{r}_{ij} \equiv \mathbf{r}_i - \mathbf{r}_j$ and $W(r, h)$ is the SPH smoothing kernel (see section 2.3.2), which drops to zero when $r=h$. The contributions of each particle to the density are therefore

weighted based on their distance from the particle of interest. The smoothing length of a particle is adaptive, ensuring a constant mass within the kernel

$$N_{sph}m_{sph} = \frac{4\pi}{3}h_i^3\rho_i, \quad (2.8)$$

where N_{sph} is the number of neighbours and m_{sph} is the SPH particle mass. This ensures the mass resolution is constant and independent of the density of the flow.

2.3.1 Fluid Equations

Different formulations of the SPH fluid equations can be derived from the Eulerian equations for the conservation of mass, momentum and thermal energy (Monaghan, 1992; Price, 2005). Gadget 2 uses the entropy formulation of SPH which evolves entropy with time rather than the thermal energy (Springel and Hernquist, 2002), and conserves both energy and entropy when adaptive smoothing lengths are used. This form of SPH provides better estimations for modelling point-like explosions and prevents the overcooling of gas in halos at high redshift when the resolution is poor. In terms of gas density ρ , entropy s and where γ is the adiabatic index, the ideal gas equation of state is given by

$$P = A(s)\rho^\gamma, \quad (2.9)$$

for some entropic function $A(s)$. The fluid equations treat the fluid as a continuous medium, with points at which we can define local variables (macroscopic properties) such as density, temperature etc. Discretization of the Euler equations lead to the following forms of equation for the conservation of mass, momentum and entropy respectively:

$$\frac{d\rho}{dt} = -\rho\nabla\cdot\mathbf{v} \quad (2.10)$$

$$\frac{dv}{dt} = -\frac{\nabla P}{\rho} + \left.\frac{d\mathbf{v}}{dt}\right|_{visc} - \nabla\Phi \quad (2.11)$$

$$\frac{dA}{dt} = \left.\frac{dA}{dt}\right|_{visc} + \left.\frac{dA}{dt}\right|_{diss} \quad (2.12)$$

where ρ , P and \mathbf{v} are the gas density, pressure and velocity respectively, adapted from Read and Hayfield (2012). This form of the equations includes extra terms compared to those in Springel and Hernquist (2002), which account for extra processes that cause

problems at fluid discontinuities if they are neglected. These are the viscous (second term of equation 2.11 and first term of equation 2.12) and dissipative (second term of equation 2.12) terms which are discussed in section 2.3.3 along with the term $\nabla\Phi$ which accounts for the acceleration due to the self-gravity of the SPH particles. The gravitational force of the gas particles is calculated in the same way as for the Nbody particles described in section 2.2 and so is omitted from the equations for the rest of this section. Equation 2.12 is not used in the standard versions of SPH, which can violate entropy conservation in certain situations, for example when a strong shock occurs. This equation comes from the requirement that $A=\text{const}$ (from equation 2.9), therefore entropy is generated only by artificial viscosity in shocks (first term) and external sources of heat (second term) (Springel and Hernquist, 2002).

The version of Gadget used for this thesis uses the SPHS formalism (SPH with a higher order dissipation switch) outlined in Read *et al.* (2010); Read and Hayfield (2012). This improves upon the standard version by allowing for a more accurate estimation of gas properties around contact discontinuities and minimising the errors in the momentum equation. Particle trajectories are predicted in advance, enabling a switch to be turned on before their paths cross which then prevents the fluid quantities from becoming multivalued (discussed in more detail in section 2.3.3).

The equation of motion of an SPH particle can be obtained by the discretised form of the momentum equation (equation 2.11), in the general form this gives the freedom of an additional parameter, ϕ , giving the equation of motion in the absence of influence from external sources.

$$\frac{d\mathbf{v}_i}{dt} = - \sum_j^N m_j \left[\frac{P_i \phi_i}{\rho_i^2 \phi_j} + \frac{P_j \phi_j}{\rho_j^2 \phi_i} \right] \nabla_i \bar{W}_{ij} \quad (2.13)$$

where m_j , P_j and ρ_j are the mass, pressure and density of particle j and $\bar{W}_{ij} = \frac{1}{2} [W_{ij}(h_i) + W_{ij}(h_j)]$ where W_{ij} is a symmetrized smoothing kernel. Standard SPH is the case where $\phi=1$, which gives the original equation of motion for an SPH particle. The SPHS formalism uses $\phi = \rho$, which then gives the equation of motion as:

$$\frac{d\mathbf{v}_i}{dt} = - \sum_j^N \frac{m_j}{\rho_i \rho_j} [P_i + P_j] \nabla_i \bar{W}_{ij} \quad (2.14)$$

2.3.2 The smoothing kernel

The type of kernel used to smooth the density distribution of the gas has an effect on the accuracy of the code. Standard SPH codes tend to use the cubic spline kernel (also used to smooth the gravitational force from Nbody particles, equation 2.6). As discussed in section 2.3.3, in order to minimise the force error $|\mathbf{E}_0|$ in the momentum equation, a large number of neighbours is required. Increasing the number of neighbours for the cubic spline kernel (and other traditional SPH kernels) however, results in instabilities which cause particles to clump together on the scale of the kernel, called the 'pairing instability'. This is due to the kernel being irregularly distributed for larger neighbour numbers (Read *et al.*, 2010; Price, 2012; Dehnen and Aly, 2012), rendering this kernel incompatible with the SPHS version of Gadget.

In order to decrease the error in equation 2.11 by increasing the number of neighbours an alternative kernel must be used. The clumping of particles, called the 'pairing instability' can be avoided by using a kernel whose Fourier transform is non-negative (Dehnen and Aly, 2012). The Wendland kernels (Wendland, 1995) are ideal candidates for an SPH smoothing kernel with large neighbour numbers as they are stable to the pairing instability for all neighbour numbers, without sacrificing additional computational time. Infact, they are some of the least computationally demanding in comparison to the more traditional kernels. For the purpose of the work in this thesis the Wendland C^2 kernel is used with 100 SPH neighbours:

$$W(r, h) = \frac{21}{2\pi h^3} \begin{cases} (1 - \frac{r}{h})^4 (1 + 4\frac{r}{h}), & 0 \leq \frac{r}{h} \leq 1 \\ 0, & \frac{r}{h} > 1 \end{cases} \quad (2.15)$$

2.3.3 Dissipation

The standard ('classic') form of SPH suffers from issues with errors and convergence at flow discontinuities (Morris, 1996; Agertz *et al.*, 2007). Representing the continuous fluid as finite particles with discrete properties results in unphysical behaviour in some situations, for example particles can approach and 'cross over' each other unlike infinitesimal points in a real fluid. This results in multivalued fluid properties at the crossing point which is exasperated in contact discontinuities with large density gradients, where two fluids with at least one property quite different from the other will approach.

Many authors have tried to overcome these issues and a few possible solutions have been proposed by (Monaghan and Gingold, 1983; Morris, 1996; Thacker *et al.*, 2000; Marri

and White, 2003). The introduction of a small amount of viscosity reduces the growth rate of the instability and allows for entropy generation across shocks. Following this, an artificial viscosity which addresses the discontinuities in momentum was introduced to the SPH fluid equations to alleviate these issues, acting to ensure that particles have single valued momentum as they approach each other while conserving energy and momentum (citations for early AV here). Gadget-2 includes a viscous force of the form (Springel, 2005):

$$\left. \frac{dv_i}{dt} \right|_{visc} = - \sum_{j=1}^N m_j \Pi_{ij} \nabla_i \bar{W}_{ij} \quad (2.16)$$

The version of Gadget used in this thesis uses SPHS (Read and Hayfield, 2012) in which Π is given as

$$\Pi_{ij} = \begin{cases} -\frac{\bar{\alpha}_{ij}}{2} \frac{v_{sig,ij} w_{ij}}{\rho_{ij}}, & \text{if } \mathbf{v}_{ij} \cdot \mathbf{r}_{ij} < 0 \\ 0, & \text{otherwise} \end{cases} \quad (2.17)$$

where $\bar{\alpha}_{ij} = (1/2)[\alpha_i + \alpha_j]$ is the viscosity parameter, c_i is the local sound speed and $v_{sig,ij} = c_i + c_j - 3w_{ij}$ is a signal velocity between two particles (see Monaghan, 1997) where $w_{ij} = (\mathbf{v}_{ij} \cdot \mathbf{r}_{ij}) / |\mathbf{t}_{ij}|$. The inclusion of artificial viscosity generates entropy across a shock, which dissipates velocity differences and converts them into heat, resulting in an additional term in equation 2.12 to account for this in the energy conservation, which is given as (Read and Hayfield, 2012):

$$\frac{dA}{dt} = -\frac{1}{2} \frac{\gamma - 1}{\rho_i^{\gamma-1}} \sum_j^N m_j \bar{\alpha}_{ij} \Pi_{ij} \mathbf{v}_{ij} \cdot \nabla_i \bar{W}_{ij} \quad (2.18)$$

where the variables are described above and γ is the adiabatic constant. An artificial viscosity of the form described here includes that for both shear and bulk viscosity, as the purpose is to correctly model entropy across a shock, it is the only bulk viscosity that is of interest. The shear viscosity, which is not required, is limited using a Balsara switch (Balsara, 1989),

$$f_{Balsara,i} = \frac{|\nabla \cdot \mathbf{v}|_i}{|\nabla \cdot \mathbf{v}|_i + |\nabla \mathbf{v}|_i + 0.0001 c_i / h_i}. \quad (2.19)$$

This is multiplied by the viscosity parameter, α , as in Cullen and Dehnen (2010) rather than Π as in other standard methods.

The inclusion of artificial viscosity alleviates the issue of particles with multivalued momentum, however Agertz *et al.* (2007) show that this alone is not enough to correctly

capture dynamical instabilities when density gradients are present, as Kelvin-Helmholtz and Rayleigh-Taylor instabilities are still suppressed. As momentum is not the only property to become multivalued as particles approach each other, similar dissipation terms are needed for the other fluid quantities (the only property that can't be multivalued is the density as it is smoothed). Price (2008) explore this and use dissipation switches that detect and correct multivalued pressures as they occur (artificial conductivity), however it is *before* the properties become multivalued that actions need to be taken, as Valcke *et al.* (2010) show that once they become multivalued, the growth of surface instabilities is still dampened.

Read and Hayfield (2012) show that there are two sources of error which create the problems in mixing for classic SPH, the \mathbf{E}_0 error in the momentum equation, which can grow by orders of magnitude at flow boundaries, delaying the onset of instabilities, and the 'local mixing instability' (LMI), caused by a discontinuity of pressure at flow boundaries. The second adaption to the standard SPH equations of motion is the dissipation term in equation 2.12 given by (Read and Hayfield, 2012)

$$\sum_j^N \frac{m_j}{\bar{\rho}_{ij}} \bar{\alpha}_{ij} v_{sig,ij}^p L_{ij} \left[A_i - A_j \left(\frac{\rho_j}{\rho_i} \right)^{\gamma-1} \right] K_{ij}, \quad (2.20)$$

where $\bar{\rho}_{ij} = [\rho_i + \rho_j] / 2$ and $K_{ij} = \mathbf{r}_{ij} \cdot \nabla_i W_{ij}$ are the symmetrized density and smoothing kernel respectively, L_{ij} is a pressure limiter (see equation 2.22), and $v_{sig,ij}^P$ is similar to the signal velocity, but here is defined to be the positive definite:

$$v_{sig,ij}^p = \begin{cases} c_i + c_j - 3w_{ij}, & \text{if } 3w_{ij} < (c_i + c_j), \\ 0, & \text{otherwise.} \end{cases} \quad (2.21)$$

Using this modified signal velocity gives more dissipation to pairs of particles that are approaching each other than those that are moving away from each other. The latter particles however, do need some small amount of entropy dissipation when they possess discretely different entropies inside the smoothing length to avoid artificial pressure waves. A similar effect can happen with excessive dissipation, so a pressure limiter is used to ensure the pressures are smooth (Read and Hayfield, 2012):

$$L_{ij} = \frac{|P_i - P_j|}{P_i + P_j} \quad (2.22)$$

This set of SPHS equations improves upon the classic version of SPH by ensuring that

all fluid quantities avoid becoming multivalued as they approach each other by detecting flow convergence before it occurs, provided by the addition of the viscosity and dissipation terms, and improves the force accuracy by allowing the use of larger neighbour numbers. This makes it possible to accurately capture shocks and instabilities as well as in AMR codes (Power *et al.*, 2014).

2.4 Radiative cooling

Radiative cooling is an essential component in astrophysical simulations in order to realistically model the gas. Without it galaxies would not form via cool gas collapsing into dark matter haloes at high redshift, and in turn would not form stars.

There are several processes by which gas cools, the most important for a primordial gas being: collisional excitation, collisional ionization, recombination and free-free emission. The cooling due to the combinations of these atomic processes is generally estimated using an optically thin cooling function; $\Lambda(\rho, u)$, which depends on both the gas density and internal energy. The cooling rate of an individual SPH particle representing a primordial gas can be therefore be estimated using the calculated temperature and density.

The standard version of Gadget-2 only includes estimates for the cooling of primordial gas above 10^4K , using the method described in Katz *et al.* (1996). The cooling function, $\Lambda(\rho, u)$ for each SPH particle is obtained by calculating the contribution from each species of ion due to recombination, reionization, excitation and free-free emission along with the number densities of H and He that each gas particle represents. The cooling function and the contributions from each process for primordial gas are shown in figure 2.1 assuming collisional ionization equilibrium. Above a temperature of 10^6K the gas is fully ionized and Bremsstrahlung free-free emissions is the primary source of cooling ($\Lambda/n_H^2 \propto T^{1/2}$), while below 10^4K the primordial gas is neutral and collisions are almost never energetic enough to ionize gas, so the cooling rate is essentially zero.

The majority of the work completed in this thesis assumes a primordial gas (or at least, a very low metallicity gas with $[\text{Fe}/\text{H}]=-3.0$), due to the high redshift at which most of the simulations take place. However it is beneficial to compare to higher metallicities to explore the effect this has on any results obtained. A rough estimation of the cooling function for gas with a metallicity higher than that of primordial (though still much less than solar), was added to the code to enable the modelling of higher metallicity gas. This was based on the cooling functions described in Sutherland and Dopita (1993), shown in

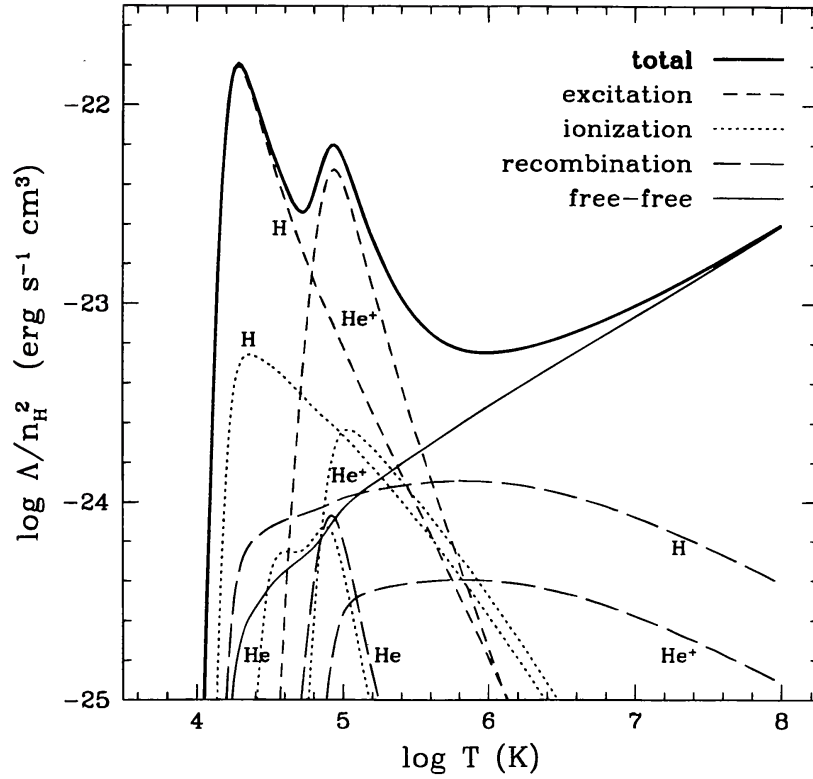


Figure 2.1: The cooling function as a function of temperature for primordial gas assuming collisional ionization equilibrium taken from Katz *et al.* (1996).

figure 2.2 for gas temperatures in the range $10^4 - 10^{8.5}$ K.

To account for cooling below 10^4 K the approximation given in Mashchenko *et al.* (2008) (equation 2.23) is included in the code which describes the radiative cooling via fine structure and metastable lines of C, N, O, Fe, S and Si, again assuming ionization equilibrium,

$$\log(\Lambda/n_H^2) = -24.81 + 2.928x - 0.6982x^2 + \log(Z/Z_\odot) \quad (2.23)$$

where $x \equiv \log(\log(\log(T)))$ and n_H is the number density of hydrogen atoms in cm^{-3} . The approximation is valid down to $T=20$ K and the desired gas metallicity can be obtained by substituting the last term.

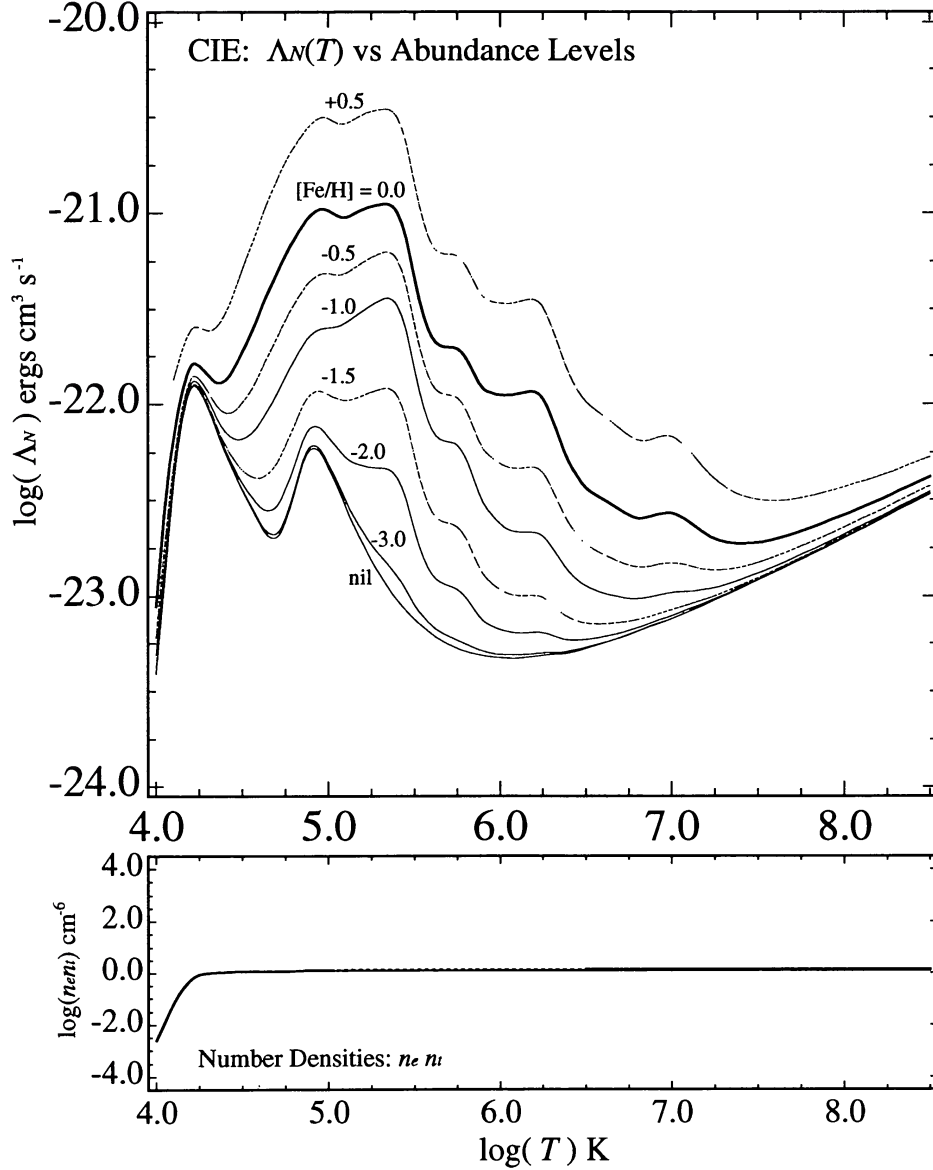


Figure 2.2: The cooling function as a function of metallicity assuming collisional ionization equilibrium taken from Sutherland and Dopita (1993). Curves from top to bottom represent metallicities of $[\text{Fe}/\text{H}] = 0.5, 0.0, -0.5, -1.0, -1.5, -2.0, -3.0$ (where $[\text{Fe}/\text{H}] = 0$ is solar) and the bottom curves represent the case for a primordial gas with zero metals, i.e. the cooling function is due to H and He only.

2.5 Star formation

Stars form in molecular clouds, which are often poorly resolved in large scale simulations, resulting in star formation being modelled via subgrid methods. The detailed physical processes involved in forming stars are omitted from simulations due to the complexity of the physics. Even when high resolution simulations can resolve both individual star forming regions (tens of pc) and star particles, to accurately model the formation of a star requires more sophisticated physical models. Star formation depends on the metallicity of the gas, the gas to dust ratios, the molecular gas content, and the degree of shielding from UV radiation, therefore accurately capturing these physical processes is beyond the scope of current galactic scale simulations.

The process of star formation in the first structures that formed at early times is not fully understood as our understanding of how gas is converted into stars under different conditions is poor. Conditions in protogalaxies or dwarf progenitors would be very different to those in our galaxy and those local to us, and so it is difficult to extrapolate star formation prescriptions that are valid for different galaxies across a range of redshifts.

Observationally, star formation correlates with the presence of molecular gas (Gao and Solomon, 2004; Wu *et al.*, 2005; Bigiel *et al.*, 2008), however this is not modelled in the majority of simulations due to both resolution limits and the computing time required to model the formation and destruction of molecules, and their cooling below 10^4K .

Currently, the most widely used method of following star formation is to estimate the likelihood of forming a star from the properties of the gas particles. Stars form from high density gas, leading most large-scale simulations to form stars from gas particles when they reach a certain defined thresholds in density or temperature (see, e.g.). This is dependant on the resolution limits, as the particle mass defines the lowest gas mass that can be resolved.

A modification to Gadget 2 defines the critical density above which a gas particle can turn into a star as:

$$\rho_{crit} = \rho_{thresh} + \rho_J \quad (2.24)$$

Where ρ_{thresh} is a density threshold set to $5.01 \times 10^{-22} \text{gcm}^{-3}$ equivalent to $300 \text{ atoms cm}^{-3}$ for the work in this thesis, this is comparable to the threshold in other simulations of dwarf galaxies ($M_* < 10^8 M_\odot$) (Governato *et al.*, 2010, 2012; Read *et al.*, 2016a). ρ_J is the local jeans density, given by:

$$\rho_J = \left(\frac{\pi k_B T}{\mu m_p G} \right)^3 (N_{ngb} m_{SPH})^{-2}, \quad (2.25)$$

where n_{ngb} and m_{SPH} are the the number of neighbours and mass of the SPH particle respectively. These two conditions ensure that only gas that is high density (high enough to be molecular in the case of this thesis) is able to form stars. The inclusion of the local Jeans density ensures that this gas is unstable to gravitational collapse by comparing the magnitude of the gravitational potential energy with that of the gas kinetic energy. Therefore, in order for a gas particle to have a chance at turning into a star it must be above the threshold density, which for the case of this thesis is high enough for the gas to be molecular, and it must also be unstable to collapse.

Star formation is an inefficient process (see, e.g. Zuckerman and Evans, 1974; Krumholz and Tan, 2007), so in addition to this criterion, a form of efficiency is included which follows from the empirical Schmidt law (Schmidt, 1959) which describes the dependance of the SFR on the gas density, $\Sigma_{SFR} \propto \Sigma_{gas}^n$. This approach is commonly used in simulations of galactic and cosmological scales (see, e.g. Katz *et al.*, 1996; Springel and Hernquist, 2003; Stinson *et al.*, 2006; Governato *et al.*, 2007). The criterion above specifies which gas particles are eligible to form a star, it is then decided probabilistically which of those go on to become a star in a time Δt using:

$$P = 1 - \exp\left(-\epsilon_{ff} \frac{\Delta t}{t_{ff}}\right) \quad (2.26)$$

Given this probability, a gas particle is then turned into a collisionless star particle with the same position, velocity and gravitational softening as the parent gas particle.

2.6 Stellar feedback

Simulating supernova explosions using SPH has been a demanding problem due to the discontinuities present at the shock front, however with newer formalisms shocks can be captured with vastly improved accuracy. There is still a problem however, with resolving the physical processes which occur over large dynamical ranges, especially in large scale simulations as feedback happens on sub resolution scales. (also a lack of detailed understanding of the physical processes involved)

Supernova feedback is commonly modelled as an injection of thermal energy into the surrounding gas particles. Due to the large scales involved in simulations on the scale of

galaxies and larger, each star particle is modelled as a single stellar population, in turn modelling the effect of it's feedback as a population. Where gas particles have a large mass (due to the low resolution), the injection of thermal energy into the gas can result in numerical overcooling (Thacker and Couchman, 2000a). The gas particles that the shock is driven into will have a large smoothed density, resulting in a cooling time that is very short compared to the dynamical time, allowing the injected energy to be immediately radiated away, greatly diminishing the effect of the SN explosion.

Several solutions to this problem have been explored, one method used to avoid the overcooling problem in low resolution simulations is to temporarily turn off cooling to allow the shell of gas to expand adiabatically, enabling the blast wave to develop (see, e.g. Thacker and Couchman, 2000b; Kay *et al.*, 2002; Brook *et al.*, 2004; Stinson *et al.*, 2006), another is to account for the energy losses by artificially raising the resulting temperature of the particles the energy is injected into (Dalla Vecchia and Schaye, 2012). A form of kinetic feedback is also used (Kay *et al.*, 2002; Dubois and Teyssier, 2008; Dalla Vecchia and Schaye, 2008), where gas particles are given a momentum kick, rather than an increase in thermal energy, which bypasses the cooling problem.

Injecting the energy as purely thermal gives a similar approximation to injecting it as kinetic energy on both small (Walch and Naab, 2015) and large (Dalla Vecchia and Schaye, 2012; Durier and Dalla Vecchia, 2012) scales. The fraction of the total SN energy injected into each neighbouring gas particle is kernel weighted depending on its distance to the star particle using the same kernel as that for estimating the density (equation 2.15). The energy per unit mass injected into a particle, j due to a SN explosion of total energy E_{SN} is:

$$E_{injected,j} = E_{SN} \frac{m_{j,sph} m_{star} W(r_j - r_*, h_*)}{\rho_*} \quad (2.27)$$

where m_{sph} is the mass of the gas particle (only present here because thermal energy is energy per unit mass), m_* is the mass of the star particle, h_* is the smoothing length of the star, which spreads the energy over 100 neighbours and ρ_{star} is the density of the star particle. This approximation is valid for the mass resolution in this thesis, where a gas particle is $10M_{\odot}$ and the injection of thermal energy is resolved. For the purposes of this thesis, stellar winds are neglected as the injection power to the ISM is dominated by the SNe explosions.

Chapter 3

Too small to succeed: The difficulty of sustaining star formation in low mass haloes

3.1 Introduction

Our current galaxy formation paradigm, hierarchical structure formation in the context of a Λ CDM cosmology, has had many notable successes on Mpc scales (e.g. Planck Collaboration *et al.*, 2015a,b; Davis *et al.*, 1985; Hernquist *et al.*, 1996; Riess *et al.*, 1998; Spergel *et al.*, 2007). The low-luminosity tail of the galaxy luminosity function remains problematic, however, with both the numbers and properties of observed stellar systems occupying dark matter haloes with masses below $10^9 M_\odot$ apparently in tension with the predictions of cosmological simulations (e.g. Klypin *et al.*, 1999; Boylan-Kolchin *et al.*, 2011, 2012; Strigari *et al.*, 2010). Given our incomplete understanding of the interplay between baryons and dark matter in the context of galaxy formation, many authors have suggested that baryon physics may be able to account for all the apparent discrepancies between Λ CDM and observations (Navarro *et al.*, 1996a; Pontzen and Governato, 2012).

It is widely expected that there should be a lower limit on the masses of dark matter haloes which host observable galaxies, of any luminosity, at $z = 0$ (e.g. Read *et al.*, 2006a, 2016b; Somerville, 2002; Sawala *et al.*, 2016b). To date, the resolution limits of numerical studies of low-mass galaxy formation in a cosmological context have meant that few meaningful results have been obtained for objects with stellar masses below $10^6 M_\odot$, effectively leaving out the majority of the dwarf satellites of the Milky Way (see Zolotov *et al.*, 2012;

Governato *et al.*, 2012; Sawala *et al.*, 2015a; Oñorbe *et al.*, 2015; Fillingham *et al.*, 2015, for the highest resolution studies to date). The lowest luminosity classical dSphs such as Ursa Minor and Draco have stellar masses of a few $\times 10^5 M_\odot$ (McConnachie, 2012), while the ultra faint dwarfs are still less luminous (Zucker *et al.*, 2006b,a; Belokurov *et al.*, 2007; Tollerud *et al.*, 2008). These pose particular challenges for numerical simulations as a complete physical picture necessitates following both internal and external processes on timescales which span at least 5 orders of magnitude. For example, the evolution of an individual SN remnant occurs on a timescale of 10^4 years while ram pressure stripping of gas due to the dSph’s orbit around the Milky Way modulates its evolution on timescales of $10^8 - 10^9$ years.

Abundance matching methods attempt to link the dwarfs we presently observe around the MW with appropriate subhaloes produced in dark matter only (DMO) simulations based on their properties (see, e.g. Strigari *et al.*, 2010; Boylan-Kolchin *et al.*, 2011; Sawala *et al.*, 2013). However this poses two problems. There is an over-abundance of low-mass subhaloes (“The Missing Satellites” problem; Klypin *et al.*, 1999; Moore *et al.*, 1999; Bullock, 2010) and an over-abundance of larger subhaloes with $V_{\max} \geq 25 \text{ km s}^{-1}$ (the “Too-Big-To-Fail” problem; Boylan-Kolchin *et al.*, 2011, 2012). With more UFDs being continually discovered thanks to surveys like the Dark Energy Survey (see e.g. Bechtol *et al.*, 2015; Drlica-Wagner *et al.*, 2015; Koposov *et al.*, 2015a), the number of Milky Way satellites may soon be broadly consistent with the predictions of DMO simulations. However, resolving the “Too-Big-To-Fail” and “Missing Satellites” problems requires knowledge of both the dark halo masses of these newly identified objects and of the detailed physics of galaxy formation in low-mass haloes. Such insight can only be obtained through simulations capable of resolving the feedback from individual star formation events. Comparing observable satellites to those produced in simulations is likely a much more complicated issue which depends heavily on other factors such as environment, reionization and the stellar IMF at very high redshifts ($z \sim 15$; Power *et al.*, 2016), all of which are poorly resolved in cosmological simulations and completely neglected in DMO simulations.

A third issue with comparison to DMO simulations is the fact that the observed rotation curves of many gas rich dwarf (low surface brightness) galaxies show evidence of cored dark matter density profiles (e.g. Kuzio de Naray *et al.*, 2006; Oh *et al.*, 2008; de Blok *et al.*, 2001; Hague and Wilkinson, 2013), rather than the cuspy profiles expected from dark matter only simulations (Navarro *et al.*, 1996b, 1997). The situation for dSphs is less clear as stars are the only kinematic tracers of the potential in the absence of gas. The literature

contains claims of both cores (e.g. Battaglia *et al.*, 2008b; Walker and Peñarrubia, 2011; Oh *et al.*, 2011; Amorisco and Evans, 2012; Agnello and Evans, 2012) and cusps (e.g. Strigari *et al.*, 2010, 2014; Richardson and Fairbairn, 2014) as well as suggestions that there is no clear evidence for either from the current available data (e.g. Breddels and Helmi, 2013, 2014; Jardel and Gebhardt, 2013). Several authors have shown that in larger satellites ($M_{\text{vir}} \geq 10^9 M_{\odot}$) with bursty SFHs, baryonic effects can transform cusps into large ~ 1 kpc cores (Gnedin and Zhao, 2002; Read and Gilmore, 2005; Governato *et al.*, 2010; Pontzen and Governato, 2012; Zolotov *et al.*, 2012).

Notwithstanding the issue of cusps versus cores, it is well established that feedback from massive stars interacting with the ISM has a significant effect on the evolution of dSphs due their low masses and shallow gravitational potential wells (Larson, 1974; Dekel and Silk, 1986; Governato *et al.*, 2010; Read *et al.*, 2006a). Kiloparsec-scale “superbubbles” and filaments have been observed in star-forming dwarfs (e.g. Hunter and Gallagher, 1997; Martin, 1996; Marlowe *et al.*, 1995; Heckman *et al.*, 2001; Ott *et al.*, 2005) with expansion speeds of $30 - 60 \text{ km s}^{-1}$. Evidence for these outflows can also be found in the high abundance of metals in the intergalactic medium (e.g. Cowie *et al.*, 1995; Songaila and Cowie, 1996; Schaye *et al.*, 2003) and the low abundance of metals contained in dSphs compared to that expected to be synthesised in SNe. For example, observational studies by Kirby *et al.* (2011c,b) found that 8 Milky Way dSphs had lost 96 per cent to 99 per cent of the metals produced by their stars.

The role of supernova feedback on dwarf galaxy evolution has been investigated by several authors. Sawala *et al.* (2010) produce dwarfs similar to those observed in the local group by simulating isolated halos with SN feedback and UV heating only. In order to produce dSph analogues they find that an injection of energy is required to eventually shut off star formation and remove all gas by $z=0$. An additional external mechanism such as UV radiation can shut off star formation much earlier, reproducing those dSphs with only a single burst of star formation. Similarly, Revaz *et al.* (2009) and Revaz and Jablonka (2012) simulate isolated dwarfs and find they still contain a significant amount of gas after ~ 14 Gyr for halo masses in the range $10^8 - 10^9 M_{\odot}$.

In this chapter, we highlight an issue which has not yet been satisfactorily discussed in the literature - namely that galaxies like the Ursa Minor dSph, which formed the majority of its stars more than 10 Gyr ago, were actively star forming for an extended period (~ 3 Gyr; Ural *et al.*, 2015) before their haloes grew to masses above $10^8 M_{\odot}$. Thus, the resolution limits of current cosmological simulations mean that they are unable to resolve the physical

processes in a dSph like Ursa Minor *during the epoch when it formed the bulk of its stellar population*.

The chemistry of the stellar populations requires enrichment of the star forming gas over time: gas retention is thus a key requirement for a successful model of early dSph evolution. Many previous numerical studies have found that haloes below $\sim 5 \times 10^7 M_\odot$ form few or no stars either due to internal effects (e.g. SNe feedback: Read *et al.*, 2016b) or external effects (e.g. reionisation Somerville, 2002; Bullock *et al.*, 2000; Okamoto and Frenk, 2009; Sawala *et al.*, 2016b). However, these simulations lack the resolution to determine whether the failure of the lowest mass haloes to form stars is a numerical artefact or a physical effect. Further, simulations of the long-term evolution of a dSph must necessarily include important details such as halo mergers and gas accretion. In our simulations, we focus our attention on the faintest of the classical dSphs around the Milky Way. We choose to model dSph progenitors with properties based on those of the Ursa Minor and Draco dSphs, which both host a predominantly old stellar population, with almost all stars having an age greater than 10Gyr (Carrera *et al.*, 2002; Ural *et al.*, 2015). These dwarfs seem to have experienced only a single, extended burst of star formation.

The structure of this chapter is as follows: in section 3.2 we describe the initial conditions for our simulations and our treatment of SNe feedback. Section 3.3 presents the results of our runs and in section 3.4 we discuss the implications of these results for our understanding of galaxy formation. Section 5 summarises our conclusions. In appendix B we present stability tests which confirm the long-term stability of our initial conditions in the absence of SNe feedback. In appendix A, we present the results of the convergence tests which we performed to confirm that our main conclusions are not sensitive to our choice of numerical resolution. Finally, in appendix C, we explicitly compare the initial growth phase of our SNe feedback bubbles to the Sedov-Taylor solution to confirm that we are indeed able to capture the main features of individual SN events.

3.2 Description of simulations

All our simulations are performed using a modified version of the N-body plus hydrodynamics code GADGET-2 (Springel, 2005), with thermal stellar feedback (described in section 3.2.2), radiative cooling and adaptive time steps. We use the SPHS formalism (Read *et al.*, 2010; Read and Hayfield, 2012) to properly resolve mixing of the multiphase gas, which develops as a result of the energy injection from SNe, and a second order Wendland

Run	No. of SNe	Energy per SN (erg)	Gas $r_{s,d}$ (kpc)	Disk scale height (kpc)	f_b	Halo C	Metallicity ([Fe/H])
Fiducial	100	10^{50}	0.10	0.013	0.16	10	Primordial
200SNe	200	10^{50}	0.10	0.013	0.16	10	Primordial
500SNe	500	10^{50}	0.10	0.013	0.16	10	Primordial
$r_g=50\text{pc}$	100	10^{50}	0.10	0.011	0.16	10	Primordial
$r_g=200\text{pc}$	100	10^{50}	0.10	0.019	0.16	10	Primordial
$f_b=0.08$	100	10^{50}	0.10	0.017	0.08	10	Primordial
$f_b=0.04$	100	10^{50}	0.10	0.019	0.04	10	Primordial
$C=4$	100	10^{50}	0.10	0.016	0.16	4	Primordial
$C=30$	100	10^{50}	0.10	0.010	0.16	30	Primordial
[Fe/H]=-2	100	10^{50}	0.10	0.013	0.16	10	-2
[Fe/H]=-1.5	100	10^{50}	0.10	0.013	0.16	10	-1.5

Table 3.1: Summary of the simulations presented in this chapter. Each case was simulated using both a spherical and flattened gas distribution. The columns represent the name of the run which we refer to in the text (1), number of SNe events (2), Energy per SN event in erg (3), scale radius of the gas distribution for the spherical case (r_s) and the disk case (r_d) in kpc (4), disk exponential scale height in kpc at r_d , ($R = 90$ to $R = 110\text{pc}$) (5), baryon fraction (6), halo concentration (7), and metallicity (8).

kernel to allow for the larger neighbour number required with SPHS while avoiding the pairing instability (Wendland, 1995; Dehnen and Aly, 2012). In our simulations, we use 100 neighbours for the SPH calculations. Both the gas smoothing and softening lengths are adaptive, with a minimum value of 0.4pc in the densest regions, and the dark matter particle softening length has a constant value of 2pc . In the majority of our simulations, we use $10M_\odot$ gas particles and $100M_\odot$ dark matter particles. However, we also explore the effect of raising or lowering the resolution of the simulations relative to these values to confirm that our conclusions are unchanged by going to higher resolution.

3.2.1 Initial conditions

Table 3.1 summarises the initial conditions for our suite of simulations. Since our goal is to explore the impact of SNe feedback produced by the first burst of star formation in a dSph progenitor, we require that our initial conditions reflect the likely properties of dSph haloes at that epoch. Observations of the Ursa Minor dSph (see e.g. Ural *et al.*, 2015) show that it formed the bulk of its stellar population over a period of approximately $2 - 3\text{Gyr}$, starting at around $z \sim 10$ when the age of the Universe was $\sim 0.5\text{Gyr}$. A number

of authors have found that the present-day properties of Ursa Minor are consistent with its occupying a $10^9 M_\odot$ halo (e.g. Mateo, 1998; Wolf *et al.*, 2010). In order to estimate the $z \sim 10$ progenitor mass for a halo with a dark matter mass of $10^9 M_\odot$ at $z = 0$ we considered the mass assembly history of dark matter haloes. We used the Parkinson *et al.* (2008) algorithm to generate several thousand realisations of Monte Carlo merger trees of low-mass haloes, fixing their virial mass at $z=0$, and determining the distribution of masses of their main progenitors at $z=10$ (and 6). We find a mass of $\sim 3 \times 10^7 M_\odot$ at $z \sim 10$, which agrees with estimations from other studies (e.g. Fakhouri *et al.*, 2010; Sawala *et al.*, 2010).

As we treat our dSph as an isolated system, external effects that will increase its size and mass are not included. The merger history of such a halo therefore sets an upper limit to the duration over which our simulation is meaningful. It is reasonable to assume that this halo mass would remain roughly constant for around 1Gyr (starting at $z=10$ and ending at $z=4$), increasing by at most a factor 3-4 (Power *et al.*, 2016). As the halo grows, mass will mostly be accreted at large radii (Zhao *et al.*, 2003) and so the impact on the central regions where the stars and gas are located, will be minimal.

In this study, we implicitly assume that a $3 \times 10^7 M_\odot$ halo at $z \sim 10$ would have had sufficient time to accrete $\sim 5 \times 10^6 M_\odot$ of gas and that this gas would have been able to cool to the densities in our initial conditions. The uncertain gas acquisition rates make it difficult to verify this assumption. However, given that gas in this halo has a virial temperature of a few $\times 10^3 K$ at $z \sim 10$, the cooling time for low metallicity gas would be $\lesssim 10^6$ yr (see eqs. 8.93 and 8.93 of Mo *et al.*, 2010). For comparison, the age of the Universe at $z \sim 10$ is ~ 0.5 Gyr. Thus, in the absence of external heating, there is certainly sufficient time for the dSph to have begun forming stars provided it had already accreted gas. Cosmological simulations are only beginning to approach the resolutions required to study the gas accretion histories of haloes below $10^8 M_\odot$ (see e.g. Sawala *et al.*, 2015b; Latif and Volonteri, 2015; Sawala *et al.*, 2016a; Wetzel *et al.*, 2016; Fitts *et al.*, 2017), so a fully consistent treatment of this aspect of the problem is outside the scope of this chapter. We note, however, that Read *et al.* (2016b) found that even a $10^7 M_\odot$ halo was able to form stars in their simulations, indicating that gas cooling is unlikely to be a challenge for such haloes.

Our fiducial model is based on the observed properties of the Draco and Ursa Minor dSphs. Both galaxies formed $\sim 3 \times 10^5 M_\odot$ of stars over $\lesssim 3$ Gyr (Dolphin *et al.*, 2005; Carrera *et al.*, 2002). Assuming a cosmic baryon fraction of 0.16, our dSph halo contains

an initial gas mass of $4.8 \times 10^6 M_\odot$. If the entire stellar population of the dSph formed from this gas, this would correspond to a star formation efficiency of ~ 6.5 percent - clearly this assumes that later accretion events increase the dark matter mass without adding to the gas content of the halo. For a Salpeter stellar initial mass function (Salpeter, 1955), the formation of a stellar mass of $3 \times 10^5 M_\odot$ would generate ~ 2000 SNe events (where we have assumed a mass range of $8 - 20 M_\odot$ for the SNe progenitors, giving $\sim 2 \times 10^4 M_\odot$ in SNe progenitors with a mean mass of $12 M_\odot$). As our simulations cover a period of 1 Gyr we would expect approximately 10^3 SNe to occur over the course of the simulation. Even if each SN deposited only 10 per cent of its total energy output (i.e. 10^{50} erg) into the gas, this would exceed the total binding energy of the gas in any of our simulations by at least a factor of two (the maximum binding energy of the gas in our simulations is $\sim 5 \times 10^{52}$ erg). However, our initial experiments showed that comparing the gas binding energy to the energy input from the SNe significantly under-estimated the gas loss from a low-mass halo as we found that the gas became unbound before the energy injected reached that of the binding energy. We reduce the number of SN events to explore the amount of energy that can be injected into the ISM before the gas becomes too hot and extended to continue to build up the rest of the stellar population over the next 1 – 2 Gyr following on from our simulations. Our fiducial model includes only 100 SNe, although we also carry out some runs with 200 or 500 SNe for those initial configurations which we find to be more resilient. We return to this issue in Section 3.4.

Dark Matter halo

In all our simulations, the dark matter halo follows a Hernquist profile (Hernquist, 1990)

$$\rho(r) = \frac{M_{200}}{2\pi} \frac{a_h}{r(r + a_h)^3} \quad (3.1)$$

where a_h is a scale radius defined by the concentration parameter from an NFW profile (Navarro *et al.*, 1996b), assuming the two profiles contain the same mass within r_{200} . The positions and velocities for the halo particles were generated allowing for the potential of the gas and stellar components using the codes `mkgalaxy` and `mkhalo` (McMillan and Dehnen, 2007) within the NEMO (Teuben, 1995) environment. In all simulations $M_{200} = 3 \times 10^7 M_\odot$. We take the halo concentration to be $c = 10$ in all but two runs, which is a reasonable value for for halos at $z \sim 10$ (Klypin *et al.*, 2011) and corresponds to the maximum concentration value at $z = 4$ where our simulations end. These values imply an

NFW scale length of 0.3 kpc and Hernquist parameters of $a_h = 0.5$ kpc and $r_{200} = 3$ kpc.

We re-run the fiducial simulation at higher and lower concentrations to investigate the effect on the resulting dwarf. Although we do not expect a dwarf progenitor to have such a high concentration at $z = 10$, we include $c = 30$ to compare with other work in which the concentration is kept constant for the lifetime of the dwarf (Read *et al.*, 2016b) at present day values. Cosmological simulations find that all halos converge to a concentration of 4 at high redshift ($z > 8$; Zhao *et al.*, 2003, 2009; Muñoz-Cuertas *et al.*, 2011), although these studies do not include the mass scales we are interested in due to resolution constraints. However, Correa *et al.* (2015) use halo mass assembly histories to investigate halo concentrations down to much smaller mass scales and find that at $z=10$ the concentration of all halos in their simulations are in the range $c \sim 3$ to $c \sim 4.5$. We therefore consider a value of $c = 4$ as an example of a low concentration value for our progenitor dSph haloes.

Baryonic components

In order to explore the effect of gas morphology on the ability of the dSph to retain its gas, we consider both spherical and disc morphologies for the initial gas distribution. In the spherical case the gas and stellar components are distributed in a smooth Hernquist profile (using the method described above for the halo) with a scale radius of 100pc, which makes both components more concentrated than the dark matter halo. The total gas and stellar masses are $4.8 \times 10^6 M_\odot$ and $10^4 M_\odot$ respectively, giving particle masses of $10 M_\odot$ for both the gas and stars. The gas follows an ideal equation of state and is assumed to be in hydrostatic equilibrium which determines the temperature profile. Having generated our initial conditions, we evolve them for 300 Myr excluding stellar feedback, to allow the components to settle fully into equilibrium (see Appendix B).

The gas disc was created using the code 'DiscGO' which creates equilibrium disc galaxies (Newton and Kay, 2013). Both gas and stellar components have the same scale length and follow an exponential surface density profile:

$$\Sigma_g(R) = \frac{M_g}{2\pi r_d^2} e^{-R/r_d} \quad (3.2)$$

The gas is assumed to be in hydrostatic equilibrium which determines the height of the gas disc. The total gas mass, stellar mass and the number of particles of each are equal to that used in the spherical case. As with the spherical case we run the initial conditions

with no feedback to allow the components to settle into equilibrium. Figure B.2 shows the disc initial conditions running for 1.25Gyr to confirm that they are indeed stable. The distribution at 300 Myr is used as the initial conditions for the run with feedback, as our stability tests showed that the initial settling of the components due to numerical fluctuations and the IC generation process had been completed by this time.

3.2.2 Cooling and Feedback

Modelling the evolution of a supernova remnant (SNR) is computationally demanding due to the large dynamic range of spatial scales over which the physics needs to be resolved. Both cosmological simulations and simulations of single galaxies lack the resolution to accurately model individual SN events and use approximations to inject energy into the ISM from a single star particle representing a stellar population. Injecting energy thermally at low resolution results in almost all of the energy being immediately radiated away before it has any effect on the ISM (Springel and Hernquist, 2002; Stinson *et al.*, 2006; Creasey *et al.*, 2011). This is due to the energy being injected into a large amount of mass (giving the particles lower temperatures, and so shorter cooling times) and the inability of the particles to react quickly to this change due to the time resolution. Solutions to this problem vary. They include delaying radiative cooling by hand (e.g Thacker and Couchman, 2000b; Kay *et al.*, 2002; Sommer-Larsen *et al.*, 2003; Brook *et al.*, 2004) or forcing the temperature of the injected particles to be higher to account for the extra energy losses (to make the cooling time longer than the dynamical time) to allow the SNR to expand and interact with the ISM (Dalla Vecchia and Schaye, 2012).

A gas particle mass of $10M_{\odot}$ enables us to resolve single SN events by injecting energy thermally, giving an isotropic effect on the closest neighbouring gas particles. Thermal energy injection at this resolution gives a good approximation to the Sedov-Taylor blast wave solution (see appendix C), enabling us to resolve SNe remnants without further numerical adjustments. Injecting the SN energy purely as thermal gives a similar approximation to using kinetic energy both on small scales (Walch and Naab, 2015) and on large scales (Dalla Vecchia and Schaye, 2012; Durier and Dalla Vecchia, 2012) provided the time stepping used allows the injected particles and their neighbours to respond promptly to the sudden energy input. Each SN event injects 10^{50} erg of thermal energy into ~ 100 neighbouring gas particles. The amount of energy each particle receives is kernel-weighted by its distance from the star particle.

We do not model star formation explicitly, as we are primarily concerned with the ability

of our model dSph to retain sufficient gas to support further star formation; therefore the only stars in the simulations are those present in the initial conditions. As discussed in section 3.2.1 we would expect $\sim 10^3$ SN over the period of time covered by the simulations assuming a single, continuous burst of star formation over ~ 3 Gyr. We include 10^3 star particles, a number of which are chosen to inject energy at random times during the course of the simulation, depending on the run. For example, in our fiducial run we have 100 SNe which translates to a rate of 1 SN every 10 Myr.

Radiative cooling of the gas is included following the method of Katz *et al.* (1996) down to 10^4 K, assuming ionisational equilibrium. We further assume that the gas is of primordial composition and do not model metals produced by supernovae in these simulations. As gas cooling is dependant on metallicity we investigate the effect the presence of metals has on our results by repeating the fiducial run for both the spherical and disk morphologies at two different metallicities: $[\text{Fe}/\text{H}] = -1.5$ and -2 . To account for cooling due to metals we use approximate cooling functions based on those described in Sutherland and Dopita (1993) for temperatures $10^4 - 10^{8.5}$ K. Cooling below 10^4 K is modelled as described in Mashchenko *et al.* (2008) via the fine structure and metastable lines of heavy elements. These cooling curves were applied to all of the gas in the simulation. This is therefore an extreme case, as the majority of metals would be those ejected by the SNe which would not be present in the initial gas and would be unlikely to be uniformly distributed through the whole dSph. The results are presented in Section 3.3.3.

We neglect external processes in the simulations such as mergers and the effect of heating from the cosmic UV background (UVB). Observations of the IGM indicate that reionization of the universe was complete by $z \sim 6$ (see e.g. Becker *et al.*, 2001; Fan *et al.*, 2003). It has been suggested by several authors that reionization could alleviate the missing satellite problem by suppressing star formation in low mass haloes or preventing them from forming stars altogether (see, e.g. Bullock *et al.*, 2000; Sawala *et al.*, 2015a). However dSphs like Ursa Minor and Draco were continuously forming stars for ~ 3 Gyr (up to $z \sim 3$) suggesting that reionization was not responsible for ending star formation in these dwarfs. It has been shown that the effects of self-shielding at high redshift are quite significant, and baryons in high density peaks are still able to cool and form stars (Susa and Umemura, 2004; Ricotti and Gnedin, 2005). Therefore those low-mass haloes that are able to maintain a high density of gas in their centres during an episode of star formation could possibly continue to form stars even after the universe has been reionized.

Our simulations run for 1Gyr so the effects of the UVB would only be relevant at the

end of our simulations and would only act to maintain the temperature of the already hot and extended gas that has been ejected from the galaxy due to the SNe feedback.

3.3 Results

As noted in the Introduction, observations of the Milky Way satellites provide evidence that they experienced extended periods of star formation which in turn indicate that they were able to retain their gas, and continue star formation, until Type Ia SNe had had time to enrich the gas with iron. Thus, a minimal requirement for a successful model of a dSph progenitor is that it be able to retain gas in its inner regions at sufficiently high densities and low temperatures to support further star formation.

We begin by exploring the impact of initial gas morphology on the ability of a dwarf galaxy progenitor to retain its gas in the presence of feedback from SNe. Sections 3.3.1 and 3.3.2 present the results from the spherical and disk gas morphologies separately: in each case we discuss the impact of each of our model parameters on the resulting evolution, under the assumption that all the gas has a metallicity of $[\text{Fe}/\text{H}]=-3$. In Section 3.3.3 we explore the impact of a higher initial gas metallicity on our conclusions.

3.3.1 Spherical gas distributions

The black curves in Figure 3.1 show the evolution of the gas density (top panels), the enclosed gas mass (middle panels) and the fraction of gas at the escape velocity (bottom panels) for simulations in which the gas distribution is initially spherical and assuming our fiducial (F) parameters. In the top four panels, the solid curves show the initial distribution and the dashed curves correspond to distributions after 1.25 Gyr. Figure 3.1(a) shows that by 1.25 Gyr the gas density has been significantly reduced throughout the dSph, with the central gas density being more than four orders of magnitude lower than its initial value. The dashed black curves in Figure 3.1(c) confirm that that by 1.25 Gyr more than 90 per cent of the gas has been moved beyond a radius of 1kpc. We have not included the results from the simulations with 200 or 500 SNe (the fiducial run has 100SNe) as the density and enclosed mass are simply reduced even further in these models.

Clearly, the energy injected by 100 SNe is sufficient to re-arrange the bulk of the gas in this simulation. This is not surprising as the total binding energy of the gas in the central 100 pc is only about 20 per cent higher than the 10^{52} ergs of thermal energy injected by 100 SNe in our models. While Figure 3.1(e) shows that less than five per cent of the gas

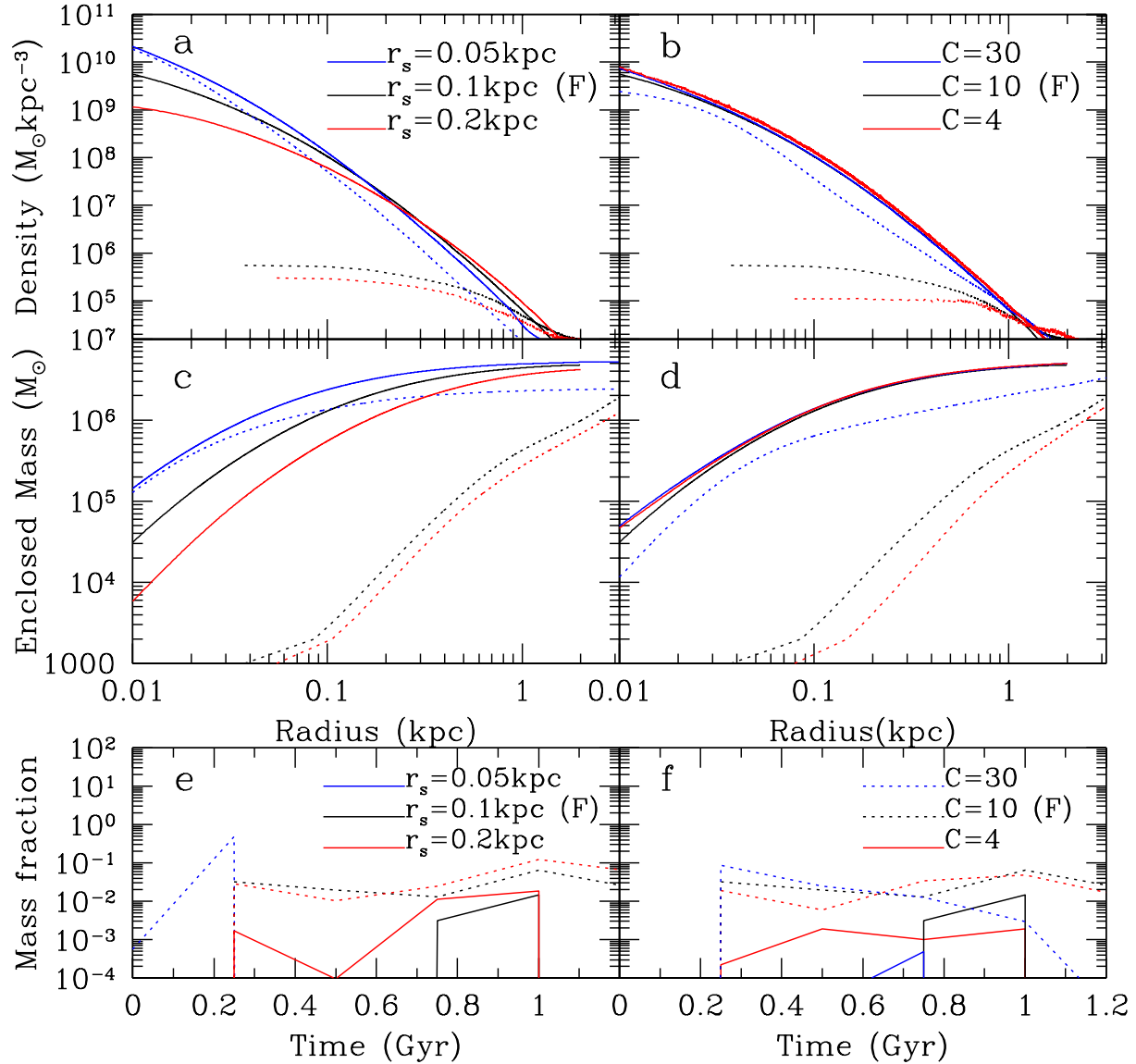


Figure 3.1: **Top, Middle:** The evolution of the gas density (top) and enclosed mass (middle) profiles for simulated dSphs with initially spherical gas distributions. The solid curves show the initial profiles and the dashed curves show the resulting profiles after 1.25 Gyr. The black curves correspond to our fiducial initial conditions, while the red and blue curves indicate changes to either the scale length of the gas distribution (left panels) or the concentration of the dark matter halo (right panels). The gas particles are binned radially with 100 particles in each bin. **Bottom:** The fraction of gas with velocities greater than the local escape velocity as a function of time for the simulations in the upper panels. Solid (dashed) curves give the fraction of gas at radii less than 1 kpc ($1 \leq r \leq 5$ kpc). (F) denotes the fiducial run.

at large radii is moving above the local escape velocity, we note that the low density of this gas (more than two orders of magnitude below the original mean gas density within 1 kpc) means both that its cooling time is very long (temperatures are below 10^4K) and it is very susceptible to removal by any external perturbation, for example ram pressure stripping by the gaseous halo of its host galaxy (at a radius of 100kpc the MW halo would strip any gas outside 10kpc, and at a radius of 10kpc would strip gas outside 2kpc (Miller and Bregman, 2013)). It is therefore very unlikely that this gas could be retained by the dSph for sufficient time to allow it to fall back into the inner regions and form additional stars.

The red and blue curves in Figure 3.1(a) show the evolution of the gas density profile in simulations with different initial gas concentrations. As expected, it is much more difficult to remove gas from the inner regions of the dSph in the case of a more concentrated initial distribution ($r_s = 0.05\text{kpc}$; blue curves) but somewhat easier to remove gas in the less concentrated case ($r_s = 0.2\text{kpc}$; red curves). The corresponding enclosed mass profiles (Figure 3.1(c)) show that in the most concentrated run, mass is only removed from the outer parts of the dwarf where the density is lower and cooling times are longer. In contrast to the models with $r_s = 0.1\text{kpc}$ or $r_s = 0.2\text{kpc}$, which retain less than 0.1 per cent of their gas content within 100 pc, in the model with $r_s = 0.05\text{kpc}$, 15 per cent of the gas initially within 100 pc remains there after 1.25 Gyr of evolution. The large differences between the final density profiles arises due to the dependance of cooling time on the gas density: $t_{\text{cool}} \propto \rho^{-1}$. The cooling times in the fiducial case ($r_s=0.1\text{kpc}$) are already long enough for the gas to be driven to large radii, so further decreasing the density ($r_s=0.2\text{kpc}$) gives a similar result, whereas for the most concentrated distribution ($r_s=0.05\text{kpc}$) the cooling times have decreased by a factor ~ 5 allowing more gas to be retained.

Overall, Figure 3.1(c) shows that a dSph with a more centrally concentrated initial gas distribution loses a larger fraction of its total gas mass: roughly 50 per cent of the gas mass is located beyond 5 kpc at the end of the simulation. However, the key point is that this dSph retains gas in the inner regions at densities where it has the potential to contribute to further star formation.

The red and blue curves in Figure 3.1(b) and (d) show the impact of dark matter halo concentration on the evolution of the gas density profile and the enclosed mass profile. As in the case of varying gas concentration, it is slightly easier to remove gas from a halo with a lower concentration and significantly more difficult for a halo with a higher concentration. However, in contrast to the results for the simulation with $r_s=0.05\text{kpc}$ for

the gas initially (the blue curves in Figure 3.1(c)), in the simulation with $c = 30$ gas is depleted all the way to the centre of the dSph, although the fraction of mass removed from within 100 pc is similar in both cases (57 per cent and 46 per cent of original mass retained for $r_s = 0.05$ kpc and $c = 30$ respectively). The potential energy of the gas within 30 pc in the $r_s = 0.05$ kpc and $c = 30$ simulations is 1×10^{52} erg and 5.8×10^{51} erg, respectively. Thus, the significantly different gas fractions within 30 pc at 1.25 Gyr seen in the two simulations explicitly demonstrates that the ability of a dSph to retain gas in its inner regions is a function not only of the depth of its gravitational potential well, but also of the gas density in the inner parts which determines the timescales on which the gas can cool.

The fraction of gas that reaches the escape velocity is shown in panels (e) and (f) of Figure 3.1 as a function of time for the same runs. The solid curves correspond to the fraction of gas particles within 1 kpc at the time of the snapshot that have velocities above their local escape velocity; the dashed curves show the same fraction for gas particles with radii in the range 1 – 5 kpc. The fraction of high velocity gas within 1 kpc is very low in all runs, only briefly reaching 1 per cent in the standard and low (gas or halo) concentration runs. This suggests that the gas remaining within 1 kpc after 1.25 Gyr will be retained by the dSph in all cases we have considered. However, only in the high (gas or halo) concentration models is the gas density sufficiently high at the end of the simulation that further star formation is likely to occur (assuming a density threshold of $7.4 \times 10^9 M_\odot \text{kpc}^{-3}$ to ensure the gas is dense enough to be mainly molecular; Read *et al.*, 2016b). The gas in the centre of these two dwarfs at the end of the simulation is cool (less than 10^4 K) and dense, and so we would expect star formation to continue.

It is interesting to note that even at radii of 1 – 5 kpc the fraction of gas particles with velocities above their local escape velocity is also low, remaining below 10 per cent for most of the simulations. In the $r_s=0.05$ kpc run, however, it exceeds 10 per cent from about $t = 100$ Myr to $t = 400$ Myr. This is because the initial gas distribution in this simulation has much lower density beyond 1 kpc than in the other runs and the outflows from SNe in the inner regions are therefore able to accelerate a large fraction of this gas to velocities above the escape velocity.

Figure 3.2 shows the response of the dSph’s dark matter halo to the evolution of the gas distribution. Following the rapid removal of gas from the centre of the dwarf, the halo central density in the simulation with our fiducial parameter choices (black curves) decreases by an order of magnitude, forming a profile with a much shallower inner log slope

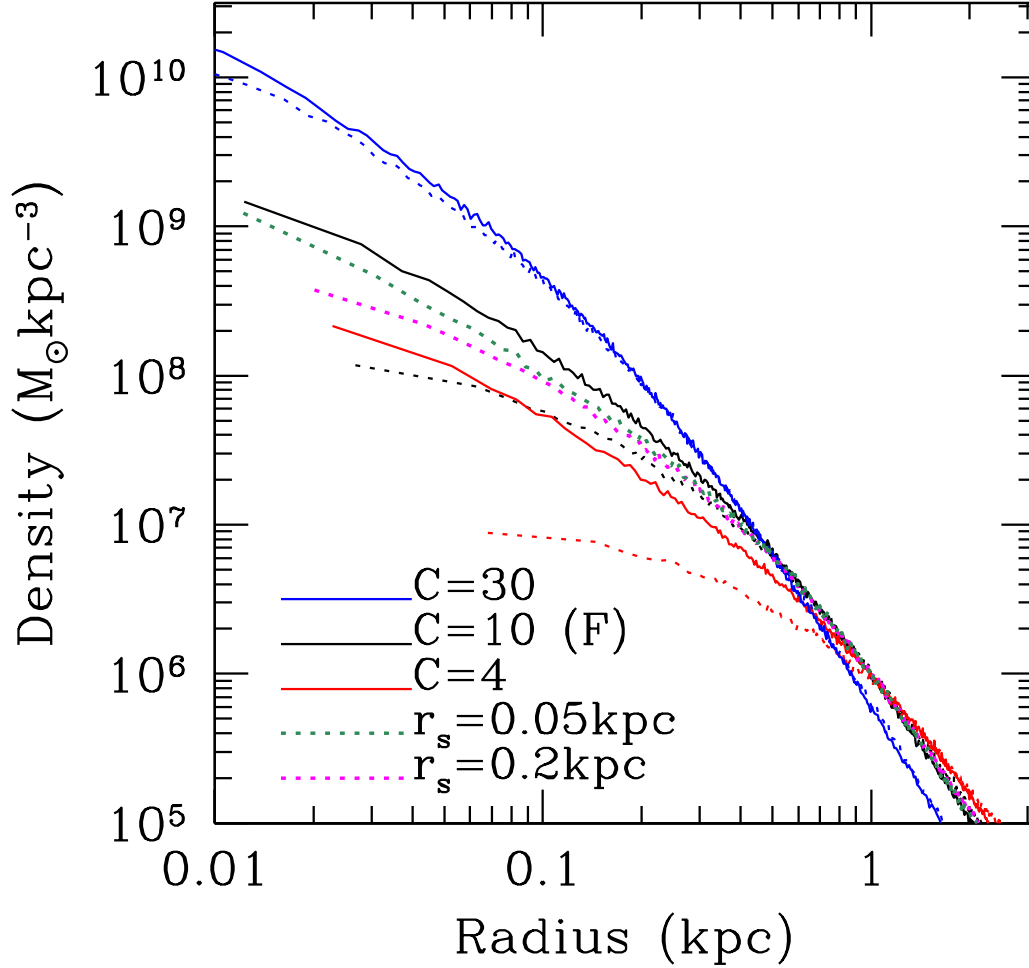


Figure 3.2: Evolution of the dark matter halo density profiles for the simulations presented in Figure 3.1. For clarity, we show the initial density profiles for the fiducial ($c = 10$, solid black curve), $c = 4$ (solid red curve) and $c = 30$ (solid blue curve) simulations only, as the initial profiles for both other models shown are indistinguishable from the fiducial model. The profiles after 1.25 Gyr of evolution are shown as dashed curves with the colours indicating the model. The halo particles are binned radially with 300 particles in each bin. (F) denotes the fiducial run.

within a radius of ~ 100 pc. In the simulation initially having less gas within 100 pc, due to a less concentrated gas distribution (the $r_s = 0.2$ kpc model; purple dashed curve), the halo profile evolves less dramatically than in the standard model, although the initial halo profiles are indistinguishable. As expected, the removal of the gas from the inner regions in these cases corresponds to a smaller change in the total gravitational potential and therefore the response of the dark matter halo is reduced. The smallest effect is seen when the gas is initially more centrally concentrated (the $r_s = 0.05$ kpc model; green dashed curve) as the retention of a significant fraction of the gas within 30 pc offsets the greater gas contribution to the mass budget in this region (gas contributes 44 per cent of the total initial potential within 30 pc, compared to 20 per cent for $c = 30$). The expulsion of gas to radii beyond 5 kpc noted above does not have a significant impact on the dark matter halo.

Only the model with a lower initial halo concentration ($c = 4$; red curves in Figure 3.2) exhibits more significant halo evolution than the standard model. This is simply because the gas initially constitutes 47 (28) per cent of the gravitational potential within 60 pc (1 kpc). The removal of this gas results in the central 100-200 pc of the dark matter halo evolving to almost uniform density. We will discuss the possible implications of the dependence of the final dark matter halo profile on initial halo concentration in Section 3.4. The halo density profile for the model with the highest halo concentration, $c = 30$ experiences no evolution over the run. The potential is dominated by the halo (the gas only contributes 20 per cent in the inner 30 pc) and only a small amount of gas is removed, leaving the structure of the halo unaffected.

The simulations presented in this section demonstrate that galaxy progenitors with similar masses to those expected for $z \sim 10$ dSphs and with initially spherical gas distributions are generally unable to retain their gas in the face of feedback from just 100 SNe. Progenitors with high concentration haloes are able to retain a higher fraction of gas, but only haloes with highly concentrated gas distributions are able to retain gas at densities which are high enough to sustain star formation.

3.3.2 Flattened gas distributions

In this section, we consider the evolution of dSph progenitors in which the initial gas distribution is a thick disk ($R_d/z_d=1.5$ for the fiducial run). Figure 3.3 shows that after 100 SNe events the disk is able to retain the majority of its gas and the density at the centre remains high enough for further star formation, in the sense that is roughly equal to

the highest density thresholds for star formation assumed in simulations (e.g. Read *et al.*, 2016b; Pontzen and Governato, 2012). This is in contrast to the evolution of initially spherical gas distributions in which 100 SNe are able to push more than 90 per cent of the gas out to radii $> 100\text{pc}$, whereas the disk retains 80 per cent of the gas initially within this radius.

The effect of increasing the number of SNe for the disk is also shown in Figure 3.3. The initial conditions are identical for all three runs and are represented by the solid black curve. The dashed black, blue and red curves show the radial density profile after 1.25Gyr for 100, 200 and 500 SNe events, respectively. 200 SNe events cause the gas density to drop by another order of magnitude, although 60 per cent of the gas still remains within the original 1kpc. As the number of SNe increases, the amount of energy injected exceeds the binding energy ($3.5 \times 10^{52}\text{erg}$) and the entire gas content of the dSph is pushed to large radii.

For the fiducial disk run, Figure 3.4 presents snapshots of the disk density and temperature in the $x - y$ plane (top and bottom rows), and density in the $x - z$ plane (middle row) at 0 Myr, 730 Myr and 1.25 Gyr in the left, middle and right columns, respectively. The snapshots are slices through $z=0$ ($y=0$) for the top and bottom (middle) rows and show the 3D density of the particles. Although there is more gas at large radii by the end of the simulation, the density of the disk in the $x - y$ plane remains similar to the initial snapshot with only a small reduction in central density. However the $x - z$ plane slice shows that the final dwarf has evolved into a more spheroidal morphology, particularly for the gas beyond about 0.25 kpc. Figure 3.5 presents the evolution of the angular momentum over time for the fiducial disk run. The total angular momentum of the gas is represented by the black curves, and the z-component by red curves. Solid curves denote values for all gas particles, while dashed curves relate only to those gas particles within 500 pc. Although the total z-component of the angular momentum in the dwarf remains almost constant during the run, the z-component within 500pc decreases to less than half of the initial value after 1.2Gyr. While the mid plane density is still relatively high near the centre compared to the initial distribution, the disk is thicker than initially, possibly making it easier for subsequent SNe to remove more gas. This final structure, shown in the right panel of Figure 3.4, is typical of all of the disk runs we considered (see Figure 3.10 which presents the corresponding halo evolution). The gas distribution becomes more spheroidal for the lower concentration runs ($c = 4$, $r_d = 0.2\text{kpc}$) and the central, higher density regions retain a more disk-like morphology for the higher concentration runs ($c = 30$, $r_s = 0.05\text{kpc}$).

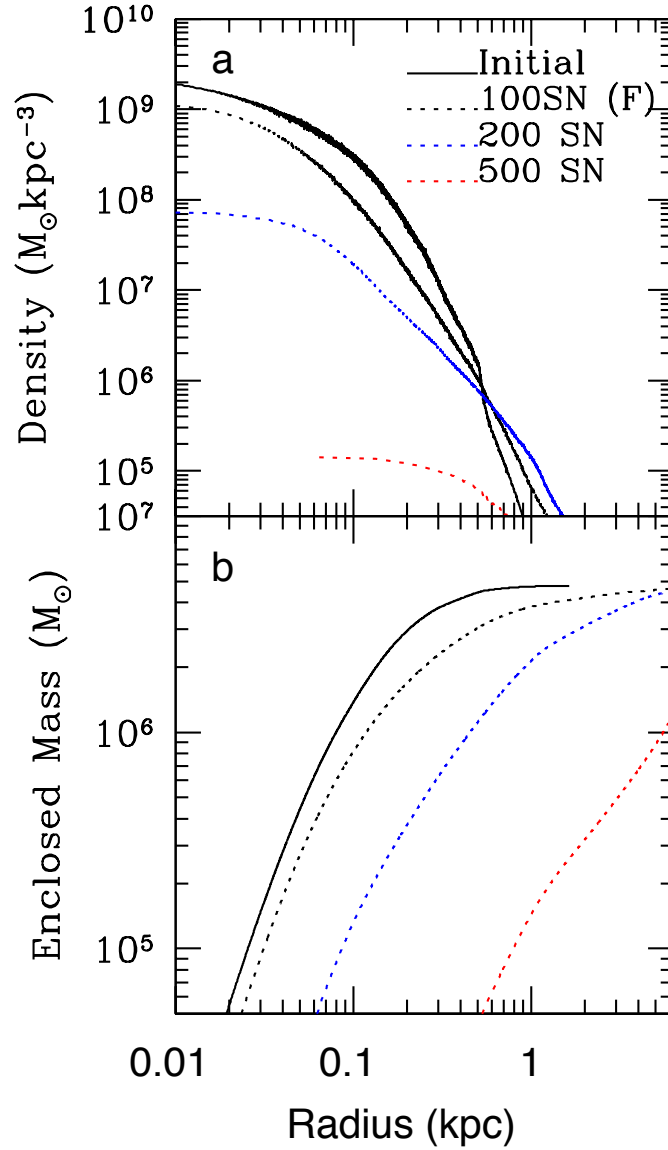


Figure 3.3: Evolution of the gas density (**top**) and enclosed mass (**bottom**) profiles for simulated dSphs with gas initially distributed in a disk. In both panels, the solid black curves show the initial profiles, and the black, blue and red dashed lines show the resulting profiles after 1.25 Gyr of evolution for simulations in which feedback from 100, 200 or 500 SNe is included. The corresponding SN rates are 0.1Myr^{-1} , 0.2Myr^{-1} and 0.5Myr^{-1} , respectively. The gas particles are binned radially with 100 particles in each bin and the three dimensional SPH particle density is averaged. (F) denotes the fiducial run.

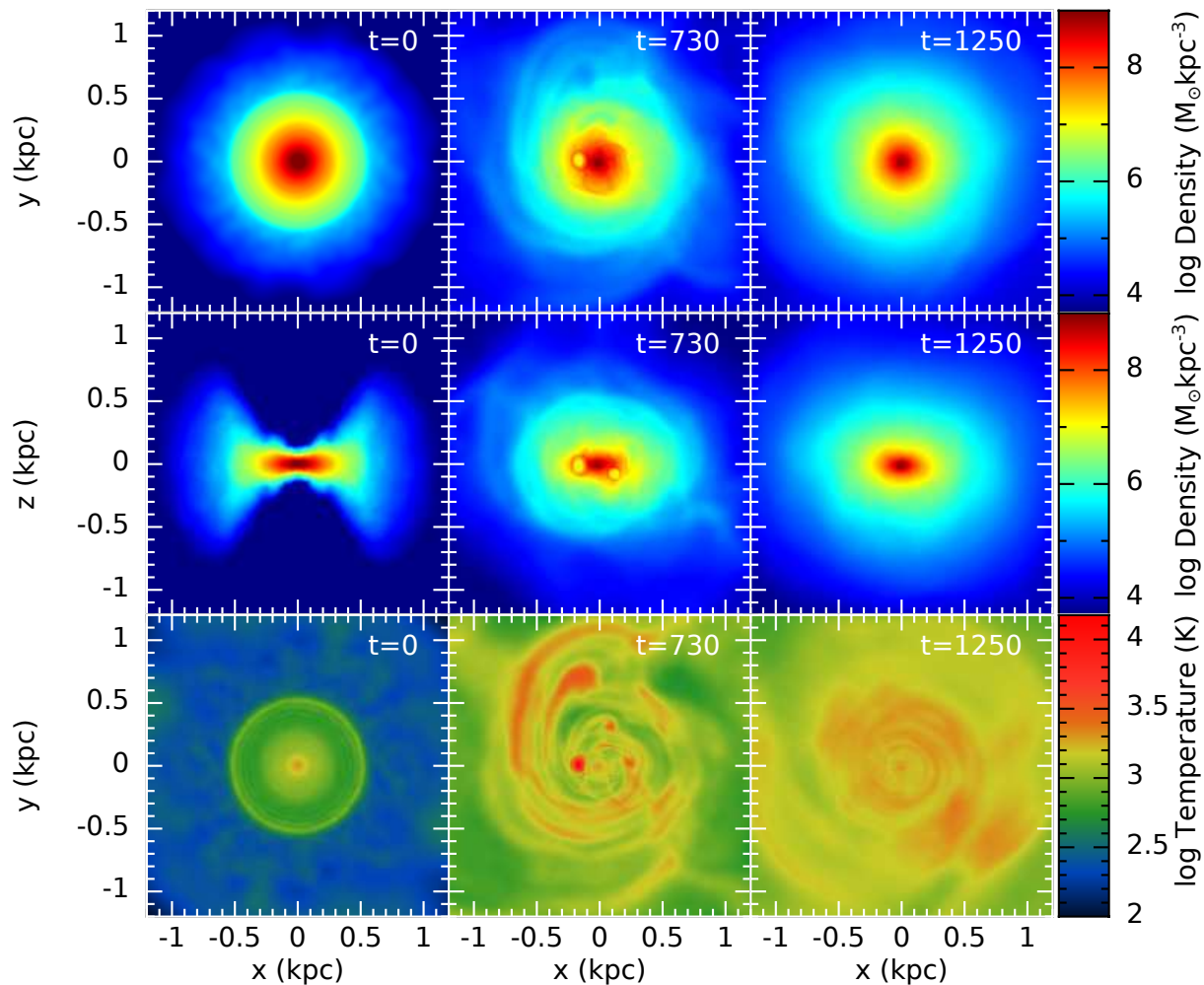


Figure 3.4: Maps showing the evolution of gas density (**top, middle**) and temperature (**bottom**) for the fiducial disk simulation. The leftmost column shows the initial conditions, the middle column shows the situation at 730 Myr and the rightmost column shows the final state at 1.25 Gyr. The quantities plotted are cross-sections showing density in the $x-y$ plane (**top**), density in the $x-z$ plane (**middle**) and temperature in the $x-y$ plane (**bottom**).

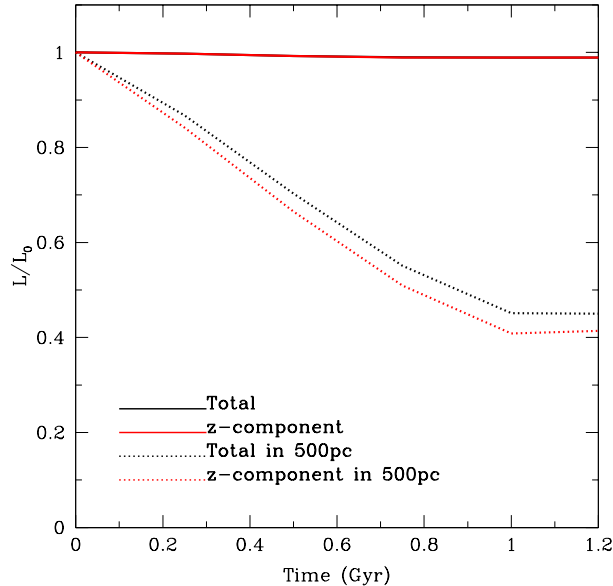


Figure 3.5: The evolution of the total angular momentum (black solid line), and z-component of angular momentum (red solid line) over time for the fiducial disk run compared to the initial values (L_0). The same values within 500pc are shown as dashed curves.

The temperature snapshots in the bottom row of Figure 3.4 show pockets of warm gas where SNe have recently exploded. Note that the warm gas in this panel is only at 10^4K as the cooling times are very short at these densities and so it has had time to cool in the interval between the explosion and the snapshot being output. The warm patches in temperature are seen in the corresponding density panels as bubbles where the shock front has pushed gas spherically outwards, leaving low density hot gas around the origin of the explosion. At the end of the simulation all of the gas is cool ($T < 10^{3.5}\text{K}$).

For comparison we show the same temperature maps for the fiducial spherical run in Figure 3.6. In the fiducial spherical run there is much more warm gas (10^4K) in the same region, as the cooling times are much longer. In the final snapshot only around a fifth of the original gas mass within 1 kpc remains and the temperatures are hotter than for the corresponding disk case. This highlights the differences between the two morphologies. In the case of the disk there is a much higher proportion of gas at higher densities leading to much shorter cooling times. In the spherical case the gas density drops off much more rapidly from the centre, leading to lower densities and longer cooling times.

The bottom row of Figure 3.4 also illustrates the shearing effect of the disk on the gas which has been heated by SNe. For example, the middle panel shows two extended regions

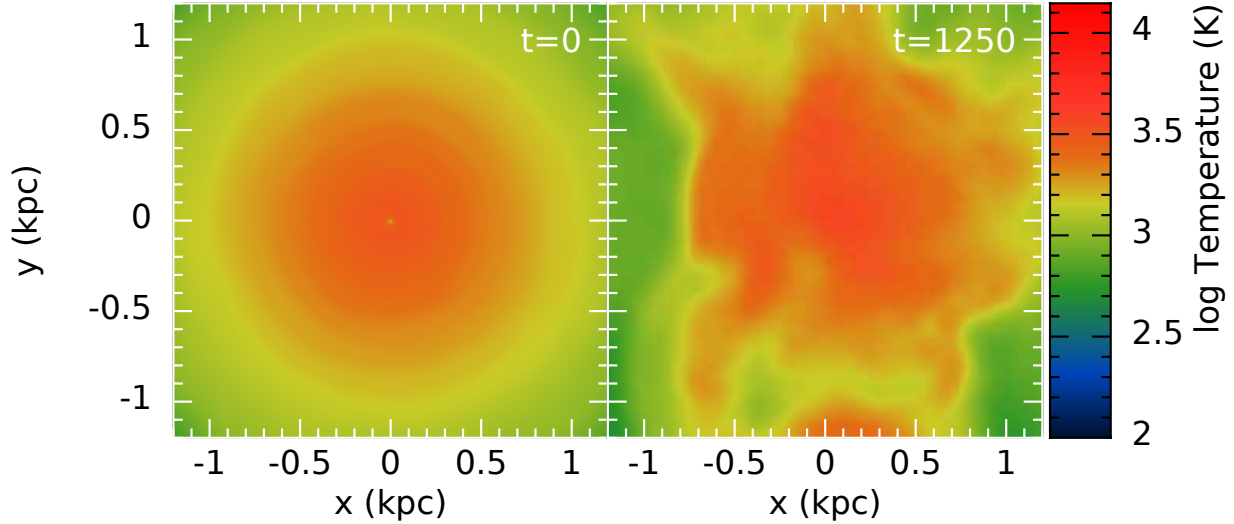


Figure 3.6: Maps showing the initial (**left**) and final (**right**:1.25Gyr) gas temperature for the fiducial spherical run in the $x - y$ plane.

in the upper left quadrant of the panel which are left over from earlier SNe explosions in regions where the gas density is too low to allow cooling on timescales shorter than the local dynamical times. This effect emphasises the ability of the disk to retain gas that would otherwise be expelled from a non-rotating system. This will also have consequences for the distribution of the metals generated by the SNe - the highly structured nature of the heated gas shows that the distribution of SNe produced is likely to be very non-uniform.

The evolution of the gas distributions in the remaining disk runs are shown in Figure 3.7. The top panels show how the evolution changes as a result of varying the initial gas concentration (left), the baryon fraction (middle) and the halo concentration (right); the corresponding enclosed mass profiles are shown in the bottom panels. All panels show the initial profiles as solid lines and the resulting profiles after 1.25Gyr as dashed lines. Figure 3.7(a) shows similar results for varying the gas concentration as in the spherical case. Interestingly, the central density for the most concentrated run (blue curve) is actually slightly higher after 1.25Gyr than at the start of the simulation. This is due to the short gas cooling times in the dense central region of this simulation. As a result, gas which is driven towards the centre by SNe occurring beyond a few 100 pc tends to cool rapidly and contribute to the build-up of a dense, cool central gas concentration.

The disk is able to retain more gas in the most concentrated case than for the corresponding spherical run, with 97 per cent of the original gas mass within 1 kpc remaining for

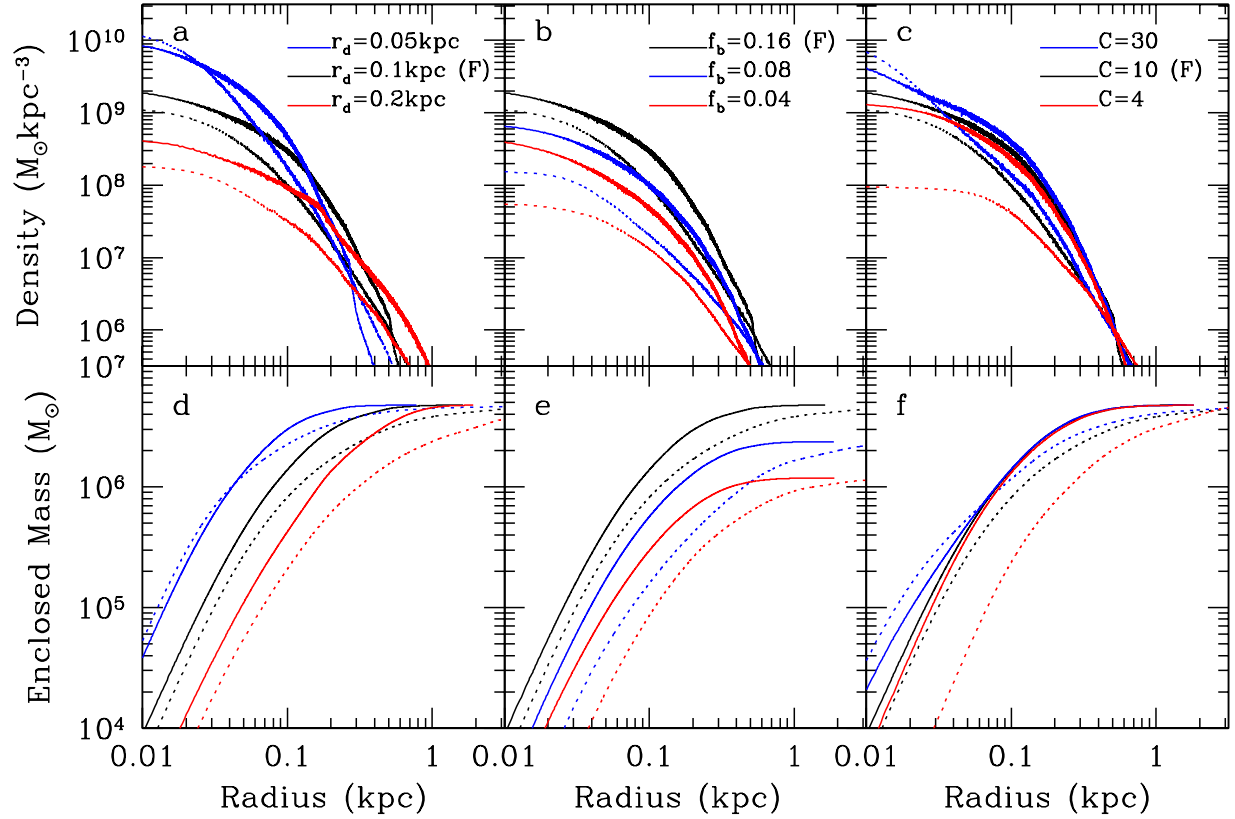


Figure 3.7: Impact on the evolution of the gas density (**top**) and enclosed mass (**bottom**) profiles of varying the model parameters for simulated dSphs with gas initially distributed in a disk. In all panels, solid curves denote initial distributions and dashed curves give the profiles after 1.25 Gyr of evolution. For ease of comparison, the black curves in each panel show the profiles for the fiducial model, while the red and blue curves correspond to models with alternative values for the initial model parameters. Panels (a) and (d) show the effect of varying the scale length r_d of the gas disk; panels (b) and (e) show the effect of varying the total baryon fraction of the initial model; in panels (c) and (f) the dark matter halo concentration is varied. (F) denotes the fiducial run.

the disk case, compared to 47 per cent in the spherical case. Increasing the initial concentration of the gas impacts the cooling times in the inner regions of both the spherical and flattened models similarly, and as a result the models with $r_s = 0.05$ kpc and $r_d = 0.05$ kpc exhibit similar central densities at the end of the simulation: the mass lost in the spherical case is mostly from radii outside 20 pc. The ability of the disk to retain significantly more gas overall, is due to the fact that higher density gas in the disk extends to larger radii. We also see a much smaller amount of gas lost from the disk models with initially less concentrated gas ($r_d = 0.2$ kpc). In the spherical case almost all the gas is ejected to larger radii with only 7.5 per cent of the original gas remaining within a radius 1 kpc, compared to 42 per cent for the case of the disk. An initially spherical gas distribution in this case results in the dwarf being destroyed by SNe feedback, whereas an initial disk configuration retains its original structure, albeit at a somewhat lower density.

Figure 3.7(b) shows the effect of reducing the initial baryon fraction of the dSph by a factor of two (blue curves) or four (red curves). Although these two runs have a lower gas mass, the number of particles is kept consistent so that the height of the disk is resolved, resulting in gas particles with masses $5M_\odot$ and $2.5M_\odot$ for $f_b=0.08$ and $f_b=0.04$ respectively. As the Figure shows, the initial reduction in the central gas density leads to a larger amount of gas being ejected from the central regions as expected. A higher fraction of gas is lost within 100pc for those models with a lower initial gas mass, 28 per cent and 30 per cent for $f_b=0.08$ and $f_b=0.04$ respectively, compared to 59 per cent for the fiducial run ($f_b=0.16$). Similarly to the fiducial run, it is the central regions where cooling times are short that are most affected by the SNe feedback, as the total mass enclosed within 1 kpc is very similar to the initial values.

Figure 3.7(c) shows the results of varying the halo concentration. Note that the central gas densities are slightly different to the fiducial run when a different halo concentration is used. This is due to the method of creating the gas distribution in the disk case, which uses the halo potential to position the gas particles while maintaining hydrostatic equilibrium. Increasing the concentration results in the stellar feedback having no significant effect on the total gas content of the dSph, as 85 per cent of the original gas mass within 1 kpc is retained. However, the distribution of gas within the dSph is very different to the fiducial run - the gas becomes much more centrally concentrated, similarly to the evolution of the gas distribution in the $r_d = 0.05$ kpc model of Figure 3.7(a). Note that in the corresponding spherical run gas is lost from the inner parts of the dwarf, decreasing the density in the centre. However, when the gas is arranged in a disk, mass is only lost from radii > 100 pc.

In the spherical case only 46 per cent of the original gas mass within 100 pc remains, whereas 82 per cent remains for the disk. This suggests that gas cooling times play a stronger role in determining whether or not a dSph will retain its gas than modest changes to the depth of the halo potential well, as the initial halo potentials are the same in both the spherical and disk cases and yet the gas densities evolve very differently. Note that the fiducial run ($c = 10$) and the $c = 30$ run both have the same gas mass within 1 kpc after 1.25 Gyr - it is the difference in their central gas densities that will determine the evolution of the dwarf at later times. The gas is much easier to remove from a halo with concentration $c = 4$, and by the end of the simulation 90 per cent of the mass within 100 pc has been removed and the central gas density has dropped by an order of magnitude.

As the runs with a higher concentration of gas ($r_s = 0.05\text{kpc}$) and dark matter ($c = 30$) retain their high initial central density after 100 SNe, we repeat the same runs with 200 and 500 SNe events. The resulting gas and halo density profiles are shown in Figure 3.8. When comparing the higher concentration run for the sphere and the disk (Figure 3.1 (b) and Figure 3.7 (c)) it seems that gas cooling time is more important for retaining gas than the depth of the potential well, as the spherical case results in gas removal from the centre of the dwarf in contrast to the corresponding disk simulations. However, if we consider the spherical and disk models separately, and look at the effect of gas or halo concentration on the ability of a halo to retain gas in the presence of larger numbers of SNe, we see a different behaviour for each initial morphology.

Following the explosion of 500 SNe, the spherical model loses all its gas even in the cases of higher concentrations of either the gas or dark matter. The gas density is reduced to less than $10^4 M_\odot \text{kpc}^{-3}$ in both cases (i.e. below the limits of the plot). After 200 SNe events, the spherical run retains more gas in the higher gas concentration case where the gas particles have shorter cooling times, resulting in the final central density being potentially high enough to host more star formation ($2.4 - 7.4 \times 10^9 M_\odot \text{kpc}^{-3}$ (Pontzen and Governato, 2012; Read *et al.*, 2016b)). This is due to both the binding energy in the inner 60 pc being slightly higher ($1.95 \times 10^{52} \text{erg}$ and $1.39 \times 10^{52} \text{erg}$ for $r_s = 0.05 \text{kpc}$ and $c = 30$ respectively) and the initial central gas density being higher, resulting in shorter gas cooling times allowing for energy to be radiated away.

When the morphology is initially spherical, a change in the gas density has a larger impact on the cooling times than for the corresponding disk models (where the cooling times are already short) and hence changing the gas density in the spherical case results in a significant change to the overall evolution. In this case, a higher initial gas density is

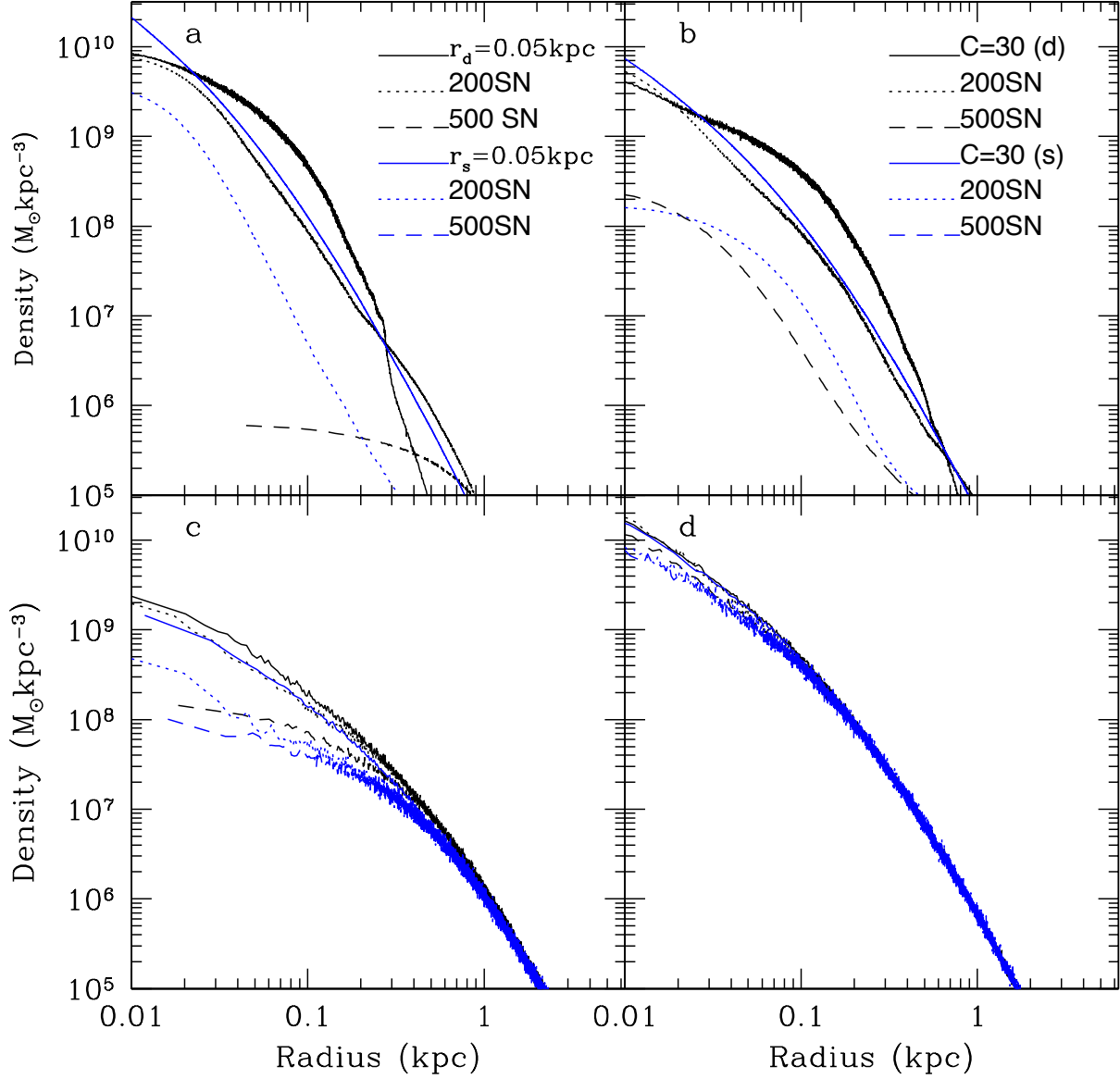


Figure 3.8: Evolution of the gas density (**top**) and halo density (**bottom**) profiles for simulated dSphs with a concentrated gas profile (**left**) and a concentrated halo profile (**right**). In all panels, the solid black and blue curves show the initial profiles for the disk and sphere respectively, and the dotted and dashed lines show the resulting profiles after 1.25 Gyr of evolution for simulations including feedback from 200 and 500 SNe. Note that the gas density curves for the spherical models with 500 SNe (blue dashed curves) fall below the lower limit of the density axis and are therefore omitted for clarity.

more effective at retaining gas than the deeper potential well due to a more concentrated dark matter halo.

For the disk morphology, 200 SNe events have a broadly similar impact to that due to 100 SNe and the central gas densities remain very close to the initial values. However, larger differences are seen after 500 SNe. The $c = 30$ run retains significantly more gas than the $r_s = 0.05 \text{ kpc}$ run after 500 SNe events, with a final central gas density of $10^8 M_\odot \text{ kpc}^{-3}$. Here the depth of the halo potential is keeping the gas bound to the dSph halo. The total binding energy of the gas is roughly the same as the injected SN energy (5.2×10^{52} for $r_s = 0.05 \text{ kpc}$ and 4.66×10^{52} for $c = 30$). In contrast to the spherical case, for the disk the higher halo concentration is more effective at retaining gas, again potentially resulting in a qualitatively different evolutionary path for the dwarf. In the case where the disk and the sphere have the same potential energy, the cooling time of the gas determines whether the dwarf will be able to retain enough gas to continue forming stars (as in the disk model) or if a large fraction of gas will be ejected (as in the spherical model). If the cooling time is long as in the spherical case, making the potential well deeper does not improve the chances of the dwarf retaining gas. However, in models for which the gas cooling time is already shorter than the dynamical time, a deeper potential well increases the fraction of dense gas which is retained.

The time evolution of the fractions of gas particles with velocities greater than that formally required to escape the potential for a selection of disk runs is shown in Figure 3.9. The solid curves show the fraction of gas located within $r < 1 \text{ kpc}$ which has velocities above the escape velocity; the dashed lines show the same for gas at $1 \text{ kpc} < r < 5 \text{ kpc}$. As expected, Figure 3.9(a) shows that as more SN energy is injected, more gas is driven above the escape velocity. In the three simulations with varying numbers of SN events, all the gas remaining within 1 kpc is below the escape velocity by the end of the run and so will stay bound to the dwarf. The fraction of gas at $r > 1 \text{ kpc}$ above the escape velocity declines towards the end of the simulation, but this gas is unlikely to fall back into the central regions due to the infall time required (the average free fall time for gas at $1 < r < 5 \text{ kpc}$ is 1 Gyr). This suggests that although only a small fraction of gas is removed from the main disk, SNe feedback is likely very important for keeping the gas hot and extended, allowing it to be removed easily by other external processes (e.g. ram pressure stripping) when the dSph falls into a host halo at lower redshifts. The same effect is seen in the simulations which vary the other model parameters. Figures 3.9(b) and (d) show results for varying the gas and halo concentration, respectively. In both cases, the fact that the

most concentrated runs give a larger fraction of gas at the escape velocity at larger radii is simply due to the fact there is less gas at these radii. Only the small mass in high velocity gas is able to reach these radii and hence a higher fraction is formally unbound. Again the fraction decreases to a negligible amount over time and this will likely stay bound to the dwarf in the absence of external perturbations.

Figure 3.10 shows the effect on halo density profile evolution of varying (a) the number of SNe events, (b) the gas concentration, (c) the baryon fraction and (d) the halo concentration, for the disk case. Increasing the number of SNe events (and hence the energy injected) decreases the central density of the halo as more gas is pushed out to large radii. This is a small decrease in comparison to the spherical case in which 100 SNe events cause an order of magnitude decrease in the central halo density due to the sudden removal of a large amount of gas. Changing the gas concentration or the baryon fraction has no effect on the density of the halo (panels b and c respectively), due to the small amount of gas removed in comparison to the spherical case.

The Figure clearly shows that the only parameter which has a significant impact on the evolution of the halo density profile of the halo is the initial halo concentration (Figure 3.10 (d)). In the simulation with halo $c = 4$, the total potential inside 60 pc is initially 52 per cent lower than in the $c = 10$ run. In addition, the gas contributes 39 per cent to the total potential inside 60 pc for the $c = 4$ run compared to 32 per cent in the $c = 10$ case. These two effects both serve to increase the impact on the dark matter profile of gas removal. The shallower potential well in the $c = 4$ run allows more gas to escape, which has a proportionately larger effect on the potential well as a whole since the gas contributes a larger fraction of the potential. This is the only run in the disk case for which the final halo density profile is significantly shallower than the initial profile. All other runs with 100 SNe do not remove enough gas to have any major impact on the halo density; while the runs with 200 and 500 SNe (panel (a)) reduce the central density by a factor of a few, the inner profile retains its initial cusp.

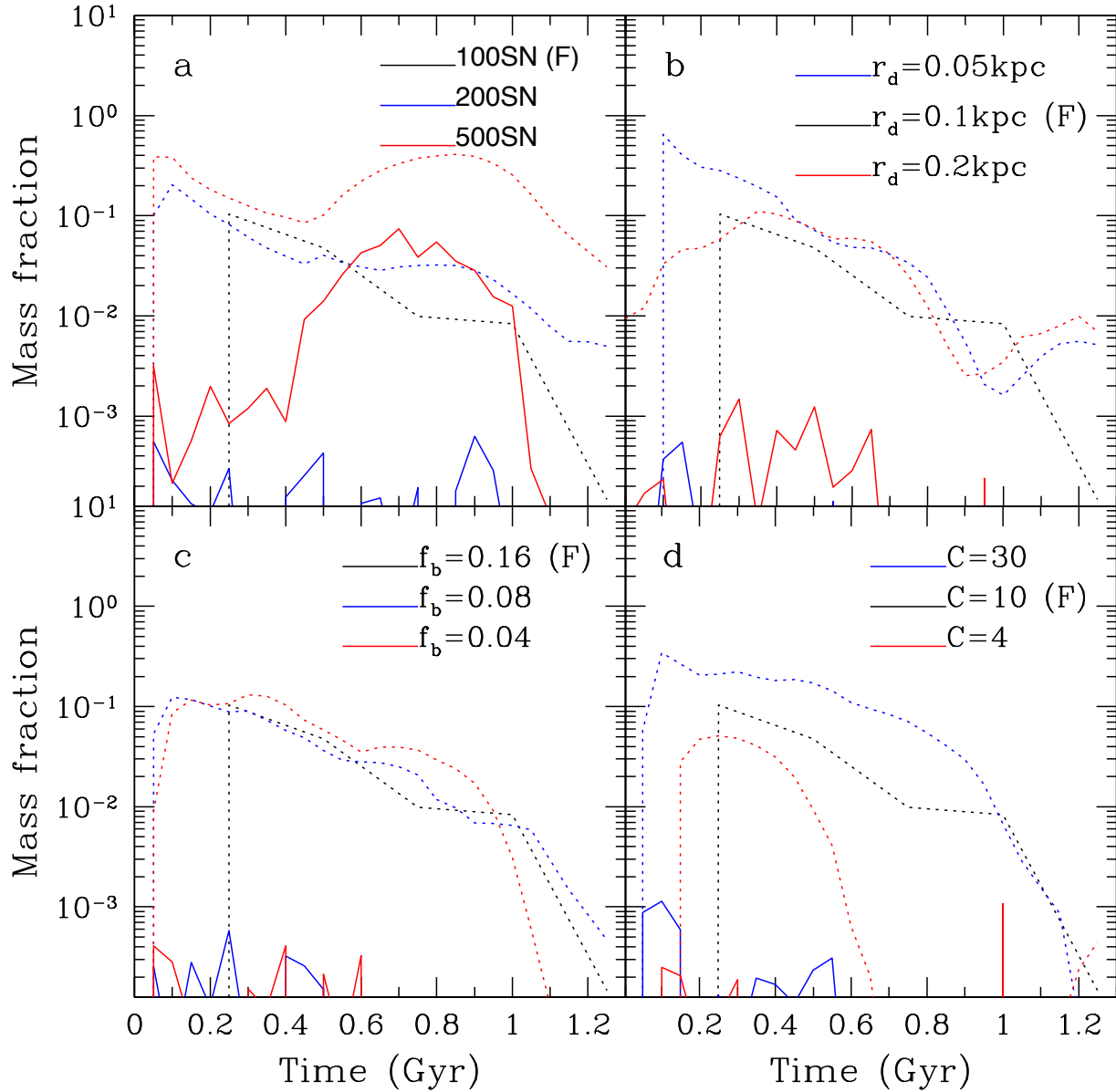


Figure 3.9: The fraction of gas particles with velocities greater than the local escape velocity as a function of time for the simulations in Figures 3.3 and 3.7. Solid curves give the fraction of gas particles above escape velocity at radii $r < 1$ kpc while the dashed curves correspond to gas particles at radii $1 \text{ kpc} < r < 5$ kpc. (F) denotes the fiducial run.

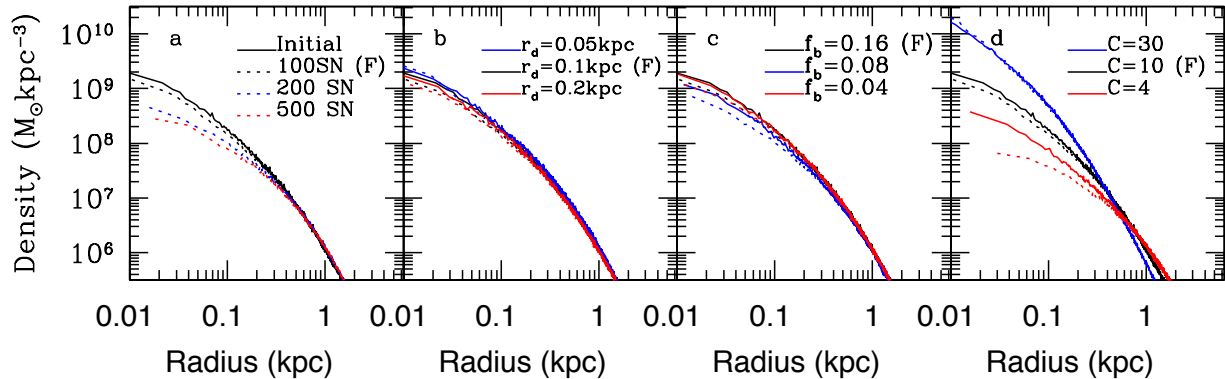


Figure 3.10: Evolution of the dark matter halo density profiles for the simulations presented in Figures 3.3 and 3.7. In all panels, the black curves show the profiles for the fiducial disk model. The red and blue curves in each panel show the effect of varying the model parameters: (a) number of SNe; (b) disk scale length; (c) baryon fraction; (d) halo concentration. Solid curves denote initial profiles, while dashed curves show the outcome of 1.25 Gyr of evolution. (F) denotes the fiducial run.

3.3.3 Metallicity

In our standard runs we assume gas of primordial composition and do not model the effects of metals produced by supernovae. We repeat the standard runs assuming a metallicity for the gas of $[\text{Fe}/\text{H}] = -1.5$ and -2 , using approximate cooling functions based on those described in Sutherland and Dopita (1993) down to 10^4K . Radiative cooling below 10^4K is included as described in Mashchenko *et al.* (2008) from the de-excitation of fine structure and metastable lines of C, N, O, Fe, S and Si. The resulting gas density profiles for the spherical and disk fiducial runs are shown in panels a and b of Figure 3.11, respectively. The initial density profile is the same for all metallicities and is represented by the black solid line, other lines show the profile at 0.4Gyr (dotted), 0.8Gyr (dashed) and 1.2Gyr (dot-dashed). The radial density profile of the primordial run over time is shown as black lines, and as red (blue) lines for $[\text{Fe}/\text{H}] = -2$ (-1.5).

For the spherical case, $[\text{Fe}/\text{H}] = -2$ (red) alters the final density profile by a small fraction, leaving the result unchanged. However, $[\text{Fe}/\text{H}] = -1.5$ (blue) shows a much larger difference, with the central density profile only reduced by less than 2 orders of magnitude, compared to four orders of magnitude for the other two cases. The difference between the runs at earlier times (0.4Gyr) is much smaller as the gas density is still relatively high resulting in short cooling times for all runs regardless of the metallicity. As the density is reduced by the continuing SNe events the role of metallicity becomes more important in determining

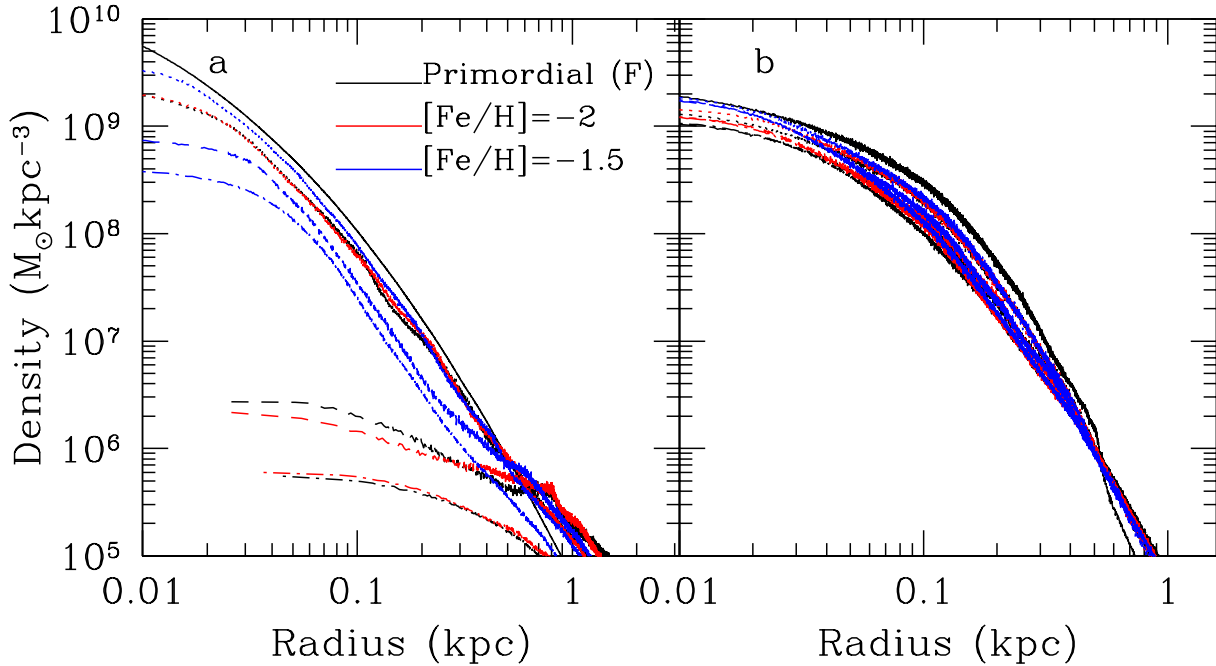


Figure 3.11: Evolution of the gas density for simulated dSphs assuming varying gas metallicities: primordial (our fiducial run, black), $[\text{Fe}/\text{H}]=-2$ (red) and $[\text{Fe}/\text{H}]=-3$ (blue) for a spherical (left) and disk (right) morphology. The different curves represent the initial profile (solid) and the density profile after 0.4Gyr (dotted), 0.8Gyr (dashed) and 1.2Gyr (dot-dashed) of evolution.

the cooling time of the gas. The difference in the resulting density profiles for the disk case is much smaller, as the cooling times in the disk are already shorter than in the spherical case due to there being a larger fraction of gas at higher densities. Even in the highest metallicity run ($[\text{Fe}/\text{H}]=-1.5$, shown in blue) the inclusion of metal cooling has very little effect on the central density, showing that here it is the density that is the most important term in calculating the cooling time.

3.4 Discussion

The simulation results presented in the previous section show that the most likely outcome of star formation in a dark matter halo of mass $3 \times 10^7 M_\odot$ is the total expulsion of most of the remaining gas from the system due to SNa feedback. The precise fraction of gas that remains within 1kpc of the halo at the end of our simulations is a strong function of the gas cooling time in the regions where the SNa explosions occur. The more rapid gas cooling in regions of high gas density has a greater impact on the ability of a halo to

retain gas than either the depth of the potential well or the initial morphology of the gas distribution. However, as our disk models have larger fractions of gas at higher densities than the spherical distributions, all the disk models retain significantly more gas than the corresponding spherical models in our simulations. We also note that for a disk-like gas distribution, the path of least resistance for outflowing gas is one that is perpendicular to the plane of the disk (see, e.g., Brook *et al.*, 2011), allowing more gas to be retained in the plane of the disk, especially in the central regions. In most of the spherical models, gas is easily expelled at all radii including the central regions. The exception to this is for the spherical model with the highest gas concentration ($r_s = 0.05\text{kpc}$) which maintains a high gas density in the centre, although gas is still lost from larger radii.

The importance of cooling time is confirmed by the impact on our results of increasing the initial gas metallicity. A global increase of the initial metallicity to $[\text{Fe}/\text{H}]=-1.5$ significantly enhances the ability of a spherical gas distribution to maintain gas at high density in the inner regions. Even for dSphs with initial gas disks, Figure 3.11(b) shows that increasing the metallicity leads to almost a doubling of the gas density within 20pc at the end of the simulation relative to a simulation assuming primordial abundances.

However, pre-enrichment of the gas to metallicities as high as $[\text{Fe}/\text{H}]\sim-1.5$ in dSph progenitors is not favoured by observations. High-resolution spectroscopic studies of the stellar populations of dSphs like Ursa Minor and Draco show that they were continuously forming stars for ~ 3 Gyr from $z\sim 12$ to $z\sim 1$ (e.g. Weisz *et al.*, 2014c). In particular, the star formation history of Ursa Minor suggests that roughly 10 percent of the stars were formed by $z\sim 10$ while almost forty percent of the stars were in place by $z\sim 4$ (Weisz *et al.*, 2014c, their Figure 1). Detailed modelling of the metallicity distribution function (MDF) of Ursa Minor favours models which include both gas infall (Kirby *et al.*, 2013) and outflows (Ural *et al.*, 2015). Further, the tentative age-metallicity relation for stars in Ursa Minor obtained by Cohen and Huang (2010) suggests that the more metal-rich tail of the metallicity distribution is populated by stars which formed more recently than the main stellar population. The inflow of gas with primordial abundances, with star formation potentially being triggered by mergers with other, similar mass haloes, could therefore explain both the MDF and the age-metallicity relation. Once the halo reached a larger mass it was able to retain enriched gas and form stars with higher $[\text{Fe}/\text{H}]$. A model in which the halo continued to form stars at a low level for sufficient time after growing its potential to give rise to stars with enhanced $[\text{Fe}/\text{H}]$ and reduced α/Fe ratios appears to be consistent with all the observed data. For example, the data in both Ural *et al.* (2015)

and Cohen and Huang (2010) suggest that only the youngest (and most metal-rich) stars in Ursa Minor exhibit reduced α/Fe .

Although a globally raised metallicity is unlikely to be the origin of the short gas cooling times required to facilitate gas retention, the higher gas densities typical in flattened morphologies remain a plausible explanation. If the gas initially has a spherical distribution, we have shown that either the dark matter must be more concentrated than is expected for typical haloes of this mass at $z \sim 10$ (Correa *et al.*, 2015), or gas cooling must have generated a gas distribution with a scale-length roughly an order of magnitude smaller than that of the dark matter, implying significantly stronger collapse than is seen in typical haloes at this mass scale (e.g. Read *et al.*, 2016b). Even in this case, the star formation would be limited to the central regions of the halo (i.e. within a few tens of pc), and a subsequent evolutionary process would be required to disperse these stars over a larger fraction of the halo. The high stellar and dark matter densities in the inner regions would mean that externally-driven processes such as the tidal sculpting usually invoked to change the morphology of dSph stellar distributions would have little effect (e.g. Read *et al.*, 2006b; Peñarrubia *et al.*, 2010). Similarly, mergers with haloes of comparable or larger masses (and hence of lower density) would be unable to inflate the spatial scale of the stellar distribution by an order of magnitude and would be more likely to result in the formation of a nucleated dwarf galaxy (e.g. Bekki, 2015; Assmann *et al.*, 2013).

Obviously, the presence of dense gas with short cooling times is a pre-requisite for further star formation. Given that only a small fraction of the stars in the less luminous dSphs (e.g. Ursa Minor, Draco and Sextans) have metallicities as high as $[\text{Fe}/\text{H}] = -1.5$ at the present epoch (Kirby *et al.*, 2013), we infer that the primary determinant of whether a dSph will exhibit extended star formation is the overall fraction of gas which is at high density when the first stars form. Although this gas may not yet have formed stars, it is only this gas which will be retained by the dSph. In other words, it is not sufficient for cooling in a dSph progenitor to achieve a high gas density solely at the centre of the halo - it must have high density gas distributed throughout the volume which will ultimately be occupied by the stellar population of the dSph. Given that a disk morphology is likely to have a larger fraction of high density gas, in particular outside the central few tens of parsecs, our simulations are consistent with the idea that the progenitors of the Milky Way dSph satellites experienced the bulk of their star formation at an epoch when their baryonic components had a disk morphology. The transformation of rotation-supported disks into pressure-supported spheroids through the action of external gravitational tides

has already been discussed by a number of authors in the literature (Mayer *et al.*, 2001b,a; Klimontowski *et al.*, 2009; Lokas *et al.*, 2012; Tomozeiu *et al.*, 2016). Nayakshin and Wilkinson (2013) have discussed the role that AGN outflows from the Milky Way could have played in that process.

In our fiducial, spherical model the gas is spread out over a sphere of radius ~ 20 kpc by the end of the 1.25 Gyr simulation. The gas at large radii (> 5 kpc) is at low enough densities to be stripped on infall to the MW and would become a part of the hot halo which is likely to have a density of few $\times 10^2 M_{\odot} \text{ kpc}^{-3}$ at a radius of 100 kpc from the Galactic Centre (Mayer *et al.*, 2006a). The gas at radii $1 \text{ kpc} < r < 5 \text{ kpc}$ could possibly fall back, although at the end of our simulations its low density means that its cooling time is very long. Observational determinations of the star formation histories of dSphs are not yet sufficiently precise to distinguish continuous star formation from bursty star formation punctuated by periods of ~ 100 Myr during which gas which remained in the halo could potentially cool and re-ignite star formation (see e.g. Weisz *et al.*, 2014c). However, if our simulated dwarf is a progenitor for a dSph like Draco or Ursa Minor we expect further star formation and outflows, which would tend to suppress the cooling and infall of the gas at these radii and we therefore need to consider further sources of low-metallicity gas.

In all our simulations, the gas distributions were initially smooth although the injection of SNe energy rapidly leads to a highly structured ISM. In a future work, we will investigate the impact of an initially clumpy ISM, such as might be produced by stellar winds prior to the onset of SNe feedback (Bourne and Power, 2016). Dense gas clumps are more resilient to feedback (Bourne and Power, 2016) and could therefore increase the amount of gas retained by the halo. In the context of AGN feedback impacting on the gas at the centre of a galaxy, Bourne *et al.* (2014) has shown that significantly more gas remains after the passage of an AGN outflow through a non-uniformly distributed ISM compared to a smooth distribution. It is therefore reasonable to expect that similar behaviour may be seen in the context of a dSph progenitor.

In this chapter, we evolved our dSph progenitors in isolation. As a result, we have neglected a number of external effects in our simulations which could potentially impact on our conclusions, namely gas accretion and reionization. The more important of these at this redshift is likely to be gas accretion. Kirby *et al.* (2013) find that a gas accretion model is a good fit to the narrow metallicity distribution functions for Ursa Minor and Draco (and, indeed, most other dSphs). Those authors find that it is unlikely that the stars which formed later in these dwarfs were composed of gas enriched by the first SNe,

but rather they formed from more pristine gas subsequently accreted onto the halo. In this case retention of the gas initially present in the dSph may not be required for further star formation. If additional gas is continually accreted by the halo as star formation proceeds, then the requirement is actually that the outflows generated by the on-going star formation are unable to prevent the accretion and cooling of this gas. Simulations by Latif and Volonteri (2015) have shown that this infall may have been filamentary: the low filling factor of these filaments would naturally increase the likelihood of gas being able to reach the central few 100 pc of the halo even in the presence of a SN-driven outflow from the dSph. Indeed Kimm *et al.* (2015) find that SN-driven outflows have very little influence (irrespective of the strength) on the rate of inflowing gas, showing that cold filamentary accretion at high redshift allows for the deposition of low-angular momentum gas in the central regions, enhancing the gas density.

Given that our simulations cover the period from of $z \sim 10$ to $z \sim 4$, it is likely that the reionization of the Universe took place during this time (reionization began between $z \sim 10$ -15 and was complete by $z \sim 6$; see e.g. Planck Collaboration *et al.*, 2016c, and references therein). It has been suggested that this could have contributed to the quenching of star formation in low mass halos (Sawala *et al.*, 2016b). Observationally, however, Ursa minor and Draco show evidence for extended star formation during this time period and beyond and no local group dSph exhibits a feature in its star formation history which is unambiguously associated with reionisation (Weisz *et al.*, 2014c). While this suggests that it is unlikely that reionization was responsible for the cessation of star formation (though see Sawala *et al.*, 2010, for a discussion of possible self-shielding of gas in dSphs during reionization), it could have played a role in limiting the supply of cold gas from accretion. In this way, it could possibly account for differences between the dSphs and the ultra faint dwarfs: those haloes whose star formation was truncated by reionization became the ultra faints, while those that survived reionization and continued their forming stars until their supply of gas was exhausted became “classical” dSphs.

In agreement with previous work (e.g. Governato *et al.*, 2010; Read and Gilmore, 2005; Navarro *et al.*, 1996a) we find that it is possible to form dark matter cores providing halo concentrations are lower at high redshift, and enough gas is ejected from the central regions. For the removal of gas to have an effect on the halo the gas in the centre must make a significant contribution to the potential and/or a significant amount of mass must be removed at once. However, as noted by Peñarrubia *et al.* (2010), if a core is formed early in the evolution a dSph satellite, it is questionable whether it could subsequently

survive to the present day without being tidally disrupted by the Milky Way.

Independent of our other model parameters, we find that the SN rate in our simulations must be below 0.5 Myr^{-1} to allow dense gas to remain in the dwarf at the end of the simulation. As discussed in section 3.2, the stellar mass of the present-day Ursa Minor would imply a rate of at least twice this (assuming a constant star formation rate). There are several possible explanations for this. First, we have assumed that all the star formation occurred in a single halo - it is possible that some of the low-metallicity stars in Ursa Minor formed in a separate halo which later merged with the main halo. Given that the halo mass has increased by at least an order of magnitude since $z \sim 10$, it is possible that at least one other halo that contributed to the dark matter content of this dSph also contained stars and therefore each individual halo could have hosted a smaller number of SNe. Secondly, we note that the star formation history for Ursa Minor presented in Weisz *et al.* (2014c) implies that approximately 10 per cent of the stars in Ursa Minor were in place by $z \sim 10$. This would correspond to a stellar mass of $1 - 2 \times 10^4 M_{\odot}$ which would result in 100-200 SNa explosions, comparable to the numbers in those of our simulations which resulted in gas retention. Thirdly, in estimating the expected numbers of SNe we have assumed a Salpeter (1955) initial mass function for the stellar population. While the stellar mass function for low-mass stars in Ursa Minor has been shown to be identical to that of the globular clusters M15 and M92 (Wyse *et al.*, 2002), the high-mass end of the mass function in an old stellar population can only be inferred indirectly from chemical signatures. Thus, it is possible that the high-mass stellar IMF in high-redshift dSphs was significantly different from that seen in star-forming regions at $z \sim 0$.

3.5 Conclusions

In this chapter, we addressed the issue of whether a typical $z = 10$ dSph progenitor could maintain an extended burst of star formation having initially acquired a gas fraction comparable to the universal baryon fraction. In contrast to many previous studies, our $z = 10$ haloes had masses of $3 \times 10^7 M_{\odot}$, appropriate for the $z = 10$ progenitors of haloes with masses of $\sim 10^9 M_{\odot}$ at $z = 0$. We included the energy injected by SN explosions, and followed the evolution of the gas distributions for 1.25Gyr. Our primary conclusion is that gas retention by haloes of this mass is very challenging and requires halo concentrations or initial gas distributions which are atypical of haloes at $z = 10$.

We varied several parameters to create our model dwarf galaxies including the mor-

phology of the initial gas distribution, the number of SNe, the gas concentration, the baryon fraction and the halo concentration. We find that the cooling time of the gas in the central regions is the most important factor to retain sufficiently high central densities to allow star formation to continue. For both spherical and disk gas morphologies increasing the gas concentration increases the central density, resulting in the gas having shorter cooling times which reduces the impact of the SNe feedback on the ISM. A flattened gas distribution (disk) is overall more efficient at retaining gas than a spherical distribution due to the fact that the gas densities are generally higher initially. However, even with a high gas or halo concentration, we find that high density gas only remains at the end of the simulation period if the number of SNe events is lower than that expected from a Salpeter IMF (assuming a total stellar mass of $\sim 3 \times 10^5 M_\odot$).

Our finding that the haloes of dSph progenitors at $z = 10$ were not typical of haloes at that redshift, combined with the data on the metallicity distributions of observed Milky Way dSph satellites, suggests that the morphology of infalling gas may be a key factor which determines the ability of a given halo to support extended star formation. Successful dSphs may therefore result from progenitors which were outliers in the distribution of halo/gas properties at $z = 10$, as well as experiencing gas accretion at an appropriate rate and with an appropriate morphology so that SN-driven outflows were unable to prevent further gas accretion. This would naturally explain the apparently non-linear mapping required for the abundance matching of haloes from cosmological simulations with observed galaxies, which gives rise to the “Too Big To Fail” problem and the apparent stochasticity of galaxy formation at the faint end of the galaxy luminosity function.

In future work, we will investigate the extent to which a clumpy initial gas distribution might affect the ability of a dSph to retain gas following an initial burst of star formation. We will also explore the impact of external AGN outflows on the evolutionary history of the dSphs as discussed in Nayakshin and Wilkinson (2013).

Chapter 4

Do AGN outflows trigger or suppress star formation in dSph progenitors?

4.1 Introduction

The dwarf spheroidal (dSph) satellites of the Milky Way represent valuable examples of the end-products of galaxy formation in low-mass haloes. Their proximity means that spectroscopic surveys have provided large data sets of their internal stellar kinematics and chemical evolution (Tolstoy *et al.*, 2006; Simon and Geha, 2007; Martin *et al.*, 2007; Walker *et al.*, 2009d,b). The development of a detailed understanding of their evolutionary histories, including both internal and external factors, is essential as input to a complete picture of galaxy formation and evolution.

In the previous chapter(3), we used high resolution hydrodynamical simulations to show that the likely $z \sim 10$ progenitors of dSphs have difficulty in retaining the high density gas needed to sustain extended star formation. In this chapter, we extend this work to explore whether an AGN outflow from the supermassive black hole (SMBH) at the centre of the Milky Way could have triggered star formation in a dSph. Our initial goal is to assess the analytical calculations of Nayakshin and Wilkinson (2013) and explore the conditions under which AGN outflows can enhance or inhibit star formation in high- z dSph progenitors.

It is now generally thought that the majority of galaxies host a SMBH at their centre. The energy released as feedback resulting from the growth of the SMBH via gas accretion has a strong influence not only on the host galaxy, but also on the extragalactic medium (Gitti *et al.*, 2007; McNamara and Nulsen, 2007). AGN drive fast outflows into

the IGM at near-relativistic speeds $v \sim 0.03 - 0.3c$ (Chartas *et al.*, 2002; Reeves *et al.*, 2003; Pounds *et al.*, 2003; Cappi, 2006; Gofford *et al.*, 2013) and are capable of driving the gas out to several kpc (Rupke and Veilleux, 2011; Sturm *et al.*, 2011; Cicone *et al.*, 2014). Observations of outflows on larger scales are lacking (see, e.g. Spence *et al.*, 2016). However, analytical arguments suggest that when the SMBH is above a critical mass, an outflow should be able to drive gas out of the galaxy completely into the IGM (King, 2005; McQuillin and McLaughlin, 2012). It has been suggested that the reason outflows are not observed at these scales is that to observe both the SMBH in its active phase and the outflowing gas simultaneously, the gas must be at radii $< 10\text{kpc}$, which is consistent with the observations. In the time taken for an outflow to reach distances larger than 10kpc , the active phase of the AGN will usually have ceased (Zubovas and King, 2016).

AGN have been observed as far back as $z \sim 6-7$ (see, e.g. Fan *et al.*, 2001; Kurk *et al.*, 2007). While the SMBH at the centre of the MW is currently dim compared to others, its mass is comparable to those observed to be active in other galaxies. There is evidence that the SMBH at the centre of the MW has been active relatively recently ($\sim 6\text{Myr}$) (Zubovas *et al.*, 2011; Zubovas and Nayakshin, 2012) when it experienced a short ($\sim 1\text{Myr}$) outburst after a suspected accretion event which coincided with a star burst in the galactic centre. We expand on the proposal by Nayakshin and Wilkinson (2013) that if the SMBH in the MW was able to drive outflows to distances comparable to that of the radius of the orbits of some of the dSphs, the ram pressure could have a significant affect on their properties and star formation histories.

Simulations have shown that ram pressure stripping by the hot, gaseous halo is able to remove significant amounts of gas from dSphs, despite the relatively low density (see e.g. Marcolini *et al.*, 2003; Mayer *et al.*, 2006b, 2007; Nichols and Bland-Hawthorn, 2011). However, it is unlikely this was responsible for the complete removal of the gas, as the very dense gas in the central regions is much more difficult to remove. It is therefore plausible that during the phase when the SMBH activity was intense, ram pressure stripping by outflowing gas could have been significant for two reasons; the density of the gas in the outflow could be much higher than that of the present day gaseous halo, and the outflow velocity is likely to be larger than the relative velocity of the hot static halo and the dSph it interacts with. Ram pressure stripping is proportional to the ram pressure of the ambient gas, $P_{ram} \propto \rho_{shell} V_{shell}^2$, where ρ is the density of the gas in the outflow and V_{shell} is the velocity of the outflow. Therefore the ability of the outflow to remove gas from the dSphs may be significant ((see Table 1 in Nayakshin and Wilkinson, 2013)).

The Local Group dSphs have a very diverse range of properties due to their very different SFHs (Tolstoy *et al.*, 2009), despite residing in haloes of roughly the same mass. It is questionable whether the local group dSphs have all followed the same evolutionary path due to their diverse range of properties. It seems external processes have influenced their evolution and taken a role in both beginning and ending their periods of star formation. The dSphs are such low mass systems that they are susceptible to these influences and are relatively easy to disrupt.

The Carina and Ursa Minor dSphs are an interesting pair of targets to compare our models to as they have qualitatively different star formation histories despite having similar stellar masses. Ursa Minor hosts a predominantly old stellar population, with star formation ceasing 10Gyr ago (see, e.g. Ural *et al.*, 2015), while Carina hosts populations of old, intermediate age and young stars. Carina is one of the few dSphs showing an episodic SFH, with distinct periods of no star formation activity between these episodes, making it an important object for understanding the evolution of galaxies.

A number of authors have investigated whether the episodic bursts of SF in Carina were possibly triggered by perigalacticon passages and passages through the MW disk (see, e.g. Pasetto *et al.*, 2011). However, when estimating the orbital history of Carina this seems unlikely as there is no correlation between the starburst and the times of the passages (Piatek *et al.*, 2003).

In this chapter, we explore the link between AGN outflows and star formation in dSphs and whether this could explain the differences in their star formation histories, depending on whether or not the outflow triggers or suppresses star formation in a dSph progenitor. We use numerical hydrodynamical simulations to test the conclusions of Nayakshin and Wilkinson (2013) and explore the conditions under which AGN outflows can enhance or inhibit star formation in high-z dSph progenitors. The structure of this chapter is as follows: section 4.2 describes the models used to represent an AGN outflow and section 4.3 describes the simulations and the set up of the initial conditions. Section 4.4 presents the results of our simulations, which we discuss in section 4.5. Finally, our conclusions are outlined in section 4.6.

4.2 Models

Zubovas and King (2012) provide a detailed description of the internal structure of an AGN outflow once it has reached the energy-driven phase of its evolution (see their Fig. 1).

Following Nayakshin and Wilkinson (2013), we represent the AGN outflow by a constant density shell of material whose density depends on the shell thickness. Zubovas and King (2012) find that for a specific heat capacity ratio $\gamma = 5/3$ (i.e. an ideal gas), the shell thickness is given by $\Delta R = R_{\text{cd}}/3$, where

$$\Delta R = R_{\text{out}} - R_{\text{cd}} \quad (4.1)$$

R_{out} is the radius of the outer shock front, and R_{cd} is the radius of the contact discontinuity between the shocked wind material and the shocked ISM material. Equivalently, $\Delta R = R_{\text{out}}/4$ - this is more useful as we can assume that initially $R_{\text{out}} \sim R_{\text{d}}$, the distance of the dSph from the centre of the Galaxy. The simulations of Zubovas and King (2012) confirm that the assumption of a constant density within the shell is reasonable to first order. Similarly, given that the density contrast between the material within the shell and the material between the inner wind shock R_{w} and R_{cd} is about a factor of \mathbf{X} , we neglect the material interior to R_{cd} and consider only the impact of the passage of the shell of shocked ISM gas.

The shell is assumed to pass the dSph with velocity V_{sh} . This means that the time taken for the shell to cross a dSph of radius $r_{\text{dwarf}} \ll R_{\text{d}}/4$ is

$$t_{\text{sh}} \sim 25 \left(\frac{R_{\text{d}}}{100 \text{ kpc}} \right) \left(\frac{1000 \text{ km s}^{-1}}{V_{\text{sh}}} \right) \text{ Myr} \quad (4.2)$$

In setting our initial conditions we make the following assumptions:

1. Velocity of outflow: this is determined by where on its orbit the dSph encounters the outflowing shell. King *et al.* (2011) find that in an isothermal halo, the velocity of the shock pattern rapidly (within 1Myr) reaches a constant value which it retains until the AGN turns off. After that time, the velocity declines. The velocity depends on the mass of the host bulge. However, for non-isothermal models, McQuillin and McLaughlin (2013) found that the shock pattern could accelerate at large radii. For the Milky Way, with a bulge dispersion of $\sim 100 \text{ km s}^{-1}$, this velocity would be $\sim 500 \text{ km s}^{-1}$ (their equation 13 with $f_{\text{c}} = f_{\text{g}}$). Thus velocities of 500 km s^{-1} and 1000 km s^{-1} should bracket plausible range.
2. Mass of outflow: We assume a fixed outflow mass of $M_{\text{sh}} = 5 \times 10^{10} M_{\odot}$. Nayakshin and Wilkinson (2013) also use a shell whose mass increases as it expands into the halo, assuming the gas follows an "NFW" profile. For the distances we are interested

in (50-100kpc), the mass of the outflow is $\sim 5 \times 10^{10} M_{\odot}$ as it increases by a negligible amount, hence using a fixed value.

3. Thickness of shell: given that the thickness is $R_{\text{out}}/4$, we need to consider likely locations of dSphs at the time of encounter based on the table in Nayakshin and Wilkinson (2013) - according to their Table 2, Carina and Ursa Minor are susceptible even when placed at the largest apocentre distances consistent with the observations. Therefore, based on estimates in their Table 1 (taken from Lux *et al.*, 2010), we will assume that $R_d = 100$ kpc, although we may also consider $R_d = 50$ kpc. Note that since the time for the shell to cross the dSph is 25-50 Myr, the dSph will not move significantly in its orbit during this time. This shell thickness gives a shell density of

$$\rho_{\text{sh}} = 3 \times 10^{-2} \left(\frac{100 \text{ kpc}}{R_d} \right)^3 \left(\frac{M_{\text{sh}}}{5 \times 10^{10} M_{\odot}} \right) \text{ cm}^{-3} \quad (4.3)$$

4. Temperature of gas in shell: Assuming an initial radius of 3 kpc, at which the energy driven flow begins (a factor 3 larger than the 1 kpc assumed in Zubovas and King (2012) because we are assuming a shell mass which is relatively large at $5 \times 10^{10} M_{\odot}$), an initial temperature of 5×10^7 K and an adiabatic expansion (i.e. $TV^{\gamma-1} = \text{constant}$) with no mass growth, yields a temperature of 10^4 K when the shell has expanded to $R_{\text{out}} = 100$ kpc. An alternative calculation using the ideal gas law for the material in the shell, assuming a uniform mass density within the shell, and assuming that the ISM into which the shell expands is the hot halo of the Milky Way with $n_{\text{H}} \leq 10^{-5} \text{ cm}^{-3}$ at a distance of 100 kpc (Mayer *et al.*, 2006b), yields a temperature of:

$$T_{\text{sh}} = 3 \times 10^4 \left(\frac{\rho_{\text{ISM}}}{250 M_{\odot} \text{ kpc}^{-3}} \right) \left(\frac{V_{\text{sh}}}{1000 \text{ km s}^{-1}} \right)^2 \left(\frac{R_d}{100 \text{ kpc}} \right)^3 \left(\frac{5 \times 10^{10} M_{\odot}}{M_{\text{sh}}} \right) \text{ K}. \quad (4.4)$$

5. Angle of incidence: We simulate two different orientations of the dwarf, face on and edge on to the outflow.
6. *The gas in the shell is assumed to behave as an ideal gas with $\gamma = 5/3$.*
7. Gas morphology in dSph: a spherical gas distribution is too easily disrupted, therefore we only consider only disk models, similar to those in chapter 3.

8. $\Delta R = R_d/4$ was derived for the case of an isothermal halo in Zubovas and King (2012). However, since it depends only on assumption of a strong shock it is essentially independent of the potential.
9. Metallicity of gas in outflow and in dSph: we assume $Z = 10^{-3} Z_\odot$.

It is interesting to note that clumps can be moved out of the disk onto halo orbits by the passage of the shock front. Once star formation has been triggered, the clumps will decouple from the ram pressure of the shock front and the resulting stars will remain within the dSph. We need to estimate the density threshold for clump disruption below which it would be entrained by the flow and the material would be lost from the dSph.

4.3 Simulations

4.3.1 Initial Conditions

Dwarf galaxy

We simulate a live dark matter halo which follows a Hernquist density profile (Hernquist, 1990)

$$\rho(r) = \frac{M_{200}}{2\pi} \frac{a_h}{r(r + a_h)^3} \quad (4.5)$$

where a_h is a scale radius defined by the concentration parameter from an NFW profile (Navarro *et al.*, 1996b), assuming the two profiles contain the same mass within r_{200} . We used the codes `mkgalaxy` and `mkhalo` (McMillan and Dehnen, 2007) within the NEMO environment (Teuben, 1995) to calculate the initial positions and velocities for the halo particles, taking into account the potential of both the gas and stellar components. In all simulations $M_{200} = 3 \times 10^7 M_\odot$ and $c = 10$, which is a reasonable value for halos at $z \sim 10$ (Klypin *et al.*, 2011). These values imply an NFW scale length of 0.3 kpc and Hernquist parameters of $a_h = 0.5$ kpc and $r_{200} = 3$ kpc. The dark matter is represented with particles of mass $100 M_\odot$ and gravitation softening 2 pc, resulting in 3×10^5 particles in total.

The gas disc was created using the code 'DiscGO' which creates equilibrium disc galaxies (Newton and Kay, 2013). Both gas and stellar components have the same scale length (r_d) and follow an exponential surface density profile:

$$\Sigma_g(R) = \frac{M_g}{2\pi r_d^2} e^{-R/r_d} \quad (4.6)$$

Two different gas scale lengths are used in the simulations presented in this chapter, $r_d=300\text{pc}$ and $r_d=400\text{pc}$. The gas is assumed to have an ideal equations of state and is assumed to be in hydrostatic equilibrium which determines the scale height of the gas disk. The total gas and stellar masses are $4.8 \times 10^6 M_\odot$ and $10^4 M_\odot$ respectively, giving particle masses of $10 M_\odot$ for both the gas and stars. Having generated our initial conditions, we evolve them for 300 Myr excluding cooling and star formation, to allow the components to settle fully into equilibrium.

Outflow

The gas particles representing the outflow are cut from a relaxed glass-like configuration, and adjusted to give a constant density of $2.064 \times 10^4 M_\odot \text{kpc}^{-3}$ corresponding to a total shell mass of $5 \times 10^{10} M_\odot$ and a shell thickness of 25 kpc as discussed in section ???. We only simulate the part of the shell of outflowing gas that will interact with the dwarf, with dimensions $25 \times 10 \times 10 \text{kpc}$. This section of outflow has a mass of $5.12 \times 10^7 M_\odot$, represented by 5.12×10^6 particles, each with a mass of $10 M_\odot$. The particles are given an x-component velocity which is varied in each run, and an internal energy corresponding to a temperature of 10^4K as discussed in section ???. This describes the properties of the outflow at a distance of 100 kpc from the centre of the host galaxy. We also simulate the outflow at a distance of 50 kpc, where the density is higher which results in a higher ram pressure. The mass and temperature are fixed and the density and shell thickness are $1.65 \times 10^5 M_\odot \text{kpc}^{-3}$ and 12.5 kpc, respectively.

Background (gaseous halo)

Our main motivation for including a low density background is to avoid the code crashing due to problems finding SPH neighbours on the edge of the constant gas distribution for the outflow. However as there is a gaseous halo present in the Milky Way this is not an unrealistic addition. As for the outflow, the gas particles representing the background are cut from a relaxed, glass-like configuration, and adjusted to give a density of $21.6 M_\odot \text{kpc}^{-3}$. The total mass is $4.3 \times 10^5 M_\odot$ and the temperature is the same as that for the outflow, 10^4K .

4.3.2 Simulation Code

All our simulations are performed using a modified version of the N-body plus hydrodynamics code GADGET-2 (Springel, 2005), including prescriptions for radiative cooling, star formation and thermal stellar feedback. We use the SPHS formalism (Read *et al.*, 2010; Read and Hayfield, 2012) to properly resolve mixing of the multiphase gas. The smoothing kernel is a second order Wendland kernel with 100 neighbours to allow for the larger neighbour number required with SPHS while suppressing the pairing instability (Wendland, 1995; Dehnen and Aly, 2012). The gas smoothing and softening lengths are both adaptive, with a minimum value of 0.4 pc in the densest regions, and the dark matter particle softening length has a constant value of 2pc. These simulations use a particle mass of $10M_{\odot}$ for gas and star particles, and $100M_{\odot}$ for the dark matter particles.

Radiative cooling of the gas is included using approximate cooling functions based on those described in Katz *et al.* (1996) down to 10^4 K. Cooling below 10^4 K is modelled as described in Mashchenko *et al.* (2008) via the fine structure and metastable lines of heavy elements down to 20K. Throughout this chapter we assume a metallicity of $[\text{Fe}/\text{H}]=-3$.

We model star formation using a density threshold:

$$\rho_{crit} = \rho_{thresh} + \rho_J \quad (4.7)$$

Where ρ_{thresh} is $5.01 \times 10^{-22} \text{gcm}^{-3}$, equivalent to 300atomcm^{-3} . This ensures that stars form only in regions that are dense enough to be molecular gas. ρ_J is the local Jeans density, given by

$$\rho_J = \left(\frac{\pi k_B T}{\mu m_p G} \right)^3 (n_{ngb} m_{sph})^{-2} \quad (4.8)$$

where $n_{ngb}=100$, is the number of neighbours of a gas particle and m_{sph} is the SPH particle mass. This further ensures only gas unstable to gravitational collapse is converted into stars. Particles that fulfill this criterion are then turned into star particles with a probability $P = 1 - \exp(-0.1\delta t/t_{ff})$, where δt is the current timestep of the particle and t_{ff} is the local free-fall time. Due to our high mass resolution we model the formation of single stars, however as we are only interested in the possible triggering of star formation we do not model any other details, and form stars of a constant mass.

Stellar feedback is modelled by injecting thermal energy into the nearest 100 SPH neighbours, kernel weighted depending on their distance to the star particle. In these simulations we use a probability of a star particle going exploding as a SN of 0.2 percent,

assuming the total mass of stars that form over an extended period to be that of the Ursa Minor and Draco dSphs, $\sim 3 \times 10^5 M_\odot$.

4.4 Results

Gunn and Gott (1972) approximate the stripping radius for an axisymmetric disk system, outside of which gas is removed as the radius where the restoring force per unit area $\sim 2\pi G \Sigma_g \Sigma_{dg}$ is equal to the ram pressure of the shell $P_{ram} = \rho_{sh} v_{sh}^2$. Σ_g is the surface density of the gas and Σ_{dg} is the total surface density (including stars and dark matter), and ρ_{sh} , v_{sh} are the density and velocity of the outflow respectively. Thus gas will be stripped at radii where:

$$P_{ram} \geq 2\pi G \Sigma(r)_g \Sigma(r)_{dg} \quad (4.9)$$

Figure 4.1 compares the restoring force of the gas in the dwarf orientated edge-on (solid lines) and face-on (dashed lines) to the outflow, and the pressure of the gas disk (dot-dashed lines) in our model dwarfs with $r_s=300\text{pc}$ (black lines) and $r_s=400\text{pc}$ (blue lines). The values for the ram pressure of the outflow are plotted as horizontal lines for outflow velocities of 250 km s^{-1} (green line), 500 km s^{-1} (orange line) and 1000 km s^{-1} (red line) assuming a distance of 100 kpc from the host galaxy. For our model dwarfs we expect all gas outside of the stripping radius, where the restoring force drops below the ram pressure of the shell, to be removed by the passage of the outflow. Figure 4.2 compares the restoring forces and gas pressures for the same disks, to the ram pressures from an outflow at a distance of 50 kpc from the host galaxy for outflow velocities of 500 km s^{-1} (red line) and 1000 km s^{-1} (green line).

Nayakshin and Wilkinson (2013) suggest that the outflow is capable of compressing gas in the dwarf and inducing star formation in regions where the internal gas pressure in the dwarf is lower than the ram pressure of the outflow $P_{shell} > P_{disk}$. Gas that fulfils this criterion and is at radii smaller than the stripping radius defined above, could be compressed, allowing it to reach the densities required for star formation, rather than being expelled from the galaxy. We keep these two requirements for gas removal and star formation in mind and refer to these figures as we describe the results of our simulations.

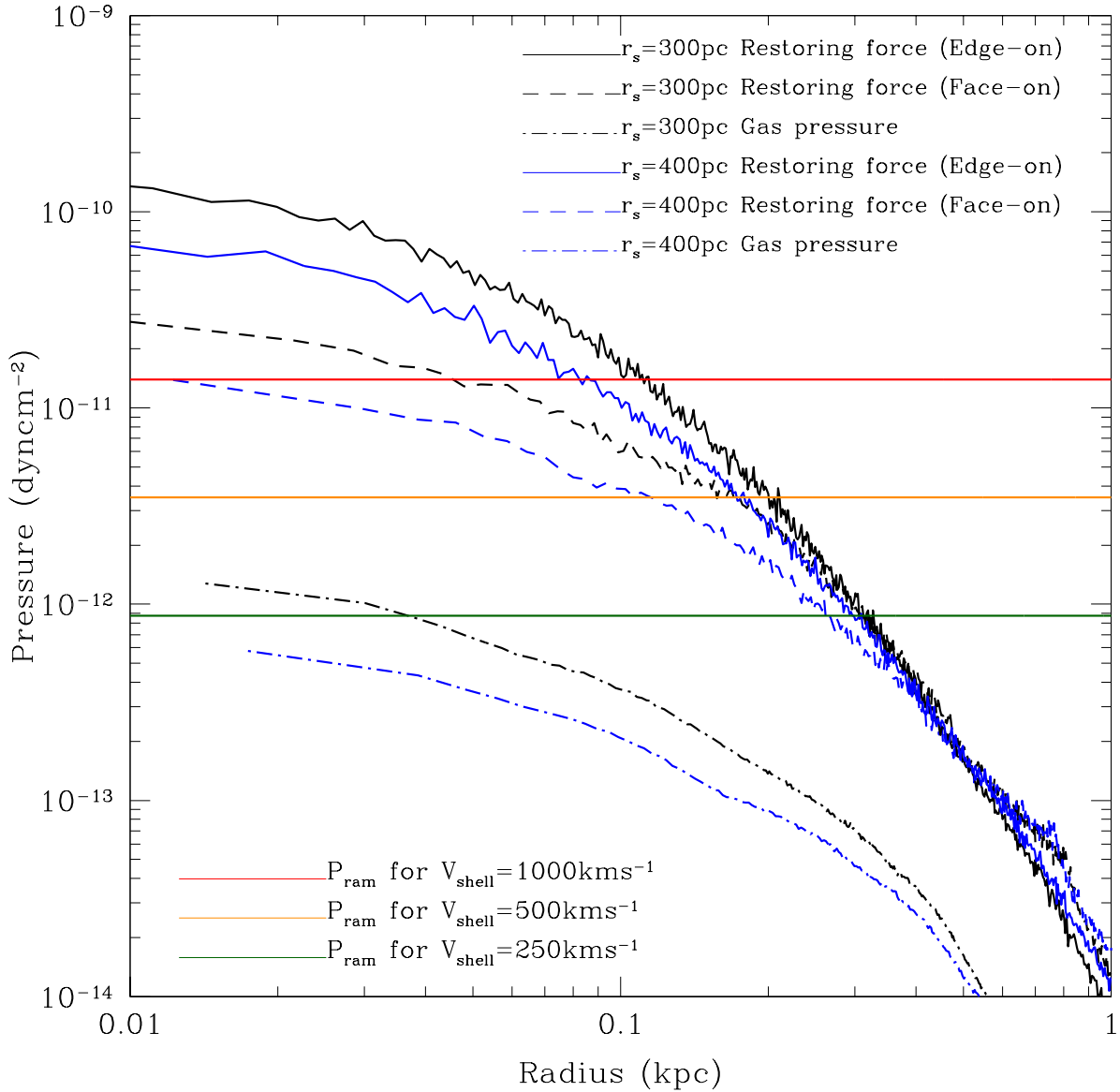


Figure 4.1: Restoring force for the disk orientated edge-on (solid curves) and face-on (dashed curves) to the outflow, and the gas pressure in the disk (dot-dashed curves) as a function of radius for disks with scale radii of 300pc and 400pc (black and blue lines respectively). The ram pressure due to the outflow is plotted for the outflow velocities of 250kms⁻¹ (green horizontal line), 500kms⁻¹ (orange horizontal line) and 1000kms⁻¹ (red horizontal line) positioned at 100kpc from the host galaxy.

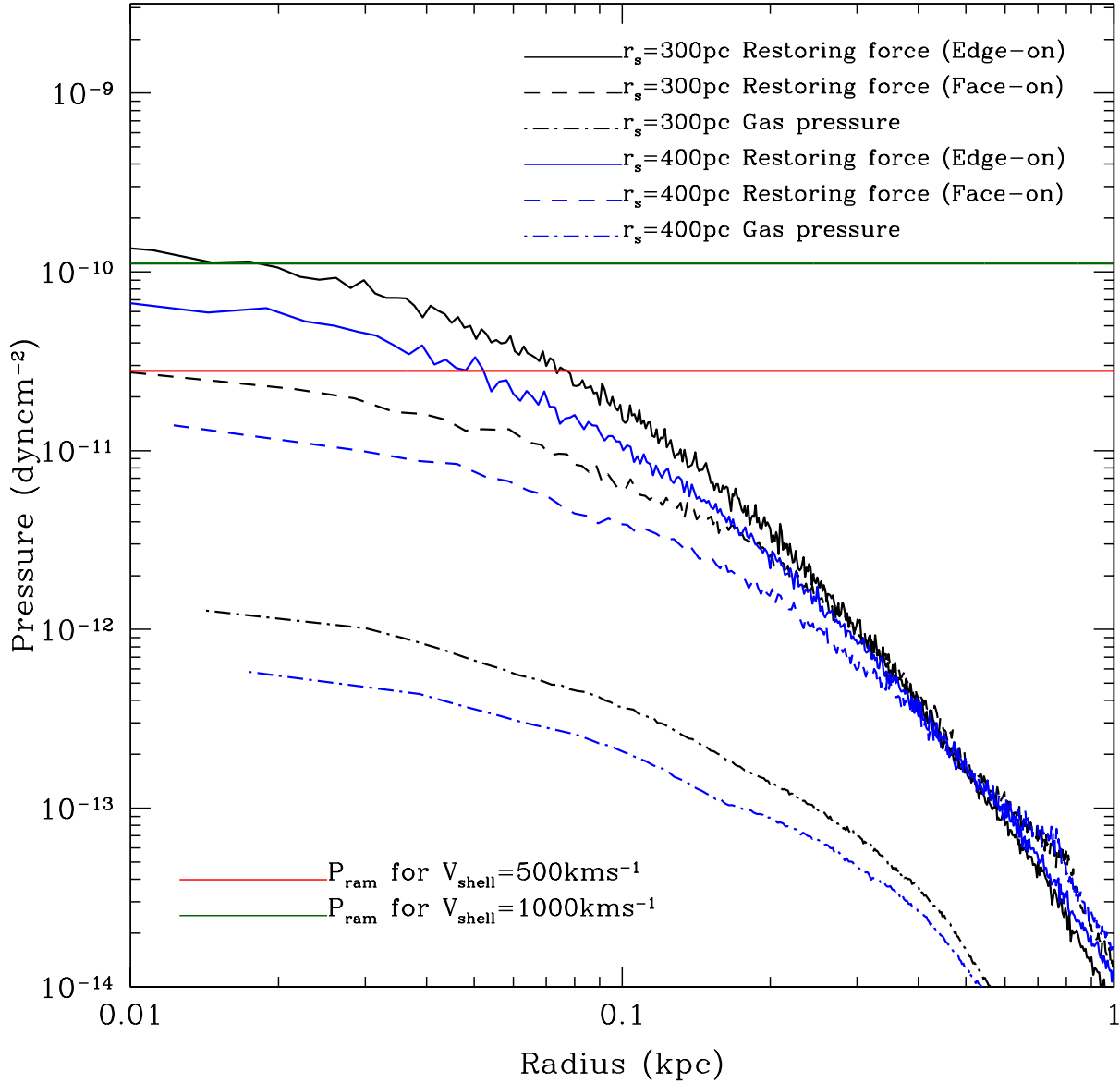


Figure 4.2: Restoring force for the disk orientated edge-on (solid lines) and face-on (dashed lines) to the outflow, and the gas pressure in the disk (dot-dashed lines) as a function of radius for disks with scale radii of 300pc and 400pc (black and blue lines respectively). The ram pressure due to the outflow is plotted for the disk positioned at 50kpc from the host galaxy with an outflow velocity of 500kms⁻¹ (red line) and 1000kms⁻¹ (green line).

4.4.1 Outflow velocities of 250kms^{-1}

Compact disk

Figure 4.3 shows the 3D gas density profiles (first row), enclosed gas mass profiles (second row), and the stellar surface density profiles (bottom row) for the isolated disk (first column) and for two orientations of the disk with respect to the outflow; edge-on (middle column) and face-on (last column) for $r_s=300\text{pc}$ and an outflow velocity of 250kms^{-1} at a distance of 100kpc from the host galaxy. Different line colours (and styles) represent the profiles at different times, the black (solid) curves show the initial profiles at $t=0$, the blue dotted curves show the profiles at $t=156\text{Myr}$ and the red (dashed) curves show the profiles at $t=375\text{Myr}$. The isolated disk is able to cool which leads to a density increase of several orders of magnitude in the central regions (left column, first row), enabling star formation. The enclosed mass profile shows the gas inside 100pc is collapsing towards the centre (left column, bottom row). Both the edge-on (middle column) and face-on (right column) orientations also show an increase in central gas density of the same order, despite the presence of the outflow. The only differences between the isolated run and those containing the outflow is at radii $> 100\text{pc}$ where the gas is stripped by the passage of the outflow. The central regions ($r < 100\text{pc}$) in all three simulations are very similar. All enclosed mass profiles (second row) show a similar increase in mass as the gas collapses to high densities, only the gas distribution in the outer regions differ. A significant amount of gas has been removed at larger radii, leaving $2 \times 10^6 M_\odot$ and $1 \times 10^6 M_\odot$ within 1kpc for the edge-on and face-on cases respectively. The edge-on disk has gas stripped outside a radius of 100pc , while the face-on disk has gas stripped further in, outside a radius of 50pc , due to the lower restoring force. Comparing this to figure 4.1, we see that gas is actually stripped much further in than we expected from the approximations. The black solid (edge-on) and dashed (face-on) curves in figure 4.1 cross the line representing the ram pressure for an outflow with a velocity of 250kms^{-1} at $300\text{-}400\text{pc}$.

At the end of the simulation, these dwarfs all have gas particles at sufficiently high densities to allow continued star formation. Note that the stripping is not instantaneous (especially for the edge-on orientation), the blue dotted lines here represent the time when the outflow has completely passed over the gas disk of the dwarf, by which time, only a minimal amount of gas is lost. As the simulations continues more gas is lost from the outer regions. The central regions therefore, do not appear to have been affected by the outflow, as gas is still able to cool and collapse to high densities more than 200Myr after

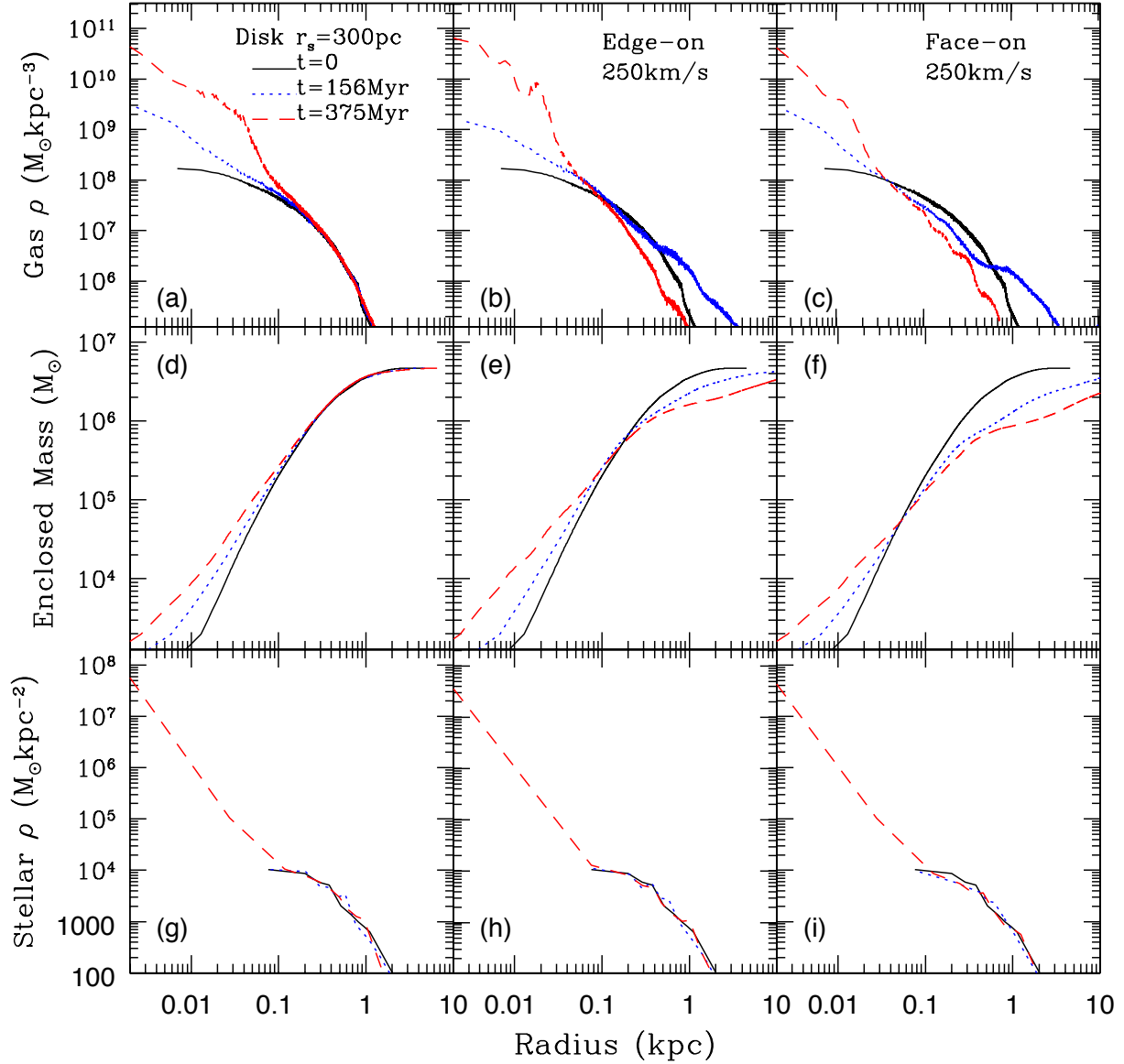


Figure 4.3: The evolution of the 3D gas density profile (top row), enclosed gas mass (second row) and stellar surface density profile (bottom row) for runs of an isolated disk (first column), a disk positioned edge-on to the outflow (second column) and a disk face-on to the outflow (third column) for a scale radius of $r_s=300 \text{ pc}$ and an outflow velocity of 250 km s^{-1} . Solid black curves show the initial profile at $t=0$ and dotted blue curves and dashed red curves show the profiles at 156 Myr and 375 Myr , respectively.

the interaction.

All three disks form stars during the simulation, the bottom row of Figure 4.3 shows the stellar surface density for the disk with $r_s = 300\text{pc}$ and an outflow velocity of 250kms^{-1} . As with the gas density profiles, the stellar density profiles are all similar in the central regions. A large number of stars are formed in the centre of the disks where the gas density is very high, resulting in a very centrally concentrated population. The passage of the outflow does not appear to have hindered star formation in the disks in either orientation due to the fact that the central regions are not affected. The blue dotted lines here represent the time when the outflow has completely passed over the dwarf, we can see no new star formation occurs until after it has passed. The structure of the halo is unaffected by the passage of the outflow despite a significant amount of gas being removed.

Extended disk

Figure 4.4 shows the 3D gas density profiles (top row), the gas enclosed gas mass profiles (second row) and the stellar surface density profiles (bottom row) for the isolated disk and for two orientations of the disk with respect to the outflow for $r_s=400\text{pc}$ and an outflow velocity of 250kms^{-1} . The initial profiles are shown by the solid black curves, and the dotted blue and dashed red curves show the profiles at $t=156\text{Myr}$ and $t=375\text{Myr}$ respectively. As for the isolated disk with $r_s=300\text{pc}$, the gas is able to cool and reach high densities, increasing the central density by several orders of magnitude (top row, left column). Note that in this dwarf, the time required to reach densities high enough for star formation is longer than for a dwarf with $r_s=300\text{pc}$ as the density is lower, hence the cooling times are longer. The passage of the outflow is therefore able to prevent the gas in these lower density disks from reaching the higher densities, keeping the central density around the same value for the edge-on orientation (top row, middle column), and reducing it by around two orders of magnitude in the face-on orientation (top row, left column). Here the orientation of the gas disk with respect to the outflow determines whether or not the dwarf can host any further star formation in the future. As the central density is still high when positioned edge-on to the outflow, it is possible that this gas could cool and form stars (assuming no other external effects prevent this). In this case the gas is only removed at radii $>100\text{pc}$ and the dwarf retains ~ 20 percent ($1 \times 10^6 M_\odot$) of the initial gas mass within 1kpc . The outflow has a larger impact on the face-on dwarf, removing mass from all radii leaving only 4 percent of the initial gas mass within 1kpc .

The radius where the enclosed mass profiles starts to decline can be compared to the

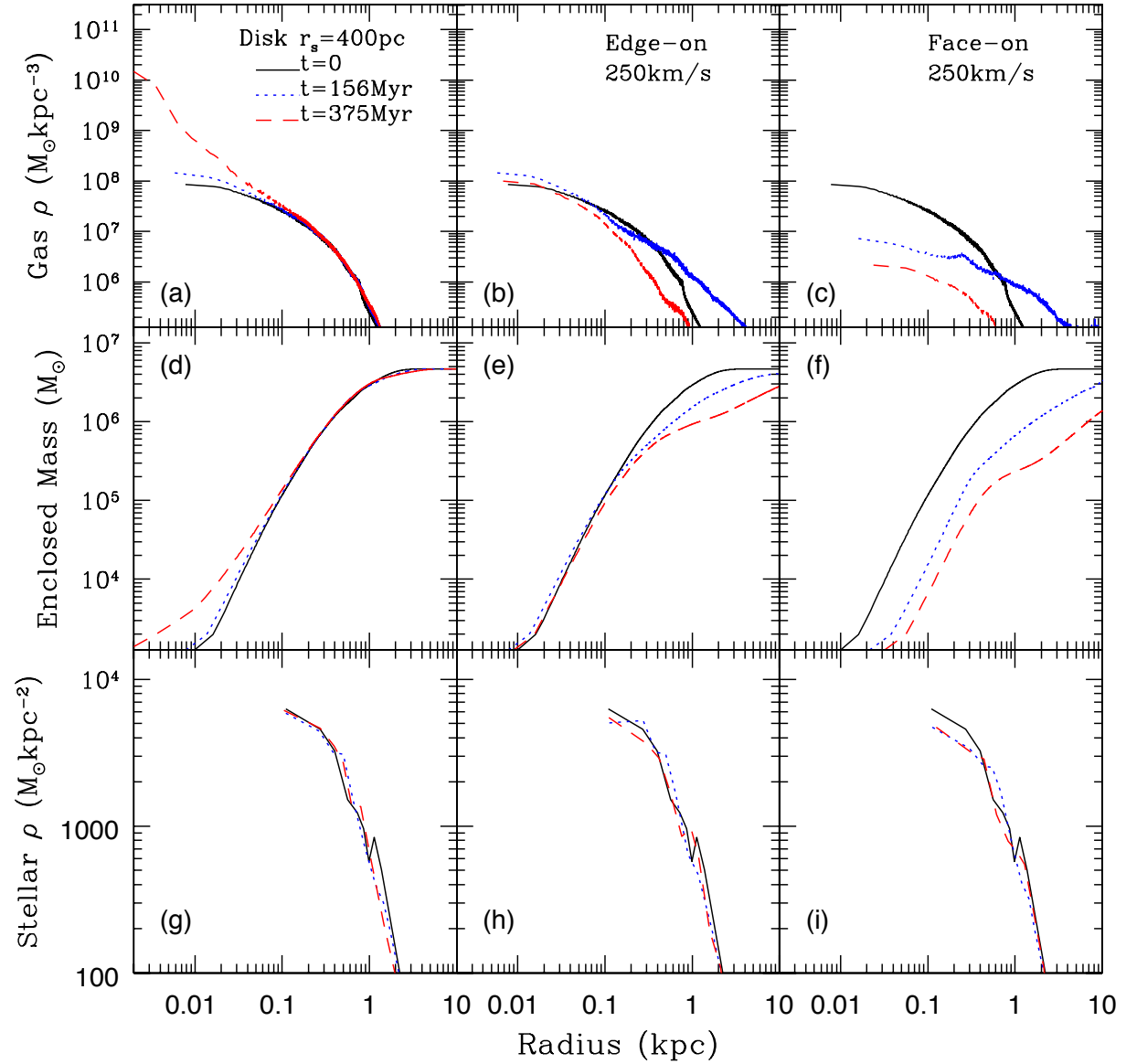


Figure 4.4: Evolution of the 3D gas density profile (top row), enclosed gas mass (second row) and the stellar surface density profile (bottom row) for runs of an isolated disk (first column), a disk edge-on to the outflow (second column) and a disk face-on to the outflow (third column) for a scale radius of $r_s=400\text{pc}$ and a outflow velocity of 250km s^{-1} . Solid black curves show the initial profile at $t=0$ and dotted blue curves and dashed red curves show the profiles at 156Myr and 375Myr , respectively.

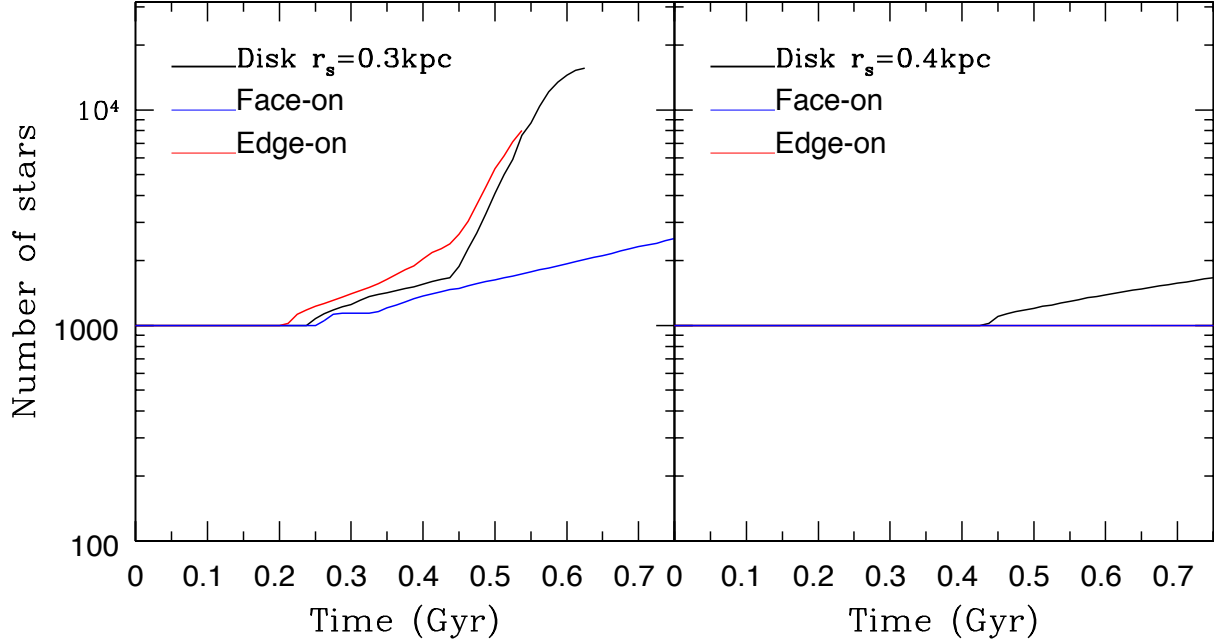


Figure 4.5: The number of stars formed over time for disks with $r_s=300\text{pc}$ (left) and $r_s=400\text{pc}$ (right). The solid black lines represent an isolated disk (black) and the same disk orientated face-on (blue) and edge-on (red) to an outflow with a speed of 250kms^{-1} .

stripping radius. As with the higher density disk, we see gas stripped further in than we would expect from figure 4.1. Both the edge-on and face-on profiles (blue solid and dashed lines) fall below the line representing the ram pressure (green line) at 300-400pc. This radius is similar to the disk with $r_s=300\text{pc}$ as the restoring forces are comparable at large radii. The edge-on orientation only loses gas from $r>100\text{pc}$. However in contrast, the face-on disk loses gas from all radii, though the slope is similar that of the initial profile and does show a decline in the mass profile outside $\sim 400\text{pc}$ where we would expect the gas to be stripped.

The bottom row of Figure 4.4 shows the stellar surface density profile. No new stars are formed in these simulations, in this case the presence of the outflow prevents any new stars from forming compared to the isolated case. The removal of gas doesn't appear to have altered the density profile of the stars present initially, and has not effected the profile of the dark matter halo.

The number of stars formed in the simulations with an outflow velocity of 250kms^{-1} is shown in figure 4.5, for the isolated disks (solid black lines) with $r_s=300\text{pc}$ (left panel) and $r_s=400\text{pc}$ (right panel), and for disks orientated edge-on (red lines) and face-on (blue

lines). The presence of the outflow does trigger star formation slightly earlier in the disk positioned edge-on with $r_s = 300\text{pc}$.

Stars form in all three runs for the disk with $r_s=300\text{pc}$. The face-on disk forms fewer stars than the isolated disk, so the outflow hinders star formation in this case. The edge-on disk starts forming stars slightly earlier than in the isolated case as it is triggered earlier by the outflow, and at least initially this disk forms a few more stars than the isolated disk. For a disk with a scale radius of $r_s=400\text{pc}$ (right panel) the presence of the outflow prevents any star formation, only the isolated disk has some low level star formation at later times when the gas has reached high enough densities.

4.4.2 Outflow velocities of 500kms^{-1}

Compact disk

Figure 4.6 shows the gas density profiles (top row) and the enclosed gas mass (second row) for a disk with $r_s=300\text{pc}$ and an outflow velocity of 500kms^{-1} positioned at 100kpc (first and second column) and 50kpc (third and fourth column) from the host galaxy. Compared to the isolated case, the disks that interact with the outflow are lower density at all radii in both orientations. The edge-on disk, 100kpc away from the host (first column) retains gas, and has a similar density profile to that initially, but the density has decreased at all radii compared to the original profile. From the enclosed mass profile (bottom row) we see there is $\sim 10^6 M_\odot$ of gas left in 1kpc , so around 80 percent of the gas mass is lost due to the passage of the outflow. As with the other simulations of the edge-on orientation, the majority of the gas is stripped from larger radii, $\sim 200 - 300\text{pc}$, in agreement with figure 4.1. This dwarf could possibly host further star formation as the resulting central gas density is still relatively high. Although a significant amount of gas has been stripped from the dwarf, this is exclusively outside of $\sim 200\text{pc}$, leaving the enclosed mass in the central 100pc unchanged. For an edge-on disk, positioned 50kpc away from the host (third column) the higher ram pressure lowers the central density by roughly another two orders of magnitude, preventing star formation and leaving only around $10^5 M_\odot$ of gas within 1kpc . Referring back to figure 4.2 we expect a large amount of gas to be stripped from this dwarf, with a stripping radius of $\sim 80\text{pc}$. We don't see a decline in the mass profile until around 400pc , but the profile is decreased at all radii with respect to the initial profile, as gas is removed all the way to the centre.

When the dwarf is orientated face-on to the outflow, almost all the gas is removed from

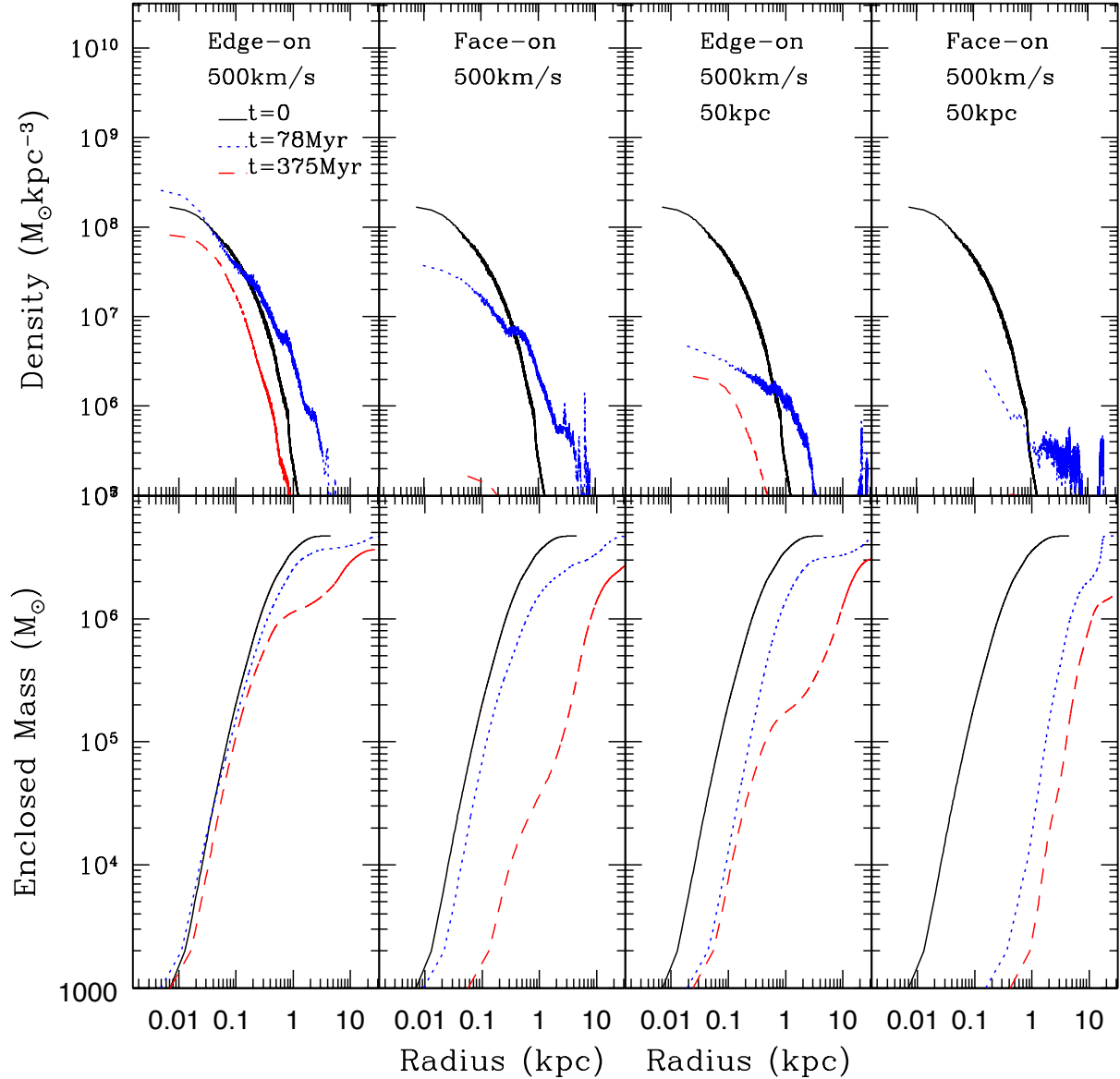


Figure 4.6: Evolution of the 3D gas density profile (top row) and the enclosed gas mass (bottom row) for disks placed at distances of 100kpc and 50kpc, of a disk edge-on to the outflow (first and third column) and a disk face-on to the outflow (second and fourth column) for a scale radius of $r_s=300\text{pc}$ and an outflow velocity of 500kms^{-1} . Each panel shows three different stages of the simulation, $t=0, 78$ & 375Myr are represented by black solid, blue dotted, and red dashed lines respectively. $t=78\text{Myr}$ is the time when the outflow has completely passed the disk.

the dwarfs at both distances (100kpc: second column, 50kpc: last column), as they retain only $\sim 10^4 M_\odot$ within 1kpc. It is unlikely there will be any future star formation in these two dwarfs. The remaining gas will be easily removed by other processes such as ram pressure stripping by the hot halo of the Milky Way. We don't expect the face-on disk to be completely stripped at an outflow velocity of 500 km s^{-1} . Figure 4.1 suggests a stripping radius of $\sim 200 \text{ pc}$ for this dwarf (comparing the orange line and blue dashed curve). from figure 4.1 (orange line), which estimates a stripping radius of $\sim 200 \text{ pc}$ for this dwarf (blue dashed line). However for the same dwarf at a distance of 50kpc, we do expect all gas to be removed as the ram pressure is larger than the restoring force at all radii in figure 4.2 (black dashed curve and red line).

The stellar surface densities and halo densities for these runs remain unchanged, even in the cases where the vast majority of gas is removed as shown in figure 4.7. The stellar surface density profile (first row), the stellar enclosed mass (second row), the halo density (third row) and the halo enclosed mass (bottom row) are shown for a disk scale radius of $r_s=300 \text{ pc}$ and an outflow velocity of 500 km s^{-1} at a distance of 100kpc (second and third columns) and 50kpc (fourth and fifth columns) from the host galaxy. No new stars are formed for either disk in these simulations as the impact of the outflow has prevented the gas in these dwarfs from cooling and forming stars during the simulation. The surface density of the original population of stars is unchanged (middle and right columns, top row), as well as the enclosed mass (middle and right columns, second row). The outflow is able to remove the vast majority of gas from the face-on dwarf at either distance, leaving behind a halo with very small amount of gas and the original population of stars (those present before the passage of the outflow). When the disk is positioned edge-on at a distance of 100kpc, 20 percent of the original gas remains, retaining a reasonably high density in the centre, suggesting that future star formation is possible if the gas in the central regions can cool and reach the required densities. When positioned at 50kpc the edge-on disk will have the same fate as those orientated face-on as the low density gas will be easier to remove by other external processes. Therefore it is likely three out of four of these scenarios result in gas-free dark matter halos with an old stellar population.

Extended disk

Figure 4.8 shows the gas density profile (top row) and enclosed mass profile (bottom row) for a disk with $r_s=400 \text{ pc}$ with an outflow velocity of 500 km s^{-1} for an edge-on (first and third columns) and face-on (second and fourth columns) orientation at distances of 100kpc

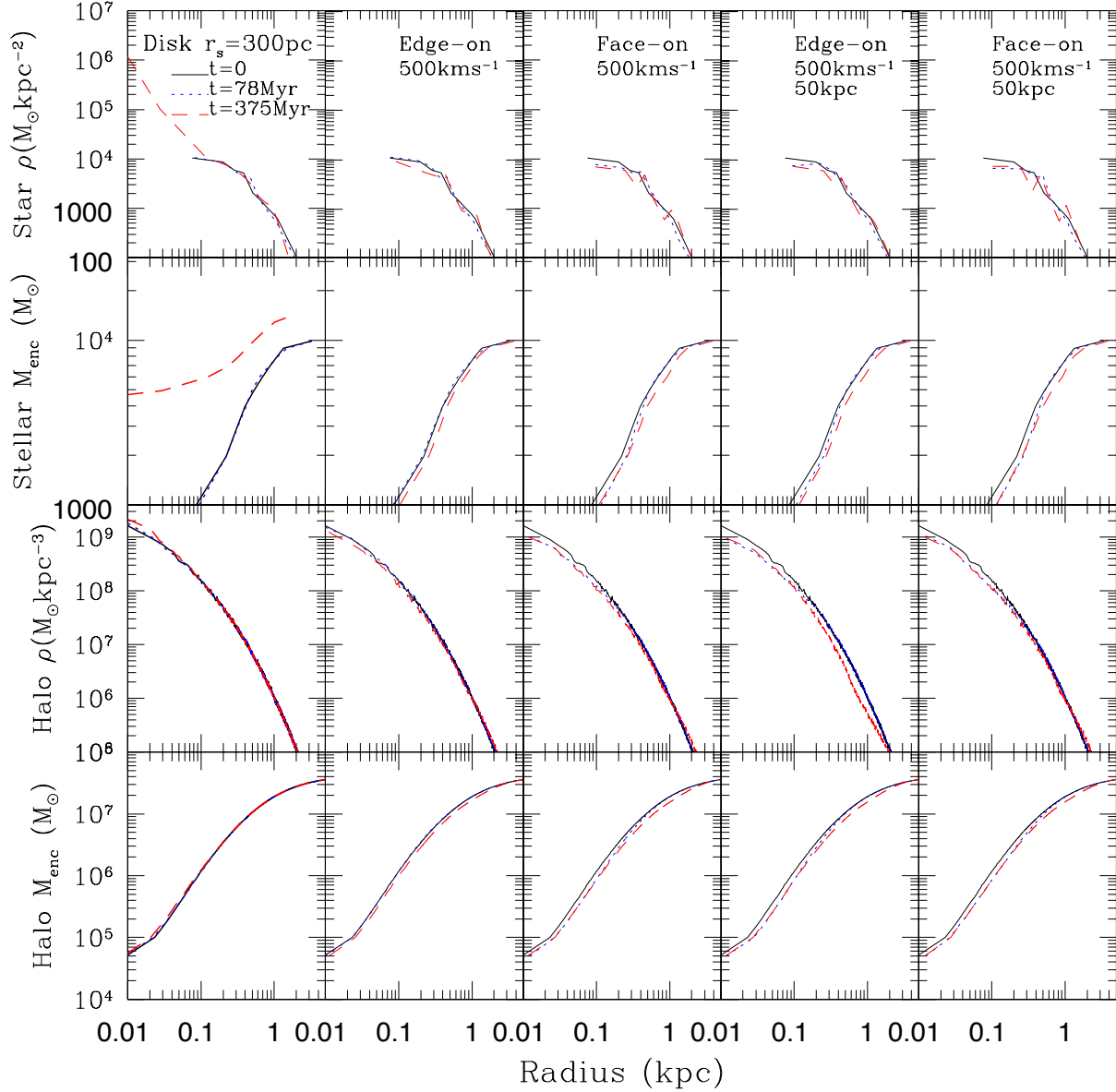


Figure 4.7: Stellar surface density profile (top row), enclosed stellar mass (second row, taken in 2D), the halo density profile (third row) and the enclosed halo mass (bottom row) for runs of an isolated disk (first column), a disk edge-on to the outflow (second column) and a disk face-on to the outflow (third column) for a scale radius of $r_s=300\text{pc}$ and an outflow velocity of 500kms^{-1} . Each panel shows three different stages of the simulation, $t=0, 78$ & 375Myr are represented by black solid, blue dotted, and red dashed lines respectively. $t=78\text{Myr}$ is the time when the outflow has completely passed the disk.

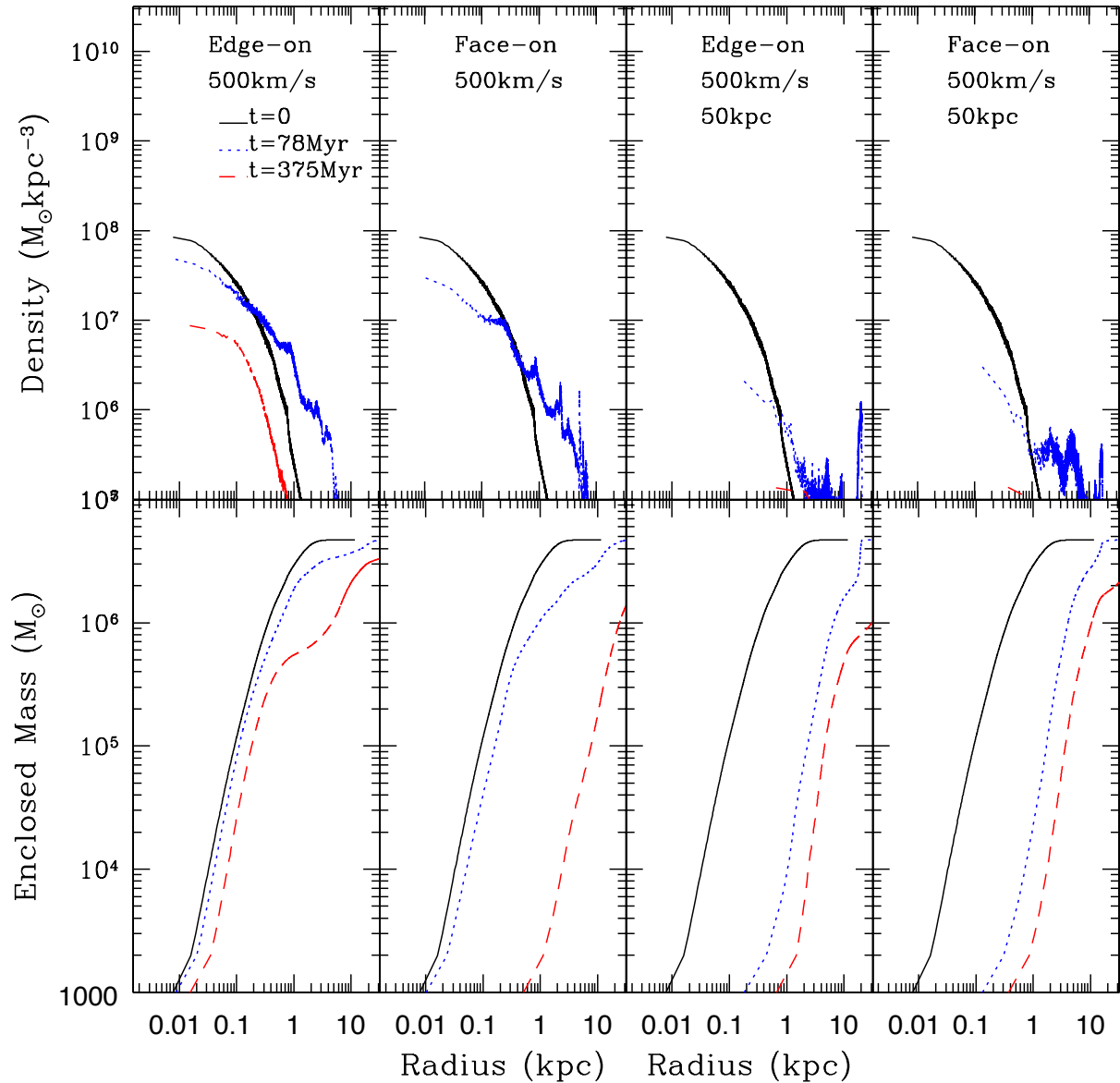


Figure 4.8: Evolution of the 3D gas density profile (top row) and the enclosed gas mass (bottom row) for disks placed at distances of 100kpc and 50kpc, of a disk edge-on to the outflow (first and third column) and a disk face-on to the outflow (second and fourth column) for a scale radius of $r_s=400\text{pc}$ and an outflow velocity of 500kms^{-1} . Each panel shows three different stages of the simulation, $t=0,78$ & 375Myr are represented by black solid, blue dotted, and red dashed lines respectively. $t=78\text{Myr}$ is the time when the outflow has completely passed the disk.

and 50kpc respectively. Compared to the the isolated disk, the gas density is lower for the all disks in the presence of the outflow at all radii. The edge-on disk has gas stripped from all radii, lowering the central density by around an order of magnitude, decreasing the probability of star formation in the central regions. At the end of the simulation there is only $\sim 5 \times 10^5 M_{\odot}$ of gas in 1kpc. Note the outflow is disrupting the gas distribution in the central regions ($r < 100\text{pc}$) for the edge-on disk, whereas previously only gas at larger radii was affected. From figure 4.1 we expect the gas outside a radius of 200pc to be stripped; the decline in the mass profile occurs at a larger radius than this, at $\sim 400\text{-}500\text{pc}$. However gas is lost from all radii, unlike the same simulation with the higher density disk in figure 4.6. In the remaining simulations shown in this figure virtually all of the gas is removed, leaving only $\sim 10^3 M_{\odot}$ in the central 1kpc.

For the face-on dwarf (second column) there is virtually no gas left in the dwarf at the end of the simulation. Based on figure 4.1 we don't expect this much to be stripped, as the stripping radius is around 100pc. Both of the orientations positioned at 50kpc from the host galaxy also lose almost all of their gas (fourth and fifth columns). Looking at figure 4.2 we do expect all of the gas to be removed from the face-on dwarf (blue dashed line) as the ram pressure is larger than the restoring force at all radii (red line). However we expect some gas to be left in the centre of the dwarf orientated edge-on (blue solid line) at least out to $\sim 50\text{pc}$. In these last three cases the passage of the outflow again leaves behind a halo devoid of gas, hosting the original population of stars that formed before the dwarf fell into the halo of the host galaxy. The stellar surface density and halo profiles are unaffected by the removal of gas in these dwarfs. Note that just after the outflow has completely passed over the dwarf there is still a large amount of high density gas left in the dwarfs positioned 100kpc from the host galaxy as it takes time for the gas to move out and away from the dwarf. In contrast when the dwarf is positioned at 50kpc, the higher ram pressure of the outflow does more damage instantaneously.

4.4.3 Outflow velocities of 1000kms^{-1}

Compact disk

The models with the highest ram pressure are shown in figure 4.9 for the disk with $r_s = 300\text{pc}$, with outflow velocity of 1000kms^{-1} . As before the 3D gas density (top row) and enclosed mass profile (bottom row) are plotted for edge-on and face-on orientations positioned 100kpc (first and second) and 50kpc (third and fourth) from the host galaxy.

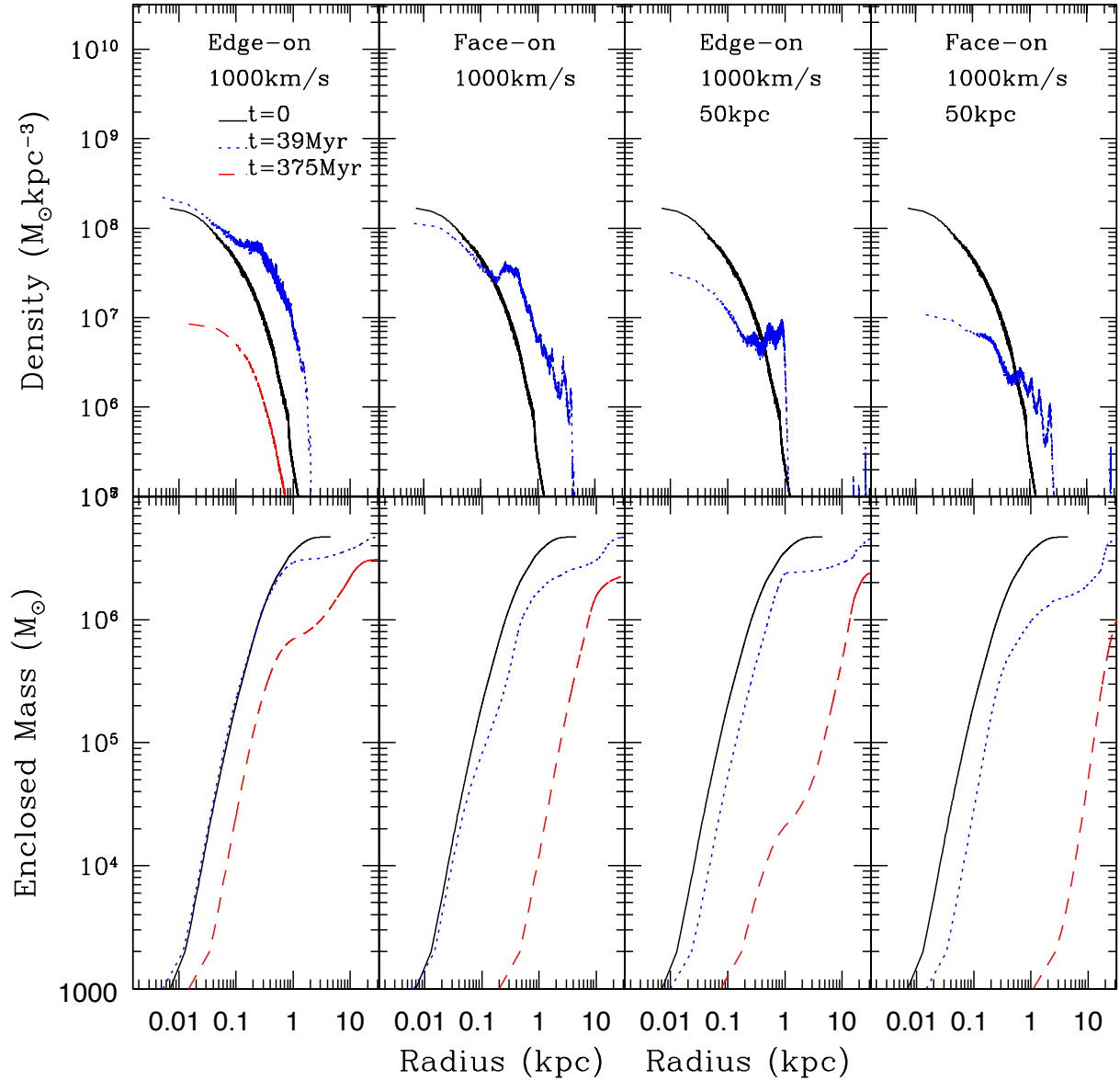


Figure 4.9: Evolution of the 3D gas density profile (top row) and the enclosed gas mass (bottom row) for disks placed at distances of 100 kpc and 50 kpc, for a disk edge-on to the outflow (first and third column) and a disk face-on to the outflow (second and fourth column) for a scale radius of $r_s=300$ pc and an outflow velocity of 1000 km s^{-1} . Each panel shows three different stages of the simulation, $t=0, 31$ & 375 Myr are represented by black solid, blue dotted, and red dashed lines respectively. $t=31$ Myr is the time when the outflow has completely passed the disk.

The only simulation in this case with a non-negligible amount of gas remaining in the dwarf at the end is the edge-on dwarf at 100kpc from the host galaxy (first column). Even in this case the central density decreases by around an order of magnitude, preventing the gas from forming any stars. The enclosed mass profile shows that gas is removed from all radii, with only $8 \times 10^5 M_{\odot}$ remaining within 1kpc after 375Myr. Comparing with the black solid line in figure 4.1 and the red line which represents the ram pressure of the outflow, we can see that we expect gas to be removed outside of ~ 100 pc, yet gas is removed from the centre and the decline in the enclosed mass profile is at around 500pc. Figure 4.1 also shows that we expect the face-on case (black dashed line) to retain some gas in the centre, and gas outside of ~ 50 pc to be stripped. However, in the simulation, the outflow removes almost all of the gas from this dwarf (column two), leaving less than $10^4 M_{\odot}$ in the central 1kpc. Both orientations positioned at 50kpc from the host galaxy lose the majority of their gas (third and fourth columns), the edge-on dwarf retains more gas, around $10^4 M_{\odot}$ within 1kpc, while the face-on dwarf has no gas left inside this radius after 375Myr. These are in agreement with figure 4.2, where the ram pressure due to the outflow is represented by the green line, which is higher than the restoring force for the edge-on disk as far in as 20pc, and larger than the restoring force for the face-on disk at all radii. Again the stellar surface density profile and the halo density profile are unaffected and the impact of the outflow leaves these three dwarfs in haloes devoid of gas, hosting an old stellar population with very little chance of any further star formation.

Extended disk

The equivalent plots for the disk with $r_s=400$ pc are shown in figure 4.10. Again, three out of four of these dwarfs are left with a negligible amount of gas after 375Myr. The edge-on disk at a distance of 100kpc (first column) retains the most gas here, but as the central density has decreased by two orders of magnitude (an order of magnitude more than the same simulation for the higher density disk) it is unlikely any further star formation will occur. Gas is removed from all radii, resulting in just $2 \times 10^5 M_{\odot}$ remaining within 1kpc at the end of the simulation. Figure 4.1 estimates the stripping radius of this dwarf at this ram pressure (blue solid lines and red solid line) to be 100pc, however we see a decline in the enclosed mass profile at around 500pc, and it is lower than the initial profile at all radii. When the outflow is moving at 1000 km s^{-1} the face-on disk has almost all of its' gas removed, which we do expect from figure 4.1 as the ram pressure (red line) is greater than the restoring force of the disk at all radii. Both orientations of the dwarf positioned

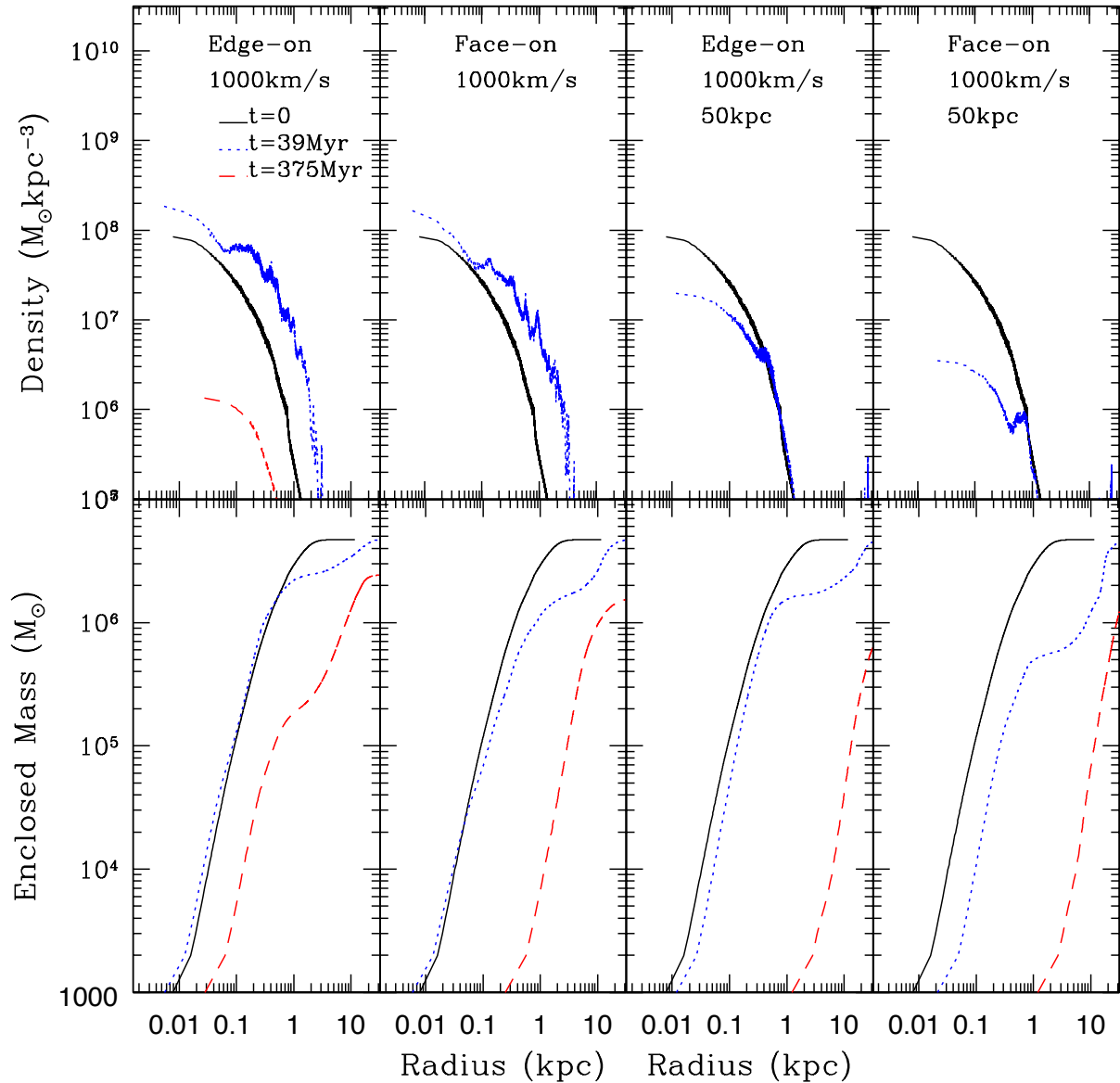


Figure 4.10: Evolution of the 3D gas density profile (top row) and the enclosed gas mass (bottom row) for disks placed at distances of 100 kpc and 50 kpc, for a disk edge-on to the outflow (first and third column) and a disk face-on to the outflow (second and fourth column) for a scale radius of $r_s=400 \text{ pc}$ and an outflow velocity of 1000 km s^{-1} . Each panel shows three different stages of the simulation, $t=0, 39$ & 375 Myr are represented by black solid, blue dotted, and red dashed lines respectively. $t=39 \text{ Myr}$ is the time when the outflow has completely passed the disk.

50kpc away from the host galaxy (third and fourth columns) also lose all of their gas, which is expected from figure 4.2 as the ram pressure (green line) is above the restoring force for the edge-on disk up to the central 50pc (blue solid line) and is greater than the restoring force of the face-on disk at all radii (dashed blue line). No new stars form in these dwarfs during the simulation and no new stars are likely to form for the remainder of the lifetimes of the dwarf (assuming no new gas is accreted). The stellar surface density and halo density profiles remain unchanged, again leaving haloes devoid of gas hosting an old stellar population.

It is interesting to note that after increasing the outflow velocity from 250kms^{-1} by a factor of two and then four, the edge-on dwarf with a scale radius $r_s=300\text{pc}$, still retains around the same order of magnitude of gas within 1kpc ($\sim 10^6 M_\odot$). Increasing the outflow density by a factor of ~ 5 has a larger impact than increasing the ram pressure by a factor of 16 (through increasing the outflow velocity). The highest ram pressure of our model outflow at a distance of 100kpc from the host galaxy is $\sim 10^{-11}\text{dyn cm}^{-2}$, whereas the maximum ram pressure at a distance of 50kpc is $\sim 10^{-10}\text{dyn cm}^{-2}$. Dwarfs that are closer to the host galaxy when the outflow occurs will encounter the outflow at higher ram pressures (as the density of the outflowing shell of gas is higher), and those further away will experience lower ram pressures, even if the velocity of the outflow has doubled or quadrupled in the time it has traveled that distance.

Table 4.1 shows the root mean square of each component of the velocity for the disk with $r_s=300\text{pc}$. For the isolated disk the z-component of the gas velocity retains a small value, similar to the initial values. It actually decreases due to the gas collapsing to the centre where the density increases by a couple of orders of magnitude. For an outflow velocity of 250kms^{-1} the edge-on orientation shows an increase in the x-component of velocity (the direction of the outflow) when using all radii, the majority of gas contributing to this higher rms value is gas that has been stripped and is moving away from the disk. When looking at only the gas within 1kpc, the values are still comparable to those initially, although the z component has doubled and the x and y components have decreased slightly. The stellar component also has values similar to those initially, with the changes caused by the new stars that have formed. The stars formed in the simulation (column six) are more centrally concentrated than those initially present as indicated by the lower rms velocities.

The face-on disk has a larger change in the z component of velocity (the direction of the outflow in this case), although it is most obvious when looking at all of the gas. As before, most of this gas is gas moving away from the disk as it has been stripped. However it is

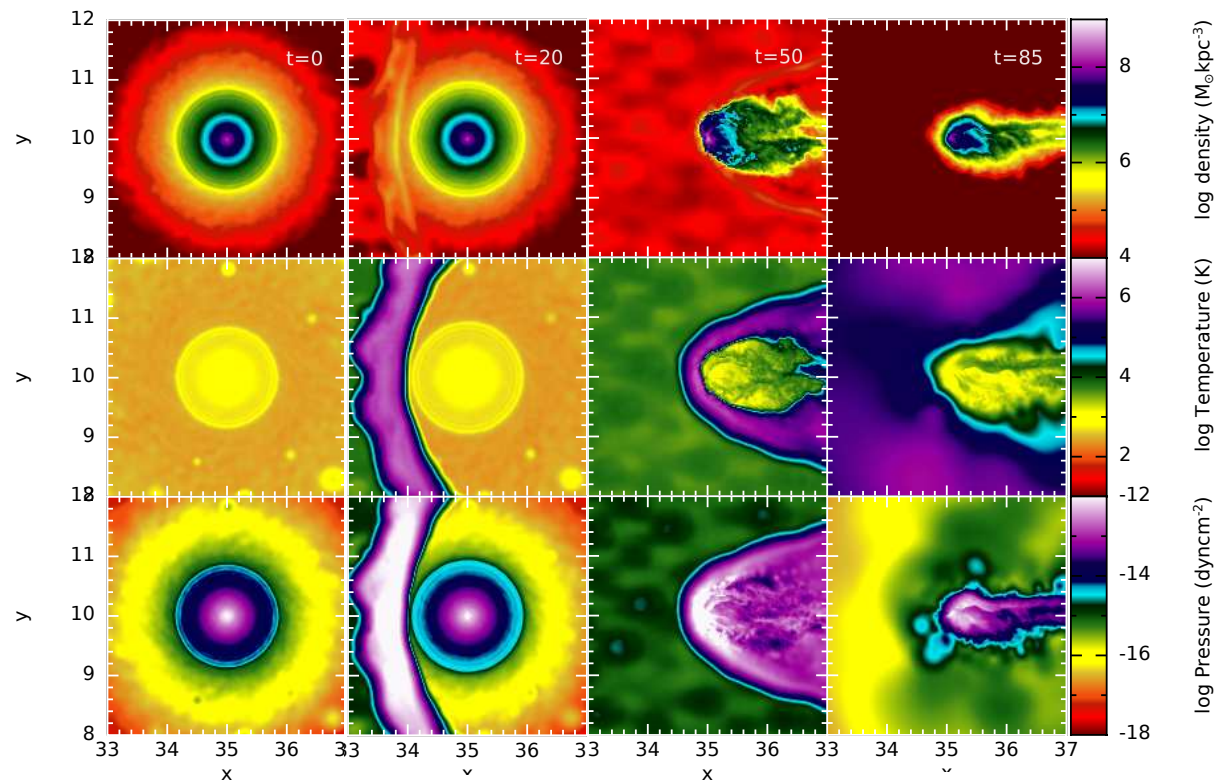


Figure 4.11: Snapshots showing the evolution of the gas density (top row), temperature (middle row) and pressure (bottom row) for a disk with $r_s=300\text{pc}$ at a distance of 100kpc from the Galaxy, orientated edge-on to an outflow with a velocity of 500kms^{-1} . The left column shows the initial conditions, and the second, third and fourth column show the gas at 20, 50 and 85Myr respectively.

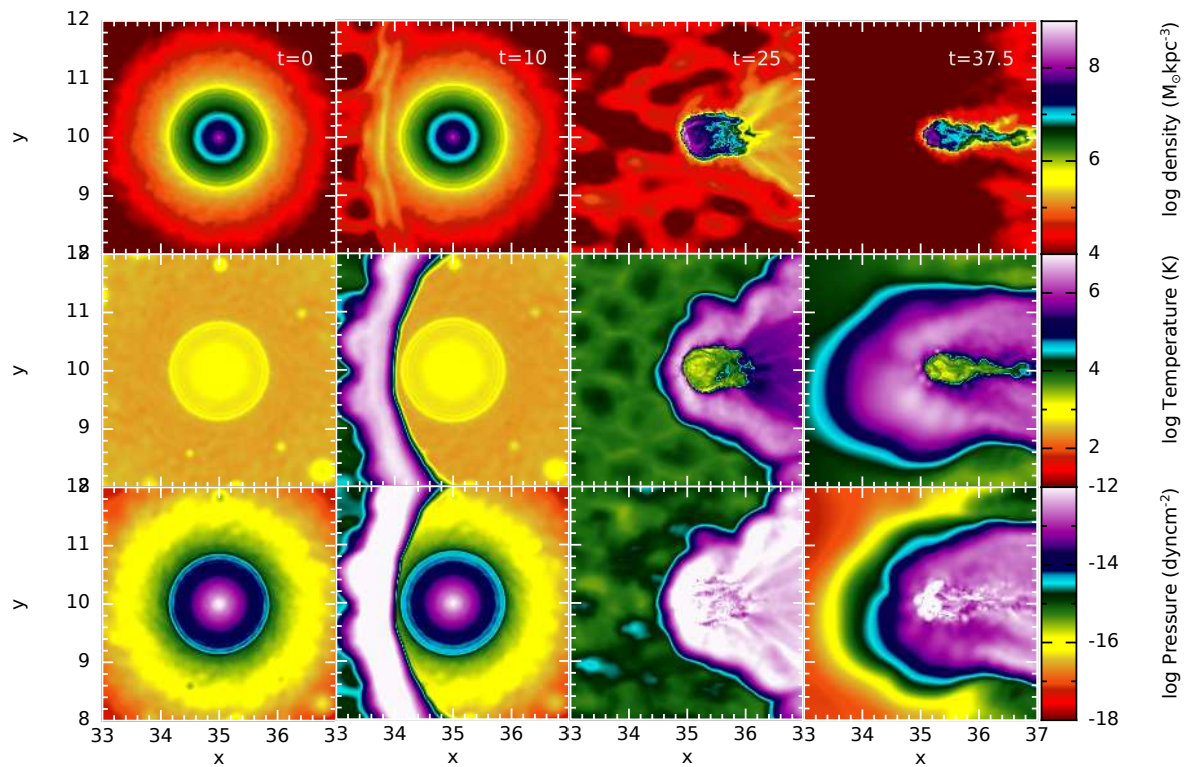


Figure 4.12: Snapshots showing the evolution of the gas density (top row), temperature (middle row) and pressure (bottom row) for a disk with $r_s=300\text{pc}$ at a distance of 100kpc from the Galaxy, orientated edge-on to an outflow with a velocity of 1000kms^{-1} . The left column shows the initial conditions, and the second, third and fourth column show the gas at 10, 25 and 37.5Myr respectively.

Table 4.1: List of root mean square (rms) velocities (in kms^{-1}) for the simulations with a disk scale radius $r_s = 300\text{pc}$. The first column describes the simulation, the second and third columns show the rms velocity of the all gas and the gas within 1kpc respectively. The fourth column show the rms for all stars, and the fifth and sixth columns show the rms for the stars present initially, and the new stars formed in the simulation.

Run	Gas (all)	Gas (1kpc)	Stars (all)	Stars (initial)	Stars (new)
<i>r_s</i> =300pc					
Initial x rms	5.87970	5.99084	6.26745		
Initial y rms	5.85730	5.96653	6.41621		
Initial z rms	1.58250	0.781699	3.35044		
Disk x rms	5.92209	6.22107	5.28956	6.19183	2.53816
Disk y rms	5.97084	6.27850	5.52431	6.53622	2.26838
Disk z rms	0.939275	0.404904	3.08075	3.68702	0.980154
Edge-on x (250kms^{-1})	75.8030	4.22330	4.73059	5.63907	3.29575
Edge-on y (250kms^{-1})	7.48751	4.41540	4.89541	6.02620	2.97778
Edge-on z (250kms^{-1})	7.08411	1.55623	2.59442	3.30244	1.27553
Face-on x (250kms^{-1})	8.56751	4.06987	4.78604	5.31882	1.93081
Face-on y (250kms^{-1})	8.65144	4.06207	4.93956	5.49412	1.94618
Face-on z (250kms^{-1})	120.289	3.21630	2.99388	3.24662	1.82886
Edge-on x (500kms^{-1})	187.537	3.30033	5.45624		
Edge-on y (500kms^{-1})	17.4817	2.63240	5.49091		
Edge-on z (500kms^{-1})	17.2966	1.98212	3.08484		
Face-on x (500kms^{-1})	24.1053	3.02546	4.73384		
Face-on y (500kms^{-1})	24.2547	2.66423	5.33122		
Face-on z (500kms^{-1})	267.525	4.51003	2.85416		
Edge-on x (1000kms^{-1})	440.331	2.51874	5.20044		
Edge-on y (1000kms^{-1})	52.7527	2.25648	5.46820		
Edge-on z (1000kms^{-1})	50.1711	1.66518	2.91281		
Dwarf at 50kpc					
Edge-on x (500km/s)	268.288	2.87816	4.86285		
Edge-on y (500km/s)	24.3577	1.92493	5.36674		
Edge-on x (500km/s)	28.1446	1.60062	2.76856		
Edge-on x (1000km/s)	627.320	4.35391	4.92708		
Edge-on y (1000km/s)	56.9247	2.23151	5.27806		
Edge-on z (1000km/s)	61.1586	2.27181	2.72240		

also larger within 1 kpc and has become similar to the values of the x and y components. The gas in this dwarf is now no longer distributed in a thin disk, but is 'puffed up' and more similar to a spherical morphology. The velocities of the original population of stars are similar to the initial values, while the values for the new stars formed in the simulation indicate a more spherical distribution.

When the outflow velocity is 500kms^{-1} the edge-on disk has x and y component rms values for the gas within 1kpc lower than that initially, and the z component is larger and more comparable to the x and y values. Again the values for the stars are similar to the initial values suggesting they are still in a disk and the outflow has had no impact on their distribution. The disk positioned face-on to the outflow has a z component that is larger than those for x and y, even within 1kpc, meaning the shape of the gas distribution is now more spherical and it has lost its' disk-like structure.

Interestingly the rms velocities for the stellar components for the four runs with a higher ram pressure are similar to the initial values suggesting they stay in a distribution similar to that they started with despite the large amount of gas that is lost.

Table 2 shows the rms for each component of the velocity for the disk with $r_s=400\text{pc}$. For the isolated disk the z-component of the gas retains a small value, similar to the initial values. The isolated disk in this case retains values very similar to the initial values after 375Myr. When the disk is positioned edge-on to the outflow, the x and y values decrease slightly, the z value increases but is still small compared to the x and y values. The disk positioned face-on with an outflow velocity of 250kms^{-1} shows more of a difference, with the z value becoming greater than those for x and y, even within 1 kpc.

The outflow doesn't appear to have had any effect on the old stellar population in both of these cases. When the outflow velocity is 500kms^{-1} the x and y components are decreased slightly for the edge-on case, while the z component is still low. For the face-on disk at this velocity there is a negligible amount of gas within 1 kpc as the majority has been stripped. As for the runs for the disk with $r_s=300\text{pc}$, the passage of the outflow does not appear to have had an effect on the rms velocities of the original stellar population when the simulation ended (even in the highest ram pressure runs). No new stars were formed in these simulations.

Figures 4.11 and 4.12 show snapshots of the gas density (top row), temperature (middle row) and pressure (bottom row) for a cross section through the midplane of the disk ($z=0$) for the initial conditions and at three different times representing when the outflow first comes into contact with the disk (second column), while the outflow is passing through

Table 4.2: List of rms velocities (in kms^{-1}) for the simulations with a disk scale radius $r_s = 400\text{pc}$. The first column describes the simulation, the second and third columns show the rms velocity of the all gas and the gas within 1kpc respectively. The fourth column show the rms for all stars, and the fifth and sixth columns show the rms for the stars present initially, and the new stars formed in the simulation.

Run	Gas (all)	Gas (1kpc)	Stars (all)	Stars (initial)	Stars (new)
$r_s=400\text{pc}$ Initial x rms	5.76203	5.90382	6.04937		
Initial y rms	5.80792	5.96245	6.31562		
Initial z rms	2.05675	0.796227	3.22605		
Disk x rms	5.60090	6.06488	6.01815		
Disk y rms	5.63358	6.09833	6.11627		
Disk z rms	1.27832	0.416806	3.47449		
Edge-on x (250kms^{-1})	86.7809	3.86171	5.23721		
Edge-on y (250kms^{-1})	8.09096	2.79933	5.83183		
Edge-on z (250kms^{-1})	8.01428	1.77410	2.99660		
Face-on x (250kms^{-1})	10.3555	2.96604	4.95286		
Face-on y (250kms^{-1})	10.1767	2.88375	5.47364		
Face-on z (250kms^{-1})	140.498	4.22485	2.83351		
Edge-on x (500kms^{-1})	215.821	3.33426	5.13226		
Edge-on y (500kms^{-1})	21.4835	2.28207	5.49235		
Edge-on z (500kms^{-1})	19.6432	1.79333	2.80609		
Edge-on x (1000kms^{-1})	510.604	2.83446	4.92707		
Edge-on y (1000kms^{-1})	68.0897	2.26983	5.40622		
Edge-on z (1000kms^{-1})	63.0744	1.61401	2.67283		

the disk and a bow shock is present (third column), and when the outflow has just finished passing the disk (fourth column). The shock front is visible in these snapshots as the layer with an increased gas density, temperature and pressure, and it forms a bow shock as it wraps around the densest regions of the dwarf galaxy. Discussion of these two figures is continued in section 3.4.

4.5 Discussion

In this chapter we have explored the impact of ram pressure stripping by an outflow from the AGN of a host galaxy on a population of satellites. We have used two different model dwarf galaxies, orientated either face-on or edge-on to the outflow, assuming two different distances from the centre of the host galaxy. In each case we analysed their properties after 375Myr.

The results of these simulations show that the approximations made at the beginning of the section fail to explain the fate of the dwarf in the event of a strong shock caused by the high ram pressure due to the passage of an AGN outflow from the host galaxy. The approximate calculation fails in two specific ways: (1) the outflow can remove a significant mass of gas from the central regions in some cases, despite the restoring forces being larger than the ram pressure from the outflow, (2) only the simulations with the lowest ram pressure are able to compress the gas and form stars.

It is not just the ram pressure of the outflow that is important but the timescale on which it occurs. When the shell of supersonic outflow gas comes into contact with the gas disk of our model dwarf galaxy the difference in velocity and density causes a strong shock. This is shown in figure 4.11 which show maps of a cross section through the plane of the disk for the gas density (top row), temperature (middle row) and pressure (bottom row) for a dwarf positioned 100kpc away from the host galaxy, orientated edge-on to the outflow which has a velocity of 500kms^{-1} . The left column shows the initial conditions, and the second, third and fourth columns show the dwarf at 20, 50 and 85Myr respectively. For this case the shock is strong (Mach 42), resulting in a contact discontinuity being formed when the outflow reaches the outer regions of the gas disk in the dwarf. While the lower density gas at large radii is immediately stripped as the shocked gas forms a smooth flow around the dwarf, the high density gas in the centre causes a bow shock to form.

The outflow gas passes through the shock front and emerges on the other side with different properties which can be estimated using the Rankine-Hugonit conditions: these

require mass conservation (equation 4.10) and require the sum of thermal and ram pressures across a boundary to remain a constant value (equations 4.11).

$$\rho_1 u_1 = \rho_2 u_2 \tag{4.10}$$

$$\rho_1 u_1^2 + P_1 = \rho_2 u_2^2 + P_2 \tag{4.11}$$

Where ρ_1 , u_1 , P_1 are the pre-shock gas density, velocity and pressure, and ρ_2 , u_2 and P_2 are the same properties post-shock.

In the limit of a strong shock ($\rho_2 \gg \rho_1$) these conditions imply that the maximum density contrast (ρ_1/ρ_2) across an adiabatic shock is a factor of four. This then limits the impact of the shock as the maximum post-shock density is $\rho_2=4\rho_1$, which leads to a maximum post-shock velocity of $u_2=u_1/4$. It is necessary for the post-shock gas to emerge at subsonic speeds to preserve causality in the shock, and so the temperature required in order for the gas to be subsonic is larger than the pre-shock value. As the shock strength is increased, the post-shock thermal pressure increases, making it harder for the gas to be compressed. As the properties of the gas change across the contact discontinuity the pressure that the central regions of the dwarf feels is actually lower than the initial ram pressure of the outflow.

The increase in thermal pressure behind the bow shock for a stronger shock can be seen comparing figures 4.11 and 4.12. Both the post-shock thermal gas pressure and temperature are higher for the outflow velocity of 1000kms^{-1} compared to that for 500kms^{-1} and there is a significantly larger fraction of high pressure gas while the outflow is passing. Therefore the ram pressure of the outflow is not higher than the thermal pressure of the gas disk, making it more difficult to compress the gas in the dwarf. So possibly a higher ram pressure leads to higher gas pressures and temperatures in the disk, which acts to inhibit star formation.

We see a truncation of the mass profile in the outer regions of all of the dwarfs hit by the outflow (that have gas remaining in the halo after 375Myr). However, this doesn't always match the radii expected from figures 4.1 and 4.2. We note that the pressure is defined as the force per unit area, and does not take into consideration the amount of time this pressure is applied for. It is therefore important to consider the timescales this process acts on to estimate the impact ram pressure stripping has on satellite galaxies.

We find that the outflow can remove significant amounts of gas from our model dwarf

galaxies in all cases. The orientation of the dwarf is important as this determines the strength of the restoring force and therefore how much gas can be stripped. Dwarfs positioned face-on to the outflow are more easily stripped of their gas, while the gas in the dwarfs positioned edge-on experiences a higher restoring force. Gas disks in edge-on dwarfs also experience more compression due to gas at larger radii being pushed into the central regions.

The analytical approximations of the stripping radius based on Gunn and Gott (1972) (also see Mayer *et al.* (2006b)) are useful to estimate the gas loss in satellites experiencing ram pressure stripping, but fail to explain the resulting dwarfs in this case. The discrepancy is larger for the dwarfs orientated face-on to the outflow as in some cases they lose all of their gas, whereas we would expect them to retain some in the central regions. In every case with an outflow velocity greater than 250kms^{-1} , at either distance to the host galaxy, the face-on dwarfs are stripped of almost their entire gas distribution, starving the dwarfs of fuel for further star formation. The dwarfs orientated edge-on retain gas in the central regions in all cases when positioned at a distance of 100kpc from the host. In most cases they also retain gas at sufficiently high density to result in further star formation providing the gas is able to cool and collapse. When the dwarfs are positioned at a distance of 50kpc from the host galaxy this results in all of the gas being removed from the galaxies, with the exception of the edge-on dwarf for an outflow velocity of 500kms^{-1} . From the approximations we expect to find gas retained in the centre of both the model dwarfs in both orientations for an outflow velocity of 500kms^{-1} at a distance of 100kpc (see figure 4.1); however, only the edge-on dwarfs retain gas.

As the pressure is defined as the force per unit area, the total work done on the dwarf galaxies in our simulations over time is much larger than that implied by the ram pressure due to the time they are subjected to the passage of the outflow. Another problem with using this approximation for simulated galaxies is that Σ_g and Σ_{dg} are time dependant, as gas is gradually removed causing the surface densities to decrease, the lower restoring force will result in changes to the defined stripping radius with time.

Our simulations show that it is possible to remove all gas from a halo during one interaction with a shell of gas resulting from an external AGN outflow, without disrupting the dynamics of the rest of the galaxy. We do not consider evolution prior to falling into the halo of the host galaxy, however any processes that act upon the dwarf galaxies would only act to increase the possibility of removing more gas. If a sustained burst of star formation transforms the dark matter cusp into a core and produces a more extended gas

distribution, this would result in the restoring force resisting the removal of the gas to be lower, making it easier to remove by stripping. Inclusion of the early evolution could alter the final properties of the dwarf such as the dynamics of the stellar and dark matter components. In our model dwarfs the potential in the central regions is dominated by the halo, so removing all the gas has no effect on the existing stellar and halo components, whereas if the dwarf galaxy hosted a cored halo profile at the time it fell into the halo of the Milky Way the contribution of the potential from the gas could be larger.

Studies have suggested that simulations exploring the influence of the host galaxy require the most dark matter dominated dSphs which are devoid of gas (e.g. Ursa minor and Draco) to fall into the halo of the Milky Way early on. This is necessary to allow enough time for a number of close passages to the disk of the Milky Way to account for the gradual loss of gas from ram pressure and tidal stripping, and finally, the cessation of star formation when the entire gas component is removed (see, e.g. Mayer *et al.*, 2007).

Wheeler *et al.* (2014) suggest that whatever process is causing the environmental quenching of satellites around massive hosts is extremely inefficient as they find low quenched fractions (around 30 percent) for satellites with stellar masses in the range $10^{8.5} - 10^{9.5} M_{\odot}$. Quenching satellites via an AGN outflow could be a fairly inefficient process, as the ability of the outflow to quench the galaxies through ram pressure stripping depends on many factors including; the orientation of the satellites relative to the outflow, the distance of the satellite to the host galaxy, their surface density at the time they interact with the outflow and their position relative to the outflow, as well as the time they fell into the Milky Way halo (or other host galaxy). In this work we assume the outflow is spherical; in reality this outflow could be collimated, or could have started off as spherical close to the galaxy and gained an asymmetrical shape as it moved through the halo. An asymmetric outflow would not have the same impact on all satellites around a host galaxy, and so could possibly be responsible for differing evolutionary histories. This AGN quenching process could also have implications for the dSphs located much farther away from the Milky Way, Cetus and Tucana (at distances of 780 and 890kpc respectively), which are very difficult to explain with current models as it is doubtful their orbits would have resulted in them being close enough to the Milky Way for processes like ram pressure and tidal stripping to have had an impact. Although the density of the outflow would be much smaller at large distances, the velocity could continue to increase (McQuillin and McLaughlin, 2012), giving a ram pressure large enough to have a significant impact on the dwarf.

In general, we find that the impact of an AGN outflow does not trigger star formation in our model dwarfs, despite the ram pressure of the outflow being larger than the thermal pressure of the disk (with the exception of the central regions of our model dwarfs with $r_s=300\text{pc}$, see figure 4.1). We do see some low level star formation in the simulations with the lowest ram pressure outflow ($V_{sh}=250\text{kms}^{-1}$ at 100kpc) for the higher density dwarf with $r_s=300\text{pc}$. However, the disk is able to form a comparable number of stars in isolation and so the outflow is not necessary for this. The presence of the outflow is able to compress gas and trigger star formation slightly earlier ($\sim 30\text{Myr}$) in the edge-on orientation of this dwarf than for the same dwarf in isolation, however it is a very small effect which will not impact on the overall evolution of the dwarf. For the same simulations in the face-on orientation, the presence of the outflow hinders star formation: while it still continues at a low level, less stars are formed than for the isolated case.

The lower density disk does not form stars in isolation until at least 400Myr have passed, needing a greater amount of time for the gas to cool and collapse to reach the required densities. The presence of the outflow does not encourage star formation in either orientation. In fact it acts to prevent the central densities from increasing during the simulation and they do not reach those required for star formation.

In general, the outflow prevents star formation in dwarfs where it can occur in isolation, without any help from external effects. In cases where the densities are too low for star formation in isolation, it prevents them forming any more stars. For the outflow to compress gas in dwarf galaxy disks the gas is required to be at reasonably high densities already, which results in the outflow not being solely responsible for any star formation, since the high density gas would collapse unaided regardless of the passage of the outflow. We find that if a dwarf has a density so low that it cannot form stars (or where the cooling timescales are too long) the outflow will not compress gas to high enough densities to trigger star formation. It is difficult to see whether dwarfs with different properties could have star formation triggered in this way, as the requirement $P_{shell} > P_{disk}$ would not be fulfilled for more massive, higher density disks, where the thermal pressure would be much larger.

4.6 Conclusion

We have performed simulations to explore the impact of ram pressure stripping by an external AGN outflow, on dSph progenitors at high redshift. We find that outflows are

unlikely to trigger a burst of star formation in nearby dSphs, and will only do so in dwarfs that are able to form stars regardless of whether or not the outflow is present. If the gas density in the dwarf is sufficiently high enough to form stars then the gas will be stripped away.

Although we are not able to reproduce any detailed properties of the present day dSphs due to the focus of our simulation, we show that it is possible to remove significant amounts of gas. Ram pressure stripping from an external AGN outflow can remove the entire gas component in some scenarios, without the requirement of an early infall into the halo and several close passages with the Milky Way disk.

Removing gas via this process is more reliable than tidal stripping and ram pressure stripping by the gaseous halo. There is no need to reduce the size of the potential well by forming a cored dark matter profile or requiring SNe feedback to make the gas hot and extended as the magnitude of the ram pressure is high enough to strip the gas unaided.

The diverse SFHs of the dwarfs cannot be explained with AGN outflows, but we are able to remove all gas from some dSph progenitors, leaving behind dark haloes which still host an ancient stellar population.

Chapter 5

Cold mode accretion in dSph progenitors

5.1 Introduction

Our current understanding of galaxy formation in a Λ CDM cosmology is that small structures grow more massive through mergers and accretion of gas. The nature of the cosmic web leads to the existence of a network of dense intergalactic filaments of gas and dark matter connecting galaxies, as seen in cosmological simulations (see, e.g. Harford *et al.*, 2008; Dekel *et al.*, 2009). These filaments transport cold gas directly into the central regions of galaxies at the intersections of filaments. Several authors have found that the inflow of cold gas along filaments is the dominant mode through which most low-mass galaxies ($\leq 10^{11} M_{\odot}$) gain the bulk of their baryonic mass ('cold mode' accretion) at high redshift (Birnboim and Dekel, 2003; Kereš *et al.*, 2005, 2009; Dekel *et al.*, 2009; Brooks *et al.*, 2009).

The supply of gas from the cosmic web has a dependence both on redshift and halo mass, becoming much less efficient at low redshift, ($z < 2$) as haloes grow more massive. Cold gas can only be transported deep inside the virial radius of a halo when it is small enough to avoid the gas being shock heated, which would then take a long time to cool and settle into the galaxy disk. These simulations have found that the majority of the gas accreted on to low-mass haloes is never heated to the virial temperature of the halo, allowing it to penetrate to the centre. This has significant implications for the evolution of galaxies at early times as the gas supply will determine the fate of the smallest galaxies hosted by low-mass haloes at high redshift ($z > 10$).

Although it is difficult to untangle the origin of the visible gas around large galaxies there are possible observations of filaments feeding cold, low density gas into galaxies (detectable $\text{Ly}\alpha$ emission induced by an external source of ionizing photons e.g. the galaxy itself Rauch *et al.* (see, e.g. 2011)). The ability of these filaments to transport cold gas directly into the disk, making it readily available as fuel for star formation has significant implications for understanding the star formation histories (SFHs) of the smallest galaxies. A steady supply of gas enables the possibility of continuous star formation, absent of delays introduced when gas is expelled to larger radii by supernovae and stellar winds, which requires additional time to cool and fall back onto the disk.

The $z \sim 10$ progenitors of dwarf spheroidal galaxies lie in the redshift and halo mass ranges for which cold mode accretion is expected to be significant (Kereš *et al.*, 2005, 2009). The lowest luminosity dSphs host predominantly old stellar populations ($>13\text{Gyr}$), such as Ursa Minor, Draco and Sextans, and so these dwarfs will have been building the vast majority of their stellar populations during a time when the cold gas supply rate was high. The stellar populations of the four least luminous dSphs do not display a metal-rich cut-off, which implies that external effects from the host galaxy such as ram pressure stripping are not required to account for the Metallicity distribution functions (MDFs). This indicates that star formation in these low mass systems may have ceased before they fell into the halo of the Milky Way, and so other processes are needed to quench the galaxies of gas.

At redshifts $z \geq 10$ the progenitors of the dSphs would have resided in haloes around two orders of magnitude smaller than present, raising questions as to how they could retain enough gas after an episode of star formation to fuel a further burst. As we explored in Cashmore *et al.* (2017), lower SNe numbers than expected are required for the dwarfs in our simulations to retain a significant amount of gas for fuel to form the remainder of their stellar population. These simulations involved isolated dwarfs, neglecting the effect of the environment on the evolution of the galaxy. Detailed modelling of the metallicity distribution function (MDF) of Ursa Minor (and other low-mass dSphs) favours models including gas inflow (Kirby *et al.*, 2013), so it is plausible that dwarfs like Ursa Minor were undergoing gas accretion while they were building up the bulk of their stellar population, providing a fresh supply of primordial gas to fuel further SF.

The studies mentioned above focus on larger galaxies at moderate redshifts ($z \sim 3$). The importance of gas accretion is greater for the progenitors of dSphs as their shallow potential wells make it much more likely that a significant amount of gas is lost through

the process of stellar feedback during the formation of the first stars in the galaxy at high redshift. Although at these scales, outflowing gas resulting from SNe feedback is also more significant than that from larger galaxies, as their smaller potential wells allow large masses of gas to be ejected. This could act to disrupt and/or limit the gas accretion onto a dSph and is a potential issue for accretion of cold gas. Outflowing gas could limit the accretion of cold gas in two ways; by disrupting the transport of inflowing gas to the centre of the galaxy if they are spatially coincident, or by heating the inflowing gas to higher temperatures, preventing it from cooling and reaching the disk where it can contribute to star formation. The effect of outflowing winds produced by SNe feedback on the dense filaments of inflowing gas has been explored by several authors for larger galaxies ($M_{\text{vir}} > 10^{11} M_{\odot}$) at $z \sim 3$ (see, e.g. Theuns *et al.*, 2002; Kollmeier *et al.*, 2006; Kawata and Rauch, 2007; Oppenheimer *et al.*, 2010; Faucher-Giguère *et al.*, 2011), who found that the impact is minimal as the enriched gas tends to escape towards the low density regions, expanding into the voids and leaving the filaments intact.

Large scale cosmological simulations lack the resolution to investigate the accretion of gas on the smallest scales, therefore they mainly focus on larger galaxies at lower redshifts than we are interested in. In this chapter we run idealised high resolution simulations of isolated dSph progenitors interacting with inflowing gas to try and deepen our understanding of the cold accretion processes on these scales. We also explore the effect SNe feedback has on cold mode accretion. In section 5.2 we describe the models and the code used to simulate them, in section 5.3 we present the results, followed by a discussion in section 5.4.

5.2 Hydrodynamical simulations

The simulations presented in this chapter are performed with a modified version of the Nbody plus hydrodynamics code GADGET-2 (Springel, 2005) including prescriptions for radiative cooling, star formation and thermal stellar feedback (see chapter 2.1 for a full discussion). In order to properly resolve mixing of the multiphase gas, the SPHS formalism is used (Read *et al.*, 2010; Read and Hayfield, 2012). This requires a larger number of neighbours and we therefore use a Wendland C2 kernel with 100 neighbours to suppress the occurrence of the pairing instability (Wendland, 1995; Dehnen and Aly, 2012). The SPH particles have a constant number of neighbours which results in adaptive smoothing and gravitational softening lengths, decreasing as density increases. The collisionless particles have a constant gravitational softening length of 2pc. In all of our simulations the gas and

star particles have a mass of $10M_{\odot}$ and the dark matter particle mass is $100M_{\odot}$.

Radiative cooling of the gas is included, assuming ionization equilibrium following the method of Katz *et al.* (1996) down to 10^4K . Below 10^4K cooling is modelled as described in Mashchenko *et al.* (2008) via the fine structure and metastable lines of heavy elements. We assume a metallicity of $[\text{Fe}/\text{H}]=-3$. We use a density criterion for star formation:

$$\rho_{crit} = \rho_{thresh} + \rho_J, \quad (5.1)$$

where $\rho_{thresh}=5.01 \times 10^{-22} \text{gcm}^{-3}$, equivalent to $300 \text{ atoms cm}^{-3}$. ρ_J is the local Jeans density, given by:

$$\rho_J = \left(\frac{\pi k_B T}{\mu m_p G} \right)^3 n_{ngb} m_{sph}^{-2}, \quad (5.2)$$

where $n_{ngb}=100$ is the number of SPH neighbours and m_{sph} is the SPH particle mass. These conditions ensure that stars only form in regions where the gas is both dense enough to be molecular and unstable to gravitational collapse. Particles that fulfil this criterion are candidate star particles, and are turned into star particles with a probability $P = 1 - e^{-0.1\delta t/t_{ff}}$, where δt is the current timestep of the particle and t_{ff} is the local free fall time. Our high mass resolution enables us to form star particles that represent individual stars, however we are only interested in the possible triggering of star formation and so do not model any other properties of the stars in these simulations. In particular we form stars of a constant mass.

Stellar feedback is modelled by injecting thermal energy into 100 neighbouring gas particles. The contribution of the total energy to each particle is kernel weighted, depending on their distance from the star particle. We use a total energy of 10^{50}erg per supernova, assuming a coupling efficiency of 10 percent.

5.2.1 Initial conditions

We model the dwarf galaxy as a disk, assuming gas was able to settle and cool into low mass haloes at high redshift. The code 'DiscGO' (Newton and Kay, 2013) was used to create a gas disc which is in equilibrium with the collisionless components. The gas and stellar components follow exponential surface density profiles

$$\Sigma_g(R) = \frac{M_g}{2\pi r_d^2} e^{-R/r_d}, \quad (5.3)$$

and have the same scale length, which for the work in this chapter is $r_d=200\text{pc}$. The scale height of the gas disk is determined assuming the gas is in hydrostatic equilibrium, and the gas is assumed to have an ideal equation of state. The gas and star particles each have masses of $10M_\odot$ and the total masses are $4.8\times 10^6M_\odot$ and 10^4M_\odot , respectively. We used the codes `mkgalaxy` and `mkhalo` (McMillan and Dehnen, 2007) within the NEMO environment (Teuben, 1995) to calculate the initial positions and velocities for the halo particles, taking into account the potential of both the gas and stellar components. In all simulations $M_{200} = 3 \times 10^7 M_\odot$ and $c = 10$, which is a reasonable value for halos at $z \sim 10$ (Klypin *et al.*, 2011). These values imply an NFW scale length of 0.3 kpc and Hernquist parameters of $a_h = 0.5\text{kpc}$ and $r_{200} = 3\text{kpc}$.

We use a live dark matter halo which follows a Hernquist profile (Hernquist, 1990):

$$\rho(r) = \frac{M_{200}}{2\pi} \frac{a_h}{r(r+a_h)^3}, \quad (5.4)$$

where a_h is a scale radius, which when assuming the mass within M_{200} is the same as that for an NFW profile (Navarro *et al.*, 1996b) can be defined by the NFW concentration parameter, c .

5.2.2 Smooth Inflow

We model the smooth inflow of both gas and dark matter as a smooth, constant density filament. We chose the radius of the filament to be equal to the outer radii of each component of the dwarf galaxy. The dark matter and baryonic components have a radius of 3kpc and 1.7kpc, respectively. Both the gas and dark matter components are cut from a relaxed, glass-like particle distribution and adjusted to give a density $50\rho_{crit}=6.91 \times 10^4 M_\odot \text{kpc}^{-3}$ where ρ_{crit} is the critical density of the universe at redshift ~ 10 , given as $\rho_{crit} = 3H^2/8\pi G$. The total dark matter mass is $3\times M_{200}=9 \times 10^7 M_\odot$, giving a filament length of 46kpc. We use a cosmic baryon fraction $f_b=0.16$ to obtain the gas mass, which is $1.44 \times 10^7 M_\odot$. The gas particles are given an internal energy which ensures the filament is in hydrostatic equilibrium.

To calculate the velocity of the filament in the direction of the disk, we use an estimated accretion rate. We assume that the accretion of gas and dark matter onto the dwarf galaxy is complete by redshift ~ 3 and that the dwarf has a final total dark matter mass of $10^9 M_\odot$. Therefore allowing for material to be constantly accreted over this time period ($\sim 2.17\text{Gyr}$), the accretion rate is $\sim 4.5 \times 10^5 M_\odot \text{Myr}^{-1}$ and $\sim 7 \times 10^4 M_\odot \text{Myr}^{-1}$ for dark matter and

Table 5.1: Summary of the runs presented in this chapter, column one describes the simulation, columns two and three list the number of clumps and the velocity of the clumps of inflowing gas, column four lists the respective accretion rates for each run, and column five indicates whether or not the simulations include SNe feedback.

Run	N_{clumps}	V_{clumps} (kms $^{-1}$)	Accretion rate ($M_{\odot}\text{Myr}^{-1}$)	SN FB
(1) Clumpy accretion	700	200	14×10^4	Yes
(2) Clumpy accretion	700	100	7×10^4	Yes
(3) Clumpy accretion	700	50	3.5×10^4	Yes
(4) Clumpy accretion	1400	50	7×10^4	Yes
(5) Clumpy accretion	700	100	7×10^4	No
(6) Isolated disk	0	Yes

gas respectively. This results in a filament velocity of $\sim 220\text{kms}^{-1}$.

5.2.3 Clumpy Inflow

In order to simulate a slightly more realistic method of gas accretion we also consider the inflow of clumps of gas rather than the smooth filament described above. The number of clumps is varied according to the mass accretion rate. The clumps have a constant size and mass, and the internal energy of the gas is defined by assuming hydrostatic equilibrium. The clumps of gas are set up as constant density spheres with a total mass $10^4 M_{\odot}$ and a radius of 50pc. These clumps are simulated in isolation for $\sim 100\text{Myr}$ to allow them to relax and settle into equilibrium, after which time they have a shallow density profile. The clumps are then placed in random positions above the disk, representing an isotropic accretion of gas. The magnitude of the velocity is constant for the runs presented in this paper, the components of velocity are chosen so that each clump hits a random position on the disk. These simulations do not include accretion of dark matter. Table 5.1 lists the simulations presented in this chapter.

Table 5.1 lists the simulations presented in this chapter.

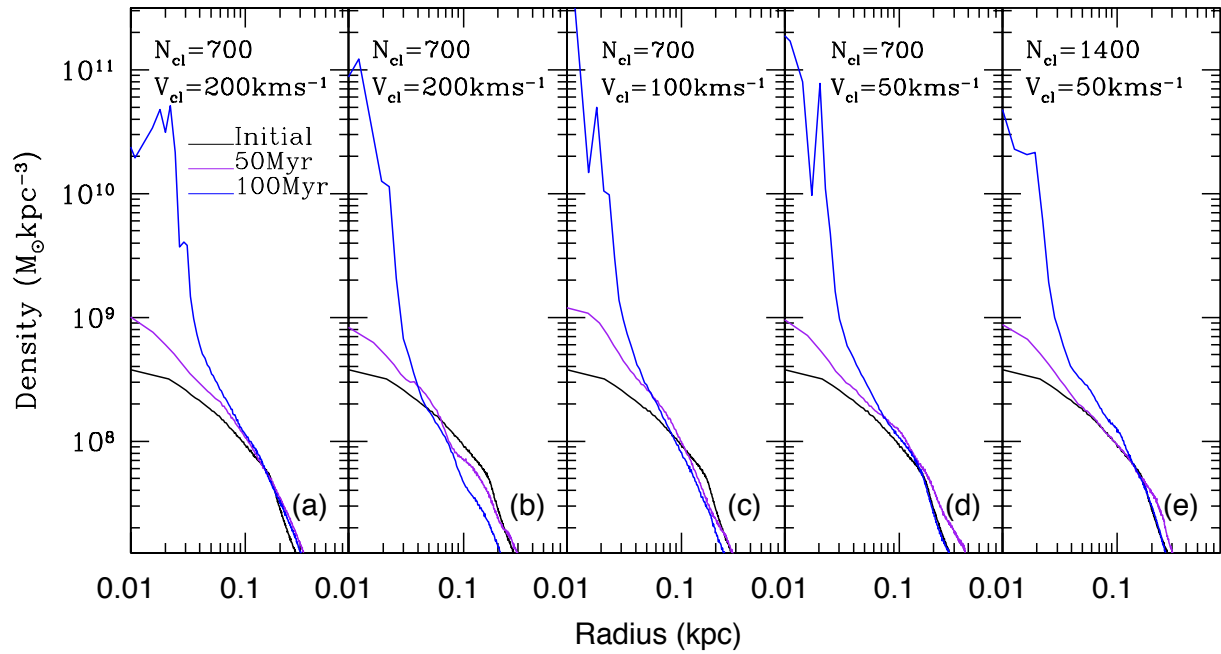


Figure 5.1: Evolution of the density profiles as a function of radius for the gas in runs 1-4 and 6. The profiles for the disk evolved in isolation are shown in panel (a). Panels (b), (c), and (d) show the results for 700 clumps at velocities of 200kms^{-1} , 100kms^{-1} and 50kms^{-1} respectively, while panel (e) shows the results for 1400 clumps at a velocity of 50kms^{-1} . Black lines show the initial density profile, and purple and blue lines show the profiles after 50Myr and 100Myr respectively.

5.3 Results

5.3.1 Clumpy Inflows

The evolution of the density profile for the runs with clumpy inflowing gas are shown in Figure 5.1. Runs with 700 clumps with velocities 200kms^{-1} , 100kms^{-1} and 50kms^{-1} are shown in panels (b), (c) and (d) respectively, and 1400 clumps at a velocity of 50kms^{-1} is shown in panel (e). Black lines represent the initial profile, and purple and blue lines are the resulting profiles after 50Myr and 100Myr. In all runs there is a significant increase in density in the central regions, covering at least two orders of magnitude. Although the inflowing gas is not solely responsible for this significant increase in density, as the gas in the disk is able to cool and collapse towards the centre.

Panels (c) and (e) have the same accretion rate but the velocities of the inflowing gas in the run with 1400 clumps is half that of the run with 700 clumps. The resulting dwarf from the run with 700 clumps with higher velocities has a central density almost an order of magnitude higher than the run with 1400 clumps. The increase in the number of clumps that collide with the disk appears to have a greater impact in the central regions, despite them having lower velocity. A greater number of impacts results in a larger amount of gas being displaced from its original position in the midplane, though this does not necessarily result in gas being completely stripped from the halo, Depending on the size of the displacement it could still be bound to the halo, and could cool and collapse towards the centre at later times. The resulting density profiles suggest that a higher central density is obtained when the number of clumps is lower, and the velocity of inflowing gas for a given number of clumps is lower, although the velocities used here only result in differences of a factor ~ 2 in the central density.

The resulting enclosed mass profiles for the same runs are shown in Figure 5.2. As seen in the evolution of the density profiles, the mass in the central regions increases in all cases. For the highest velocity run, 200kms^{-1} (panel (a)) the total mass within 1kpc decreases to $\sim 4 \times 10^6 M_{\odot}$, as the fast moving inflowing gas causes the disk to be stripped in the outer regions at radii $> 100\text{pc}$. As the velocity is decreased, more mass is retained within 1kpc. An inflow of 700 clumps at 100kms^{-1} (panel (b)) maintains the original gas mass within 1kpc, although the profile shape has changed as the mass in the central regions increases, and the mass in the outer regions decreases. The two runs with a clump velocity of 50kms^{-1} have a larger gas mass within 1kpc after 100Myr, $9 \times 10^6 M_{\odot}$ and $\sim 2 \times 10^7 M_{\odot}$ for 700 and 1400 clumps respectively.

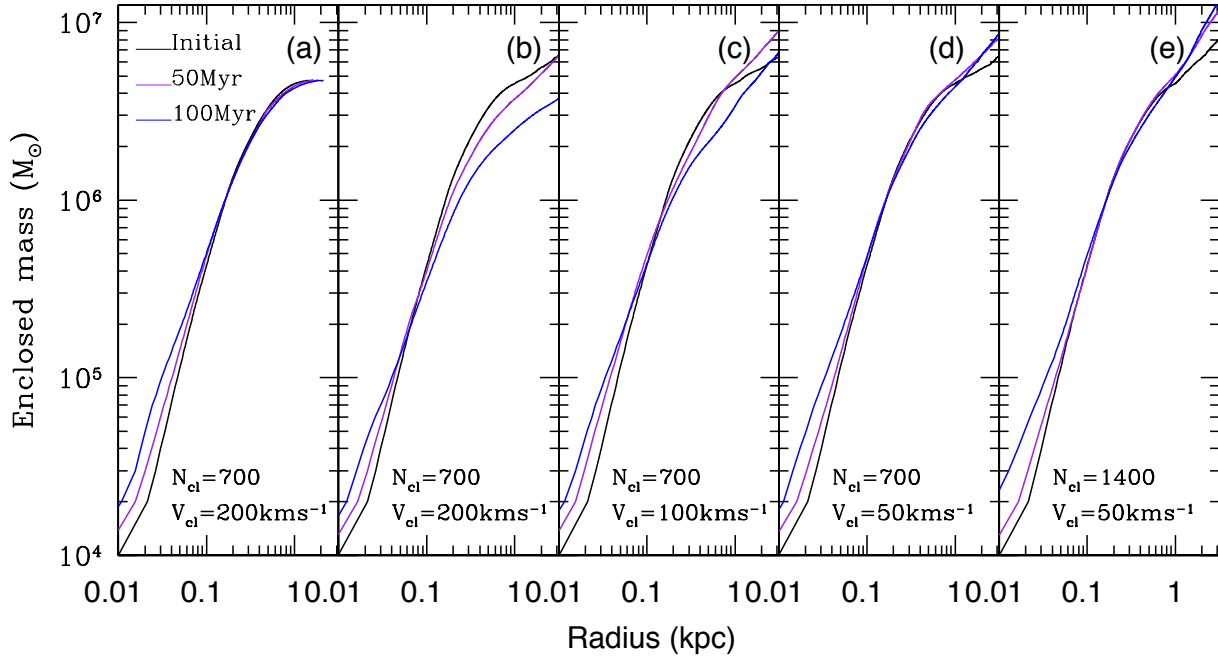


Figure 5.2: Evolution of the enclosed mass profiles as a function of radius for the gas in runs 1-4 and 6. The profiles for the disk evolved in isolation are shown in panel (a). Panels (b), (c), and (d) show the results for 700 clumps at velocities of 200kms^{-1} , 100kms^{-1} and 50kms^{-1} respectively, while panel (e) shows the results for 1400 clumps at a velocity of 50kms^{-1} . Black lines show the initial enclosed mass profile, and purple and blue lines show the profiles after 50Myr and 100Myr respectively.

Although the central gas density at the end of the run with 700 clumps (run 2) is higher than that for the run with 1400 clumps at the same accretion rate (run 4), the total amount of gas left within 1kpc after 100Myr is slightly higher for the latter. Also note that although the central density is almost an order of magnitude higher for run 2 (panel (b) figure 5.1) than for run 4 (panel (d) figure 5.1) the mass within 10pc is actually higher for the run with 1400 clumps at 50kms^{-1} . The impact of the clumps have a different effect on the central regions of these runs. Although the density is higher for run 2, the mass is lower, implying that the distribution of gas is still somewhat flattened, similar to that initially, while the central regions of run 4 have become more extended than the initial distribution, but the amount of mass has increased. So although gas is displaced from the centre of the disk when the number of clumps is increased, it is more likely to remain close to the disk (assuming the accretion rate is the same). It is clear that increasing the velocity with which the clumps impact the disk makes it more difficult to retain gas in these systems. It is unclear whether or not the extra gas that is retained would have an impact on the SFH as it is in the outer regions. Over time this could cool and collapse back towards the centre. However we have only simulated 100Myr of evolution, so if we expect more gas to be continuously accreted in this fashion, it is likely it will remain in a hot, extended state.

Inflowing gas with 700 clumps at 100kms^{-1} is compared to the same run without SNe feedback in Figure 5.3, where solid and dashed lines represent the runs with and without feedback respectively. Surprisingly, neglecting stellar feedback actually results in a decrease in the value of the central density. SNe feedback from stars near the centre of the galaxy therefore must result in gas being pushed into the central regions of the dwarf. The impact of SNe feedback does not therefore limit the amount of mass than can be accreted into the centre of the dwarf, where the density is already high. Figure 5.3 also shows the evolution of the density profile for the isolated disk (dotted lines) including SNe feedback. The gas in the disk is able to cool and collapse to the centre; the presence of SNe feedback does not prevent this (at least in the first 100Myr).

It is the combination of cooling of the original gas in the disk, SNe feedback and inflowing clumps that give the highest density increase after 100Myr. Therefore the overall impact of the inflowing gas results in a higher central density than a dwarf would experience in isolation, possibly allowing for an increase in the star formation rate in this region. It is interesting that these three runs result in relatively similar dwarfs, despite the very different processes that are occurring in each run.

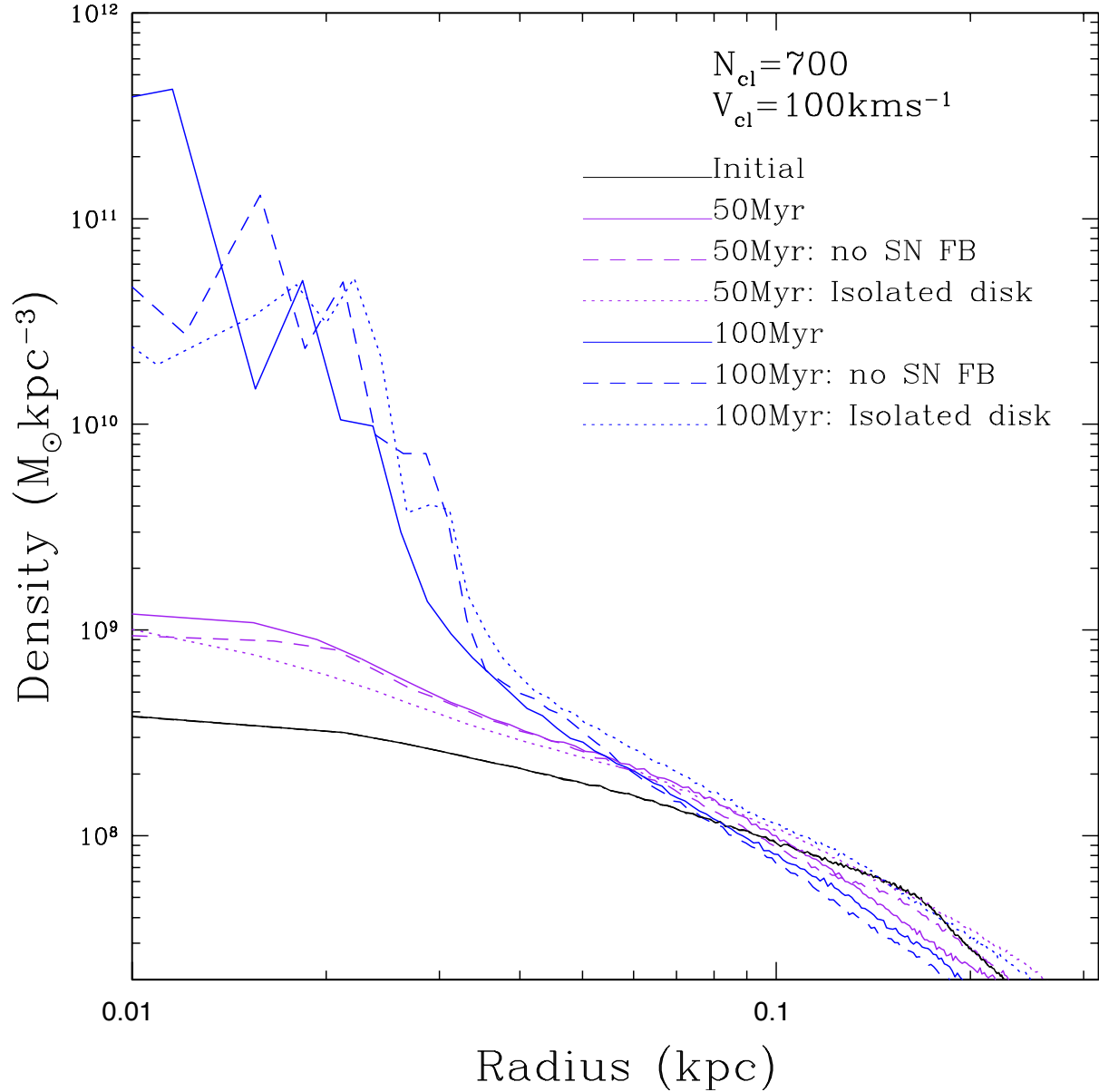


Figure 5.3: Evolution of the density profiles as a function of radius for the gas in runs 1, 5 and 6. The solid black curve shows the initial density profile of the disk (which is the same for all runs). Other solid curves show the evolution of the density profile for run 1 (700 clumps at 100 km s^{-1}). The dashed curves show the evolution of the density profile for the same run with no SNe FB (run 5) and the dotted curves show the profile for the isolated disk (run 6). Purple and blue curves represent the profiles at 50 Myr and 100 Myr respectively.

Table 5.2: The number of stars formed (column four) and accreted gas mass (column five) for each simulation presented in this chapter after a simulation time of 100Myr.

Run	N_{clumps}	V_{clumps} (kms $^{-1}$)	N_{stars}	$M_{gas,accreted}$ (M_{\odot})
(1) Clumpy accretion	700	200	198	0
(2) Clumpy accretion	700	100	673	6.4×10^4
(3) Clumpy accretion	700	50	747	1.3×10^5
(4) Clumpy accretion	1400	50	414	2.15×10^5
(5) Clumpy accretion	700	100	549	4.89×10^4
(6) Isolated disk	0	...	925	...

Figure 5.4 shows maps for the density (top row) temperature (second row) and pressure (third row) for the run with 700 clumps at a velocity of 100kms^{-1} for a slice through the $y=0$ plane. The columns represent times $t=0, 25, 50, 75$ and 100Myr respectively. The first row shows that the impact of the clumps on the disk is to strip some of the gas away in the outer regions where the density is lower. After 100Myr the dwarf no longer resembles a disk, as the gas distribution becomes much more extended and asymmetric. From the second row of figure 5.4 we can see that the passage of the clumps through the disk acts to heat the originally cold gas within the disk up to temperatures of $\sim 10^4 - 10^5\text{K}$. Therefore rather than acting as a fuel supply for star formation, the accretion of gas clumps actually may inhibit star formation through the rise in temperature of the gas.

Figure 5.5 shows the equivalent maps for the run with 1400 clumps with a velocity of 50kms^{-1} . As for the case with 700 clumps at a velocity of 100kms^{-1} the density maps in the top row show that gas is stripped from clumps passing through the outer, less dense regions of the dwarf. However in this case the lower velocity of the clumps causes less of a disturbance in the inner regions. The clumps that pass through at larger radii emerge on the other side of the dwarf with, and are not accreted. The temperature maps in the second row show that although the temperature of the gas is raised by the impact of the clumps, is it not as high as for run 2 (figure 5.4), the maximum temperature here is $\sim 10^4\text{K}$, compared to $T \geq 10^5\text{K}$ for run 2. These two runs have the same accretion rate, but differ in the number of clumps and the velocity of the clumps. Clumps with a higher velocity cause a greater disruption to the gas distribution are able to heat the gas to higher temperatures.

The number of stars formed and the mass of accreted gas for each run after 100Myr is shown in Table 5.2. As the velocity of the clumps are decreased the number of stars

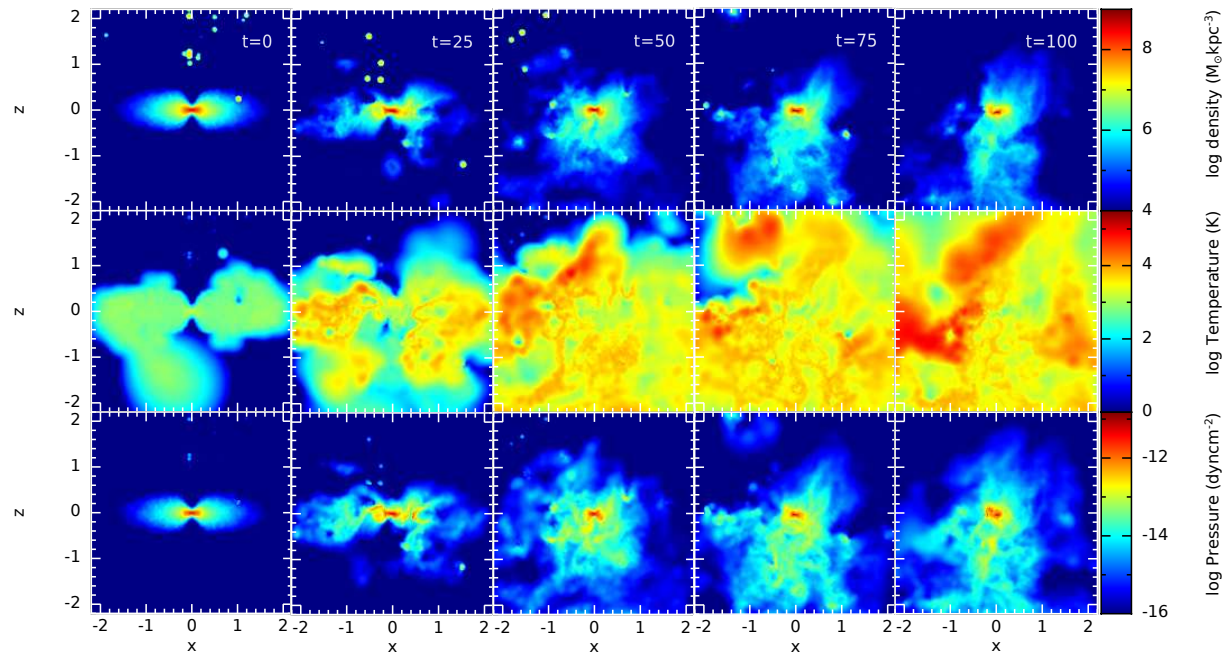


Figure 5.4: Snapshots showing the evolution of the gas density (top row), temperature (second row) and pressure (bottom row) at the beginning of the run (first column) and at 25, 50, 75 and 100Myr for the second, third, fourth and fifth rows respectively for a slice through the $y=0$ plane, for a run with 700 clumps at a velocity of 100kms^{-1} (run 2).

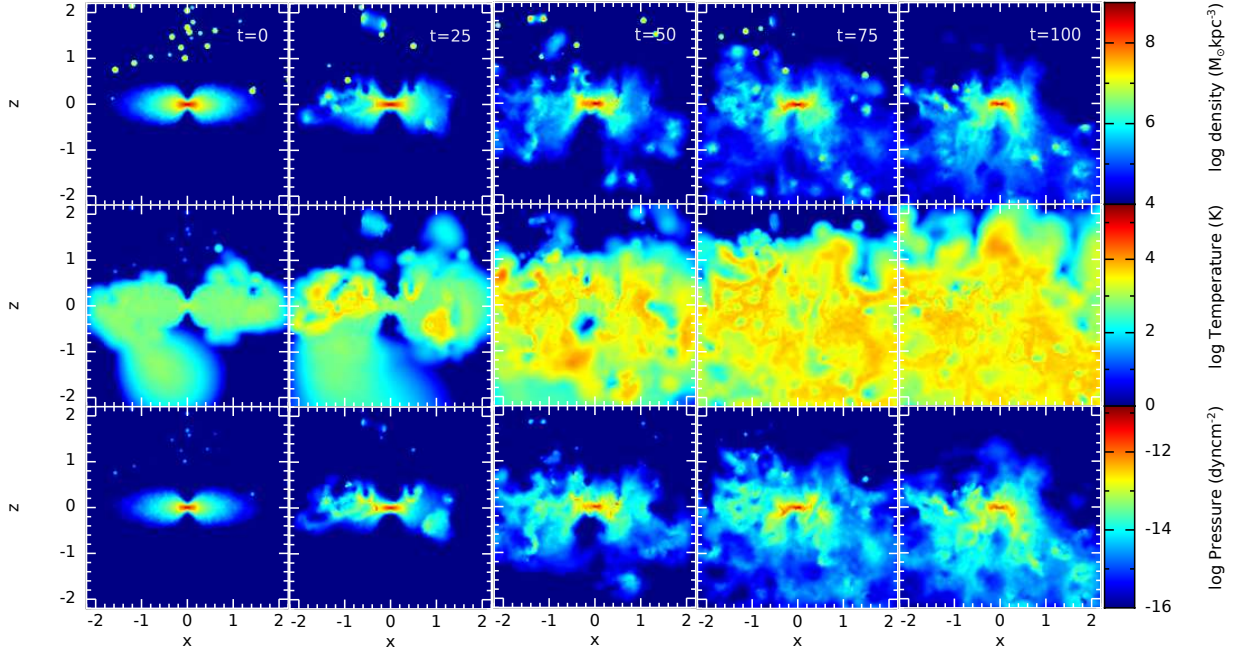


Figure 5.5: Snapshots showing the evolution of the gas density (top row), temperature (second row) and pressure (bottom row) at the beginning of the run (first column) and at 25, 50, 75 and 100Myr for the second, third, fourth and fifth rows respectively for a slice through the $y=0$ plane, for a run with 1400 clumps at a velocity of 50kms^{-1} (run 4).

formed increases for the runs with 700 clumps (rows 1-3). Increasing the number of clumps decreases the number of stars formed by almost a factor of two (runs 3 and 4) for the same clump velocity. However the accreted gas mass is larger in the case for 1400 clumps. The isolated disk forms the most stars within 100Myr, however the central densities are generally higher in the disks experiencing inflowing gas. It's possible that these disks would go on to form more stars when the gas distribution has settled after being disturbed by the inflowing clumps.

5.4 Discussion

In this chapter we have simulated the accretion of gas onto a low-mass halo using simple models of smooth and clumpy inflows. We find that the impact of inflowing gas in a clumpy, isotropic fashion can result in the stripping of gas in the outer regions of the dwarf galaxy disk, and an increase in density in the central regions of several orders of magnitude. The impact of the bombardment of the disk by clumps from all directions

drastically changes the morphology of the dwarf, and after only 100Myr it is no longer posses a disk morphology, but has an extended, asymmetric gas distribution.

The virial temperature of the simulated dwarf galaxies is $\sim 2800\text{K}$, and the inflowing clumps are colder than this, at $T \sim 20\text{K}$. Gas which experiences a strong shock will have its kinetic energy thermalized and be heated to the order of the virial temperature of the host galaxy. As the clumps collide with the disk over the whole surface area from all directions, a significant amount of gas in the dwarf is heated to temperatures higher than the virial temperature. This could potentially inhibit star formation in the disk rather than aid it, depending on the time needed for the gas to cool and fall back to the centre of the halo. As the gas is very low metallicity ($[\text{Fe}/\text{H}]=-3$) the cooling times in low density regions will be long. Higher infall velocities result in the gas in the disk being heated to higher temperatures.

If the clumps of inflowing gas were preferentially directed towards the centre of haloes, it is possible that a much smaller gas mass would be stripped. However concentrating the entire inflow on one region would concentrate the pressure into that region, possibly removing or heating the gas in the centre, preventing any further star formation from occuring. The results of these simulations imply that the distribution of inflowing gas has a large influence on the resulting morphology of the dwarf.

We do not include a gaseous halo in our simulations, and although generally gas is not expected to shock until it reaches the centre of the halo, this could possibly act to slow down the incoming clumps, reducing their impact on the gas disk. This component will ideally be included in future work.

Over the time period of these idealized simulations SNe feedback does not appear to affect the inflowing gas, though this may not be the case for a higher SN rate. In this work we assume there are 100SNe in this system over the period of 1Gyr for reasons described in chapter 3. This number is almost an order of magnitude lower than expected when considering the present day stellar populations for dwarfs like Ursa Minor and Draco. If the rate of SN were increased however, it is unlikely that bubbles of outflowing gas would disturb any inflowing clumps, as some clumps are able to punch through the midplane of the disk, where the density is highest and emerge on the other side. The density of a bubble produced by supernova feedback would need to be significantly higher to destroy the inflowing clumps. However, a more noticeable difference which may occur in the case of a larger number of SNe is the heating of inflowing gas as the bubbles expand outwards, causing the clumps to expand and diminish their impact when they later collide with the

gas disk, deeper inside the dwarf.

If star formation is primarily driven by the accretion of cold gas, this could explain how the dSph progenitors were able to continuously form stars over ~ 3 Gyr, despite gas easily being lost to the IGM due to their low masses. We find that although the inflowing clumps do strip some gas from the midplane at large radii, the gas density in the central regions increases by several orders of magnitude, which will encourage star formation. Star formation could have then ceased when the the supply of infalling gas was halted, either through a close encounter, a merger, or falling into the halo of a massive galaxy. Alternatively, the change in morphology from a dense disk into an extended, asymmetric distribution also enables gas to easily be removed by stellar feedback (see chapter 3).

As is it still unclear exactly how gas is accreted at high redshift, it is difficult to design a simple model to approximate the process. Unfortunately, even cosmological simulations which are zoomed in to a single group of galaxies are limited by resolution due to the large scales required at early times to follow the evolution of each galaxy for billions of years before it falls into the halo of their host galaxy, to the present epoch. These simulations have demonstrated the the process of accreting gas from the cosmic web is far from straightforward for very low mass systems as they are easily disturbed. In order for the total mass to increase to that estimated for the present day dSphs ($\sim 10^9 M_\odot$) over the period $z \sim 10-3$ high inflow velocities are required which risk removing the gas supply rather than adding to it. For galaxies on these mass scales higher accretion rates do not necessarily imply a larger accreted gas mass.

Gabor and Bournaud (2014) find that star formation is delayed in galaxies accreting gas with high inflow rates at high redshift as the star formation efficiency is reduced due to the inflowing gas causing turbulence and heating in the disk. Once the inflow rate decreases star formation can proceed efficiently. We note that after the simulations have been running for 100Myr, the resulting density profiles for all runs show central densities several orders of magnitude larger than that of the initial disk. If dSph progenitors at high redshift reside in different environments, or experience different levels of accretion, then gas accretion could be one of the processes that sets dwarfs on different evolutionary paths at early times, contributing to their present day diversity. To investigate this further, it would be useful to vary several parameters (for example the initial disk density, the number of SNe and the sizes and velocities of the clumps within a single run) to constrain the parameter space where accretion is most effective.

5.5 Conclusion

In this chapter I have shown that the accretion of gas in a clumpy isotropic fashion results in a build up of gas in the central regions and the stripping of gas in the outer regions of the disk. Although the central gas densities are higher in the simulations including gas inflow compared to the isolated disk, the number of stars formed is always lower when inflowing gas is present compared to the isolated disk. This is due to the heating of gas when the clumps collide with the disk and disturb the gas distribution. As the disks in the runs including inflowing gas do accrete a significant amount of gas in this time period, this will be available for further star formation at some point after the gas distribution has settled and cooled.

Outflowing gas driven by SNe feedback does not disrupt the inflowing gas in the case of clumpy accretion, despite the star formation and feedback being very centrally concentrated. It is still unclear exactly how cold gas accretion occurs in these small systems at high redshift as shown in this chapter, they are easily disrupted by the impact of inflowing gas in both the smooth and clumpy cases. More simulations are essential to further this work, cosmological simulations may provide a more realistic approach to modelling the inflowing gas, however this would compromise the high resolution required to resolve the processes occurring in these systems.

Chapter 6

Conclusions

The purpose of the thesis was to explore the processes which influence the evolution of dSph progenitors at early times and to further our understanding of how star formation and gas loss result in the population of dSphs we presently observe in the Local Group. The diverse range of properties presented by the Local Group dSphs is surprising considering the fact that they are all hosted by similar mass dark matter haloes. The ultra faint dwarfs are even more puzzling as they are hosted in even smaller dark matter haloes, making them the smallest galaxies in the present Universe, yet most host extended stellar populations. The details of how star formation would have proceeded in the very early universe, and whether the first galaxies formed stars out of purely primordial gas, or whether it was slightly enriched by even earlier star formation, is still unclear.

It is not well understood how the small haloes that hosted dSphs progenitors retained enough gas during an initial burst of star formation to fuel an extended burst over 3Gyr. Simulating isolated dwarfs is beneficial as it allows a high mass resolution, sufficient to resolve SNe and mixing of the multiphase gas which results from stellar feedback. As mentioned above, the ability of low mass haloes at high redshift with escape velocities of tens of kms^{-1} to retain gas throughout an extended episode of star formation is not well understood. An initial burst of star formation results in many SNe explosions, the combined energy of which exceeds that of the binding energy of the dwarf. We find that in order to retain enough gas for an extended period of star formation, the number of SNe must be reduced compared to that expected from using a standard IMF.

The interaction of an external AGN outflow and a possible dSph progenitor was explored for different values of the ram pressure. An external AGN outflow is an efficient way to remove the bulk of the gas from dSph progenitors at early times, cutting off their gas

supply and preventing any further star formation.

The conclusions from chapter 3 could be explained if there is a supply of inflowing gas at early times when the dSph progenitors were building up the bulk of their stellar populations. The idealized simulations presented in chapter 5 show that although clumpy inflowing gas can potentially strip gas from these galaxies in the lower density regions, it is possible to build up a reservoir of high density gas in the central regions with the accreted material. This gas can then contribute to further star formation to enable a dSph progenitor to continue forming stars despite experiencing episodes of SNe feedback.

In order to gain a deeper understanding of the processes that shape the evolution of dSph progenitors at high redshift, more high resolution simulations need to be performed at these scales rather than in cosmological simulations where these important processes are not resolved sufficiently to understand the details of low mass galaxy formation and evolution.

6.1 Final comments

This thesis has approached the issues around of our vague understanding of the physical processes that shape the evolution of dwarf galaxies by singling out and simplifying different processes. Although the dwarfs are not able to be compared with observations of the present day dSphs, it opens a window to the relative significance of different processes that occur over the lifetime of the dwarf.

To gain the full picture of how evolution proceeds in the systems at high redshift all relevant processes need to be included (UVB, SN feedback, gas accretion, presence of the host galaxy). However as we cannot do this with current cosmological simulations we can learn more from breaking it up into simple processes and investigating each one in turn. It is likely that a very complex evolution produced the diverse properties we presently observe. A possible more realistic solution would be to cosmologically simulate a portion of the very early universe at high resolution to investigate the process of gas accretion, however the galaxies could not then be compared to those we presently observe as the simulation would need to be halted at higher redshifts to remain feasible.

The dwarfs are perhaps the galaxies we most need to resolve in cosmological simulations in order to unlock the mysteries of the high redshift universe, however they are the ones that are the most difficult to study in this way.

Appendix A

Convergence test

To explore the impact of mass resolution on our conclusions, we re-run the fiducial simulation (see table 1) at mass resolutions ten times higher and ten times lower for both the sphere and the disk. We keep the mass of gas into which the SN energy is injected constant ($1000 M_{\odot}$) by changing the *number* of particles receiving energy according to the new mass resolution. Figures A.1 and A.2 show the evolution of the profiles for the gas and halo densities in the spherical and disk cases, respectively.

In the spherical case, reducing the mass resolution to $100 M_{\odot}$ significantly increases the mass of gas which remains after 1.25 Gyr. This emphasises the need for high resolution simulations to capture SNa feedback in dSph progenitors in a realistic way. We note that with $100 M_{\odot}$ resolution, only 10 neighbouring particles receive energy from a SNa which results in too much of the energy being radiated away before it can be deposited in the remaining gas. As is well-known from previous simulations, this means that at low resolution, various numerical tricks (e.g. delayed cooling etc) are required to mimic the impact of SNa feedback.

It is reassuring to note, however, that increasing the resolution by a factor 10 relative to our fiducial run has a limited impact on the evolution of the dSph in the spherical case. In particular, the SNa feedback moves almost all the gas to beyond 1 kpc in both the fiducial and higher resolution runs.

In the case of a dSph model with a gas disk, increasing the resolution has an impact on the gas distribution in the inner 100 pc. This is because the higher resolution model has longer gas cooling times in the inner regions, and the SNe are therefore more effective at removing gas from the inner parts of the dSph. However, Figure A.2 shows that beyond ~ 100 pc the profiles of both gas and dark matter are indistinguishable between the fiducial

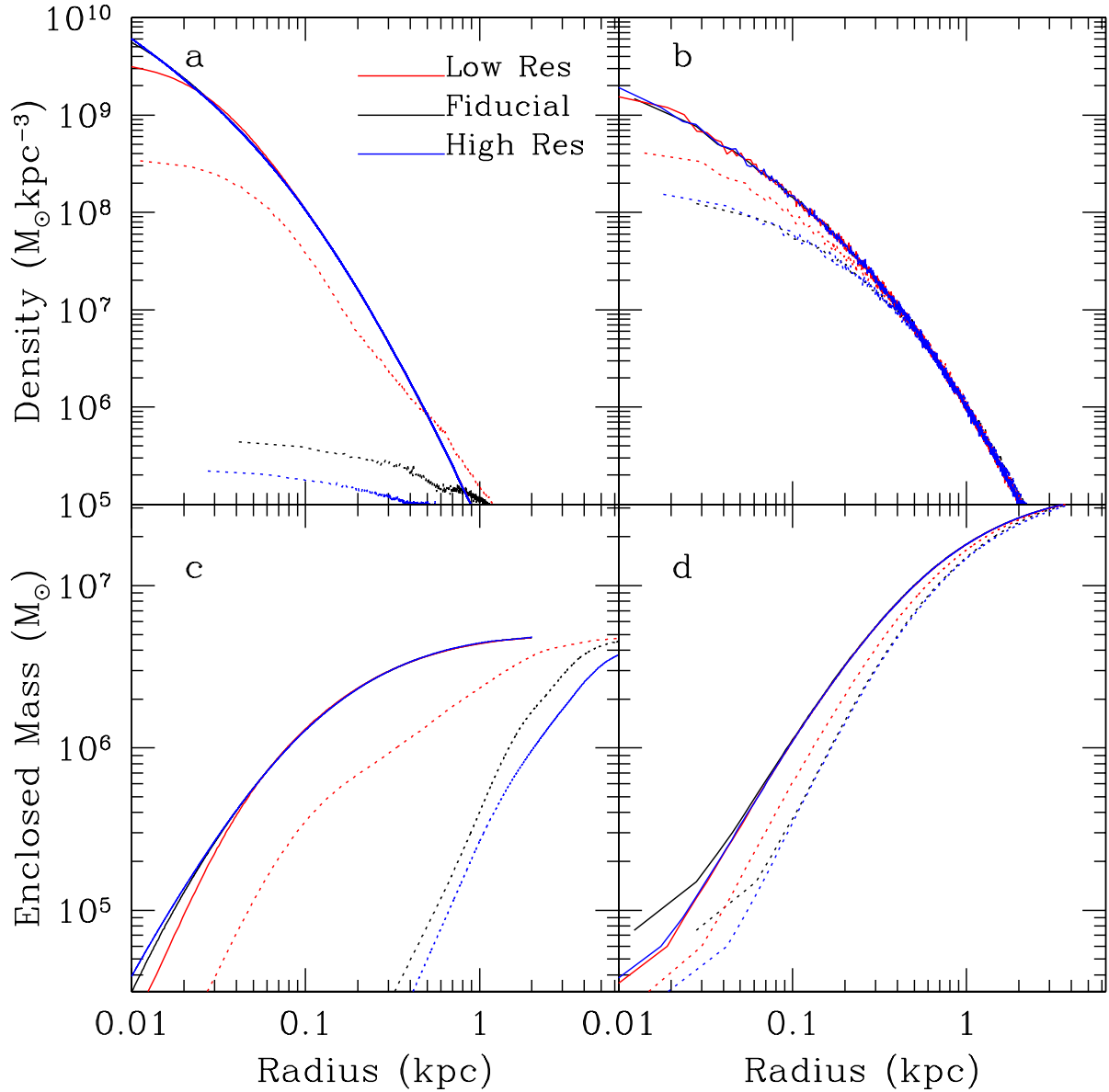


Figure A.1: Evolution of the density (**top**) and enclosed mass (**bottom**) profiles for gas (left) and dark matter (right) for simulated dSphs with an initially spherical gas distribution. In all panels, the solid curves show the initial profiles, and the blue, black and red dashed lines show the resulting profiles after 1.25 Gyr of evolution for simulations with gas particles masses of 1 M_{\odot} , 10 M_{\odot} and 100 M_{\odot} , respectively.

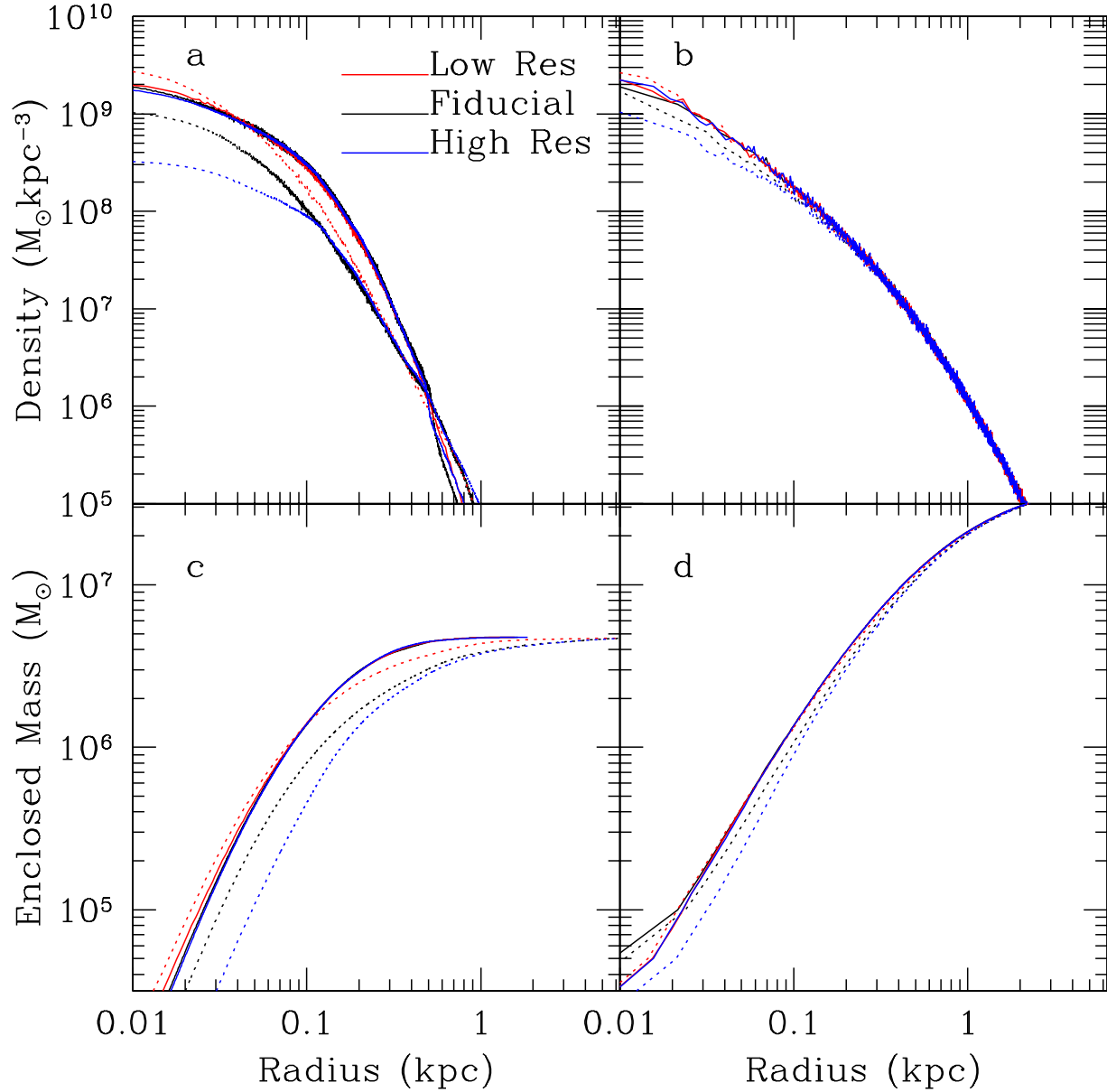


Figure A.2: Evolution of the density (**top**) and enclosed mass (**bottom**) profiles for gas (left) and dark matter (right) for simulated dSphs with gas initially distributed in a disk. In all panels, the solid curves show the initial profiles, and the blue, black and red dashed lines show the resulting profiles after 1.25 Gyr of evolution for simulations with gas particles masses of $1M_{\odot}$, $10M_{\odot}$ and $100M_{\odot}$, respectively.

and high resolution runs. The inner 100pc contain less than 10 per cent of the gas mass in the dSph and therefore we consider that we have correctly captured the evolution of the bulk of the gas in the dSph.

More importantly, we note that our conclusions based on simulations at our fiducial resolution are conservative in the sense that, if anything, we have underestimated the mass of gas that SNa feedback will remove. Our conclusion that it is difficult for a low-mass dSph progenitor halo to retain the gas needed to sustain extended star formation, and hence that the observed dSphs must have been unusual in their initial properties (gas morphology and/or concentration, halo concentration), remains valid at higher resolution.

Appendix B

Stability test

In this Appendix, we consider the long term evolution of both the spherical and disk gas distributions in order to test the stability of our initial conditions. The initial conditions were set up as in section 3.2, and the simulations were run without cooling or SN feedback for 1.25Gyr. The density profiles for the gas and halo in each distribution are shown in figures B.1 and B.2 for the sphere and disk respectively. There is some initial settling to an equilibrium configuration due to the fact that the gas and halo components are set up separately, this is complete after ~ 250 Myr, so for all the runs in the paper we allow the initial conditions to settle for 300Myr before switching on cooling and feedback.

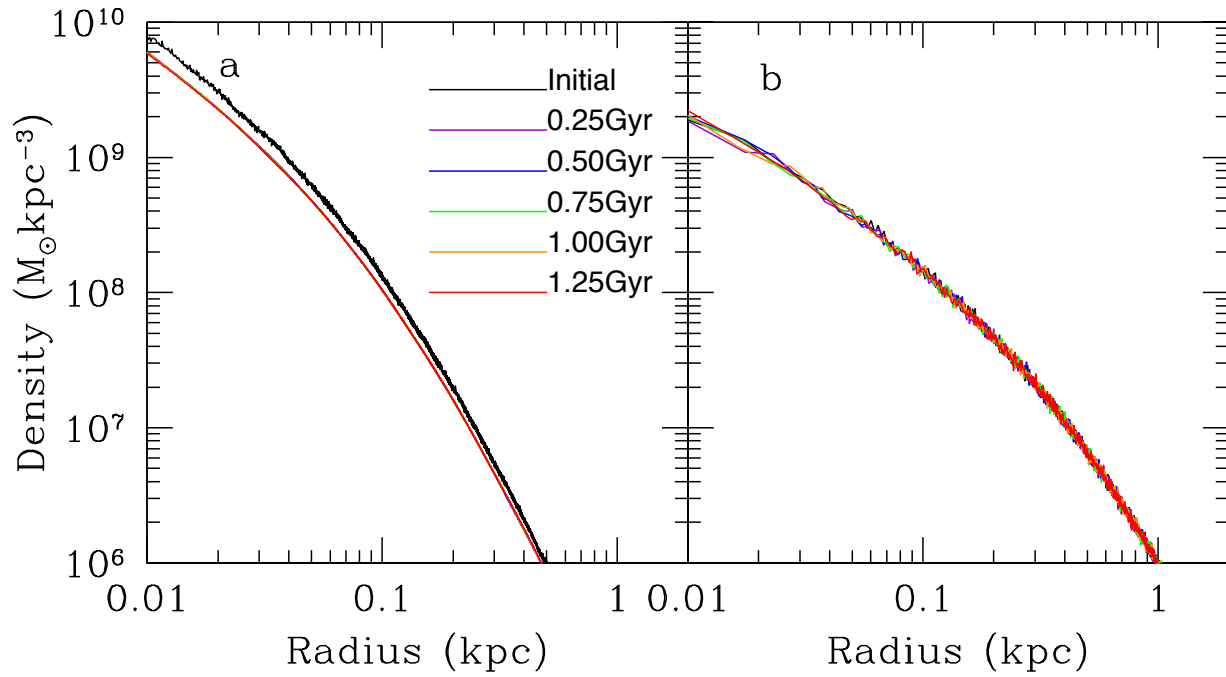


Figure B.1: Evolution of the (a) gas and (b) halo density profiles over time for gas set up in a spherical distribution with no feedback.

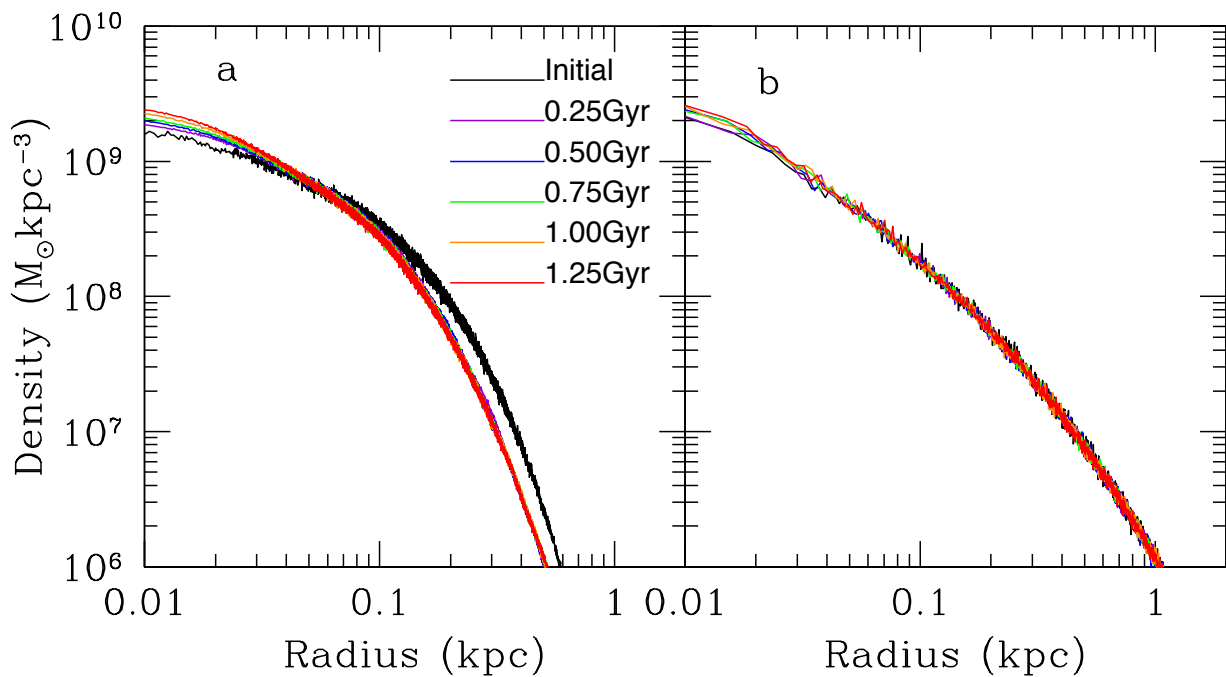


Figure B.2: Evolution of the gas (a) and halo (b) density profiles over time for gas distributed in a disk with no feedback.

Appendix C

Feedback implementations

Modelling the evolution of a SNR is computationally demanding due to the large dynamic range needed to capture physical evolution on a wide range of length scales. Large scale cosmological simulations lack the resolution needed to resolve each SN individually due to numerical over-cooling (see, e.g, Dalla Vecchia and Schaye, 2012) as the high-mass gas particles result in most of the injected energy being radiated away before it can impact the ISM .

In this appendix, we show that we can model individual SNa events with a mass resolution of $10 M_{\odot}$ by injecting the nearest 100 gas particles with 10^{50} erg of thermal energy, kernel-weighted according to their distance from the star particle. At a density of $5 \times 10^8 M_{\odot} \text{kpc}^{-3}$, this corresponds to a spherical radius of ~ 70 pc.

Although we are unable to resolve the initial 'free expansion' phase of a SNR (when the ejecta expand freely while the mass swept up by the forward shock is smaller than the mass ejected) due to the number of particles that are given energy, we can resolve the Sedov Taylor phase. In this phase, an adiabatic blast wave expands into the ISM with $r_{\text{shell}} \propto t^{2/5}$, and total energy is conserved, consisting of 73 per cent thermal and 27 per cent kinetic energy (Durier and Dalla Vecchia, 2012). The movement of the shell is still pressure-driven while the gas interior is hot. When the cooling time of the gas in the shell becomes shorter than the age of the remnant, the shock wave starts to slow. When the interior pressure is exhausted the remnant then enters the snowplough phase with $r_{\text{shell}} \propto t^{1/4}$ and is driven by momentum (momentum is conserved).

The evolution of the shell radius with time is shown in Figure C.1. The shell is defined by taking the maximum density averaged radially in bins of 1pc. The dense shell starts to form at 0.04Myr. As the Figure shows, after this time, the shell expands according to

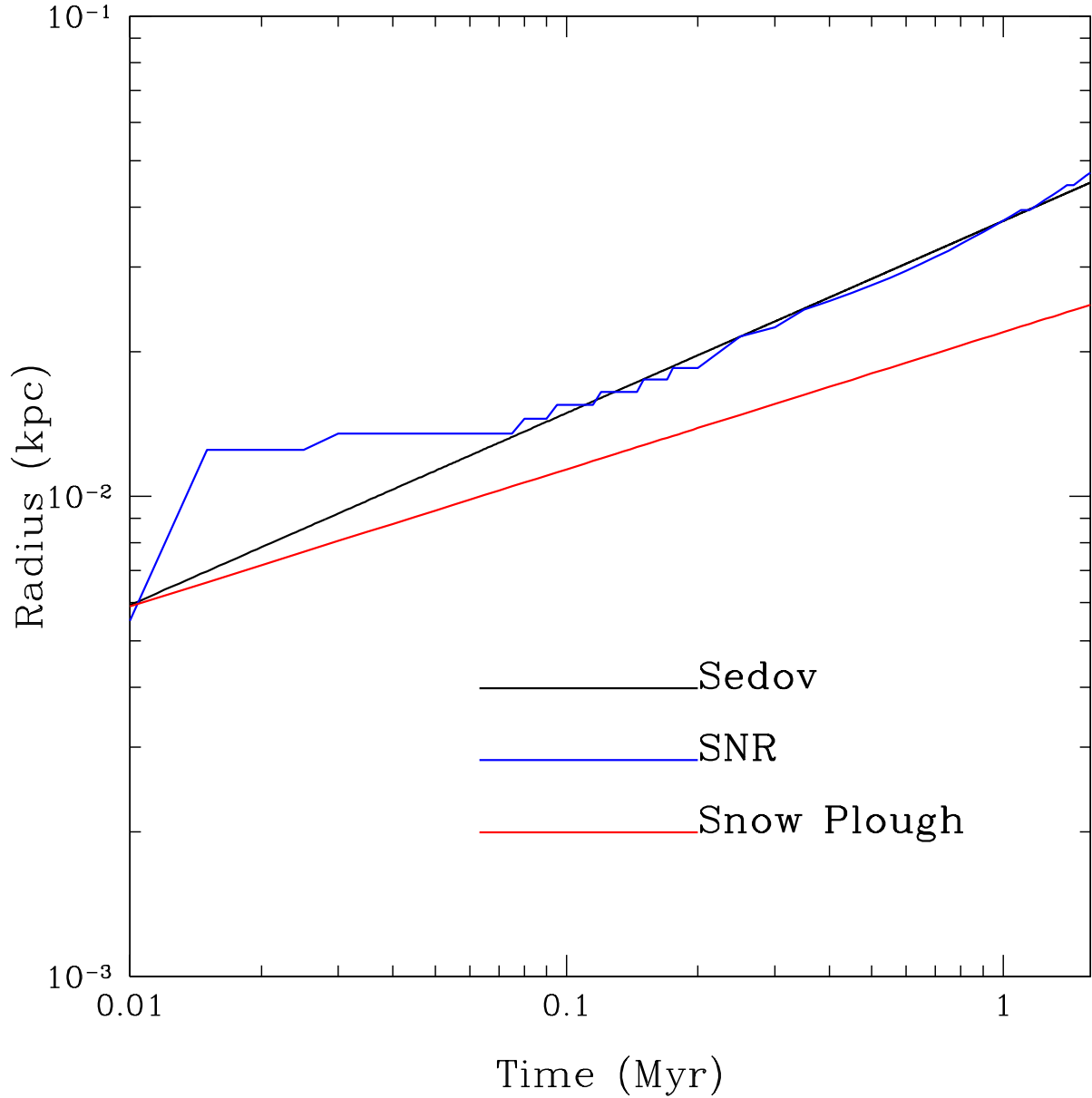


Figure C.1: Evolution of the radius of the SN-driven shell with time where the shell-radius is defined by the peak of the radial density distribution around the SNe. The dense shell forms at 0.04 Myr, and subsequently follows the Sedov-Taylor solution. The black line shows the Sedov-Taylor solution for the growth of the shock front resulting from the injection of 10^{50} ergs of purely thermal energy into a medium of uniform density $5 \times 10^8 \text{ M}_{\odot} \text{ kpc}^{-3}$. The red line shows the time evolution for the momentum-driven phase of shell growth. At later times, the evolution of the SN remnant would follow this line, in the absence of external perturbations from other SNe.

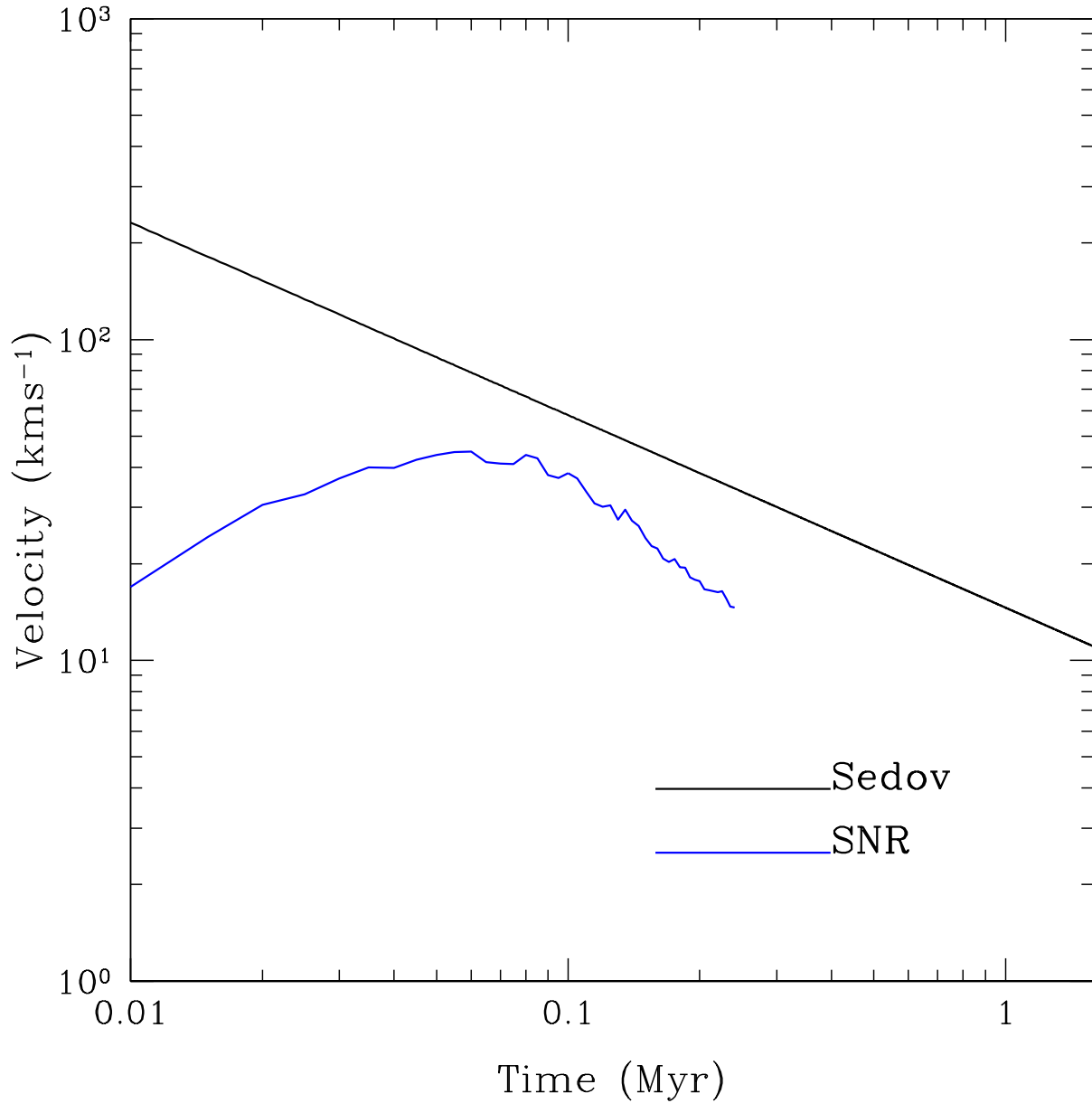


Figure C.2: Evolution of the radial velocity of the SN-driven shell with time where the shell velocity is defined by taking the peak of the average radial velocity in radial bins of width 1pc (blue). The black line shows the Sedov-Taylor solution for the velocity of the shell resulting from the injection of 10^{50} ergs of purely thermal energy into a medium of uniform density $5 \times 10^8 \text{ M}_{\odot} \text{ kpc}^{-3}$.

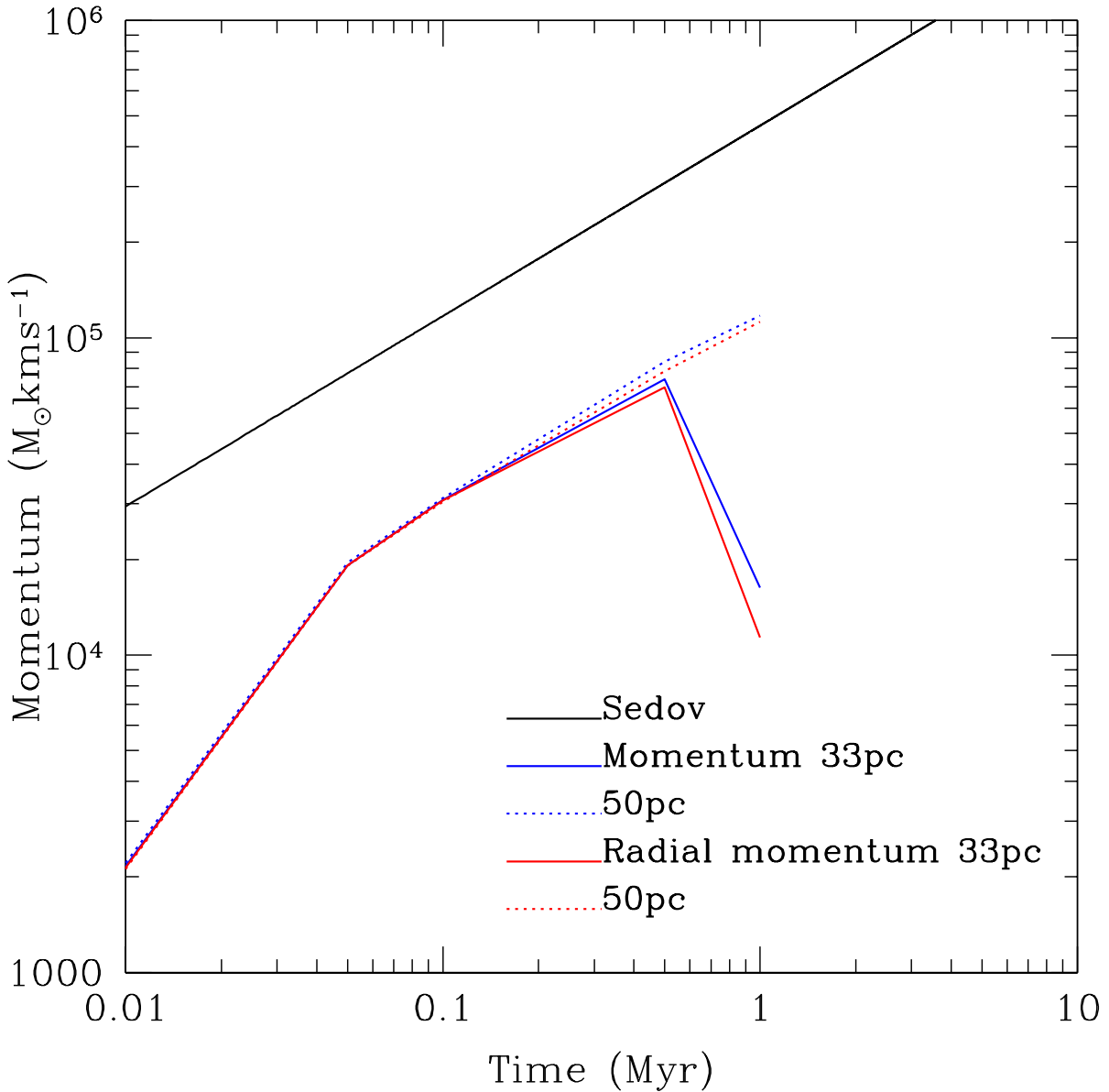


Figure C.3: Evolution of the total (blue - magnitude) and radial (red) momentum in a box of 33pc (solid lines) and 50pc (dashed lines) centred on the SN. The Sedov solution is shown by the solid black line.

the Sedov-Taylor expectation until at least 1 Myr. The initial evolution is due to the fact that we have injected thermal energy only and it therefore takes some time for this energy to be converted into radial momentum and for a well-defined shell to form. Similarly, the evolution of the radial velocity of the shell with time is shown in Figure C.2. Here the shell is defined by taking the average radial velocity in radial bins of width 1pc; the particles in the velocity peak are at slightly larger radii than those with in the density peak. Initially, the velocity is low as the energy injected is thermal; this is gradually converted to kinetic energy and after $\sim 6 \times 10^4$ years the resulting radial velocity is within a factor of two of the velocity predicted by the Sedov-Taylor solution.

Figure C.3 shows the evolution of total momentum (blue) and the radial component of momentum (red) in boxes of size 33pc and 50pc around the SNa. We chose the radius 33pc for the smaller box as this corresponds to our estimated radius of the shell at approximately 0.5 Myr. As the plot clearly shows, all the momentum in the gas is radial and therefore due to the energy input from the SNa event - the drop in radial momentum within 33pc at around 1Myr corresponds to the time when the majority of the shell leaves the 33pc box but is still included in the 50pc box. The growth of the radial momentum follows the Sedov solution, albeit with an amplitude that is about a factor of two lower. We therefore conclude that at the resolution of our simulations, the representation of SNa explosions by thermal energy injections of $\sim 10^{50}$ ergs results in approximately the correct amount of radial momentum being injected into the gas on a length scale of tens of parsecs. As the radial momentum injected is the key factor in determining the evolution of the ISM, our simulations capture all the essential physics of SNa feedback.

Bibliography

- Adén, D., Feltzing, S., Koch, A., Wilkinson, M. I., Grebel, E. K., Lundström, I., Gilmore, G. F., Zucker, D. B., Belokurov, V., Evans, N. W., and Faria, D. (2009). A photometric and spectroscopic study of the new dwarf spheroidal galaxy in Hercules. Metallicity, velocities, and a clean list of RGB members. *A&A*, **506**, 1147–1168.
- Agertz, O., Moore, B., Stadel, J., Potter, D., Miniati, F., Read, J., Mayer, L., Gawryszczak, A., Kravtsov, A., Nordlund, Å., Pearce, F., Quilis, V., Rudd, D., Springel, V., Stone, J., Tasker, E., Teyssier, R., Wadsley, J., and Walder, R. (2007). Fundamental differences between SPH and grid methods. *MNRAS*, **380**, 963–978.
- Agnello, A. and Evans, N. W. (2012). A Virial Core in the Sculptor Dwarf Spheroidal Galaxy. *ApJ*, **754**, L39.
- Amorisco, N. C. and Evans, N. W. (2012). Dark matter cores and cusps: the case of multiple stellar populations in dwarf spheroidals. *MNRAS*, **419**, 184–196.
- Angulo, R. E., Springel, V., White, S. D. M., Jenkins, A., Baugh, C. M., and Frenk, C. S. (2012). Scaling relations for galaxy clusters in the Millennium-XXL simulation. *MNRAS*, **426**, 2046–2062.
- Aparicio, A., Carrera, R., and Martínez-Delgado, D. (2001). The Star Formation History and Morphological Evolution of the Draco Dwarf Spheroidal Galaxy. *AJ*, **122**, 2524–2537.
- Appel, A. W. (1985). An Efficient Program for Many-Body Simulation. *SIAM Journal on Scientific and Statistical Computing*, vol. 6, no. 1, January 1985, p. 85-103., **6**, 85–103.
- Assmann, P., Fellhauer, M., Wilkinson, M. I., and Smith, R. (2013). A possible formation scenario for dwarf spheroidal galaxies - I. Fiducial model. *MNRAS*, **432**, 274–284.

- Babul, A. and Rees, M. J. (1992). On dwarf elliptical galaxies and the faint blue counts. *MNRAS*, **255**, 346–350.
- Balsara, D. S. (1989). Ph.D. thesis, , Univ. Illinois at Urbana-Champaign, (1989).
- Barnes, J. and Hut, P. (1986). A hierarchical $O(N \log N)$ force-calculation algorithm. *Nature*, **324**, 446–449.
- Battaglia, G., Helmi, A., Tolstoy, E., Irwin, M., Hill, V., and Jablonka, P. (2008a). The Kinematic Status and Mass Content of the Sculptor Dwarf Spheroidal Galaxy. *ApJ*, **681**, L13.
- Battaglia, G., Helmi, A., Tolstoy, E., Irwin, M., Hill, V., and Jablonka, P. (2008b). The Kinematic Status and Mass Content of the Sculptor Dwarf Spheroidal Galaxy. *ApJ*, **681**, L13–L16.
- Bechtol, K., Drlica-Wagner, A., Balbinot, E., Pieres, A., Simon, J. D., Yanny, B., Santiago, B., Wechsler, R. H., Frieman, J., Walker, A. R., Williams, P., Rozo, E., Rykoff, E. S., Queiroz, A., Luque, E., Benoit-Lévy, A., Tucker, D., Sevilla, I., Gruendl, R. A., da Costa, L. N., Fausti Neto, A., Maia, M. A. G., Abbott, T., Allam, S., Armstrong, R., Bauer, A. H., Bernstein, G. M., Bernstein, R. A., Bertin, E., Brooks, D., Buckley-Geer, E., Burke, D. L., Carnero Rosell, A., Castander, F. J., Covarrubias, R., D’Andrea, C. B., DePoy, D. L., Desai, S., Diehl, H. T., Eifler, T. F., Estrada, J., Evrard, A. E., Fernandez, E., Finley, D. A., Flaugher, B., Gaztanaga, E., Gerdes, D., Girardi, L., Gladders, M., Gruen, D., Gutierrez, G., Hao, J., Honscheid, K., Jain, B., James, D., Kent, S., Kron, R., Kuehn, K., Kuropatkin, N., Lahav, O., Li, T. S., Lin, H., Makler, M., March, M., Marshall, J., Martini, P., Merritt, K. W., Miller, C., Miquel, R., Mohr, J., Neilsen, E., Nichol, R., Nord, B., Ogando, R., Peoples, J., Petravick, D., Plazas, A. A., Romer, A. K., Roodman, A., Sako, M., Sanchez, E., Scarpine, V., Schubnell, M., Smith, R. C., Soares-Santos, M., Sobreira, F., Suchyta, E., Swanson, M. E. C., Tarle, G., Thaler, J., Thomas, D., Wester, W., Zuntz, J., and DES Collaboration (2015). Eight New Milky Way Companions Discovered in First-year Dark Energy Survey Data. *ApJ*, **807**, 50.
- Becker, R. H., Fan, X., White, R. L., Strauss, M. A., Narayanan, V. K., Lupton, R. H., Gunn, J. E., Annis, J., Bahcall, N. A., Brinkmann, J., Connolly, A. J., Csabai, I., Czarapata, P. C., Doi, M., Heckman, T. M., Hennessy, G. S., Ivezić, Ž., Knapp, G. R., Lamb, D. Q., McKay, T. A., Munn, J. A., Nash, T., Nichol, R., Pier, J. R., Richards,

- G. T., Schneider, D. P., Stoughton, C., Szalay, A. S., Thakar, A. R., and York, D. G. (2001). Evidence for Reionization at $z \sim 6$: Detection of a Gunn-Peterson Trough in a $z=6.28$ Quasar. *AJ*, **122**, 2850–2857.
- Bekki, K. (2015). Formation of Ultra-compact Blue Dwarf Galaxies and Their Evolution into Nucleated Dwarfs. *ApJ*, **812**, L14.
- Bellazzini, M., Fusi Pecci, F., and Ferraro, F. R. (1996). Environmental effects on the structure of the dwarf spheroidal galaxies. *MNRAS*, **278**, 947–952.
- Bellazzini, M., Gennari, N., Ferraro, F. R., and Sollima, A. (2004). The distance to the Leo I dwarf spheroidal galaxy from the red giant branch tip. *MNRAS*, **354**, 708–712.
- Bellazzini, M., Gennari, N., and Ferraro, F. R. (2005). The red giant branch tip and bump of the Leo II dwarf spheroidal galaxy. *MNRAS*, **360**, 185–193.
- Belokurov, V., Zucker, D. B., Evans, N. W., Wilkinson, M. I., Irwin, M. J., Hodgkin, S., Bramich, D. M., Irwin, J. M., Gilmore, G., Willman, B., Vidrih, S., Newberg, H. J., Wyse, R. F. G., Fellhauer, M., Hewett, P. C., Cole, N., Bell, E. F., Beers, T. C., Rockosi, C. M., Yanny, B., Grebel, E. K., Schneider, D. P., Lupton, R., Barentine, J. C., Brewington, H., Brinkmann, J., Harvanek, M., Kleinman, S. J., Krzesinski, J., Long, D., Nitta, A., Smith, J. A., and Snedden, S. A. (2006a). A Faint New Milky Way Satellite in Bootes. *ApJ*, **647**, L111–L114.
- Belokurov, V., Zucker, D. B., Evans, N. W., Gilmore, G., Vidrih, S., Bramich, D. M., Newberg, H. J., Wyse, R. F. G., Irwin, M. J., Fellhauer, M., Hewett, P. C., Walton, N. A., Wilkinson, M. I., Cole, N., Yanny, B., Rockosi, C. M., Beers, T. C., Bell, E. F., Brinkmann, J., Ivezić, Ž., and Lupton, R. (2006b). The Field of Streams: Sagittarius and Its Siblings. *ApJ*, **642**, L137–L140.
- Belokurov, V., Zucker, D. B., Evans, N. W., Kleyna, J. T., Koposov, S., Hodgkin, S. T., Irwin, M. J., Gilmore, G., Wilkinson, M. I., Fellhauer, M., Bramich, D. M., Hewett, P. C., Vidrih, S., De Jong, J. T. A., Smith, J. A., Rix, H.-W., Bell, E. F., Wyse, R. F. G., Newberg, H. J., Mayeur, P. A., Yanny, B., Rockosi, C. M., Gnedin, O. Y., Schneider, D. P., Beers, T. C., Barentine, J. C., Brewington, H., Brinkmann, J., Harvanek, M., Kleinman, S. J., Krzesinski, J., Long, D., Nitta, A., and Snedden, S. A. (2007). Cats and Dogs, Hair and a Hero: A Quintet of New Milky Way Companions. *ApJ*, **654**, 897–906.

- Belokurov, V., Walker, M. G., Evans, N. W., Faria, D. C., Gilmore, G., Irwin, M. J., Koposov, S., Mateo, M., Olszewski, E., and Zucker, D. B. (2008). Leo V: A Companion of a Companion of the Milky Way Galaxy? *ApJ*, **686**, L83.
- Belokurov, V., Walker, M. G., Evans, N. W., Gilmore, G., Irwin, M. J., Mateo, M., Mayer, L., Olszewski, E., Bechtold, J., and Pickering, T. (2009). The discovery of Segue 2: a prototype of the population of satellites of satellites. *MNRAS*, **397**, 1748–1755.
- Belokurov, V., Walker, M. G., Evans, N. W., Gilmore, G., Irwin, M. J., Just, D., Koposov, S., Mateo, M., Olszewski, E., Watkins, L., and Wyrzykowski, L. (2010). Big Fish, Little Fish: Two New Ultra-faint Satellites of the Milky Way. *ApJ*, **712**, L103–L106.
- Benson, A. J., Frenk, C. S., Lacey, C. G., Baugh, C. M., and Cole, S. (2002). The effects of photoionization on galaxy formation - II. Satellite galaxies in the Local Group. *MNRAS*, **333**, 177–190.
- Bernard, E. J., Monelli, M., Gallart, C., Drozdovsky, I., Stetson, P. B., Aparicio, A., Cassisi, S., Mayer, L., Cole, A. A., Hidalgo, S. L., Skillman, E. D., and Tolstoy, E. (2009). The ACS LCID Project. I. Short-Period Variables in the Isolated Dwarf Spheroidal Galaxies Cetus and Tucana. *ApJ*, **699**, 1742–1764.
- Bigiel, F., Leroy, A., Walter, F., Brinks, E., de Blok, W. J. G., Madore, B., and Thornley, M. D. (2008). The Star Formation Law in Nearby Galaxies on Sub-Kpc Scales. *AJ*, **136**, 2846–2871.
- Birnboim, Y. and Dekel, A. (2003). Virial shocks in galactic haloes? *MNRAS*, **345**, 349–364.
- Bonanos, A. Z., Stanek, K. Z., Szentgyorgyi, A. H., Sasselov, D. D., and Bakos, G. Á. (2004). The RR Lyrae Distance to the Draco Dwarf Spheroidal Galaxy. *AJ*, **127**, 861–867.
- Bond, J. R. and Efstathiou, G. (1984). Cosmic background radiation anisotropies in universes dominated by nonbaryonic dark matter. *ApJ*, **285**, L45–L48.
- Bond, J. R., Efstathiou, G., and Silk, J. (1980). Massive neutrinos and the large-scale structure of the universe. *Physical Review Letters*, **45**, 1980–1984.
- Bourne, M. A. and Power, C. (2016). Simulating feedback from nuclear clusters: the impact of multiple sources. *MNRAS*, **456**, L20–L24.

- Bourne, M. A., Nayakshin, S., and Hobbs, A. (2014). Black hole feedback in a multiphase interstellar medium. *MNRAS*, **441**, 3055–3064.
- Boylan-Kolchin, M., Bullock, J. S., and Kaplinghat, M. (2011). Too big to fail? The puzzling darkness of massive Milky Way subhaloes. *MNRAS*, **415**, L40–L44.
- Boylan-Kolchin, M., Bullock, J. S., and Kaplinghat, M. (2012). The Milky Way’s bright satellites as an apparent failure of Λ CDM. *MNRAS*, **422**, 1203–1218.
- Breddels, M. A. and Helmi, A. (2013). Model comparison of the dark matter profiles of Fornax, Sculptor, Carina and Sextans. *A&A*, **558**, A35.
- Breddels, M. A. and Helmi, A. (2014). Complexity on Dwarf Galaxy Scales: A Bimodal Distribution Function in Sculptor. *ApJ*, **791**, L3.
- Brook, C. B., Kawata, D., Gibson, B. K., and Flynn, C. (2004). Stellar halo constraints on simulated late-type galaxies. *MNRAS*, **349**, 52–56.
- Brook, C. B., Governato, F., Roškar, R., Stinson, G., Brooks, A. M., Wadsley, J., Quinn, T., Gibson, B. K., Snaith, O., Pilkington, K., House, E., and Pontzen, A. (2011). Hierarchical formation of bulgeless galaxies: why outflows have low angular momentum. *MNRAS*, **415**, 1051–1060.
- Brooks, A. M. and Zolotov, A. (2014). Why Baryons Matter: The Kinematics of Dwarf Spheroidal Satellites. *ApJ*, **786**, 87.
- Brooks, A. M., Governato, F., Quinn, T., Brook, C. B., and Wadsley, J. (2009). The Role of Cold Flows in the Assembly of Galaxy Disks. *ApJ*, **694**, 396–410.
- Bullock, J. S. (2010). Notes on the Missing Satellites Problem. *ArXiv e-prints*.
- Bullock, J. S., Kravtsov, A. V., and Weinberg, D. H. (2000). Reionization and the Abundance of Galactic Satellites. *ApJ*, **539**, 517–521.
- Bullock, J. S., Stewart, K. R., Kaplinghat, M., Tollerud, E. J., and Wolf, J. (2010). Stealth Galaxies in the Halo of the Milky Way. *ApJ*, **717**, 1043–1053.
- Busha, M. T., Wechsler, R. H., Behroozi, P. S., Gerke, B. F., Klypin, A. A., and Primack, J. R. (2011). Statistics of Satellite Galaxies around Milky-Way-like Hosts. *ApJ*, **743**, 117.

- Cannon, R. D., Hawarden, T. G., and Tritton, S. B. (1977). A new Sculptor-type dwarf elliptical galaxy in Carina. *MNRAS*, **180**, 81P–82P.
- Cappi, M. (2006). Relativistic blue- and red-shifted absorption lines in AGNs. *Astronomische Nachrichten*, **327**, 1012.
- Carlin, J. L., Grillmair, C. J., Muñoz, R. R., Nidever, D. L., and Majewski, S. R. (2009). Kinematics and Metallicities in the Boötes III Stellar Overdensity: A Disrupted Dwarf Galaxy? *ApJ*, **702**, L9–L13.
- Carrera, R., Aparicio, A., Martínez-Delgado, D., and Alonso-García, J. (2002). The Star Formation History and Spatial Distribution of Stellar Populations in the Ursa Minor Dwarf Spheroidal Galaxy. *AJ*, **123**, 3199–3209.
- Cashmore, C. R., Wilkinson, M. I., Power, C., and Bourne, M. (2017). Too small to succeed: the difficulty of sustaining star formation in low-mass haloes. *MNRAS*, **468**, 451–468.
- Castellani, M., Marconi, G., and Buonanno, R. (1996). The Tucana dwarf Galaxy. *A&A*, **310**, 715–721.
- Chan, T. K., Kereš, D., Oñorbe, J., Hopkins, P. F., Muratov, A. L., Faucher-Giguère, C.-A., and Quataert, E. (2015). The impact of baryonic physics on the structure of dark matter haloes: the view from the FIRE cosmological simulations. *MNRAS*, **454**, 2981–3001.
- Chartas, G., Brandt, W. N., Gallagher, S. C., and Garmire, G. P. (2002). CHANDRA Detects Relativistic Broad Absorption Lines from APM 08279+5255. *ApJ*, **579**, 169–175.
- Chou, M.-Y., Majewski, S. R., Cunha, K., Smith, V. V., Patterson, R. J., Martínez-Delgado, D., Law, D. R., Crane, J. D., Muñoz, R. R., Garcia López, R., Geisler, D., and Skrutskie, M. F. (2007). A 2MASS All-Sky View of the Sagittarius Dwarf Galaxy. V. Variation of the Metallicity Distribution Function along the Sagittarius Stream. *ApJ*, **670**, 346–362.
- Cicone, C., Maiolino, R., Sturm, E., Graciá-Carpio, J., Feruglio, C., Neri, R., Aalto, S., Davies, R., Fiore, F., Fischer, J., García-Burillo, S., González-Alfonso, E., Hailey-

- Dunsheath, S., Piconcelli, E., and Veilleux, S. (2014). Massive molecular outflows and evidence for AGN feedback from CO observations. *A&A*, **562**, A21.
- Cohen, J. G. and Huang, W. (2010). The Chemical Evolution of the Ursa Minor Dwarf Spheroidal Galaxy. *ApJ*, **719**, 931–949.
- Cole, S., Aragon-Salamanca, A., Frenk, C. S., Navarro, J. F., and Zepf, S. E. (1994). A Recipe for Galaxy Formation. *MNRAS*, **271**, 781.
- Cole, S., Lacey, C. G., Baugh, C. M., and Frenk, C. S. (2000). Hierarchical galaxy formation. *MNRAS*, **319**, 168–204.
- Coleman, M. G. and de Jong, J. T. A. (2008). A Deep Survey of the Fornax dSph. I. Star Formation History. *ApJ*, **685**, 933–946.
- Coleman, M. G., de Jong, J. T. A., Martin, N. F., Rix, H.-W., Sand, D. J., Bell, E. F., Pogge, R. W., Thompson, D. J., Hippelein, H., Giallongo, E., Ragazzoni, R., DiPaola, A., Farinato, J., Smareglia, R., Testa, V., Bechtold, J., Hill, J. M., Garnavich, P. M., and Green, R. F. (2007). The Elongated Structure of the Hercules Dwarf Spheroidal Galaxy from Deep Large Binocular Telescope Imaging. *ApJ*, **668**, L43–L46.
- Correa, C. A., Wyithe, J. S. B., Schaye, J., and Duffy, A. R. (2015). The accretion history of dark matter haloes - III. A physical model for the concentration-mass relation. *MNRAS*, **452**, 1217–1232.
- Correnti, M., Bellazzini, M., and Ferraro, F. R. (2009). Red Clump stars in the Boötes III stellar system. *MNRAS*, **397**, L26–L30.
- Cowie, L. L., Songaila, A., Kim, T.-S., and Hu, E. M. (1995). The metallicity and internal structure of the Lyman-alpha forest clouds. *AJ*, **109**, 1522–1530.
- Creasey, P., Theuns, T., Bower, R. G., and Lacey, C. G. (2011). Numerical overcooling in shocks. *MNRAS*, **415**, 3706–3720.
- Crnojević, D., Sand, D. J., Zaritsky, D., Spekkens, K., Willman, B., and Hargis, J. R. (2016). Deep Imaging of Eridanus II and Its Lone Star Cluster. *ApJ*, **824**, L14.
- Cullen, L. and Dehnen, W. (2010). Inviscid smoothed particle hydrodynamics. *MNRAS*, **408**, 669–683.

- Da Costa, G. S., Hatzidimitriou, D., Irwin, M. J., and McMahon, R. G. (1991). The radial velocity and metal abundance of the Sextans dwarf spheroidal galaxy. *MNRAS*, **249**, 473–480.
- Dalla Vecchia, C. and Schaye, J. (2008). Simulating galactic outflows with kinetic supernova feedback. *MNRAS*, **387**, 1431–1444.
- Dalla Vecchia, C. and Schaye, J. (2012). Simulating galactic outflows with thermal supernova feedback. *MNRAS*, **426**, 140–158.
- Dall’Ora, M., Clementini, G., Kinemuchi, K., Ripepi, V., Marconi, M., Di Fabrizio, L., Greco, C., Rodgers, C. T., Kuehn, C., and Smith, H. A. (2006). Variable Stars in the Newly Discovered Milky Way Satellite in Bootes. *ApJ*, **653**, L109–L112.
- Dark Energy Survey Collaboration, Abbott, T., Abdalla, F. B., Aleksić, J., Allam, S., Amara, A., Bacon, D., Balbinot, E., Banerji, M., Bechtol, K., Benoit-Lévy, A., Bernstein, G. M., Bertin, E., Blazek, J., Bonnett, C., Bridle, S., Brooks, D., Brunner, R. J., Buckley-Geer, E., Burke, D. L., Caminha, G. B., Capozzi, D., Carlsen, J., Carnero-Rosell, A., Carollo, M., Carrasco-Kind, M., Carretero, J., Castander, F. J., Clerkin, L., Collett, T., Conselice, C., Croce, M., Cunha, C. E., D’Andrea, C. B., da Costa, L. N., Davis, T. M., Desai, S., Diehl, H. T., Dietrich, J. P., Dodelson, S., Doel, P., Drlica-Wagner, A., Estrada, J., Etherington, J., Evrard, A. E., Fabbri, J., Finley, D. A., Flaugh, B., Foley, R. J., Fosalba, P., Frieman, J., García-Bellido, J., Gaztanaga, E., Gerdes, D. W., Giannantonio, T., Goldstein, D. A., Gruen, D., Gruendl, R. A., Guarnieri, P., Gutierrez, G., Hartley, W., Honscheid, K., Jain, B., James, D. J., Jeltima, T., Jouvel, S., Kessler, R., King, A., Kirk, D., Kron, R., Kuehn, K., Kuropatkin, N., Lahav, O., Li, T. S., Lima, M., Lin, H., Maia, M. A. G., Makler, M., Manera, M., Maraston, C., Marshall, J. L., Martini, P., McMahon, R. G., Melchior, P., Merson, A., Miller, C. J., Miquel, R., Mohr, J. J., Morice-Atkinson, X., Naidoo, K., Neilsen, E., Nichol, R. C., Nord, B., Ogando, R., Ostrovski, F., Palmese, A., Papadopoulos, A., Peiris, H. V., Peoples, J., Percival, W. J., Plazas, A. A., Reed, S. L., Refregier, A., Romer, A. K., Roodman, A., Ross, A., Roza, E., Rykoff, E. S., Sadeh, I., Sako, M., Sánchez, C., Sanchez, E., Santiago, B., Scarpine, V., Schubnell, M., Sevilla-Noarbe, I., Sheldon, E., Smith, M., Smith, R. C., Soares-Santos, M., Sobreira, F., Soumagnac, M., Suchyta, E., Sullivan, M., Swanson, M., Tarle, G., Thaler, J., Thomas, D., Thomas, R. C., Tucker, D., Vieira, J. D., Vikram, V., Walker, A. R., Wechsler, R. H., Weller, J.,

- Wester, W., Whiteway, L., Wilcox, H., Yanny, B., Zhang, Y., and Zuntz, J. (2016). The Dark Energy Survey: more than dark energy - an overview. *MNRAS*, **460**, 1270–1299.
- Davis, M., Efstathiou, G., Frenk, C. S., and White, S. D. M. (1985). The evolution of large-scale structure in a universe dominated by cold dark matter. *ApJ*, **292**, 371–394.
- de Blok, W. J. G. and Bosma, A. (2002). High-resolution rotation curves of low surface brightness galaxies. *A&A*, **385**, 816–846.
- de Blok, W. J. G., McGaugh, S. S., Bosma, A., and Rubin, V. C. (2001). Mass Density Profiles of Low Surface Brightness Galaxies. *ApJ*, **552**, L23–L26.
- de Boer, T. J. L., Tolstoy, E., Hill, V., Saha, A., Olszewski, E. W., Mateo, M., Starkenburg, E., Battaglia, G., and Walker, M. G. (2012a). The star formation and chemical evolution history of the Fornax dwarf spheroidal galaxy. *A&A*, **544**, A73.
- de Boer, T. J. L., Tolstoy, E., Hill, V., Saha, A., Olsen, K., Starkenburg, E., Lemasle, B., Irwin, M. J., and Battaglia, G. (2012b). The star formation and chemical evolution history of the sculptor dwarf spheroidal galaxy. *A&A*, **539**, A103.
- de Boer, T. J. L., Tolstoy, E., Lemasle, B., Saha, A., Olszewski, E. W., Mateo, M., Irwin, M. J., and Battaglia, G. (2014). The episodic star formation history of the Carina dwarf spheroidal galaxy. *A&A*, **572**, A10.
- de Jong, J. T. A., Martin, N. F., Rix, H.-W., Smith, K. W., Jin, S., and Macciò, A. V. (2010). The Enigmatic Pair of Dwarf Galaxies Leo IV and Leo V: Coincidence or Common Origin? *ApJ*, **710**, 1664–1671.
- Dehnen, W. (2005). Phase-space mixing and the merging of cusps. *MNRAS*, **360**, 892–900.
- Dehnen, W. and Aly, H. (2012). Improving convergence in smoothed particle hydrodynamics simulations without pairing instability. *MNRAS*, **425**, 1068–1082.
- Dekel, A. and Silk, J. (1986). The origin of dwarf galaxies, cold dark matter, and biased galaxy formation. *ApJ*, **303**, 39–55.
- Dekel, A., Birnboim, Y., Engel, G., Freundlich, J., Goerdt, T., Mumcuoglu, M., Neistein, E., Pichon, C., Teyssier, R., and Zinger, E. (2009). Cold streams in early massive hot haloes as the main mode of galaxy formation. *Nature*, **457**, 451–454.

- Di Cintio, A., Brook, C. B., Dutton, A. A., Macciò, A. V., Stinson, G. S., and Knebe, A. (2014). A mass-dependent density profile for dark matter haloes including the influence of galaxy formation. *MNRAS*, **441**, 2986–2995.
- Dolphin, A. E., Weisz, D. R., Skillman, E. D., and Holtzman, J. A. (2005). Star Formation Histories of Local Group Dwarf Galaxies. *ArXiv Astrophysics e-prints*.
- Drlica-Wagner, A., Bechtol, K., Rykoff, E. S., Luque, E., Queiroz, A., Mao, Y.-Y., Wechsler, R. H., Simon, J. D., Santiago, B., Yanny, B., Balbinot, E., Dodelson, S., Fausti Neto, A., James, D. J., Li, T. S., Maia, M. A. G., Marshall, J. L., Pieres, A., Stringer, K., Walker, A. R., Abbott, T. M. C., Abdalla, F. B., Allam, S., Benoit-Lévy, A., Bernstein, G. M., Bertin, E., Brooks, D., Buckley-Geer, E., Burke, D. L., Carnero Rosell, A., Carrasco Kind, M., Carretero, J., Crocce, M., da Costa, L. N., Desai, S., Diehl, H. T., Dietrich, J. P., Doel, P., Eifler, T. F., Evrard, A. E., Finley, D. A., Flaugher, B., Fosalba, P., Frieman, J., Gaztanaga, E., Gerdes, D. W., Gruen, D., Gruendl, R. A., Gutierrez, G., Honscheid, K., Kuehn, K., Kuropatkin, N., Lahav, O., Martini, P., Miquel, R., Nord, B., Ogando, R., Plazas, A. A., Reil, K., Roodman, A., Sako, M., Sanchez, E., Scarpine, V., Schubnell, M., Sevilla-Noarbe, I., Smith, R. C., Soares-Santos, M., Sobreira, F., Suchyta, E., Swanson, M. E. C., Tarle, G., Tucker, D., Vikram, V., Wester, W., Zhang, Y., Zuntz, J., and DES Collaboration (2015). Eight Ultra-faint Galaxy Candidates Discovered in Year Two of the Dark Energy Survey. *ApJ*, **813**, 109.
- Drlica-Wagner, A., Bechtol, K., Allam, S., Tucker, D. L., Gruendl, R. A., Johnson, M. D., Walker, A. R., James, D. J., Nidever, D. L., Olsen, K. A. G., Wechsler, R. H., Cioni, M. R. L., Conn, B. C., Kuehn, K., Li, T. S., Mao, Y.-Y., Martin, N. F., Neilsen, E., Noel, N. E. D., Pieres, A., Simon, J. D., Stringfellow, G. S., van der Marel, R. P., and Yanny, B. (2016). An Ultra-faint Galaxy Candidate Discovered in Early Data from the Magellanic Satellites Survey. *ApJ*, **833**, L5.
- Dubois, Y. and Teyssier, R. (2008). On the onset of galactic winds in quiescent star forming galaxies. *A&A*, **477**, 79–94.
- Durier, F. and Dalla Vecchia, C. (2012). Implementation of feedback in smoothed particle hydrodynamics: towards concordance of methods. *MNRAS*, **419**, 465–478.
- Ellis, R. S. (1997). Faint Blue Galaxies. *ARA&A*, **35**, 389–443.

- Fakhouri, O., Ma, C.-P., and Boylan-Kolchin, M. (2010). The merger rates and mass assembly histories of dark matter haloes in the two Millennium simulations. *MNRAS*, **406**, 2267–2278.
- Fan, X., Narayanan, V. K., Lupton, R. H., Strauss, M. A., Knapp, G. R., Becker, R. H., White, R. L., Pentericci, L., Leggett, S. K., Haiman, Z., Gunn, J. E., Ivezić, Ž., Schneider, D. P., Anderson, S. F., Brinkmann, J., Bahcall, N. A., Connolly, A. J., Csabai, I., Doi, M., Fukugita, M., Geballe, T., Grebel, E. K., Harbeck, D., Hennessy, G., Lamb, D. Q., Miknaitis, G., Munn, J. A., Nichol, R., Okamura, S., Pier, J. R., Prada, F., Richards, G. T., Szalay, A., and York, D. G. (2001). A Survey of $z > 5.8$ Quasars in the Sloan Digital Sky Survey. I. Discovery of Three New Quasars and the Spatial Density of Luminous Quasars at $z \sim 6$. *AJ*, **122**, 2833–2849.
- Fan, X., Strauss, M. A., Schneider, D. P., Becker, R. H., White, R. L., Haiman, Z., Gregg, M., Pentericci, L., Grebel, E. K., Narayanan, V. K., Loh, Y.-S., Richards, G. T., Gunn, J. E., Lupton, R. H., Knapp, G. R., Ivezić, Ž., Brandt, W. N., Collinge, M., Hao, L., Harbeck, D., Prada, F., Schaye, J., Strateva, I., Zakamska, N., Anderson, S., Brinkmann, J., Bahcall, N. A., Lamb, D. Q., Okamura, S., Szalay, A., and York, D. G. (2003). A Survey of $z > 5.7$ Quasars in the Sloan Digital Sky Survey. II. Discovery of Three Additional Quasars at $z > 6$. *AJ*, **125**, 1649–1659.
- Faucher-Giguère, C.-A., Kereš, D., and Ma, C.-P. (2011). The baryonic assembly of dark matter haloes. *MNRAS*, **417**, 2982–2999.
- Fillingham, S. P., Cooper, M. C., Wheeler, C., Garrison-Kimmel, S., Boylan-Kolchin, M., and Bullock, J. S. (2015). Taking care of business in a flash: constraining the time-scale for low-mass satellite quenching with ELVIS. *MNRAS*, **454**, 2039–2049.
- Fitts, A., Boylan-Kolchin, M., Elbert, O. D., Bullock, J. S., Hopkins, P. F., Oñorbe, J., Wetzel, A., Wheeler, C., Faucher-Giguère, C.-A., Kereš, D., Skillman, E. D., and Weisz, D. R. (2017). fire in the field: simulating the threshold of galaxy formation. *MNRAS*, **471**, 3547–3562.
- Fox, A. J., Richter, P., Wakker, B. P., Lehner, N., Howk, J. C., Ben Bekhti, N., Bland-Hawthorn, J., and Lucas, S. (2013). The COS/UVES Absorption Survey of the Magellanic Stream. I. One-tenth Solar Abundances along the Body of the Stream. *ApJ*, **772**, 110.

- Fraternali, F., Tolstoy, E., Irwin, M. J., and Cole, A. A. (2009). Life at the periphery of the Local Group: the kinematics of the Tucana dwarf galaxy. *A&A*, **499**, 121–128.
- Gabor, J. M. and Bournaud, F. (2014). Delayed star formation in high-redshift stream-fed galaxies. *MNRAS*, **437**, L56–L60.
- Gallart, C., Freedman, W. L., Aparicio, A., Bertelli, G., and Chiosi, C. (1999). The Star Formation History of the Local Group Dwarf Galaxy Leo I. *AJ*, **118**, 2245–2261.
- Gao, Y. and Solomon, P. M. (2004). The Star Formation Rate and Dense Molecular Gas in Galaxies. *ApJ*, **606**, 271–290.
- Garrison-Kimmel, S., Rocha, M., Boylan-Kolchin, M., Bullock, J. S., and Lally, J. (2013). Can feedback solve the too-big-to-fail problem? *MNRAS*, **433**, 3539–3546.
- Geha, M., Blanton, M. R., Masjedi, M., and West, A. A. (2006). The Baryon Content of Extremely Low Mass Dwarf Galaxies. *ApJ*, **653**, 240–254.
- Geha, M., Blanton, M. R., Yan, R., and Tinker, J. L. (2012). A Stellar Mass Threshold for Quenching of Field Galaxies. *ApJ*, **757**, 85.
- Genel, S., Vogelsberger, M., Springel, V., Sijacki, D., Nelson, D., Snyder, G., Rodriguez-Gomez, V., Torrey, P., and Hernquist, L. (2014). Introducing the Illustris project: the evolution of galaxy populations across cosmic time. *MNRAS*, **445**, 175–200.
- Gingold, R. A. and Monaghan, J. J. (1977). Smoothed particle hydrodynamics - Theory and application to non-spherical stars. *MNRAS*, **181**, 375–389.
- Gitti, M., McNamara, B. R., Nulsen, P. E. J., and Wise, M. W. (2007). Cosmological Effects of Powerful AGN Outbursts in Galaxy Clusters: Insights from an XMM-Newton Observation of MS 0735+7421. *ApJ*, **660**, 1118–1136.
- Gnedin, O. Y. and Zhao, H. (2002). Maximum feedback and dark matter profiles of dwarf galaxies. *MNRAS*, **333**, 299–306.
- Gofford, J., Reeves, J. N., Tombesi, F., Braitto, V., Turner, T. J., Miller, L., and Cappi, M. (2013). The Suzaku view of highly ionized outflows in AGN - I. Statistical detection and global absorber properties. *MNRAS*, **430**, 60–80.

- Governato, F., Willman, B., Mayer, L., Brooks, A., Stinson, G., Valenzuela, O., Wadsley, J., and Quinn, T. (2007). Forming disc galaxies in Λ CDM simulations. *MNRAS*, **374**, 1479–1494.
- Governato, F., Brook, C., Mayer, L., Brooks, A., Rhee, G., Wadsley, J., Jonsson, P., Willman, B., Stinson, G., Quinn, T., and Madau, P. (2010). Bulgeless dwarf galaxies and dark matter cores from supernova-driven outflows. *Nature*, **463**, 203–206.
- Governato, F., Zolotov, A., Pontzen, A., Christensen, C., Oh, S. H., Brooks, A. M., Quinn, T., Shen, S., and Wadsley, J. (2012). Cuspy no more: how outflows affect the central dark matter and baryon distribution in Λ cold dark matter galaxies. *MNRAS*, **422**, 1231–1240.
- Greivich, J. and Putman, M. E. (2009). H I in Local Group Dwarf Galaxies and Stripping by the Galactic Halo. *ApJ*, **696**, 385–395.
- Grebel, E. K. and Gallagher, III, J. S. (2004). The Impact of Reionization on the Stellar Populations of Nearby Dwarf Galaxies. *ApJ*, **610**, L89–L92.
- Grebel, E. K., Gallagher, III, J. S., and Harbeck, D. (2003). The Progenitors of Dwarf Spheroidal Galaxies. *AJ*, **125**, 1926–1939.
- Greco, C., Dall’Ora, M., Clementini, G., Ripepi, V., Di Fabrizio, L., Kinemuchi, K., Marconi, M., Musella, I., Smith, H. A., Rodgers, C. T., Kuehn, C., Beers, T. C., Catelan, M., and Pritzl, B. J. (2008). On the Newly Discovered Canes Venatici II dSph Galaxy. *ApJ*, **675**, L73.
- Grillmair, C. J. (2009). Four New Stellar Debris Streams in the Galactic Halo. *ApJ*, **693**, 1118–1127.
- Gunn, J. E. and Gott, III, J. R. (1972). On the Infall of Matter Into Clusters of Galaxies and Some Effects on Their Evolution. *ApJ*, **176**, 1.
- Guo, Q. and White, S. D. M. (2009). High-redshift galaxy populations and their descendants. *MNRAS*, **396**, 39–52.
- Guo, Q., White, S., Boylan-Kolchin, M., De Lucia, G., Kauffmann, G., Lemson, G., Li, C., Springel, V., and Weinmann, S. (2011). From dwarf spheroidals to cD galaxies: simulating the galaxy population in a Λ CDM cosmology. *MNRAS*, **413**, 101–131.

- Hague, P. R. and Wilkinson, M. I. (2013). Dark matter in disc galaxies - I. A Markov Chain Monte Carlo method and application to DDO 154. *MNRAS*, **433**, 2314–2333.
- Harford, A. G., Hamilton, A. J. S., and Gnedin, N. Y. (2008). Intergalactic baryon-rich regions at high redshift. *MNRAS*, **389**, 880–888.
- Hargis, J. R., Willman, B., and Peter, A. H. G. (2014). Too Many, Too Few, or Just Right? The Predicted Number and Distribution of Milky Way Dwarf Galaxies. *ApJ*, **795**, L13.
- Harrington, R. G. and Wilson, A. G. (1950). Two New Stellar Systems in Leo. *PASP*, **62**, 118–120.
- Heckman, T. M., Armus, L., and Miley, G. K. (1990). On the nature and implications of starburst-driven galactic superwinds. *ApJS*, **74**, 833–868.
- Heckman, T. M., Lehnert, M. D., Strickland, D. K., and Armus, L. (2000). Absorption-Line Probes of Gas and Dust in Galactic Superwinds. *ApJS*, **129**, 493–516.
- Heckman, T. M., Sembach, K. R., Meurer, G. R., Strickland, D. K., Martin, C. L., Calzetti, D., and Leitherer, C. (2001). FUSE Observations of Outflowing O VI in the Dwarf Starburst Galaxy NGC 1705. *ApJ*, **554**, 1021–1034.
- Hernquist, L. (1990). An analytical model for spherical galaxies and bulges. *ApJ*, **356**, 359–364.
- Hernquist, L., Katz, N., Weinberg, D. H., and Miralda-Escudé, J. (1996). The Lyman-Alpha Forest in the Cold Dark Matter Model. *ApJ*, **457**, L51.
- Hinshaw, G., Larson, D., Komatsu, E., Spergel, D. N., Bennett, C. L., Dunkley, J., Nolte, M. R., Halpern, M., Hill, R. S., Odegard, N., Page, L., Smith, K. M., Weiland, J. L., Gold, B., Jarosik, N., Kogut, A., Limon, M., Meyer, S. S., Tucker, G. S., Wollack, E., and Wright, E. L. (2013). Nine-year Wilkinson Microwave Anisotropy Probe (WMAP) Observations: Cosmological Parameter Results. *ApJS*, **208**, 19.
- Hodge, P. W. (1961). The Fornax dwarf galaxy. I. The globulars clusters. *AJ*, **66**, 83–84.
- Hoefl, M., Yepes, G., Gottlöber, S., and Springel, V. (2006). Dwarf galaxies in voids: suppressing star formation with photoheating. *MNRAS*, **371**, 401–414.

- Hoefl, M., Yepes, G., and Gottlöber, S. (2008). Too Small to Form a Galaxy: How the UV Background Determines the Baryon Fraction. In J. I. Davies and M. J. Disney, editors, *Dark Galaxies and Lost Baryons*, volume 244 of *IAU Symposium*, pages 279–283.
- Homma, D., Chiba, M., Okamoto, S., Komiyama, Y., Tanaka, M., Tanaka, M., Ishigaki, M. N., Akiyama, M., Arimoto, N., Garmilla, J. A., Lupton, R. H., Strauss, M. A., Furusawa, H., Miyazaki, S., Murayama, H., Nishizawa, A. J., Takada, M., Usuda, T., and Wang, S.-Y. (2016). A New Milky Way Satellite Discovered in the Subaru/Hyper Suprime-Cam Survey. *ApJ*, **832**, 21.
- Hunter, D. A. and Gallagher, III, J. S. (1997). An Emission-line Study of Supergiant Ionized Filaments in Irregular Galaxies. *ApJ*, **475**, 65–82.
- Hurley-Keller, D., Mateo, M., and Nemeč, J. (1998). The Star Formation History of the Carina Dwarf Galaxy. *AJ*, **115**, 1840–1855.
- Ibata, R. A., Gilmore, G., and Irwin, M. J. (1994). A dwarf satellite galaxy in Sagittarius. *Nature*, **370**, 194–196.
- Ibata, R. A., Wyse, R. F. G., Gilmore, G., Irwin, M. J., and Suntzeff, N. B. (1997). The Kinematics, Orbit, and Survival of the Sagittarius Dwarf Spheroidal Galaxy. *AJ*, **113**, 634–655.
- Irwin, M. and Hatzidimitriou, D. (1995). Structural parameters for the Galactic dwarf spheroidals. *MNRAS*, **277**, 1354–1378.
- Irwin, M. J., Bunclark, P. S., Bridgeland, M. T., and McMahon, R. G. (1990). A new satellite galaxy of the Milky Way in the constellation of Sextans. *MNRAS*, **244**, 16P–19P.
- Jardel, J. R. and Gebhardt, K. (2013). Variations in a Universal Dark Matter Profile for Dwarf Spheroidals. *ApJ*, **775**, L30.
- Karachentsev, I. D., Karachentseva, V. E., Huchtmeier, W. K., and Makarov, D. I. (2004). A Catalog of Neighboring Galaxies. *AJ*, **127**, 2031–2068.
- Katz, N., Weinberg, D. H., and Hernquist, L. (1996). Cosmological Simulations with TreeSPH. *ApJS*, **105**, 19.

- Kauffmann, G. and White, S. D. M. (1993). The merging history of dark matter haloes in a hierarchical universe. *MNRAS*, **261**.
- Kauffmann, G., White, S. D. M., and Guiderdoni, B. (1993). The Formation and Evolution of Galaxies Within Merging Dark Matter Haloes. *MNRAS*, **264**, 201.
- Kawata, D. and Rauch, M. (2007). Galactic Wind Signatures around High-Redshift Galaxies. *ApJ*, **663**, 38–52.
- Kay, S. T., Pearce, F. R., Frenk, C. S., and Jenkins, A. (2002). Including star formation and supernova feedback within cosmological simulations of galaxy formation. *MNRAS*, **330**, 113–128.
- Kazantzidis, S., Lokas, E. L., Callegari, S., Mayer, L., and Moustakas, L. A. (2011). On the Efficiency of the Tidal Stirring Mechanism for the Origin of Dwarf Spheroidals: Dependence on the Orbital and Structural Parameters of the Progenitor Disky Dwarfs. *ApJ*, **726**, 98.
- Kereš, D., Katz, N., Weinberg, D. H., and Davé, R. (2005). How do galaxies get their gas? *MNRAS*, **363**, 2–28.
- Kereš, D., Katz, N., Fardal, M., Davé, R., and Weinberg, D. H. (2009). Galaxies in a simulated Λ CDM Universe - I. Cold mode and hot cores. *MNRAS*, **395**, 160–179.
- Kim, D. and Jerjen, H. (2015). Horologium II: A Second Ultra-faint Milky Way Satellite in the Horologium Constellation. *ApJ*, **808**, L39.
- Kim, D., Jerjen, H., Mackey, D., Da Costa, G. S., and Milone, A. P. (2015). A Hero’s Dark Horse: Discovery of an Ultra-faint Milky Way Satellite in Pegasus. *ApJ*, **804**, L44.
- Kim, D., Jerjen, H., Geha, M., Chiti, A., Milone, A. P., Da Costa, G., Mackey, D., Frebel, A., and Conn, B. (2016). Portrait of a Dark Horse: a Photometric and Spectroscopic Study of the Ultra-faint Milky Way Satellite Pegasus III. *ApJ*, **833**, 16.
- Kimm, T., Cen, R., Devriendt, J., Dubois, Y., and Slyz, A. (2015). Towards simulating star formation in turbulent high- z galaxies with mechanical supernova feedback. *MNRAS*, **451**, 2900–2921.
- King, A. (2005). The AGN-Starburst Connection, Galactic Superwinds, and $M_{BH}-\sigma$. *ApJ*, **635**, L121–L123.

- King, A. R., Zubovas, K., and Power, C. (2011). Large-scale outflows in galaxies. *MNRAS*, **415**, L6–L10.
- Kirby, E. N., Martin, C. L., and Finlator, K. (2011a). Metals Removed by Outflows from Milky Way Dwarf Spheroidal Galaxies. *ApJ*, **742**, L25.
- Kirby, E. N., Martin, C. L., and Finlator, K. (2011b). Metals Removed by Outflows from Milky Way Dwarf Spheroidal Galaxies. *ApJ*, **742**, L25.
- Kirby, E. N., Lanfranchi, G. A., Simon, J. D., Cohen, J. G., and Guhathakurta, P. (2011c). Multi-element Abundance Measurements from Medium-resolution Spectra. III. Metallicity Distributions of Milky Way Dwarf Satellite Galaxies. *ApJ*, **727**, 78.
- Kirby, E. N., Cohen, J. G., Guhathakurta, P., Cheng, L., Bullock, J. S., and Gallazzi, A. (2013). The Universal Stellar Mass-Stellar Metallicity Relation for Dwarf Galaxies. *ApJ*, **779**, 102.
- Kirby, E. N., Simon, J. D., and Cohen, J. G. (2015). Spectroscopic Confirmation of the Dwarf Galaxies Hydra II and Pisces II and the Globular Cluster Laevens 1. *ApJ*, **810**, 56.
- Kirby, E. N., Cohen, J. G., Simon, J. D., Guhathakurta, P., Thygesen, A. O., and Duggan, G. E. (2017). Triangulum II. Not Especially Dense After All. *ApJ*, **838**, 83.
- Klimentowski, J., Łokas, E. L., Kazantzidis, S., Mayer, L., and Mamon, G. A. (2009). Tidal evolution of discy dwarf galaxies in the Milky Way potential: the formation of dwarf spheroidals. *MNRAS*, **397**, 2015–2029.
- Klypin, A., Kravtsov, A. V., Valenzuela, O., and Prada, F. (1999). Where Are the Missing Galactic Satellites? *ApJ*, **522**, 82–92.
- Klypin, A. A., Trujillo-Gomez, S., and Primack, J. (2011). Dark Matter Halos in the Standard Cosmological Model: Results from the Bolshoi Simulation. *ApJ*, **740**, 102.
- Koch, A., Grebel, E. K., Wyse, R. F. G., Kleyna, J. T., Wilkinson, M. I., Harbeck, D. R., Gilmore, G. F., and Evans, N. W. (2006). Complexity on Small Scales: The Metallicity Distribution of the Carina Dwarf Spheroidal Galaxy. *AJ*, **131**, 895–911.
- Koch, A., Wilkinson, M. I., Kleyna, J. T., Gilmore, G. F., Grebel, E. K., Mackey, A. D., Evans, N. W., and Wyse, R. F. G. (2007a). Stellar Kinematics and Metallicities in the

- Leo I Dwarf Spheroidal Galaxy-Wide-Field Implications for Galactic Evolution. *ApJ*, **657**, 241–261.
- Koch, A., Kleyna, J. T., Wilkinson, M. I., Grebel, E. K., Gilmore, G. F., Evans, N. W., Wyse, R. F. G., and Harbeck, D. R. (2007b). Stellar Kinematics in the Remote Leo II Dwarf Spheroidal Galaxy-Another Brick in the Wall. *AJ*, **134**, 566–578.
- Koch, A., Wilkinson, M. I., Kleyna, J. T., Irwin, M., Zucker, D. B., Belokurov, V., Gilmore, G. F., Fellhauer, M., and Evans, N. W. (2009). A Spectroscopic Confirmation of the Bootes II Dwarf Spheroidal. *ApJ*, **690**, 453–462.
- Kollmeier, J. A., Miralda-Escudé, J., Cen, R., and Ostriker, J. P. (2006). Galactic Wind Effects on the Ly α Absorption in the Vicinity of Galaxies. *ApJ*, **638**, 52–71.
- Koposov, S. and Belokurov, V. (2008). Observational Constraints on the “Missing Satellite” Problem from SDSS. *Astrophysics and Space Science Proceedings*, **5**, 195.
- Koposov, S. E., Gilmore, G., Walker, M. G., Belokurov, V., Wyn Evans, N., Fellhauer, M., Gieren, W., Geisler, D., Monaco, L., Norris, J. E., Okamoto, S., Peñarrubia, J., Wilkinson, M., Wyse, R. F. G., and Zucker, D. B. (2011). Accurate Stellar Kinematics at Faint Magnitudes: Application to the Boötes I Dwarf Spheroidal Galaxy. *ApJ*, **736**, 146.
- Koposov, S. E., Belokurov, V., Torrealba, G., and Evans, N. W. (2015a). Beasts of the Southern Wild : Discovery of nine Ultra Faint satellites in the vicinity of the Magellanic Clouds. *ApJ*, **805**, 130.
- Koposov, S. E., Belokurov, V., Torrealba, G., and Evans, N. W. (2015b). Beasts of the Southern Wild: Discovery of Nine Ultra Faint Satellites in the Vicinity of the Magellanic Clouds. *ApJ*, **805**, 130.
- Koposov, S. E., Casey, A. R., Belokurov, V., Lewis, J. R., Gilmore, G., Worley, C., Hourihane, A., Randich, S., Bensby, T., Bragaglia, A., Bergemann, M., Carraro, G., Costado, M. T., Flaccomio, E., Francois, P., Heiter, U., Hill, V., Jofre, P., Lando, C., Lanzafame, A. C., de Laverny, P., Monaco, L., Morbidelli, L., Sbordone, L., Mikolaitis, Š., and Ryde, N. (2015c). Kinematics and Chemistry of Recently Discovered Reticulum 2 and Horologium 1 Dwarf Galaxies. *ApJ*, **811**, 62.

- Kormendy, J. (1985). Families of ellipsoidal stellar systems and the formation of dwarf elliptical galaxies. *ApJ*, **295**, 73–79.
- Kravtsov, A. V., Gnedin, O. Y., and Klypin, A. A. (2004). The Tumultuous Lives of Galactic Dwarfs and the Missing Satellites Problem. *ApJ*, **609**, 482–497.
- Krumholz, M. R. and Tan, J. C. (2007). Slow Star Formation in Dense Gas: Evidence and Implications. *ApJ*, **654**, 304–315.
- Kurk, J. D., Walter, F., Fan, X., Jiang, L., Riechers, D. A., Rix, H.-W., Pentericci, L., Strauss, M. A., Carilli, C., and Wagner, S. (2007). Black Hole Masses and Enrichment of $z \sim 6$ SDSS Quasars. *ApJ*, **669**, 32–44.
- Kuzio de Naray, R., McGaugh, S. S., de Blok, W. J. G., and Bosma, A. (2006). High-Resolution Optical Velocity Fields of 11 Low Surface Brightness Galaxies. *ApJS*, **165**, 461–479.
- Laevens, B. P. M., Martin, N. F., Ibata, R. A., Rix, H.-W., Bernard, E. J., Bell, E. F., Sesar, B., Ferguson, A. M. N., Schlafly, E. F., Slater, C. T., Burgett, W. S., Chambers, K. C., Flewelling, H., Hodapp, K. A., Kaiser, N., Kudritzki, R.-P., Lupton, R. H., Magnier, E. A., Metcalfe, N., Morgan, J. S., Price, P. A., Tonry, J. L., Wainscoat, R. J., and Waters, C. (2015a). A New Faint Milky Way Satellite Discovered in the Pan-STARRS1 3π Survey. *ApJ*, **802**, L18.
- Laevens, B. P. M., Martin, N. F., Bernard, E. J., Schlafly, E. F., Sesar, B., Rix, H.-W., Bell, E. F., Ferguson, A. M. N., Slater, C. T., Sweeney, W. E., Wyse, R. F. G., Huxor, A. P., Burgett, W. S., Chambers, K. C., Draper, P. W., Hodapp, K. A., Kaiser, N., Magnier, E. A., Metcalfe, N., Tonry, J. L., Wainscoat, R. J., and Waters, C. (2015b). Sagittarius II, Draco II and Laevens 3: Three New Milky Way Satellites Discovered in the Pan-STARRS 1 3π Survey. *ApJ*, **813**, 44.
- Larson, R. B. (1974). Effects of supernovae on the early evolution of galaxies. *MNRAS*, **169**, 229–246.
- Latif, M. A. and Volonteri, M. (2015). Assessing inflow rates in atomic cooling haloes: implications for direct collapse black holes. *MNRAS*, **452**, 1026–1044.
- Lavery, R. J. (1990). Local Group Dwarf Galaxy in Tucana. *IAU Circ.*, **5139**.

- Lewis, G. F., Ibata, R. A., Chapman, S. C., McConnachie, A., Irwin, M. J., Tolstoy, E., and Tanvir, N. R. (2007). Inside the whale: the structure and dynamics of the isolated Cetus dwarf spheroidal. *MNRAS*, **375**, 1364–1370.
- Li, T. S., Simon, J. D., Drlica-Wagner, A., Bechtol, K., Wang, M. Y., García-Bellido, J., Frieman, J., Marshall, J. L., James, D. J., Strigari, L., Pace, A. B., Balbinot, E., Zhang, Y., Abbott, T. M. C., Allam, S., Benoit-Lévy, A., Bernstein, G. M., Bertin, E., Brooks, D., Burke, D. L., Carnero Rosell, A., Carrasco Kind, M., Carretero, J., Cunha, C. E., D’Andrea, C. B., da Costa, L. N., DePoy, D. L., Desai, S., Diehl, H. T., Eifler, T. F., Flaughner, B., Goldstein, D. A., Gruen, D., Gruendl, R. A., Gschwend, J., Gutierrez, G., Krause, E., Kuehn, K., Lin, H., Maia, M. A. G., March, M., Menanteau, F., Miquel, R., Plazas, A. A., Romer, A. K., Sanchez, E., Santiago, B., Schubnell, M., Sevilla-Noarbe, I., Smith, R. C., Sobreira, F., Suchyta, E., Tarle, G., Thomas, D., Tucker, D. L., Walker, A. R., Wechsler, R. H., Wester, W., Yanny, B., and (DES Collaboration (2017)). Farthest Neighbor: The Distant Milky Way Satellite Eridanus II. *ApJ*, **838**, 8.
- Lokas, E. L., Majewski, S. R., Kazantzidis, S., Mayer, L., Carlin, J. L., Nidever, D. L., and Moustakas, L. A. (2012). The Shapes of Milky Way Satellites: Looking for Signatures of Tidal Stirring. *ApJ*, **751**, 61.
- Lucy, L. B. (1977). A numerical approach to the testing of the fission hypothesis. *AJ*, **82**, 1013–1024.
- Ludlow, A. D., Benítez-Llambay, A., Schaller, M., Theuns, T., Frenk, C. S., Bower, R., Schaye, J., Crain, R. A., Navarro, J. F., Fattahi, A., and Oman, K. A. (2017). Mass-Discrepancy Acceleration Relation: A Natural Outcome of Galaxy Formation in Cold Dark Matter Halos. *Physical Review Letters*, **118**(16), 161103.
- Luque, E., Santiago, B., Pieres, A., Marshall, J. L., Pace, A. B., Kron, R., Drlica-Wagner, A., Queiroz, A., Balbinot, E., dal Ponte, M., Fausti Neto, A., da Costa, L. N., Maia, M. A. G., Walker, A. R., Abdalla, F. B., Allam, S., Annis, J., Bechtol, K., Benoit-Lévy, A., Bertin, E., Brooks, D., Carnero Rosell, A., Carrasco Kind, M., Carretero, J., Crocce, M., Davis, C., Doel, P., Eifler, T. F., Flaughner, B., García-Bellido, J., Gerdes, D. W., Gruen, D., Gruendl, R. A., Gutierrez, G., Honscheid, K., James, D. J., Kuehn, K., Kuropatkin, N., Miquel, R., Nichol, R. C., Plazas, A. A., Sanchez, E., Scarpine, V., Schindler, R., Sevilla-Noarbe, I., Smith, M., Soares-Santos, M., Sobreira, F., Suchyta,

- E., Tarle, G., and Thomas, D. (2017). Deep SOAR follow-up photometry of two Milky Way outer-halo companions discovered with Dark Energy Survey. *ArXiv e-prints*.
- Lux, H., Read, J. I., and Lake, G. (2010). Determining orbits for the Milky Way’s dwarfs. *MNRAS*, **406**, 2312–2324.
- Lynden-Bell, D. and Lynden-Bell, R. M. (1995). Ghostly streams from the formation of the Galaxy’s halo. *MNRAS*, **275**, 429–442.
- Majewski, S. R., Skrutskie, M. F., Weinberg, M. D., and Ostheimer, J. C. (2003). A Two Micron All Sky Survey View of the Sagittarius Dwarf Galaxy. I. Morphology of the Sagittarius Core and Tidal Arms. *ApJ*, **599**, 1082–1115.
- Marcolini, A., Brighenti, F., and D’Ercole, A. (2003). Three-dimensional simulations of the interstellar medium in dwarf galaxies - I. Ram pressure stripping. *MNRAS*, **345**, 1329–1339.
- Marlowe, A. T., Heckman, T. M., Wyse, R. F. G., and Schommer, R. (1995). Observations of the impact of starbursts on the interstellar medium in dwarf galaxies. *ApJ*, **438**, 563–589.
- Marri, S. and White, S. D. M. (2003). Smoothed particle hydrodynamics for galaxy-formation simulations: improved treatments of multiphase gas, of star formation and of supernovae feedback. *MNRAS*, **345**, 561–574.
- Martin, C. L. (1996). Kinematic Evidence for Superbubbles in I ZW 18: Constraints on the Star Formation History and Chemical Evolution. *ApJ*, **465**, 680.
- Martin, N. F., Ibata, R. A., Chapman, S. C., Irwin, M., and Lewis, G. F. (2007). A Keck/DEIMOS spectroscopic survey of faint Galactic satellites: searching for the least massive dwarf galaxies. *MNRAS*, **380**, 281–300.
- Martin, N. F., de Jong, J. T. A., and Rix, H.-W. (2008). A Comprehensive Maximum Likelihood Analysis of the Structural Properties of Faint Milky Way Satellites. *ApJ*, **684**, 1075–1092.
- Martin, N. F., Nidever, D. L., Besla, G., Olsen, K., Walker, A. R., Vivas, A. K., Gruendl, R. A., Kaleida, C. C., Muñoz, R. R., Blum, R. D., Saha, A., Conn, B. C., Bell, E. F., Chu, Y.-H., Cioni, M.-R. L., de Boer, T. J. L., Gallart, C., Jin, S., Kunder, A., Majewski,

- S. R., Martinez-Delgado, D., Monachesi, A., Monelli, M., Monteagudo, L., Noël, N. E. D., Olszewski, E. W., Stringfellow, G. S., van der Marel, R. P., and Zaritsky, D. (2015). Hydra II: A Faint and Compact Milky Way Dwarf Galaxy Found in the Survey of the Magellanic Stellar History. *ApJ*, **804**, L5.
- Martin, N. F., Geha, M., Ibata, R. A., Collins, M. L. M., Laevens, B. P. M., Bell, E. F., Rix, H.-W., Ferguson, A. M. N., Chambers, K. C., Wainscoat, R. J., and Waters, C. (2016). Is Draco II one of the faintest dwarf galaxies? First study from Keck/DEIMOS spectroscopy. *MNRAS*, **458**, L59–L63.
- Marzke, R. O. and da Costa, L. N. (1997). The Galaxy Luminosity Function at $z \leq 0.05$: Dependence on Color. *AJ*, **113**, 185.
- Mashchenko, S., Wadsley, J., and Couchman, H. M. P. (2008). Stellar Feedback in Dwarf Galaxy Formation. *Science*, **319**, 174.
- Mateo, M., Olszewski, E. W., Pryor, C., Welch, D. L., and Fischer, P. (1993). The Carina dwarf spheroidal galaxy - How dark is it? *AJ*, **105**, 510–526.
- Mateo, M., Olszewski, E. W., and Walker, M. G. (2008). The Velocity Dispersion Profile of the Remote Dwarf Spheroidal Galaxy Leo I: A Tidal Hit and Run? *ApJ*, **675**, 201–233.
- Mateo, M. L. (1998). Dwarf Galaxies of the Local Group. *ARA&A*, **36**, 435–506.
- Mathewson, D. S., Cleary, M. N., and Murray, J. D. (1974). The Magellanic stream. *ApJ*, **190**, 291–296.
- Mayer, L., Governato, F., Colpi, M., Moore, B., Quinn, T., Wadsley, J., Stadel, J., and Lake, G. (2001a). The Metamorphosis of Tidally Stirred Dwarf Galaxies. *ApJ*, **559**, 754–784.
- Mayer, L., Governato, F., Colpi, M., Moore, B., Quinn, T., Wadsley, J., Stadel, J., and Lake, G. (2001b). Tidal Stirring and the Origin of Dwarf Spheroidals in the Local Group. *ApJ*, **547**, L123–L127.
- Mayer, L., Mastropietro, C., Wadsley, J., Stadel, J., and Moore, B. (2006a). Simultaneous ram pressure and tidal stripping; how dwarf spheroidals lost their gas. *MNRAS*, **369**, 1021–1038.

- Mayer, L., Mastropietro, C., Wadsley, J., Stadel, J., and Moore, B. (2006b). Simultaneous ram pressure and tidal stripping; how dwarf spheroidals lost their gas. *MNRAS*, **369**, 1021–1038.
- Mayer, L., Kazantzidis, S., Mastropietro, C., and Wadsley, J. (2007). Early gas stripping as the origin of the darkest galaxies in the Universe. *Nature*, **445**, 738–740.
- McConnachie, A. W. (2012). The Observed Properties of Dwarf Galaxies in and around the Local Group. *AJ*, **144**, 4.
- McConnachie, A. W. and Irwin, M. J. (2006). Structural properties of the M31 dwarf spheroidal galaxies. *MNRAS*, **365**, 1263–1276.
- McMillan, P. J. and Dehnen, W. (2007). Initial conditions for disc galaxies. *MNRAS*, **378**, 541–550.
- McNamara, B. R. and Nulsen, P. E. J. (2007). Heating Hot Atmospheres with Active Galactic Nuclei. *ARA&A*, **45**, 117–175.
- McQuillin, R. C. and McLaughlin, D. E. (2012). Momentum-driven feedback and the M- σ relation in non-isothermal galaxies. *MNRAS*, **423**, 2162–2176.
- McQuillin, R. C. and McLaughlin, D. E. (2013). Black hole wind speeds and the M - σ relation. *MNRAS*, **434**, 1332–1338.
- Miller, M. J. and Bregman, J. N. (2013). The Structure of the Milky Way’s Hot Gas Halo. *ApJ*, **770**, 118.
- Mo, H., van den Bosch, F. C., and White, S. (2010). *Galaxy Formation and Evolution*. Cambridge University Press.
- Monaco, L., Bellazzini, M., Ferraro, F. R., and Pancino, E. (2004). The distance to the Sagittarius dwarf spheroidal galaxy from the red giant branch tip. *MNRAS*, **353**, 874–878.
- Monaghan, J. J. (1992). Smoothed particle hydrodynamics. *ARA&A*, **30**, 543–574.
- Monaghan, J. J. (1997). SPH and Riemann Solvers. *Journal of Computational Physics*, **136**, 298–307.

- Monaghan, J. J. and Gingold, R. A. (1983). Shock Simulation by the Particle Method SPH. *Journal of Computational Physics*, **52**, 374–389.
- Monaghan, J. J. and Lattanzio, J. C. (1985). A refined particle method for astrophysical problems. *A&A*, **149**, 135–143.
- Moore, B., Ghigna, S., Governato, F., Lake, G., Quinn, T., Stadel, J., and Tozzi, P. (1999). Dark Matter Substructure within Galactic Halos. *ApJ*, **524**, L19–L22.
- Moretti, M. I., Dall’Ora, M., Ripepi, V., Clementini, G., Di Fabrizio, L., Smith, H. A., DeLee, N., Kuehn, C., Catelan, M., Marconi, M., Musella, I., Beers, T. C., and Kinemuchi, K. (2009). The Leo IV Dwarf Spheroidal Galaxy: Color-Magnitude Diagram and Pulsating Stars. *ApJ*, **699**, L125–L129.
- Morris, J. P. (1996). A study of the stability properties of smooth particle hydrodynamics. *PASA*, **13**, 97–102.
- Muñoz, R. R., Carlin, J. L., Frinchaboy, P. M., Nidever, D. L., Majewski, S. R., and Patterson, R. J. (2006). Exploring Halo Substructure with Giant Stars: The Dynamics and Metallicity of the Dwarf Spheroidal in Boötes. *ApJ*, **650**, L51–L54.
- Muñoz-Cuartas, J. C., Macciò, A. V., Gottlöber, S., and Dutton, A. A. (2011). The redshift evolution of Λ cold dark matter halo parameters: concentration, spin and shape. *MNRAS*, **411**, 584–594.
- Navarro, J. F., Eke, V. R., and Frenk, C. S. (1996a). The cores of dwarf galaxy haloes. *MNRAS*, **283**, L72–L78.
- Navarro, J. F., Frenk, C. S., and White, S. D. M. (1996b). The Structure of Cold Dark Matter Halos. *ApJ*, **462**, 563.
- Navarro, J. F., Frenk, C. S., and White, S. D. M. (1997). A Universal Density Profile from Hierarchical Clustering. *ApJ*, **490**, 493–508.
- Nayakshin, S. and Wilkinson, M. I. (2013). A link between feedback outflows and satellite galaxy suppression. *MNRAS*, **433**, 324–331.
- Newberg, H. J., Yanny, B., Rockosi, C., Grebel, E. K., Rix, H.-W., Brinkmann, J., Csabai, I., Hennessy, G., Hindsley, R. B., Ibata, R., Ivezić, Z., Lamb, D., Nash, E. T., Odenkirchen, M., Rave, H. A., Schneider, D. P., Smith, J. A., Stolte, A., and York, D. G.

- (2002). The Ghost of Sagittarius and Lumps in the Halo of the Milky Way. *ApJ*, **569**, 245–274.
- Newton, R. D. A. and Kay, S. T. (2013). A study of AGN and supernova feedback in simulations of isolated and merging disc galaxies. *MNRAS*, **434**, 3606–3627.
- Nichols, M. and Bland-Hawthorn, J. (2011). Gas Depletion in Local Group Dwarfs on ~ 250 kpc Scales: Ram Pressure Stripping Assisted by Internal Heating at Early Times. *ApJ*, **732**, 17.
- Norris, J. E., Yong, D., Venn, K. A., Gilmore, G., Casagrande, L., and Dotter, A. (2017). The Populations of Carina. II. Chemical Enrichment. *ApJS*, **230**, 28.
- Oñorbe, J., Boylan-Kolchin, M., Bullock, J. S., Hopkins, P. F., Kereš, D., Faucher-Giguère, C.-A., Quataert, E., and Murray, N. (2015). Forged in FIRE: cusps, cores and baryons in low-mass dwarf galaxies. *MNRAS*, **454**, 2092–2106.
- Oh, S.-H., de Blok, W. J. G., Walter, F., Brinks, E., and Kennicutt, Jr., R. C. (2008). High-Resolution Dark Matter Density Profiles of THINGS Dwarf Galaxies: Correcting for Noncircular Motions. *AJ*, **136**, 2761–2781.
- Oh, S.-H., Brook, C., Governato, F., Brinks, E., Mayer, L., de Blok, W. J. G., Brooks, A., and Walter, F. (2011). The Central Slope of Dark Matter Cores in Dwarf Galaxies: Simulations versus THINGS. *AJ*, **142**, 24.
- Okamoto, S., Arimoto, N., Yamada, Y., and Onodera, M. (2008a). A Suprime-Cam study of the stellar population of the Ursa Major I dwarf spheroidal galaxy. *A&A*, **487**, 103–108.
- Okamoto, T. and Frenk, C. S. (2009). The origin of failed subhaloes and the common mass scale of the Milky Way satellite galaxies. *MNRAS*, **399**, L174–L178.
- Okamoto, T., Gao, L., and Theuns, T. (2008b). Mass loss of galaxies due to an ultraviolet background. *MNRAS*, **390**, 920–928.
- Olszewski, E. W. and Aaronson, M. (1985). The URSA Minor dwarf galaxy - Still an old stellar system. *AJ*, **90**, 2221–2238.

- Oppenheimer, B. D., Davé, R., Kereš, D., Fardal, M., Katz, N., Kollmeier, J. A., and Weinberg, D. H. (2010). Feedback and recycled wind accretion: assembling the $z = 0$ galaxy mass function. *MNRAS*, **406**, 2325–2338.
- Ott, J., Walter, F., and Brinks, E. (2005). A Chandra X-ray survey of nearby dwarf starburst galaxies - II. Starburst properties and outflows. *MNRAS*, **358**, 1453–1471.
- Parkinson, H., Cole, S., and Helly, J. (2008). Generating dark matter halo merger trees. *MNRAS*, **383**, 557–564.
- Pasetto, S., Grebel, E. K., Berczik, P., Chiosi, C., and Spurzem, R. (2011). Orbital evolution of the Carina dwarf galaxy and self-consistent determination of star formation history. *A&A*, **525**, A99.
- Peñarrubia, J., Benson, A. J., Walker, M. G., Gilmore, G., McConnachie, A. W., and Mayer, L. (2010). The impact of dark matter cusps and cores on the satellite galaxy population around spiral galaxies. *MNRAS*, **406**, 1290–1305.
- Peñarrubia, J., Pontzen, A., Walker, M. G., and Koposov, S. E. (2012). The Coupling between the Core/Cusp and Missing Satellite Problems. *ApJ*, **759**, L42.
- Peebles, P. J. E. (1970). Structure of the Coma Cluster of Galaxies. *AJ*, **75**, 13.
- Pettini, M., Shapley, A. E., Steidel, C. C., Cuby, J.-G., Dickinson, M., Moorwood, A. F. M., Adelberger, K. L., and Giavalisco, M. (2001). The Rest-Frame Optical Spectra of Lyman Break Galaxies: Star Formation, Extinction, Abundances, and Kinematics. *ApJ*, **554**, 981–1000.
- Piatek, S., Pryor, C., Olszewski, E. W., Harris, H. C., Mateo, M., Minniti, D., and Tinney, C. G. (2003). Proper Motions of Dwarf Spheroidal Galaxies from Hubble Space Telescope Imaging. II. Measurement for Carina. *AJ*, **126**, 2346–2361.
- Pietrzyński, G., Gieren, W., Szewczyk, O., Walker, A., Rizzi, L., Bresolin, F., Kudritzki, R.-P., Nalewajko, K., Storm, J., Dall’Ora, M., and Ivanov, V. (2008). The Araucaria Project: the Distance to the Sculptor Dwarf Spheroidal Galaxy from Infrared Photometry of RR Lyrae Stars. *AJ*, **135**, 1993–1997.
- Pietrzyński, G., Górski, M., Gieren, W., Ivanov, V. D., Bresolin, F., and Kudritzki, R.-P. (2009). The Araucaria Project. Infrared Tip of the Red Giant Branch Distances to the Carina and Fornax Dwarf Spheroidal Galaxies. *AJ*, **138**, 459–465.

- Planck Collaboration, Aghanim, N., Arnaud, M., Ashdown, M., Aumont, J., Baccigalupi, C., Banday, A. J., Barreiro, R. B., Bartlett, J. G., Bartolo, N., and et al. (2015a). Planck 2015 results. XI. CMB power spectra, likelihoods, and robustness of parameters. *ArXiv e-prints*.
- Planck Collaboration, Ade, P. A. R., Aghanim, N., Arnaud, M., Ashdown, M., Aumont, J., Baccigalupi, C., Banday, A. J., Barreiro, R. B., Bartlett, J. G., and et al. (2015b). Planck 2015 results. XIII. Cosmological parameters. *ArXiv e-prints*.
- Planck Collaboration, Ade, P. A. R., Aghanim, N., Arnaud, M., Ashdown, M., Aumont, J., Baccigalupi, C., Banday, A. J., Barreiro, R. B., Bartlett, J. G., and et al. (2016a). Planck 2015 results. XIII. Cosmological parameters. *A&A*, **594**, A13.
- Planck Collaboration, Adam, R., Aghanim, N., Ashdown, M., Aumont, J., Baccigalupi, C., Ballardini, M., Banday, A. J., Barreiro, R. B., Bartolo, N., Basak, S., Battye, R., Benabed, K., Bernard, J.-P., Bersanelli, M., Bielewicz, P., Bock, J. J., Bonaldi, A., Bonavera, L., Bond, J. R., Borrill, J., Bouchet, F. R., Boulanger, F., Bucher, M., Burigana, C., Calabrese, E., Cardoso, J.-F., Carron, J., Chiang, H. C., Colombo, L. P. L., Combet, C., Comis, B., Couchot, F., Coulais, A., Crill, B. P., Curto, A., Cuttaia, F., Davis, R. J., de Bernardis, P., de Rosa, A., de Zotti, G., Delabrouille, J., Di Valentino, E., Dickinson, C., Diego, J. M., Doré, O., Douspis, M., Ducout, A., Dupac, X., Elsner, F., Enßlin, T. A., Eriksen, H. K., Falgarone, E., Fantaye, Y., Finelli, F., Forastieri, F., Frailis, M., Fraisse, A. A., Franceschi, E., Frolov, A., Galeotta, S., Galli, S., Ganga, K., Génova-Santos, R. T., Gerbino, M., Ghosh, T., González-Nuevo, J., Górski, K. M., Gruppuso, A., Gudmundsson, J. E., Hansen, F. K., Helou, G., Henrot-Versillé, S., Herranz, D., Hivon, E., Huang, Z., Ilić, S., Jaffe, A. H., Jones, W. C., Keihänen, E., Keskitalo, R., Kisner, T. S., Knox, L., Krachmalnicoff, N., Kunz, M., Kurki-Suonio, H., Lagache, G., Lähteenmäki, A., Lamarre, J.-M., Langer, M., Lasenby, A., Lattanzi, M., Lawrence, C. R., Le Jeune, M., Levrier, F., Lewis, A., Liguori, M., Lilje, P. B., López-Caniego, M., Ma, Y.-Z., Macías-Pérez, J. F., Maggio, G., Mangilli, A., Maris, M., Martin, P. G., Martínez-González, E., Matarrese, S., Mauri, N., McEwen, J. D., Meinhold, P. R., Melchiorri, A., Mennella, A., Migliaccio, M., Miville-Deschênes, M.-A., Molinari, D., Moneti, A., Montier, L., Morgante, G., Moss, A., Naselsky, P., Natoli, P., Oxborrow, C. A., Pagano, L., Paoletti, D., Partridge, B., Patanchon, G., Patrizzii, L., Perdereau, O., Perotto, L., Pettorino, V., Piacentini, F., Plaszczyński, S., Polastri, L., Polenta, G., Puget, J.-L., Rachen, J. P., Racine, B., Reinecke, M., Remazeilles, M.,

Renzi, A., Rocha, G., Rossetti, M., Roudier, G., Rubiño-Martín, J. A., Ruiz-Granados, B., Salvati, L., Sandri, M., Savelainen, M., Scott, D., Sirri, G., Sunyaev, R., Suur-Uski, A.-S., Tauber, J. A., Tenti, M., Toffolatti, L., Tomasi, M., Tristram, M., Trombetti, T., Valiviita, J., Van Tent, F., Vielva, P., Villa, F., Vittorio, N., Wandelt, B. D., Wehus, I. K., White, M., Zacchei, A., and Zonca, A. (2016b). Planck intermediate results. XLVII. Planck constraints on reionization history. *A&A*, **596**, A108.

Planck Collaboration, Adam, R., Aghanim, N., Ashdown, M., Aumont, J., Baccigalupi, C., Ballardini, M., Banday, A. J., Barreiro, R. B., Bartolo, N., Basak, S., Battye, R., Benabed, K., Bernard, J.-P., Bersanelli, M., Bielewicz, P., Bock, J. J., Bonaldi, A., Bonavera, L., Bond, J. R., Borrill, J., Bouchet, F. R., Bucher, M., Burigana, C., Calabrese, E., Cardoso, J.-F., Carron, J., Chiang, H. C., Colombo, L. P. L., Combet, C., Comis, B., Coulais, A., Crill, B. P., Curto, A., Cuttaia, F., Davis, R. J., de Bernardis, P., de Rosa, A., de Zotti, G., Delabrouille, J., Di Valentino, E., Dickinson, C., Diego, J. M., Doré, O., Douspis, M., Ducout, A., Dupac, X., Elsner, F., Enßlin, T. A., Eriksen, H. K., Falgarone, E., Fantaye, Y., Finelli, F., Forastieri, F., Frailis, M., Fraisse, A. A., Franceschi, E., Frolov, A., Galeotta, S., Galli, S., Ganga, K., Génova-Santos, R. T., Gerbino, M., Ghosh, T., González-Nuevo, J., Górski, K. M., Gruppuso, A., Gudmundsson, J. E., Hansen, F. K., Helou, G., Henrot-Versillé, S., Herranz, D., Hivon, E., Huang, Z., Ili, S., Jaffe, A. H., Jones, W. C., Keihänen, E., Keskitalo, R., Kisner, T. S., Knox, L., Krachmalnicoff, N., Kunz, M., Kurki-Suonio, H., Lagache, G., Lähteenmäki, A., Lamarre, J.-M., Langer, M., Lasenby, A., Lattanzi, M., Lawrence, C. R., Le Jeune, M., Levrier, F., Lewis, A., Liguori, M., Lilje, P. B., López-Caniego, M., Ma, Y.-Z., Macías-Pérez, J. F., Maggio, G., Mangilli, A., Maris, M., Martín, P. G., Martínez-González, E., Matarrese, S., Mauri, N., McEwen, J. D., Meinhold, P. R., Melchiorri, A., Mennella, A., Migliaccio, M., Miville-Deschênes, M.-A., Molinari, D., Moneti, A., Montier, L., Morgante, G., Moss, A., Naselsky, P., Natoli, P., Oxborrow, C. A., Pagano, L., Paoletti, D., Partridge, B., Patanchon, G., Patrizzii, L., Perdereau, O., Perotto, L., Pettorino, V., Piacentini, F., Plaszczyński, S., Polastri, L., Polenta, G., Puget, J.-L., Rachen, J. P., Racine, B., Reinecke, M., Remazeilles, M., Renzi, A., Rocha, G., Rossetti, M., Roudier, G., Rubiño-Martín, J. A., Ruiz-Granados, B., Salvati, L., Sandri, M., Savelainen, M., Scott, D., Sirri, G., Sunyaev, R., Suur-Uski, A.-S., Tauber, J. A., Tenti, M., Toffolatti, L., Tomasi, M., Tristram, M., Trombetti, T., Valiviita, J., Van Tent, F., Vielva, P., Villa, F., Vittorio, N., Wandelt, B. D., Wehus, I. K., White, M., Zacchei, A., and Zonca, A. (2016c). Planck intermediate results. XLVII. Planck constraints on reionization history.

ArXiv e-prints.

- Pontzen, A. and Governato, F. (2012). How supernova feedback turns dark matter cusps into cores. *MNRAS*, **421**, 3464–3471.
- Pounds, K. A., Reeves, J. N., King, A. R., Page, K. L., O’Brien, P. T., and Turner, M. J. L. (2003). A high-velocity ionized outflow and XUV photosphere in the narrow emission line quasar PG1211+143. *MNRAS*, **345**, 705–713.
- Power, C., Navarro, J. F., Jenkins, A., Frenk, C. S., White, S. D. M., Springel, V., Stadel, J., and Quinn, T. (2003). The inner structure of Λ CDM haloes - I. A numerical convergence study. *MNRAS*, **338**, 14–34.
- Power, C., Read, J. I., and Hobbs, A. (2014). The formation of entropy cores in non-radiative galaxy cluster simulations: smoothed particle hydrodynamics versus adaptive mesh refinement. *MNRAS*, **440**, 3243–3256.
- Power, C., Wynn, G. A., Robotham, A. S. G., Lewis, G. F., and Wilkinson, M. I. (2016). *ArXiv Astrophysics e-prints.*
- Press, W. H. and Schechter, P. (1974). Formation of Galaxies and Clusters of Galaxies by Self-Similar Gravitational Condensation. *ApJ*, **187**, 425–438.
- Price, D. (2005). *Smoothed Particle Hydrodynamics*. Ph.D. thesis, PhD Thesis, 2005.
- Price, D. J. (2008). Modelling discontinuities and Kelvin Helmholtz instabilities in SPH. *Journal of Computational Physics*, **227**, 10040–10057.
- Price, D. J. (2012). Smoothed particle hydrodynamics and magnetohydrodynamics. *Journal of Computational Physics*, **231**, 759–794.
- Rauch, M., Becker, G. D., Haehnelt, M. G., Gauthier, J.-R., Ravindranath, S., and Sargent, W. L. W. (2011). Filamentary infall of cold gas and escape of Ly α and hydrogen ionizing radiation from an interacting high-redshift galaxy. *MNRAS*, **418**, 1115–1126.
- Read, J. I. and Gilmore, G. (2005). Mass loss from dwarf spheroidal galaxies: the origins of shallow dark matter cores and exponential surface brightness profiles. *MNRAS*, **356**, 107–124.

- Read, J. I. and Hayfield, T. (2012). SPHS: smoothed particle hydrodynamics with a higher order dissipation switch. *MNRAS*, **422**, 3037–3055.
- Read, J. I., Pontzen, A. P., and Viel, M. (2006a). On the formation of dwarf galaxies and stellar haloes. *MNRAS*, **371**, 885–897.
- Read, J. I., Wilkinson, M. I., Evans, N. W., Gilmore, G., and Kleyna, J. T. (2006b). The importance of tides for the Local Group dwarf spheroidals. *MNRAS*, **367**, 387–399.
- Read, J. I., Wilkinson, M. I., Evans, N. W., Gilmore, G., and Kleyna, J. T. (2006c). The tidal stripping of satellites. *MNRAS*, **366**, 429–437.
- Read, J. I., Hayfield, T., and Agertz, O. (2010). Resolving mixing in smoothed particle hydrodynamics. *MNRAS*, **405**, 1513–1530.
- Read, J. I., Agertz, O., and Collins, M. L. M. (2016a). Dark matter cores all the way down. *MNRAS*, **459**, 2573–2590.
- Read, J. I., Agertz, O., and Collins, M. L. M. (2016b). Dark matter cores all the way down. *MNRAS*.
- Reeves, J. N., O’Brien, P. T., and Ward, M. J. (2003). A Massive X-Ray Outflow from the Quasar PDS 456. *ApJ*, **593**, L65–L68.
- Revaz, Y. and Jablonka, P. (2012). The dynamical and chemical evolution of dwarf spheroidal galaxies with GEAR. *A&A*, **538**, A82.
- Revaz, Y., Jablonka, P., Sawala, T., Hill, V., Letarte, B., Irwin, M., Battaglia, G., Helmi, A., Shetrone, M. D., Tolstoy, E., and Venn, K. A. (2009). The dynamical and chemical evolution of dwarf spheroidal galaxies. *A&A*, **501**, 189–206.
- Richardson, T. and Fairbairn, M. (2014). On the dark matter profile in Sculptor: breaking the β degeneracy with Virial shape parameters. *MNRAS*, **441**, 1584–1600.
- Richter, P., Fox, A. J., Wakker, B. P., Lehner, N., Howk, J. C., Bland-Hawthorn, J., Ben Bekhti, N., and Fechner, C. (2013). The COS/UVES Absorption Survey of the Magellanic Stream. II. Evidence for a Complex Enrichment History of the Stream from the Fairall 9 Sightline. *ApJ*, **772**, 111.

- Ricotti, M. and Gnedin, N. Y. (2005). Formation Histories of Dwarf Galaxies in the Local Group. *ApJ*, **629**, 259–267.
- Riess, A. G., Filippenko, A. V., Challis, P., Clocchiatti, A., Diercks, A., Garnavich, P. M., Gilliland, R. L., Hogan, C. J., Jha, S., Kirshner, R. P., Leibundgut, B., Phillips, M. M., Reiss, D., Schmidt, B. P., Schommer, R. A., Smith, R. C., Spyromilio, J., Stubbs, C., Suntzeff, N. B., and Tonry, J. (1998). Observational Evidence from Supernovae for an Accelerating Universe and a Cosmological Constant. *AJ*, **116**, 1009–1038.
- Rupke, D. S. N. and Veilleux, S. (2011). Integral Field Spectroscopy of Massive, Kiloparsec-scale Outflows in the Infrared-luminous QSO Mrk 231. *ApJ*, **729**, L27.
- Salpeter, E. E. (1955). The Luminosity Function and Stellar Evolution. *ApJ*, **121**, 161.
- Sarajedini, A. and Layden, A. C. (1995). A photometric study of the globular cluster M54 and the sagittarius dwarf galaxy: Evidence for three distinct populations. *AJ*, **109**, 1086–1094.
- Saviane, I., Held, E. V., and Piotto, G. (1996). CCD photometry of the Tucana dwarf galaxy. *A&A*, **315**, 40–51.
- Sawala, T., Scannapieco, C., Maio, U., and White, S. (2010). Formation of isolated dwarf galaxies with feedback. *MNRAS*, **402**, 1599–1613.
- Sawala, T., Frenk, C. S., Crain, R. A., Jenkins, A., Schaye, J., Theuns, T., and Zavala, J. (2013). The abundance of (not just) dark matter haloes. *MNRAS*, **431**, 1366–1382.
- Sawala, T., Frenk, C. S., Fattahi, A., Navarro, J. F., Bower, R. G., Crain, R. A., Dalla Vecchia, C., Furlong, M., Jenkins, A., McCarthy, I. G., Qu, Y., Schaller, M., Schaye, J., and Theuns, T. (2015a). Bent by baryons: the low-mass galaxy-halo relation. *MNRAS*, **448**, 2941–2947.
- Sawala, T., Frenk, C. S., Fattahi, A., Navarro, J. F., Bower, R. G., Crain, R. A., Dalla Vecchia, C., Furlong, M., Helly, J. C., Jenkins, A., Oman, K. A., Schaller, M., Schaye, J., Theuns, T., Trayford, J., and White, S. D. M. (2015b). The APOSTLE simulations: solutions to the Local Group’s cosmic puzzles. *ArXiv e-prints*.
- Sawala, T., Frenk, C. S., Fattahi, A., Navarro, J. F., Bower, R. G., Crain, R. A., Dalla Vecchia, C., Furlong, M., Helly, J. C., Jenkins, A., Oman, K. A., Schaller, M., Schaye,

- J., Theuns, T., Trayford, J., and White, S. D. M. (2016a). The APOSTLE simulations: solutions to the Local Group’s cosmic puzzles. *MNRAS*, **457**, 1931–1943.
- Sawala, T., Frenk, C. S., Fattahi, A., Navarro, J. F., Theuns, T., Bower, R. G., Crain, R. A., Furlong, M., Jenkins, A., Schaller, M., and Schaye, J. (2016b). The chosen few: the low-mass haloes that host faint galaxies. *MNRAS*, **456**, 85–97.
- Schaye, J., Aguirre, A., Kim, T.-S., Theuns, T., Rauch, M., and Sargent, W. L. W. (2003). Metallicity of the Intergalactic Medium Using Pixel Statistics. II. The Distribution of Metals as Traced by C IV. *ApJ*, **596**, 768–796.
- Schaye, J., Crain, R. A., Bower, R. G., Furlong, M., Schaller, M., Theuns, T., Dalla Vecchia, C., Frenk, C. S., McCarthy, I. G., Helly, J. C., Jenkins, A., Rosas-Guevara, Y. M., White, S. D. M., Baes, M., Booth, C. M., Camps, P., Navarro, J. F., Qu, Y., Rahmati, A., Sawala, T., Thomas, P. A., and Trayford, J. (2015). The EAGLE project: simulating the evolution and assembly of galaxies and their environments. *MNRAS*, **446**, 521–554.
- Schmidt, M. (1959). The Rate of Star Formation. *ApJ*, **129**, 243.
- Schneider, A., Smith, R. E., and Reed, D. (2013). Halo mass function and the free streaming scale. *Monthly Notices of the Royal Astronomical Society*, **433**(2), 1573–1587.
- Shapley, H. (1938). Two Stellar Systems of a New Kind. *Nature*, **142**, 715–716.
- Shen, S., Madau, P., Guedes, J., Mayer, L., Prochaska, J. X., and Wadsley, J. (2013). The Circumgalactic Medium of Massive Galaxies at $z \sim 3$: A Test for Stellar Feedback, Galactic Outflows, and Cold Streams. *ApJ*, **765**, 89.
- Simon, J. D. and Geha, M. (2007). The Kinematics of the Ultra-faint Milky Way Satellites: Solving the Missing Satellite Problem. *ApJ*, **670**, 313–331.
- Simon, J. D., Geha, M., Minor, Q. E., Martinez, G. D., Kirby, E. N., Bullock, J. S., Kaplinghat, M., Strigari, L. E., Willman, B., Choi, P. I., Tollerud, E. J., and Wolf, J. (2011). A Complete Spectroscopic Survey of the Milky Way Satellite Segue 1: The Darkest Galaxy. *ApJ*, **733**, 46.
- Simon, J. D., Li, T. S., Drlica-Wagner, A., Bechtol, K., Marshall, J. L., James, D. J., Wang, M. Y., Strigari, L., Balbinot, E., Kuehn, K., Walker, A. R., Abbott, T. M. C., Allam, S.,

- Annis, J., Benoit-Lévy, A., Brooks, D., Buckley-Geer, E., Burke, D. L., Carnero Rosell, A., Carrasco Kind, M., Carretero, J., Cunha, C. E., D'Andrea, C. B., da Costa, L. N., DePoy, D. L., Desai, S., Doel, P., Fernandez, E., Flaugher, B., Frieman, J., García-Bellido, J., Gaztanaga, E., Goldstein, D. A., Gruen, D., Gutierrez, G., Kuropatkin, N., Maia, M. A. G., Martini, P., Menanteau, F., Miller, C. J., Miquel, R., Neilsen, E., Nord, B., Ogando, R., Plazas, A. A., Romer, A. K., Rykoff, E. S., Sanchez, E., Santiago, B., Scarpine, V., Schubnell, M., Sevilla-Noarbe, I., Smith, R. C., Sobreira, F., Suchyta, E., Swanson, M. E. C., Tarle, G., Whiteway, L., Yanny, B., and DES Collaboration (2017). Nearest Neighbor: The Low-mass Milky Way Satellite Tucana III. *ApJ*, **838**, 11.
- Somerville, R. S. (2002). Can Photoionization Squelching Resolve the Substructure Crisis? *ApJ*, **572**, L23–L26.
- Somerville, R. S. and Primack, J. R. (1999). Semi-analytic modelling of galaxy formation: the local Universe. *MNRAS*, **310**, 1087–1110.
- Somerville, R. S., Hopkins, P. F., Cox, T. J., Robertson, B. E., and Hernquist, L. (2008). A semi-analytic model for the co-evolution of galaxies, black holes and active galactic nuclei. *MNRAS*, **391**, 481–506.
- Sommer-Larsen, J., Götz, M., and Portinari, L. (2003). Galaxy Formation: Cold Dark Matter, Feedback, and the Hubble Sequence. *ApJ*, **596**, 47–66.
- Songaila, A. and Cowie, L. L. (1996). Metal enrichment and Ionization Balance in the Lyman Alpha Forest at $Z = 3$. *AJ*, **112**, 335.
- Spence, R. A. W., Zaurín, J. R., Tadhunter, C. N., Rose, M., Cabrera-Lavers, A., Spoon, H., and Muñoz-Tuñón, C. (2016). No evidence for large-scale outflows in the extended ionized halo of ULIRG Mrk273. *MNRAS*, **459**, L16–L20.
- Spergel, D. N., Bean, R., Doré, O., Nolta, M. R., Bennett, C. L., Dunkley, J., Hinshaw, G., Jarosik, N., Komatsu, E., Page, L., Peiris, H. V., Verde, L., Halpern, M., Hill, R. S., Kogut, A., Limon, M., Meyer, S. S., Odegard, N., Tucker, G. S., Weiland, J. L., Wollack, E., and Wright, E. L. (2007). Three-Year Wilkinson Microwave Anisotropy Probe (WMAP) Observations: Implications for Cosmology. *ApJS*, **170**, 377–408.
- Springel, V. (2005). The cosmological simulation code GADGET-2. *MNRAS*, **364**, 1105–1134.

- Springel, V. and Hernquist, L. (2002). Cosmological smoothed particle hydrodynamics simulations: the entropy equation. *MNRAS*, **333**, 649–664.
- Springel, V. and Hernquist, L. (2003). Cosmological smoothed particle hydrodynamics simulations: a hybrid multiphase model for star formation. *MNRAS*, **339**, 289–311.
- Springel, V., Yoshida, N., and White, S. D. M. (2001a). GADGET: a code for collisionless and gasdynamical cosmological simulations. *New Astronomy*, **6**, 79–117.
- Springel, V., White, S. D. M., Tormen, G., and Kauffmann, G. (2001b). Populating a cluster of galaxies - I. Results at $z=0$. *MNRAS*, **328**, 726–750.
- Stinson, G., Seth, A., Katz, N., Wadsley, J., Governato, F., and Quinn, T. (2006). Star formation and feedback in smoothed particle hydrodynamic simulations - I. Isolated galaxies. *MNRAS*, **373**, 1074–1090.
- Strigari, L. E., Bullock, J. S., Kaplinghat, M., Simon, J. D., Geha, M., Willman, B., and Walker, M. G. (2008). A common mass scale for satellite galaxies of the Milky Way. *Nature*, **454**, 1096–1097.
- Strigari, L. E., Frenk, C. S., and White, S. D. M. (2010). Kinematics of Milky Way satellites in a Lambda cold dark matter universe. *MNRAS*, **408**, 2364–2372.
- Strigari, L. E., Frenk, C. S., and White, S. D. M. (2014). Dynamical models for the Sculptor dwarf spheroidal in a Lambda CDM universe. *ArXiv e-prints*.
- Sturm, E., González-Alfonso, E., Veilleux, S., Fischer, J., Graciá-Carpio, J., Hailey-Dunsheath, S., Contursi, A., Poglitsch, A., Sternberg, A., Davies, R., Genzel, R., Lutz, D., Tacconi, L., Verma, A., Maiolino, R., and de Jong, J. A. (2011). Massive Molecular Outflows and Negative Feedback in ULIRGs Observed by Herschel-PACS. *ApJ*, **733**, L16.
- Susa, H. and Umemura, M. (2004). Formation of Dwarf Galaxies during the Cosmic Reionization. *ApJ*, **600**, 1–16.
- Sutherland, R. S. and Dopita, M. A. (1993). Cooling functions for low-density astrophysical plasmas. *ApJS*, **88**, 253–327.

- Teuben, P. (1995). The Stellar Dynamics Toolbox NEMO. In R. A. Shaw, H. E. Payne, and J. J. E. Hayes, editors, *Astronomical Data Analysis Software and Systems IV*, volume 77 of *Astronomical Society of the Pacific Conference Series*, page 398.
- Thacker, R. J. and Couchman, H. M. P. (2000a). High Resolution Simulation of Galaxy Formation with Feedback. *ArXiv Astrophysics e-prints*.
- Thacker, R. J. and Couchman, H. M. P. (2000b). Implementing Feedback in Simulations of Galaxy Formation: A Survey of Methods. *ApJ*, **545**, 728–752.
- Thacker, R. J., Tittley, E. R., Pearce, F. R., Couchman, H. M. P., and Thomas, P. A. (2000). Smoothed Particle Hydrodynamics in cosmology: a comparative study of implementations. *MNRAS*, **319**, 619–648.
- Theuns, T., Viel, M., Kay, S., Schaye, J., Carswell, R. F., and Tzanavaris, P. (2002). Galactic Winds in the Intergalactic Medium. *ApJ*, **578**, L5–L8.
- Thoul, A. A. and Weinberg, D. H. (1996). Hydrodynamic Simulations of Galaxy Formation. II. Photoionization and the Formation of Low-Mass Galaxies. *ApJ*, **465**, 608.
- Tollerud, E. J., Bullock, J. S., Strigari, L. E., and Willman, B. (2008). Hundreds of Milky Way Satellites? Luminosity Bias in the Satellite Luminosity Function. *ApJ*, **688**, 277–289.
- Tolstoy, E., Hill, V., Irwin, M., Helmi, A., Battaglia, G., Letarte, B., Venn, K., Jablonka, P., Shetrone, M., Arimoto, N., Abel, T., Primas, F., Kaufer, A., Szeifert, T., Francois, P., and Sadakane, K. (2006). The Dwarf galaxy Abundances and Radial-velocities Team (DART) Large Programme - A Close Look at Nearby Galaxies. *The Messenger*, **123**.
- Tolstoy, E., Hill, V., and Tosi, M. (2009). Star-Formation Histories, Abundances, and Kinematics of Dwarf Galaxies in the Local Group. *ARA&A*, **47**, 371–425.
- Tomozeiu, M., Mayer, L., and Quinn, T. (2016). The Evolution of Dwarf Galaxy Satellites with Different Dark Matter Density Profiles in the ErisMod Simulations. I. The Early Infalls. *ApJ*, **818**, 193.
- Torrealba, G., Koposov, S. E., Belokurov, V., Irwin, M., Collins, M., Spencer, M., Iбата, R., Mateo, M., Bonaca, A., and Jethwa, P. (2016a). At the survey limits: discovery of the Aquarius 2 dwarf galaxy in the VST ATLAS and the SDSS data. *MNRAS*, **463**, 712–722.

- Torrealba, G., Koposov, S. E., Belokurov, V., and Irwin, M. (2016b). The feeble giant. Discovery of a large and diffuse Milky Way dwarf galaxy in the constellation of Crater. *MNRAS*, **459**, 2370–2378.
- Trujillo-Gomez, S., Klypin, A., Primack, J., and Romanowsky, A. J. (2011). Galaxies in Λ CDM with Halo Abundance Matching: Luminosity-Velocity Relation, Baryonic Mass-Velocity Relation, Velocity Function, and Clustering. *ApJ*, **742**, 16.
- Ural, U., Cescutti, G., Koch, A., Kleyna, J., Feltzing, S., and Wilkinson, M. I. (2015). An inefficient dwarf: chemical abundances and the evolution of the Ursa Minor dwarf spheroidal galaxy. *MNRAS*, **449**, 761–770.
- Valcke, S., de Rijcke, S., Rödiger, E., and Dejonghe, H. (2010). Kelvin-Helmholtz instabilities in smoothed particle hydrodynamics. *MNRAS*, **408**, 71–86.
- van den Bergh, S. (1994). The evolutionary history of low-luminosity local group dwarf galaxies. *ApJ*, **428**, 617–619.
- Vogelsberger, M., Genel, S., Springel, V., Torrey, P., Sijacki, D., Xu, D., Snyder, G., Nelson, D., and Hernquist, L. (2014a). Introducing the Illustris Project: simulating the coevolution of dark and visible matter in the Universe. *MNRAS*, **444**, 1518–1547.
- Vogelsberger, M., Genel, S., Springel, V., Torrey, P., Sijacki, D., Xu, D., Snyder, G., Bird, S., Nelson, D., and Hernquist, L. (2014b). Properties of galaxies reproduced by a hydrodynamic simulation. *Nature*, **509**, 177–182.
- Walch, S. and Naab, T. (2015). The energy and momentum input of supernova explosions in structured and ionized molecular clouds. *MNRAS*, **451**, 2757–2771.
- Walker, M. G. and Peñarrubia, J. (2011). A Method for Measuring (Slopes of) the Mass Profiles of Dwarf Spheroidal Galaxies. *ApJ*, **742**, 20.
- Walker, M. G., Mateo, M., Olszewski, E. W., Gnedin, O. Y., Wang, X., Sen, B., and Woodroffe, M. (2007). Velocity Dispersion Profiles of Seven Dwarf Spheroidal Galaxies. *ApJ*, **667**, L53–L56.
- Walker, M. G., Mateo, M., Olszewski, E. W., Peñarrubia, J., Wyn Evans, N., and Gilmore, G. (2009a). A Universal Mass Profile for Dwarf Spheroidal Galaxies? *ApJ*, **704**, 1274–1287.

- Walker, M. G., Mateo, M., Olszewski, E. W., Sen, B., and Woodroffe, M. (2009b). Clean Kinematic Samples in Dwarf Spheroidals: An Algorithm for Evaluating Membership and Estimating Distribution Parameters When Contamination is Present. *AJ*, **137**, 3109–3138.
- Walker, M. G., Belokurov, V., Evans, N. W., Irwin, M. J., Mateo, M., Olszewski, E. W., and Gilmore, G. (2009c). Leo V: Spectroscopy of a Distant and Disturbed Satellite. *ApJ*, **694**, L144–L147.
- Walker, M. G., Mateo, M., and Olszewski, E. W. (2009d). Stellar Velocities in the Carina, Fornax, Sculptor, and Sextans dSph Galaxies: Data From the Magellan/MMFS Survey. *AJ*, **137**, 3100–3108.
- Walker, M. G., Mateo, M., Olszewski, E. W., Bailey, III, J. I., Koposov, S. E., Belokurov, V., and Evans, N. W. (2015). Magellan/M2FS Spectroscopy of the Reticulum 2 Dwarf Spheroidal Galaxy. *ApJ*, **808**, 108.
- Walker, M. G., Mateo, M., Olszewski, E. W., Koposov, S., Belokurov, V., Jethwa, P., Nidever, D. L., Bonnavard, V., Bailey, III, J. I., Bell, E. F., and Loebman, S. R. (2016). Magellan/M2FS Spectroscopy of Tucana 2 and Grus 1. *ApJ*, **819**, 53.
- Walsh, S. M., Jerjen, H., and Willman, B. (2007). A Pair of Boötes: A New Milky Way Satellite. *ApJ*, **662**, L83–L86.
- Wannier, P., Wrixon, G. T., and Wilson, R. W. (1972). A Survey of Positive Velocity Neutral Hydrogen above the Galactic Plane between $l = 2520$ and $l = 3220$. *A&A*, **18**, 224.
- Weisz, D. R., Dolphin, A. E., Skillman, E. D., Holtzman, J., Gilbert, K. M., Dalcanton, J. J., and Williams, B. F. (2014a). The Star Formation Histories of Local Group Dwarf Galaxies. I. Hubble Space Telescope/Wide Field Planetary Camera 2 Observations. *ApJ*, **789**, 147.
- Weisz, D. R., Dolphin, A. E., Skillman, E. D., Holtzman, J., Gilbert, K. M., Dalcanton, J. J., and Williams, B. F. (2014b). The Star Formation Histories of Local Group Dwarf Galaxies. II. Searching For Signatures of Reionization. *ApJ*, **789**, 148.

- Weisz, D. R., Dolphin, A. E., Skillman, E. D., Holtzman, J., Gilbert, K. M., Dalcanton, J. J., and Williams, B. F. (2014c). The Star Formation Histories of Local Group Dwarf Galaxies. II. Searching For Signatures of Reionization. *ApJ*, **789**, 148.
- Wendland, H. (1995). *Adv. Comp. Math.*, **4**, 389.
- Wetzel, A. R., Hopkins, P. F., Kim, J.-h., Faucher-Giguère, C.-A., Kereš, D., and Quataert, E. (2016). Reconciling Dwarf Galaxies with Λ CDM Cosmology: Simulating a Realistic Population of Satellites around a Milky Way-mass Galaxy. *ApJ*, **827**, L23.
- Wheeler, C., Phillips, J. I., Cooper, M. C., Boylan-Kolchin, M., and Bullock, J. S. (2014). The surprising inefficiency of dwarf satellite quenching. *MNRAS*, **442**, 1396–1404.
- White, S. D. M. (1976). The dynamics of rich clusters of galaxies. *MNRAS*, **177**, 717–733.
- White, S. D. M. (1978). Simulations of merging galaxies. *MNRAS*, **184**, 185–203.
- Whiting, A. B., Hau, G. K. T., and Irwin, M. (1999). A New Local Group Galaxy in Cetus. *AJ*, **118**, 2767–2774.
- Willman, B., Blanton, M. R., West, A. A., Dalcanton, J. J., Hogg, D. W., Schneider, D. P., Wherry, N., Yanny, B., and Brinkmann, J. (2005a). A New Milky Way Companion: Unusual Globular Cluster or Extreme Dwarf Satellite? *AJ*, **129**, 2692–2700.
- Willman, B., Dalcanton, J. J., Martinez-Delgado, D., West, A. A., Blanton, M. R., Hogg, D. W., Barentine, J. C., Brewington, H. J., Harvanek, M., Kleinman, S. J., Krzesinski, J., Long, D., Neilsen, Jr., E. H., Nitta, A., and Snedden, S. A. (2005b). A New Milky Way Dwarf Galaxy in Ursa Major. *ApJ*, **626**, L85–L88.
- Wilson, A. G. (1955). Sculptor-Type Systems in the Local Group of Galaxies. *PASP*, **67**, 27–29.
- Wolf, J., Martinez, G. D., Bullock, J. S., Kaplinghat, M., Geha, M., Muñoz, R. R., Simon, J. D., and Avedo, F. F. (2010). Accurate masses for dispersion-supported galaxies. *MNRAS*, **406**, 1220–1237.
- Wu, J., Evans, II, N. J., Gao, Y., Solomon, P. M., Shirley, Y. L., and Vanden Bout, P. A. (2005). Connecting Dense Gas Tracers of Star Formation in our Galaxy to High-z Star Formation. *ApJ*, **635**, L173–L176.

- Wyse, R. F. G., Gilmore, G., Houdashelt, M. L., Feltzing, S., Hebb, L., Gallagher, III, J. S., and Smecker-Hane, T. A. (2002). Faint stars in the Ursa Minor dwarf spheroidal galaxy: implications for the low-mass stellar initial mass function at high redshift. *New Astronomy*, **7**, 395–433.
- York, D. G., Adelman, J., Anderson, Jr., J. E., Anderson, S. F., Annis, J., Bahcall, N. A., Bakken, J. A., Barkhouser, R., Bastian, S., Berman, E., Boroski, W. N., Bracker, S., Briegel, C., Briggs, J. W., Brinkmann, J., Brunner, R., Burles, S., Carey, L., Carr, M. A., Castander, F. J., Chen, B., Colestock, P. L., Connolly, A. J., Crocker, J. H., Csabai, I., Czarapata, P. C., Davis, J. E., Doi, M., Dombeck, T., Eisenstein, D., Ellman, N., Elms, B. R., Evans, M. L., Fan, X., Federwitz, G. R., Fiscelli, L., Friedman, S., Frieman, J. A., Fukugita, M., Gillespie, B., Gunn, J. E., Gurbani, V. K., de Haas, E., Haldeman, M., Harris, F. H., Hayes, J., Heckman, T. M., Hennesy, G. S., Hindsley, R. B., Holm, S., Holmgren, D. J., Huang, C.-h., Hull, C., Husby, D., Ichikawa, S.-I., Ichikawa, T., Ivezić, Ž., Kent, S., Kim, R. S. J., Kinney, E., Klaene, M., Kleinman, A. N., Kleinman, S., Knapp, G. R., Korienek, J., Kron, R. G., Kunszt, P. Z., Lamb, D. Q., Lee, B., Leger, R. F., Limmongkol, S., Lindenmeyer, C., Long, D. C., Loomis, C., Loveday, J., Lucinio, R., Lupton, R. H., MacKinnon, B., Mannery, E. J., Mantsch, P. M., Margon, B., McGehee, P., McKay, T. A., Meiksin, A., Merelli, A., Monet, D. G., Munn, J. A., Narayanan, V. K., Nash, T., Neilsen, E., Neswold, R., Newberg, H. J., Nichol, R. C., Nicinski, T., Nonino, M., Okada, N., Okamura, S., Ostriker, J. P., Owen, R., Pauls, A. G., Peoples, J., Peterson, R. L., Petravick, D., Pier, J. R., Pope, A., Pordes, R., Prosapio, A., Rechenmacher, R., Quinn, T. R., Richards, G. T., Richmond, M. W., Rivetta, C. H., Rockosi, C. M., Ruthmansdorfer, K., Sandford, D., Schlegel, D. J., Schneider, D. P., Sekiguchi, M., Sergey, G., Shimasaku, K., Siegmund, W. A., Smee, S., Smith, J. A., Snedden, S., Stone, R., Stoughton, C., Strauss, M. A., Stubbs, C., SubbaRao, M., Szalay, A. S., Szapudi, I., Szokoly, G. P., Thakar, A. R., Tremonti, C., Tucker, D. L., Uomoto, A., Vanden Berk, D., Vogeley, M. S., Waddell, P., Wang, S.-i., Watanabe, M., Weinberg, D. H., Yanny, B., Yasuda, N., and SDSS Collaboration (2000). The Sloan Digital Sky Survey: Technical Summary. *AJ*, **120**, 1579–1587.
- Zhao, D. H., Jing, Y. P., Mo, H. J., and Börner, G. (2003). Mass and Redshift Dependence of Dark Halo Structure. *ApJ*, **597**, L9–L12.
- Zhao, D. H., Jing, Y. P., Mo, H. J., and Börner, G. (2009). Accurate Universal Models

- for the Mass Accretion Histories and Concentrations of Dark Matter Halos. *ApJ*, **707**, 354–369.
- Zolotov, A., Brooks, A. M., Willman, B., Governato, F., Pontzen, A., Christensen, C., Dekel, A., Quinn, T., Shen, S., and Wadsley, J. (2012). Baryons Matter: Why Luminous Satellite Galaxies have Reduced Central Masses. *ApJ*, **761**, 71.
- Zubovas, K. and King, A. (2012). Clearing Out a Galaxy. *ApJ*, **745**, L34.
- Zubovas, K. and King, A. (2016). The small observed scale of AGN-driven outflows, and inside-out disc quenching. *MNRAS*, **462**, 4055–4066.
- Zubovas, K. and Nayakshin, S. (2012). Fermi bubbles in the Milky Way: the closest AGN feedback laboratory courtesy of Sgr A*? *MNRAS*, **424**, 666–683.
- Zubovas, K., King, A. R., and Nayakshin, S. (2011). The Milky Way’s Fermi bubbles: echoes of the last quasar outburst? *MNRAS*, **415**, L21–L25.
- Zucker, D. B., Belokurov, V., Evans, N. W., Kleyna, J. T., Irwin, M. J., Wilkinson, M. I., Fellhauer, M., Bramich, D. M., Gilmore, G., Newberg, H. J., Yanny, B., Smith, J. A., Hewett, P. C., Bell, E. F., Rix, H.-W., Gnedin, O. Y., Vidrih, S., Wyse, R. F. G., Willman, B., Grebel, E. K., Schneider, D. P., Beers, T. C., Kniazev, A. Y., Barentine, J. C., Brewington, H., Brinkmann, J., Harvanek, M., Kleinman, S. J., Krzesinski, J., Long, D., Nitta, A., and Snedden, S. A. (2006a). A Curious Milky Way Satellite in Ursa Major. *ApJ*, **650**, L41–L44.
- Zucker, D. B., Belokurov, V., Evans, N. W., Wilkinson, M. I., Irwin, M. J., Sivarani, T., Hodgkin, S., Bramich, D. M., Irwin, J. M., Gilmore, G., Willman, B., Vidrih, S., Fellhauer, M., Hewett, P. C., Beers, T. C., Bell, E. F., Grebel, E. K., Schneider, D. P., Newberg, H. J., Wyse, R. F. G., Rockosi, C. M., Yanny, B., Lupton, R., Smith, J. A., Barentine, J. C., Brewington, H., Brinkmann, J., Harvanek, M., Kleinman, S. J., Krzesinski, J., Long, D., Nitta, A., and Snedden, S. A. (2006b). A New Milky Way Dwarf Satellite in Canes Venatici. *ApJ*, **643**, L103–L106.
- Zuckerman, B. and Evans, II, N. J. (1974). Models of massive molecular clouds. *ApJ*, **192**, L149–L152.